ABSTRACT

Title of dissertation: DYNAMICS OF NEAR-ALPHA TITANIUM WELDING

Brett William Neuberger, Doctor of Philosophy, 2004

Dissertation directed by: Associate Professor Sreeramamurthy Ankem
Department of Materials Science and Engineering

Typically, when gas tungsten arc welding (GTAW) is employed to join near-alpha titanium alloys, the resulting weld fusion zone (FZ) is much harder than that of the base metal (BM), thereby leading to lost ductility. The aim of this investigation was to improve FZ ductility of Ti-5Al-1Sn-1V-1Zr-0.8Mo by modifying filler metal chemistry. In this regard, metallic yttrium was added to the filler metal and aluminum concentration reduced. It was believed that additions of yttrium would lead to formation of yttria in the weld melt, thereby promoting heterogeneous nucleation. Since oxygen and aluminum both act as alpha-stabilizers, expected pickup of oxygen during the welding process will be offset by the aluminum reduction.

Tensile testing indicated that modified filler metal welds showed a dramatic increase in ductility of the FZ. Fracture toughness testing showed that while J_{IC} values decreased in all welds, the tearing modulus, T, in modified filler metal welds was significantly higher than that of matching filler metal welds. Microhardness mapping of the weld zones illustrated that modified filler metal welds were significantly softer than matching filler metal welds. Microstructural examinations were completed through the use of optical, SEM and TEM studies, indicating that there was a presence of nano-particles in the weld FZ. XPS analysis identified these particles as yttrium oxysulfate.

WDS analysis across the welds' heat affected zones demonstrated that there is an internal diffusion of oxygen from the BM into the FZ.

Research results indicate yttrium oxysulfide particles form in the weld pool, act as a drag force on the solidification front and limit growth of prior-beta grain boundaries. The reduced prior-beta grain size and removal of interstitial oxygen from the matrix in modified filler metal welds, further enhanced by oxidation of yttrium oxysulfide to yttrium oxysulfate, leads to increased ductility in the weld's FZ. Addition of yttrium to the weld also acts to modify the surface tension of the melt, leading to an increased weld depth penetration. Results of this work indicate that the goals of this project and a significant advancement in the understanding of yttrium effects on titanium grain refinement have been achieved.

DYNAMICS OF NEAR-ALPHA TITANIUM WELDING

by

Brett William Neuberger

Dissertation submitted to the Faculty of the Graduate School of the
University of Maryland, College Park in partial fulfillment
of the requirements for the degree of
Doctor of Philosophy
2004

Advisory Committee:

Associate Professor Sreeramamurthy Ankem, Chair/Advisor
Professor Aris Christou
Associate Professor Isabel Lloyd
Professor Lourdes Salamanca-Riba
Associate Professor Evanghelos Zafiriou

ACKNOWLEDGEMENTS

First and foremost I would like to thank my wife Carla, whose never-ending support, encouragement, and self-sacrifices have allowed me to complete my graduate studies. Without her, none of this would be possible.

I would like to thank my advisor Dr. S. Ankem for giving me this research project and allowing me the freedom to express and investigate my own ideas, for providing guidance and insight when needed most and for his friendship. Without his dedication to me and this project, this dissertation would not have materialized.

I would like to thank John Cataldi of the Physics Machine Shop for all his help in fabricating specimens and test equipment, Tiejun (Tim) Zhang, Laboratory Manager for the Center for Microanalysis, for all his help in imaging specimens both under SEM and TEM and Dr. Bindhu Varughese, XPS Facility Manager of the Chemistry Department, who analyzed my specimens free of charge. I am especially indebted to Dr. Phil Piccoli, who spent many hours helping me with the microprobe and WDS measurements. I offer my sincere gratitude to Dr. Edward Metzbower of the Naval Research Laboratories Materials Science and Technology Division for allowing me use of their facilities and to Dr. Deug Moon who instructed me on the use of their microhardness mapping equipment. I would like to thank my colleagues Allan Jaworski, Jr., for all his help in using the TEM, review of this thesis and for his friendship throughout graduate school and Greg Oberson for his thorough review of this thesis. I would also like to thank the entire faculty, staff and students of the Materials Science and Engineering Department for their support and assistance in response to my random questions.

I would like to thank all of the Committee members for taking time out of their busy schedules to review this work and for providing helpful insight when needed. I am deeply appreciative to Dr. Julie Christodoulou and Dr. George Yoder of the Office of Naval Research for their interest in this project and for valuable suggestions throughout the entire course of this project.

I gratefully acknowledge James Grauman of TIMET for materials supplied to this project and to Mike Wells of the Naval Surface Warfare Center for additional materials and discussions on this project. Finally, I am very grateful for the financial support provided by the Office of Naval Research under grant number 140310591 and the National Defense Science and Engineering Graduate Fellowship Program.

TABLE OF CONTENTS

LIST OF TABLES

LIST OF FIGURES

I. INTRODUCTION

I.1 Background

Titanium has one of the highest strength-to-weight ratios of any of today's materials and is capable of operating under high temperature applications [1]. Table 1 compares the properties of titanium with other structural materials. Titanium offers a long life, requires little maintenance, is highly corrosion resistant and is one of the most biocompatible materials. These properties are what have enabled titanium to find uses in the aerospace and defense industries as well as new uses in the commercial manufacturing sector. Traditional aerospace and defense industry uses include military aircraft frames and engines, navy ship and submarine hulls and piping, and tank and fighting vehicle armor. New commercial uses include golf clubs, bicycles, medical implants and jewelry.

Table 1: Properties of titanium and other structural materials [2].

Property	Titanium	1020 Steel	18-8 Stainless	7075 Aluminum
Structure	HCP	BCC	FCC	FCC
Specific weight, [kg/m^3]	4429	7751	7751	2768
Ultimate tensile strength, annealed, [MN/m^2]	551.6	344.7	620.5	82.7
Young's modulus, E, [GN/m^2]	110.3	206.8	206.8	68.9
Shear modulus, G, [GN/m^2]	41.4	79.3	79.3	27.6
Melting point, [K]	1941	1700	1700	933
Thermal conductivity, k, [kJ/m/sec]	83.1	311.5	91.4	664.6

Titanium can exist in one of two crystal forms [1]. A low temperature α phase is a hexagonal close packed (hcp) structure, while a high temperature β phase exists in the body centered cubic (bcc) structure. Titanium in its pure form will undergo an allotropic transformation from the hcp (α) phase to the bcc (β) phase as temperature is raised

through 1155.7 K (882.5°C). The β phase is then stable to the titanium melting point, 1941.2 K (1668°C). The phase transformation temperature can be raised or lowered depending upon what types of alloying elements are added to the pure titanium. Elements that cause little change at all or cause the transition temperature to increase are known as α stabilizers. Alloying elements that cause the transition temperature to lower are known as β stabilizers. Accordingly, titanium alloys can be classified as "α," "β," and "α+β" alloys.

Alpha alloys are produced by α stabilizers such as C, O, N, Al, Ga and Sn. These alloys are characterized by medium strength, good toughness and are generally very weldable. They possess excellent mechanical properties at cryogenic temperatures and the highly alloyed α and near-α alloys offer optimum high temperature creep strength and oxidation resistance as well.

Beta stabilizers such as V, Nb, Cr, Fe, Mn, Ta and Mo produce β alloys which are characterized by their extreme formability as they are heat treatable and generally weldable. These alloys are capable of high strengths and offer good creep resistance at intermediate temperatures. They are prone to ductile-to-brittle transformation, as with other bcc-phase alloys, and are therefore unsuitable for low temperature applications.

Alpha + beta alloys support a mixture of both α and β phases, and usually contain both α and β stabilizers. These alloys generally have good fabricability and high room temperature strength. They offer moderate elevated temperature strength, but their high temperature creep strength is not as good as most α alloys. Alpha + beta alloys may contain anywhere between 10 to 50% β phase at room temperature, but if they contain

over 20%, they are not weldable. Alpha + beta properties are controlled by heat treatment that adjusts the microstructure and precipitation state of the β component.

A near-α titanium alloy will be the concentration of this work due to its good strength and weldability and its high fracture toughness. The α-stabilizing solute is typically a non-transition metal or simple metal (SM). When this SM is dissolved into the titanium, very few electrons appear in the Fermi band as most go to states within the lower part of the band [1]. The *d*-electrons of the titanium will tend to avoid the SM atoms, thereby, in effect, diluting the titanium sublattice. This causes any existing Ti-Ti bond directionality to be emphasized, which preserves the hcp structure of the titanium crystal. The SM added to titanium thereby causes fields of Ti-like α stability to be eventually terminated by intermetallic compounds of the composition Ti_3SM, which is also hexagonal in structure. Alpha stabilizers are therefore quite rapid solution strengtheners in hcp solid solution or bcc alloys.

I.2 Welding Techniques

In general, when an α+β titanium alloy is welded, a decrease in ductility and increase in strength results, compared to the parent material. As β stabilizer percentage is increased, strength will increase, but ductility drops dramatically. A dilute α+β or near-α titanium alloy has lower strength but higher ductility.

The common techniques to weld titanium include electron beam welding (EBW), gas tungsten arc welding (GTAW), gas metal arc welding (GMAW), plasma arc welding (PAW) and laser beam welding (LBW) [3]. A diagram of a GTAW apparatus can be seen in Figure 1 [4]. The welding techniques themselves can have an effect on the resulting microstructure and thus affect the strength and ductility of the weld. The

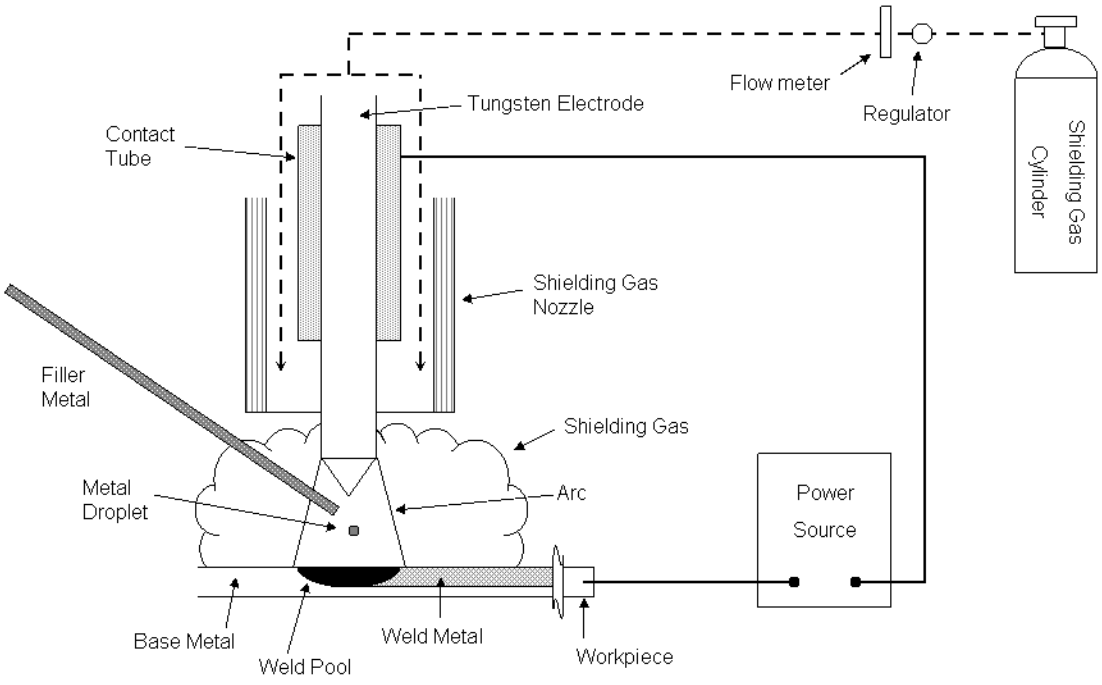

Figure 1: Schematic diagram of GTAW apparatus showing important parameters. Tungsten electrode, shielding gas nozzle and contact tube are actually contained inside the weld torch.

cooling rate of a weld is inversely proportional to its heat input [5]. In EBW and LBW, there is a low energy input and therefore a rapid cooling rate. GTAW, GMAW and PAW have higher heat inputs and as a result have slower cooling rates [6].

Gas tungsten arc welding (GTAW) is also known as HeliArc, tungsten inert gas (TIG) and tungsten arc welding. The key components and parameters associated with GTAW include the arc, shielding gas, weld speed, power source and filler metal. GTAW is used extensively for welding stainless steel, Al, Mg, Ca and reactive materials such as Ti and Ta. The sizes of material that may be welded range from under a millimeter to several centimeters in thickness.

Advantages of GTAW include [7]:

- Produces high quality, low distortion welds.
- Free of spatter, associated with other methods.
- Can be used with or without filler wire.
- Can be used with a range of power supplies.
- Welds almost all metals, including dissimilar ones.
- Gives precise control of welding heat.

Limitations of GTAW include [7]:

- Produces lower deposition rates than consumable electrode arc welding processes.
- Requires slightly more dexterity and welder coordination then gas metal arc welding (GMAW) or shielded metal arc welding (SMAW) for manual welding.
- Less economical than consumable electrode arc welding for thick sections greater than 9.5 mm.

- Problematic in drafty environments because of difficulty in shielding the weld zone properly.

Additional problems that may be encountered in GTAW include [7]:

- Tungsten inclusions if the electrode is allowed to contact the weld pool.
- Contamination of the weld metal if proper shielding of the filler metal by the gas stream is not maintained.
- Low tolerance for contaminants in filler or base metal.
- Contamination or porosity, caused by coolant leakage from water-cooled torches.
- Arc blow or arc deflection, as with other processes.

Main components of the GTA Welder include the torch, electrodes, power supply, wire feed system, cables, hoses and gas regulators [7]. The torch holds the tungsten electrode that conducts the current to arc and provides a means of shielding the arc and molten metal. If the torch is rated <200 A, it is usually gas cooled via the shield gas. Ratings >200 A or continuously operating systems are generally water-cooled.

The electrodes in the GTA Welder are non-consumable and are either pure tungsten or a tungsten alloy. These electrodes are classified as to their chemical composition. The shape of the tip of the electrode can influence the resulting shape of the weld. If the electrode contains included angles from 60 to 120°, the resulting weld has good penetration and depth-to-width ratio. Smaller included angles (5 to 30°) are used for grooved weld joints in order to eliminate arcing to the part sidewalls.

The power supply associated with the GTAW process is usually a constant current type with a drooping (negative) volt-ampere curve. The basic wire-feed system consists of a means to grip the wire, pull it from a spool and push it through the guide tube to the

point of welding. The cables, hoses and gas regulators serve to deliver the electricity, water and inert gas necessary for the process, to the torch.

The process parameters associated with GTAW include the welding current, shielding gases and filler metals. The welding current is one of the most important because it is directly related to the depth of penetration, deposition rate, welding speed and overall quality of the weld. There are three choices for welding currents:

1) DC electrode negative (DCEN)
2) DC electrode positive (DCEP)
3) AC

The welding current may be either pulsed or non-pulsed. The non-pulsed is what is standard in welding operations. The pulsed however, will produce the maximum amount of penetration while minimizing the total heat applied to the component being welded. It will also allow the weld pool to cool during weld pulses, resulting in a different microstructure.

For the shielding gases, helium was originally used, but argon is predominantly in use today. The Ar gas is the less expensive of the two and has a low ionization potential (15.7 eV), making it easier to form an arc plasma than with other shield gases. The Ar is also 1.4x heavier than air, thereby causing the air to be displaced, which results in excellent shielding of the molten weld pool. Helium has a 24.5 eV ionization potential, which causes operation at a higher arc voltage, and results in a higher heat input for a given arc length and current. This can be a benefit in some welding cases, such as for Cu and Al.

Parameters associated with the shielding gas include purity, flow rate and backup purge. For most metals, gases with a 99.995% purity (or 50 ppm impurities) are acceptable. However, the highly reactive metals such as Ti, Ta and Mo, require impurities to be <50 ppm. Typical gas flow rates for Ar and He are 7 L/min and 14 L/min respectively. The higher flow rate of the He is attributed to its lower density. A backup purge is very important to prevent atmospheric contamination of the molten pool. Atmospheric contamination may result in cracking, porosity, scaling and an unacceptable appearance. For this reason, trailing devices or weld chambers should be used.

Use of GTAW filler metals depends on the thickness of the component to be welded. If a material is <3.2 mm, it may be welded without the use of a filler metal. Thicker materials require filler metal additions for successful welds. The filler metals can be manually added in straight length or automatically from a roll or coil and may be added cold or hot. Often a preplaced filler material that may be of several configurations, known as a welding insert, will be used to aid in root-pass welding.

I.3 Weld Zone Transformations

Solidification of a weld in an $\alpha+\beta$ titanium alloy generally takes place in an epitaxial manner [8]. Beta crystals will decompose in the solid state after further cooling takes place. This solid-state transformation may either occur by diffusion into an α phase or martensitically to the α' phase. Often a mixture of both will be present as the actual mode of transformation will depend upon alloy chemistry and cooling rates. The as-welded microstructure may therefore contain a mixture of α, α', and retained β phases. When a near-α titanium alloy is rapidly cooled from the β phase through the equilibrium

α+β region, a resulting structure of martensite is formed. Less rapid cooling from the same temperature provides an opportunity for α phase nucleation and growth, yielding the characteristic Widmanstätten structure [1]. Higher cooling rates will also produce thin α and α′ which provide a poor medium for energy absorption, resulting in a lower toughness [5]. The greater the α plate width, the greater the weld ductility. This is often increased by a post weld heat treatment (PWHT). In addition to martensite, characteristic microstructures in titanium alloy welds can include [1]: (a) Equiaxed α and a small amount of intergranular β. (b) Equiaxed and acicular α and a small amount of intergranular β. (c) Equiaxed α in an acicular α (transformed β) matrix. (d) Small amount of equiaxed α in an acicular α (transformed β) matrix. (e) Plate-like acicular α (transformed β); α at prior β grain boundaries. (f) Blocky and plate-like acicular α (transformed β); α at prior β grain boundaries.

The low heat input, rapidly cooled resulting microstructures are a lath-type or "massive" martensite and/or acicular martensite [9]. Massive martensite transformation takes place on a large scale and involves considerable structural coherence. It will consist of large irregular zones of the size 50-100 μm, which are subdivided into parallel arrays of fine platelets <1 μm across. When the coherency between the platelets is lost, a partially disordered array of individual platelets results, which are known as the acicular, needle-like, martensite. The reason that these rapidly cooled dilute alloys transform to the lath-type martensite is due to the fact that a high M_s temperature favors slip in the β phase ahead of the α′ plate, which reduces the shape strain of the martensite transformation [9]. The high heat input, slower cooling rate of the GTAW produces a microstructure consisting of a mixture of lamellar α and β phases formed strictly by

diffusion, which is known as the Widmanstätten structure [9]. These Widmanstätten structures closely resemble the acicular martensitic structures, therefore requiring TEM analysis for distinction.

Diffusional transformations may occur through several modes of α nucleation and growth. The more diffusional α that is present, the better the toughness of the welded specimen. The transition from diffusional to shear growth (and vice versa) is not a sharply defined one. The hcp phase formed by the diffusional transformation exhibits the same habit plane and orientation as that of the β phase transformation due to shear [9].

GTAW produces an entirely lamellar grain microstructure. The lamellar α is characterized by a greater fracture toughness, fatigue crack propagation resistance and creep strength. An equiaxed α microstructure would yield superior tensile ductility, fatigue crack initiation resistance and elevated temperature flow characteristics [10]. Acicular structures in the as-welded material are easily obtained by cooling from the β phase field. To obtain an equiaxed structure from the acicular structure, mechanical deformation below the β transition temperature, followed by a recrystallization heat treatment is required. PWHT's, which are often performed to increase the ductility of a weld, will only coarsen the microstructure without altering its lamellar character [8].

In the PWHT, the welded materials metastable microstructure will seek to attain a thermodynamic equilibrium by two important reactions [8, 9]:

1) Formation of the β phase in the martensite, which will lower the β-stabilizer content and thus result in the equilibrium α phase in composition; and,

2) Precipitation of α in retained metastable β.

High temperatures and long times of PWHT will result in considerable coarsening of the α phase at both the grain boundary and within the grain, thereby, increasing the energy absorbing capacity as a result of the improved ductility.

When welding titanium, two distinct microstructural regions form during the process [11]:

1) Fusion zone (FZ) – melting, solidification and solid state transformations; and,
2) Heat affected zone (HAZ) – phase transformations in solid state only.

A diagram of the weld zone can be seen in Figure 2.

In the HAZ, there exist two separate regions in which experiments have shown that there is a coexistence of bcc and hcp in a partially transformed outer region and a single-phase bcc in a fully transformed inner region [11]. The larger grain size in the fully transformed HAZ is attributed to a combination of increased time at temperature in the single phase field and the fact that grain growth rapidly accelerates as the relative fraction of the β phase approaches unity. Microstructural history of the FZ and HAZ are as follows:

FZ: hcp $\rightarrow$ bcc $\rightarrow$ liquid $\rightarrow$ bcc $\rightarrow$ hcp

HAZ: hcp $\rightarrow$ bcc $\rightarrow$ hcp.

FZ grain growth occurs via epitaxial solidification. In epitaxial solidification of the FZ, grain size is dictated by the near HAZ grain size [5]. In the near HAZ, there is a complete transformation from equiaxed primary α. This is due to exposure of the inner region to temperatures greater than the β transition temperature for a sufficiently long time period [12]. This fully transformed region produces a large grain structure, thus

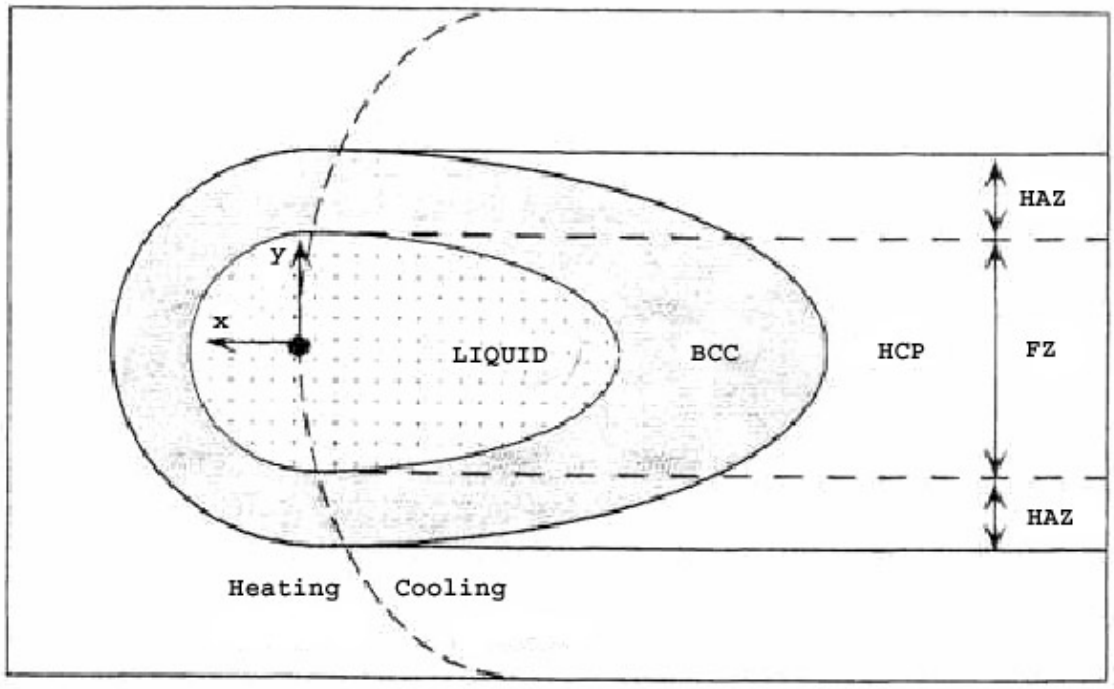

Figure 2: Diagram illustrating the weld zone in titanium. The molten metal liquid pool is surrounded by a bcc phase field, which is surrounded by a hcp phase field. The FZ represents the areas of the weld that have undergone melting and solidification. The HAZ represents the areas that have been heated above the beta-transus temperature.

leading to wider FZ grains that increase continuously with increasing energy input [12]. This leads to a coarse β phase, which is directly related to a decrease in ductility.

I.4 Refining Weld Microstructures

There have been several methods used to refine the grain structure of welds in the past. Since in α+β titanium alloys, it has been seen that a large prior-β grain size and an acicular, at least partially martensitic matrix structure produces extremely low tensile ductility in the FZ weld structure, the methods aim to reduce the prior-β grain size and eliminate the acicular martensite structure. While it is very desirable to control the solidified grain structure, this is a very difficult process due to the high temperatures and high temperature gradients associated with welding and the nature of the epitaxial growth process. Ductility cannot be improved via heat input alteration because a high energy input will coarsen the prior-β grains, while a low heat input will result in a faster cooling rate and an increase in the aspect ratio of the intragranular structure [8]. Methods that have been tried include heterogeneous nucleation, mechanical deformation, electromagnetic stirring, microcooler inoculation, pulsed welding currents, introduction of vibrations by mechanical, sonic and ultrasonic means and surface nucleation induced by gas impingement.

Sunderasan et al [8] showed that by using a pulsed alternating current in GTAW of titanium alloys, an as-welded structure with a much-improved ductility resulted. It was seen that the AC pulsing promoted decomposition of the β phase by diffusional reaction rather than shear, thus leading to less martensite α′ formation. The pulsing of the weld current affected the temperature distribution, caused thermal fluctuations and

enhanced fluid motion in the weld pool. The thermal fluctuations caused the maximum thermal gradient at the weld boundary to change with time. Therefore, instead of a few favorably oriented grains growing over long distances, newer grains became favorably oriented with respect to the instantaneous direction of the maximum thermal gradient. The mechanical agitation of the pool by the pulsing served to bring dendrite fragments ahead of the solid-liquid interface, thereby serving as sites for heterogeneous growth which block the columnar grain size and appreciably improve ductility.

Murthy et al [10] sought to obtain a more bimodal (equiaxed and lamellar) weld structure from the resulting lamellar α morphology of an EB weld zone in a Ti-Al-Mn, near-α alloy. In order to obtain the equiaxed structures, a thermomechanical process on the weld consisting of hot rolling and a recrystallization treatment was performed. While this process did produce a more equiaxed structure, surprisingly it did not lead to as good a combination of ductility and toughness as that resulting from a simple PWHT of the as-welded material.

While heterogeneous nucleation has been used extensively in C-Mn steel fabrications, little research has been done concerning titanium alloys. The major alloying elements associated with affecting the toughness of these steel welds include C, Mn, Si, Mo and Ni. Minor alloying elements include Ti, Al, Mg, Ca, Ce and B. Impurities that have been determined to be detrimental to the weld toughness are O, S, P and N.

Abson and Pargeter [13] provide a thorough review of factors influencing the as-deposited strength, microstructure and toughness of manual metal arc welds in C-Mn steel. Additions of rare earth metals (REM's), calcium, magnesium and zirconium tend to increase toughness when added in appropriate amounts. Cerium and yttrium in the

ranges 0.15 to 0.20% and 0.04 to 0.10% respectively, added to rutile coated electrodes, yield a large increase in toughness. These additions serve to interact strongly with oxygen and sulfur, thereby reducing the inclusion content. The REM's will tend to increase the impact toughness by refining grain size and offering an improved resistance to hydrogen induced cracking.

Oxygen additions [13] will tend to reduce the upper shelf toughness of weld metals where fracture occurs by microvoid coalescence. The O content will also have both a direct and indirect influence on the lower shelf toughness. The larger O inclusions will be able to initiate cleavage fracture and assist in the formation of coarse transformation products in the as-deposited microstructure. Very low O concentrations will, however, also have an adverse effect on toughness. The low levels will allow the formation of coarse as-deposited microstructures. Optimum levels have been found to be in the range 0.02 to 0.06%. Lower levels would be desirable if there was a way to control microstructure.

Norman et al [14] used an aluminum alloy to demonstrate that a combination of high welding speeds and low power densities in TIG welding provided the thermal conditions required to form equiaxed grains in the weld pool, provided heterogeneous nucleation sites were available. They believed that the nucleation catalysts were broken dendrite fragments and TiB_2 particles that remained in the alloy from casting. By using the higher welding speed and low power density, nucleants were not allowed to re-melt in the weld pool and were thus available as nucleation sites. Grain refining additions of Ti and Zr that were added to the weld filler decreased the welding speed at which the columnar to equiaxed grain transition occurred.

The effects of boron additions to welds of the near-α titanium alloy Ti-6Al-2Nb-1Ta-1Mo (Ti-6211) have been studied by Lewis et al [15]. It was seen that a weld metal with a higher B content (0.004 wt%) had an average toughness value 40% lower than a standard weldment with a low B content (0.002 wt%). The low B content fractured transgranularly while the high B content sample fractured along long columnar prior-β grain boundaries. The low B alloy microstructure showed a more equiaxed grain structure than the high B alloy, which had a more epitaxial columnar prior-β grain. A peretectoid reaction of $\beta + TiB \rightarrow \alpha$ was proposed as the mechanism by which only 40 ppm of B can suppress the martensite transformation in a near-α Ti alloy weld FZ by providing nucleation sites for α Ti in the form of submicroscopic particles of TiB. It was suggested that some TiB particles in the weld filler do not entirely dissolve or they reform at very high temperatures upon solidification in the FZ. If this was indeed the case however, the higher B content alloy should possess the more equiaxed grains rather than having an epitaxial lamellar grain growth as was seen. It may rather be that these particles nucleate out below the alloy's melting temperature in the solid. These particles could then suppress the transformation of β to martensite upon cooling of the weld FZ by providing a site that is preferential for the nucleation and growth of the α phase from β throughout the whole microstructure.

Yttrium has been used in the past to alter the microstructure of as-cast titanium alloys by retarding β grain growth [15-17]. The reasons for these yttrium additions included attempts to improve the mechanical properties of the alloys and to improve the alloy's hot workability (due to an increase in ductility of the alloy), thereby reducing processing costs. Seagle et al [16] demonstrated that the additions of yttrium and yttria

on the order of 300-1000 ppm, when added to ingot melts of Ti-6Al-4V, significantly reduced the grain size of the alloy. This led to an increase in the reduction of area and elongation when subjected to tensile testing. The decrease in grain diameter with increasing yttrium concentration corresponded to an increase in the number of yttria particles present acting as barriers to grain growth. Rath et al [17] added 0.5 wt.% Y to Ti-6Al-4V and found that second phase dispersoids developed in the melt and were of the size 20-100 nm. The addition of the yttrium caused significant grain refinement leading to improved ductility. It was seen that the Y not only refined β grains but also retarded grain growth at elevated temperatures. Expected dispersion strengthening resulting from the yttria particles was found to be offset by the loss of interstitial oxygen. Ankem et al [18] found that additions of 25 ppm Y to Ti-5Al significantly refined and randomized the alpha platelet colonies in the alloy. No yttria particles were seen to be present under both SEM and TEM investigation.

Yttrium has also been studied by researchers [19-22] concerning heterogeneous nucleation in titanium alloy welds. Typically, in titanium alloys, a PWHT is necessary to give good fracture toughness and ductility. However, control of the FZ prior-β grain size is necessary for structural reliability to prevent a continuous grain boundary path for a crack to follow. Simpson [19] chose yttrium due to its low solubility in titanium and its high affinity for oxygen (-377 kJ/mol free energy of formation per O atom for Y vs. -293 kJ/mol for Ti at 1977 K (1704°C)). Phase diagrams for Ti-Y [23] and Y-O [24] can be seen in Figures 3 & 4 respectively. It was shown that the FZ grain size was reduced by as much as 20x with Y additions compared to those obtained with no additions. These Y

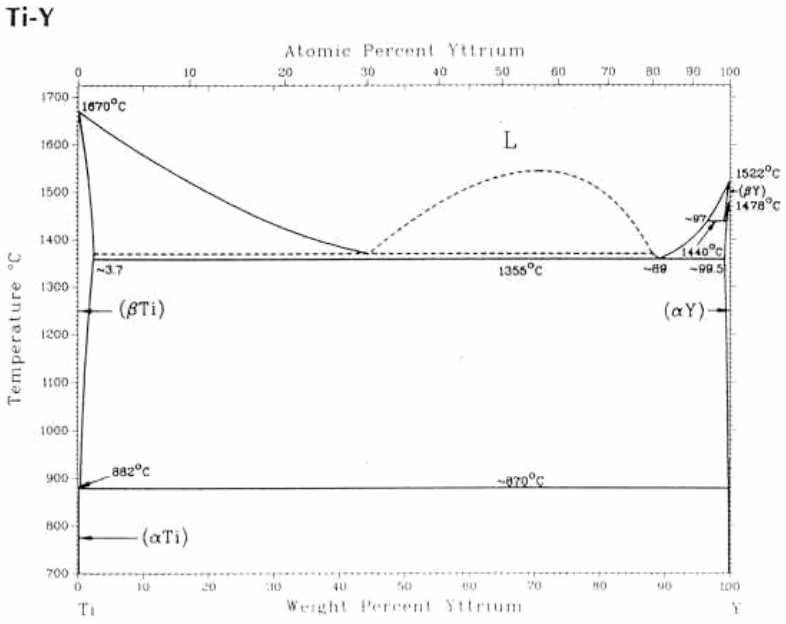

Figure 3: Ti-Y phase diagram [23].

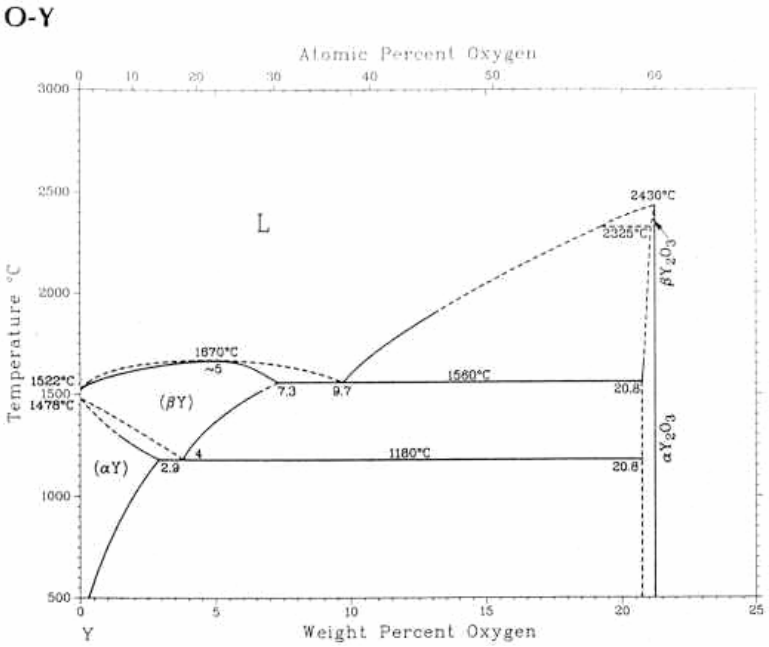

Figure 4: O-Y phase diagram [24].

additions were made to a Ti-6Al-6V-2Sn thin sheet weld.

By adding Y, Simpson [19] believed that yttria (Y_2O_3) particles would form and that these would control the grain size by acting as heterogeneous nucleation sites and/or restrict grain growth by pinning grain boundaries. A 16% decrease in grain size with an addition of 80 ppm Y was observed. At a concentration of 300 ppm Y, the average FZ grain size was reduced by 35%, with the large columnar grains at the center of the weld (which are the last to solidify) being reduced by 75-80%. This increased reduction at the center of the weld was suggested to result from yttria precipitates forming and being dragged by the advancing solid/liquid interfaces during solidification. This was evidenced by high yttria concentrations at the grain boundaries and in rows parallel to these boundaries within the grains themselves. As the solidification process continues, the yttria particles will continue to build up at the S/L interface, causing the drag effect to increase, resulting in increased undercooling and heterogeneous nucleation at the last places to solidify in the weld, namely the weld center.

The yttria precipitates in Simpson's work [19] were suspected to form at concentrations of 80 ppm Y and less, although they were not visible by conventional light microscopy until the Y concentration reached 300 ppm. Simpson also noted that much of the Y added to the weld filler metal was lost during the actual welding. The amount of decrease ranged between a factor of 2 to 7x, with higher amounts being lost as greater Y concentrations were added to the filler metal.

Simpson [19] also saw that between 200 and 300 ppm Y, an increase in yield strength and a decrease in ductility begins. Above 300 ppm, a dramatic decrease in mechanical properties (toughness and ductility) was noticed. It is also interesting to note

that the Ti-662 filler metal showed an increasing concentration of weld metal oxygen with increasing Y content, while the Ti-64 filler metal showed a decreasing oxygen content with increasing Y. These results were not discussed, but it may be that the alloy content of the filler metal has an effect on the Y scavenging ability of oxygen, which in turn can affect the strength and toughness of the weld.

Fracture surfaces on Simpson's [19] specimens containing no Y showed a step-like cleavage fracture in the as-welded condition with the entire fracture path being transgranular. When Y was added, the amount of intergranular fracture increased in proportion to the concentration of Y. This mode of fracture was also seen in Chasteen and Horowitz's [20] research of a Ti-5Al-5Sn-2Mo-2Zr-0.25S alloy with 250 ppm Y added. Their research showed low toughness values to be associated with large prior-β grain sizes in non-Y specimens and intergranular failure in Y specimens. There were no reports of yttria particles seen at all anywhere in the specimen.

Misra et al [21] studied the affect of varying concentrations on Ti-6Al-4V multipass, GTA welds. The concentration of Y was obtained by varying the speed rate of a filler wire containing 0.5 wt.% Y and by dual feeding a weld wire with no Y. It was found that the grain structure changed from equiaxed to long columnar as the Y concentration decreased. At 0.4 wt.%, it was observed that the grains still grew epitaxially from the previous pass interface even though many Y compound particles were observed to be uniformly distributed at the interface. They speculated that the Y does not interfere with epitaxial growth. Yttria particles were evenly distributed throughout the grains in the equiaxed portion of the samples and were not segregated to the grain boundaries. However, no report was made of yttria in the portions of the

specimen where the grains were columnar in nature. It was concluded that whether the FZ was growth controlled or nucleation controlled depended upon the amount of supercooling, ΔT. Since minor elements are known to decrease the $\Delta T_{critical}$ required for nucleation, $\Delta T_{critical}$ may be $< \Delta T_{weld}$, thus, the time required for a new grain to heterogeneously nucleate may be smaller than that of a grain to epitaxially grow across a bead.

Building on Simpson's and Misra's work, Nordin et al [22] made Y additions to Ti-6Al-2Nb-1Ta-1Mo (Ti-6211) weld metal in attempts to refine the grain structure and reduce its cracking susceptibility. Yttrium was added as a thin foil laid down with a filler metal wire in a shallow (1 mm x 1 mm) groove in a 13 mm thick plate. Two weld passes were then made to obtain desired yttrium concentration. It was seen that the Y additions to the weld pool had a drastic effect on bead morphology. Increasing Y concentrations showed a plateau development with the depth of the development increasing with increasing Y concentration. This plateau development, seen by decanting the weld with a high pressure Ar blast, indicated that the direction of advance of the S/L interface had changed. Increasing Y additions were also seen to increase weld pool turbulence as was also the case with Misra [21] and Simpson [19].

Nordin et al's [22] yttrium additions promoted nucleation in the FZ which, resulted in the refinement of the as-solidified grain structure. They believed that the increase in the rate of heterogeneous nucleation was caused by increases in the undercooling at the S/L interface during solidification, rather then yttria particles strictly providing more heterogeneous nucleation sites. This increase in undercooling was believed to be a result of changes in the fluid flow and heat extraction due to the yttrium

particle additions to the weld pool. Yttrium additions were seen to decrease the FZ depth while maintaining the FZ width thereby indicating that the decreased penetration was caused by a reduction in the heat input available for melting. It was believed that the increased turbulence in the weld pool created by Y addition increased the heat transfer from the FZ and decreased the available heat.

I.5 Heat Affected Zone Softening

Another problem that has been seen in welding near-α titanium alloys is heat affected zone softening. Ankem et al [25] performed hardness testing across a Ti-6211 weld zone and found that in addition to the normal hardening of the FZ, a decrease in hardness, as compared to the base metal, can be seen in the HAZ.

Since hardness will give an indication as to the strength and toughness of the metal, this softened area is likely to be a failure point when the weld is subjected to a tensile stress. This phenomenon has yet to be examined by other researchers, despite its obvious importance in determining failure characteristics of welded pieces. One possibility for this softening may be oxygen migration from the HAZ to the FZ during the weld process, but further investigation will be necessary to determine its exact cause.

I.6 Summary

It has been seen that to produce a tougher, more ductile weld in titanium without PWHT, it is necessary to reduce the prior-β grain size and/or promote heterogeneous nucleation. The material that should be chosen as a catalyst for this process should not be very soluble in titanium or should be able to easily form a compound with one or more of

the alloying elements in the titanium that will not be soluble. This element or compound should have a higher melting temperature than titanium, would ideally have a small disregistry, and possess a large surface area and high roughness. This would lead to a smaller degree of undercooling and thus not allow as much time for oxygen diffusion into the weld zones from the ambient and base metal. One would also like it to posses a high diffusion constant so that it will compete with the diffusionless martensite transformation. These processes may also lead to a higher cooling rate of the weld zone, thus not exposing the HAZ to a high temperature for as long a period, thereby possibly lowering the fully transformed region's grain size. This would lower the prior-β grain size and again lead to an increase in ductility. Another desirable characteristic would be a high affinity for oxygen, such that the element or compound will form discrete particles with any oxygen that diffuses into the weld zone and thereby not allow interaction of the oxygen with the titanium.

For these reasons, the element yttrium has been chosen for study at concentrations < 300 ppm in a near-α titanium alloy, Ti-5Al-1Sn-1Zr-1V-0.8Mo (Ti-5111). This alloy was designed by Timet Corporation in conjunction with the Navy for use in submarine applications. This alloy has been designed for high toughness, good weldability, stress-corrosion cracking resistance, and room temperature creep resistance. Its key characteristics that make it ideally suited for maritime application include excellent corrosion resistance and high toughness. While personnel at the Naval Surface Warfare Center – Carderock were studying this alloy, it was seen that when this alloy was welded with matching filler metal, the fusion zone hardens with a corresponding decrease in ductility. Another potential problem expected during welding is the heat affected zone

softening discussed previously. This research project was undertaken to improve the mechanical properties in this titanium alloys weld zone.

II. WELD AND FILLER METAL PLATES

Two, 17.78 cm x 16.19 cm x 2.54 cm plates of Ti-5Al-1Sn-1Zr-1V-0.8Mo (Ti-5111) (ASTM Grade 32) [26], with chemistry shown in Table 2, were machined with V-grooves on each side (as shown in Figure 5) of the plate for gas tungsten arc welding (GTAW). Two filler metal, 0.635 cm thick plates were prepared by vacuum arc melting, followed by forging and rolling by Timet Co. The chemistries of these plates are shown in Table 3. One of these plates was manufactured with chemistry matching that of the plates to be welded while the other plate was produced with an additional 60 ppm Y and a reduction of 0.5% in Al content. These plates were then cut into thin slices, each of which measures 0.635 cm x 0.32 cm x 17.78 cm, for use as filler metal strips. These 2.54 cm thick plates, along with the filler metal strips, were hand polished and then cleaned in a pickle bath of 60 vol.% H_2O-35 vol.% HNO_3-5 vol.% HF in order to remove any oxide produced during machining. These plates were then sent to Tricor Metals of Wooster, Ohio, for GTAW.

Table 2: Chemistry of Ti-5111 plates. All compositions in wt.% unless noted otherwise.

Ti-5111 Plate										
Al	Sn	Zr	V	Mo	Fe	Si	C	O	N	H ppm
4.92	1.00	1.05	1.00	0.789	0.085	0.092	0.009	0.094	0.006	37

Table 3: Chemistry of filler metals. All compositions in wt.% unless noted otherwise.

Matching Filler Metal – Vacuum Arc Melt											
Al	Sn	Zr	V	Mo	Fe	Si	Y ppm	C	O	N	H ppm
4.80	0.91	0.98	0.92	0.69	0.029	0.012	<4	0.006	0.094	0.003	55
Modified Filler Metal – Vacuum Arc Melt											
4.40	0.97	1.09	0.96	0.75	0.041	0.013	60	0.008	0.091	0.004	46
Modified Filler Metal – Plasma Melt											
4.4	1.0	1.0	1.0	0.75	0.01	0.15	268	-	0.089	-	-

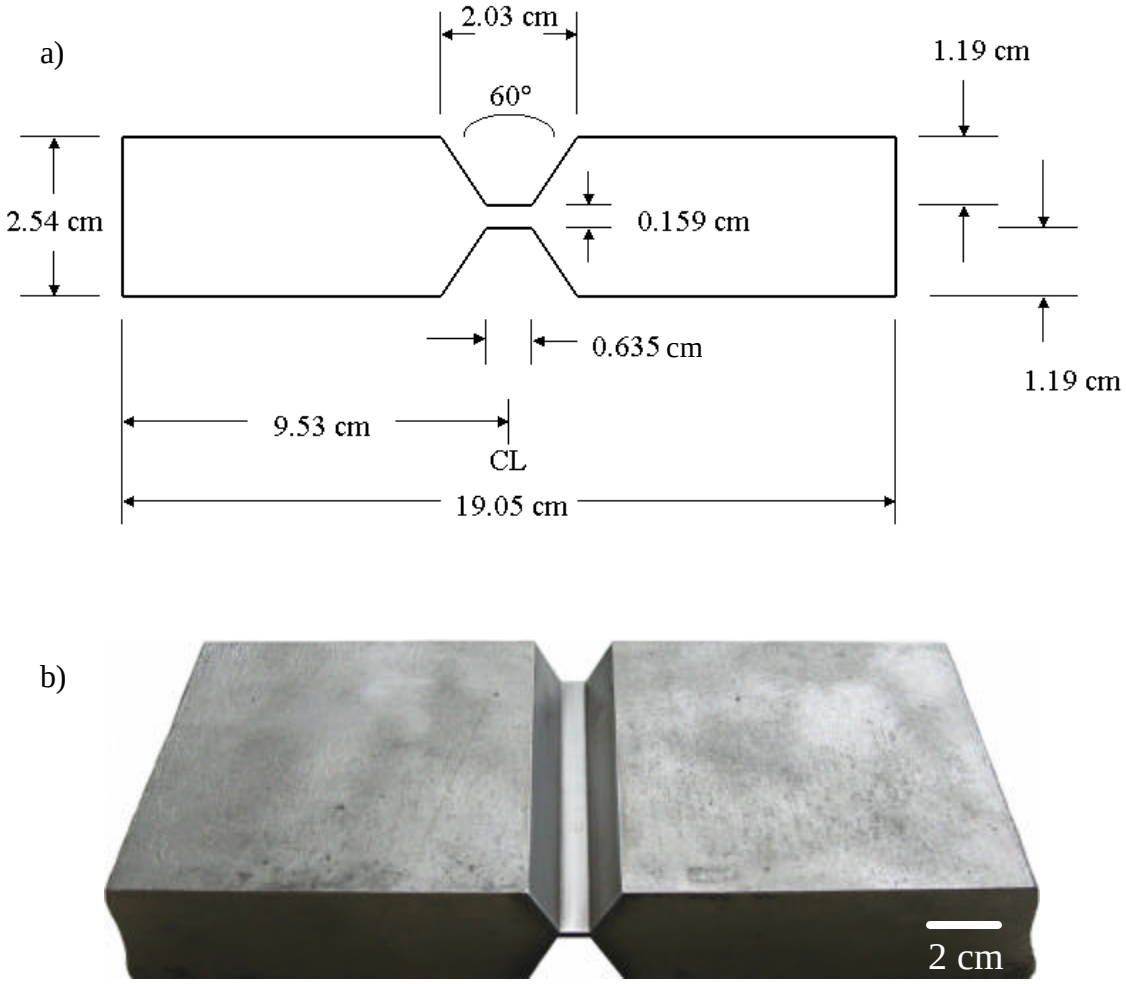

Figure 5: Double-V grooves machined into all weld plates, (a) schematic drawing and (b) actual plates after machining and polishing.

It is seen in Tables 2 & 3 that the main chemistry changes of the modified filler metals involve the reduction in aluminum content and addition of metallic yttrium. It is noted that there are minor differences in other elements, but these are not expected to cause any significant difference in βTT or room temperature mechanical properties. Concerning the chemistry changes to the filler metals, the following reasons for these changes are given:

- *Metallic* Y addition: It was believed that yttria particles will form in the melt, thereby acting as heterogeneous nucleation sites, resulting in a smaller degree of super-cooling necessary for solidification. This reduces the time of exposure of liquid titanium to the atmosphere and O pickup. Furthermore, the yttria particles are also expected to reduce the prior-β grain size coarsening.

- Al reduction: Since O and Al both act as α-stabilizers, the expected pickup of O during the welding process will be offset by the Al reduction. This is expected to maintain the βTT and keep the β–α ratio in the FZ similar to that of the base metal.

It should be noted that while attempting to obtain the yttrium modified filler metal plate, a chemistry of 200 ppm yttrium was desired. During the arc melt process, it is believed that the yttrium segregated to the edges and was removed prior to forging, resulting in the plate retaining only approximately 60 ppm yttrium. A third filler metal plate approximately 0.16 cm thick was made via a plasma melt in an attempt to retain more yttrium during the melt process. The chemistry of this plate can also be seen in Table 3, with it containing 268 ppm Y and 4.5%Al. This filler metal plate was used to weld one more double-V groove Ti-5111 plate with the same chemistry as that of the

others and that was 19.05 cm x 10.80 cm x 2.54 cm in dimension. While it is known that there is slightly different chemistry between this filler metal plate and the other filler metal plates and that more weld passes were required, results from this weld are added for comparison.

The weld parameters for the first two, 2.54 cm thick plates can be seen in Table 4. A total of 8 passes were made for each V-groove at travel speeds of 6.35 cm/min. Filler metal strips were added during each pass. Welding was performed as similarly as possible between the matching filler metal (designated as plate 0) and modified filler metal – 60 ppm Y (designated as plate 1). The GTAW process was carried out inside a glove box in > 99.99% pure argon gas.

Table 4: Gas tungsten arc welding parameters for plates 0 & 1.

Pass	Amps	Volts
1	200-247	14.0-15.4
2	273-320	15.7-17.8
3, 4, 5, 6	265-295	15.6-16.4
7, 8	199-289	14.0-16.5

The weld parameters for the third plate can be seen in Table 5. A total of 12 passes were performed on the top side while 11 passes were required for the back side at travel speeds of 20.32 cm/min. The modified filler metal – 268 ppm Y (designated as plate 2) was gas tungsten arc welded with as similar as possible conditions as the previous two plates and was again carried out inside a glove box with > 99.99% pure argon gas.

Table 5: Gas tungsten arc welding parameters for plate 2.

Pass	Amps	Volts
1	178-179	13.0
2	200-215	13.6
3, 4, 5, 6, 7	234-269	14.9-16.5
8, 9, 10	209-255	15.2-16.4
11, 12	188-214	14.5-15.4

It was noted during the welding process that the modified filler metal with yttrium significantly improved the penetration of the welds. It was seen that even after two weld passes had been deposited on each side of plate 1, the penetration was evident on the back side of the weld. Plate 0 did not indicate penetration on the back side of the plate even after the first pass. This increased penetration may be a result of a decrease in the surface tension of the weld pool due to the yttrium present or some sort of yttrium particle formation and will be discussed further later. This decrease in surface tension is also evidenced by the fact that with increasing yttrium concentration, the ripples in the solidified weld pool became much more evident, as seen in Figures 6 & 7.

Final yttrium concentrations in the fusion zone after welding were determined and can be seen in Table 6. It can be seen that some yttrium was lost during the GTA weld process as was the case with previous research by Simpson [19]. The final welded plates will be referred to in the rest of this paper as Weld 0, Weld 1 and Weld 2 corresponding to final yttrium concentrations in the weld zone as <1 ppm, 53 ppm and 200 ppm.

Table 6: Final fusion zone yttrium concentrations ***after*** welding.

	Weld 0	Weld 1	Weld 2
Y concentration (ppm)	<1	53	200

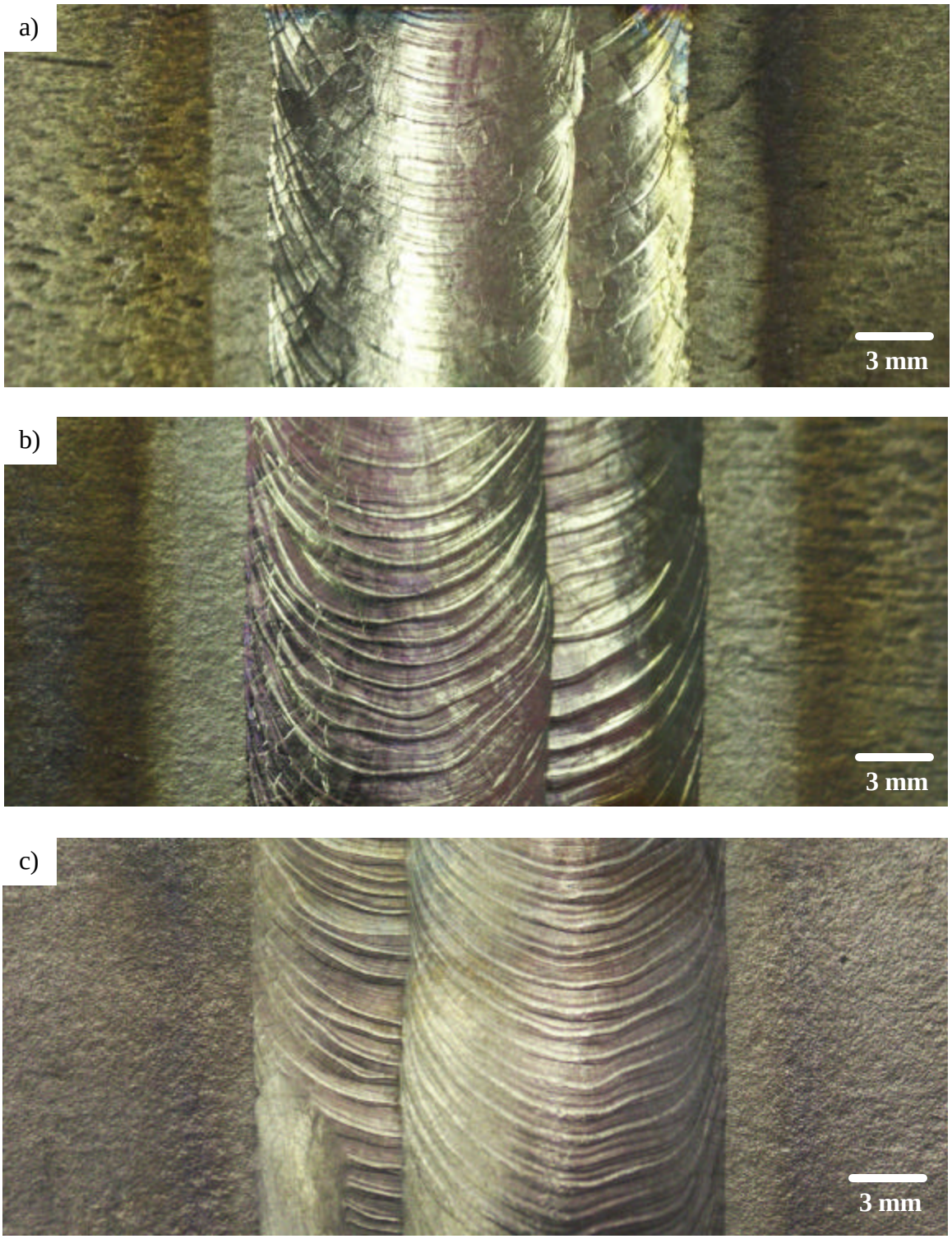

Figure 6: Optical pictures of weld zone surface of the FZ showing extent of surface rippling with increase in yttrium concentration. (a) Matching filler metal; (b) Modified 50 ppm Y filler metal; (c) Modified 200 ppm Y filler metal.

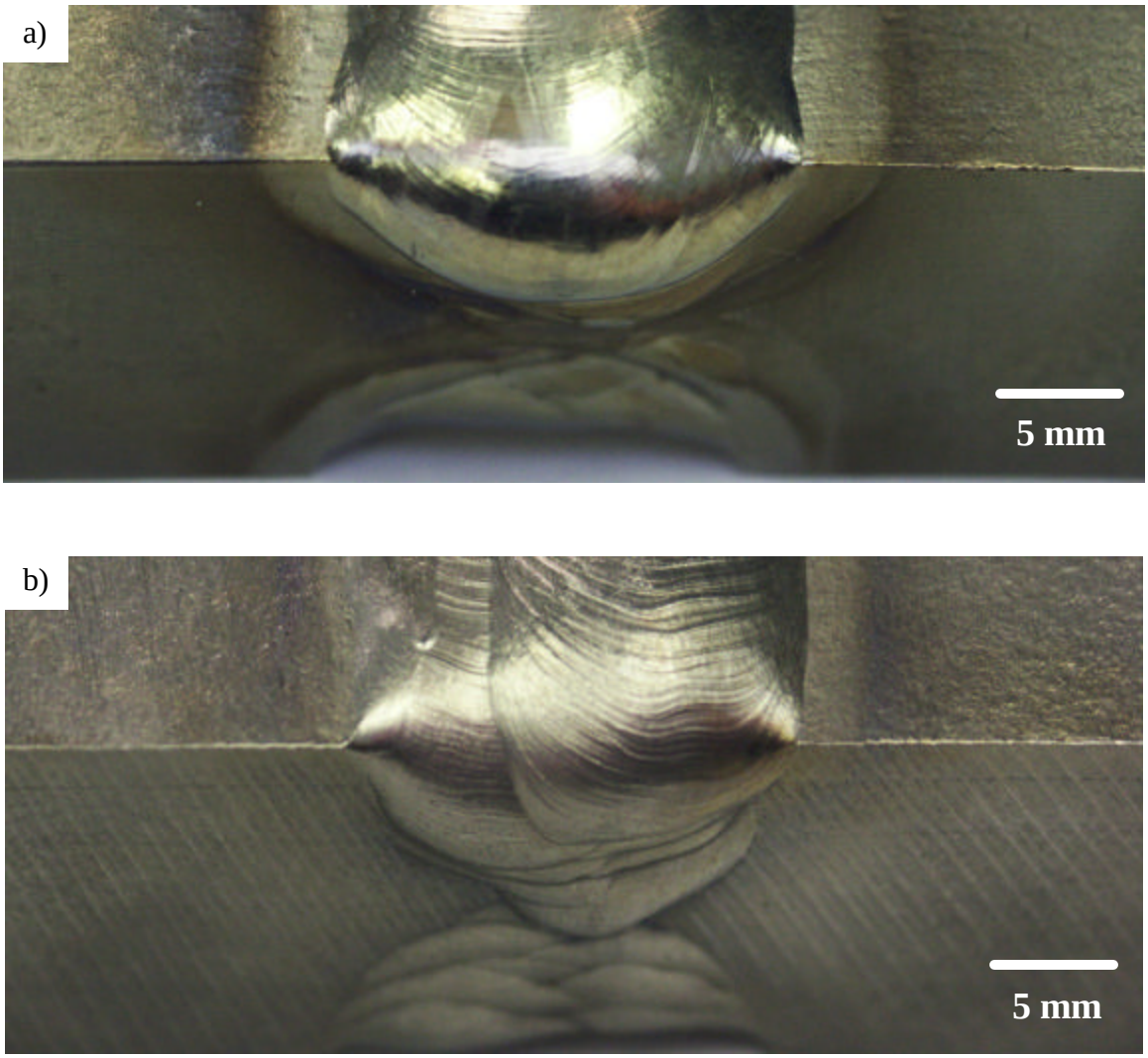

Figure 7: Optical pictures showing FZ surface rippling effects due to increasing yttrium concentrations. (a) Matching filler metal; (b) Modified 200 ppm.

III. MACROSTRUCTURE REFINEMENT

Specimens approximately 0.635 cm in thickness were sectioned from Welds 0, 1 and 2 after removing approximately 0.635 cm from the ends of the weld plates. These specimens were then cut to an approximate length of 7.62 cm with the weld zone in the center. The specimens were then polished on a Buehler tabletop polish unit using polishing paper to a grit of 800 and then chemically polished using a Buehler Mastermet colloidal silica polishing suspension on a Buehler Chemomet polishing pad. This polishing process produced an extremely fine mirrored surface. The surface was then etched using Kroll's reagent (88 vol.% H_2O, 10 vol.% HNO_3, and 2 vol.% HF).

The additions of yttrium to the welds did not result in any significant amounts of heterogeneous nucleation. While there were limited amounts of heterogeneous nucleation that did take place in the modified filler metal weld zones, as evidenced in Figure 8, the main effect of the yttrium additions was to reduce the width of the columnar structures of the prior-β grains across the fusion zone. An interesting result concerning the additions of Y was noted at the end of the weld at the plate edges. Namely, a much higher degree of heterogeneous nucleation took place here, as shown in Figure 9, as compared to the rest of the weld plate area. This may indicate that yttrium particles are forming in the melt and are being pushed forward towards the edge of the plate by the force of the arc weld. Weld zone macrostructures are shown in Figures 10-12. Prior-β grain sizes measured across the fusion zone at various areas in the weld are shown in Table 7.

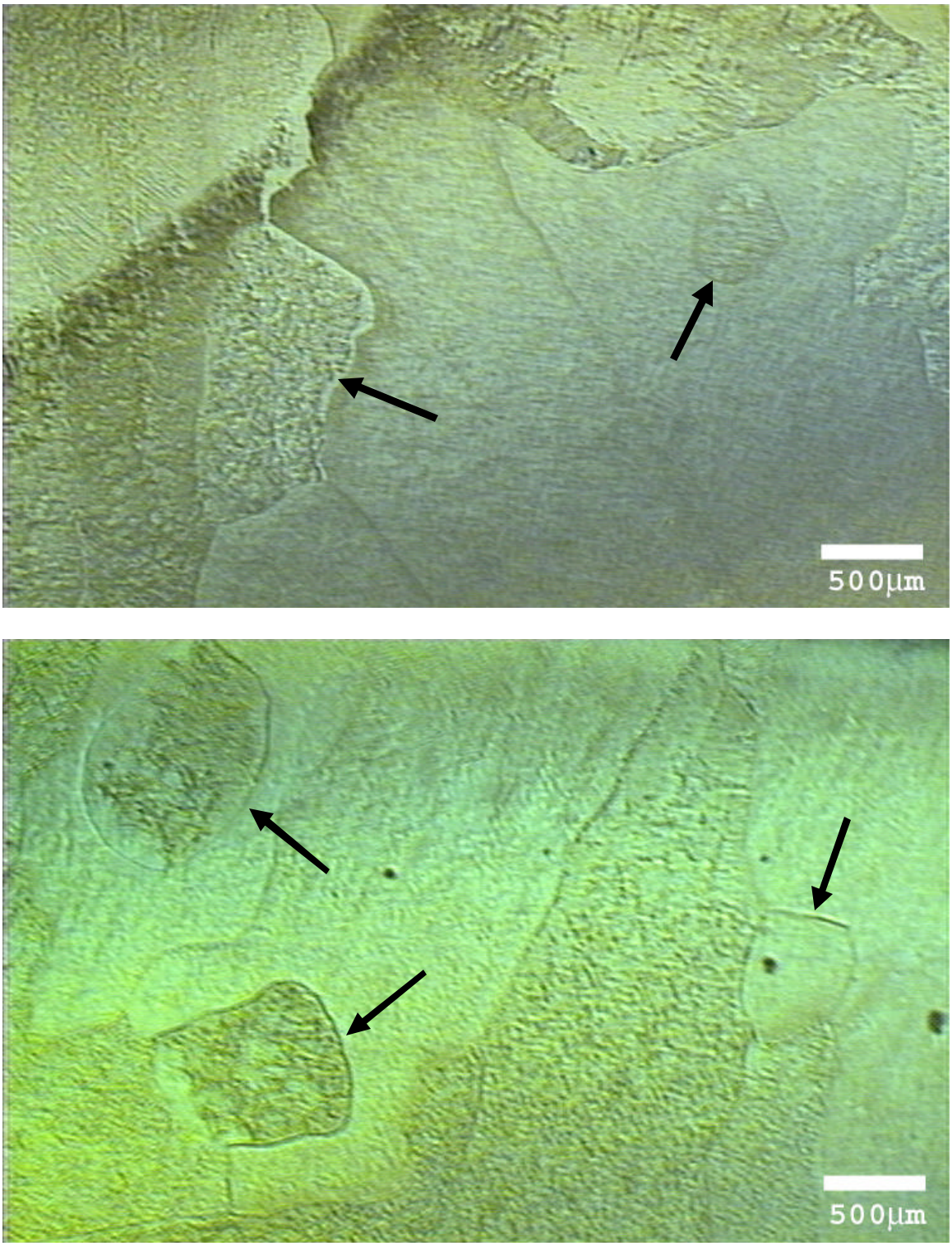

Figure 8: Ti5111 modified 50 ppm Y filler metal fusion zone where arrows point out heterogeneous nucleation sites.

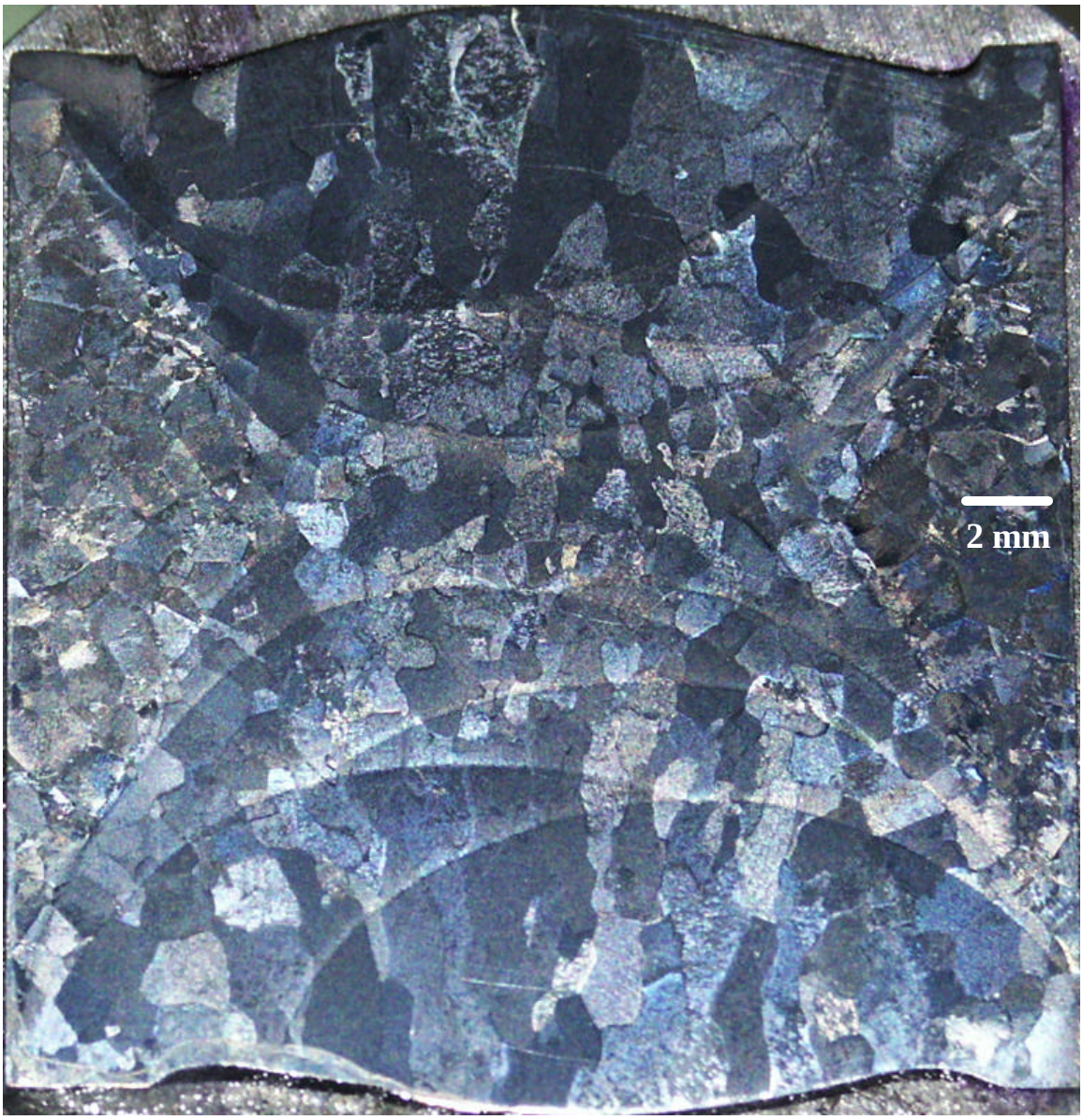

Figure 9: Weld zone macrostructure of Weld 1 (50 ppm Y) near edge of weld plate. Note the greater abundance of heterogeneously nucleated grains.

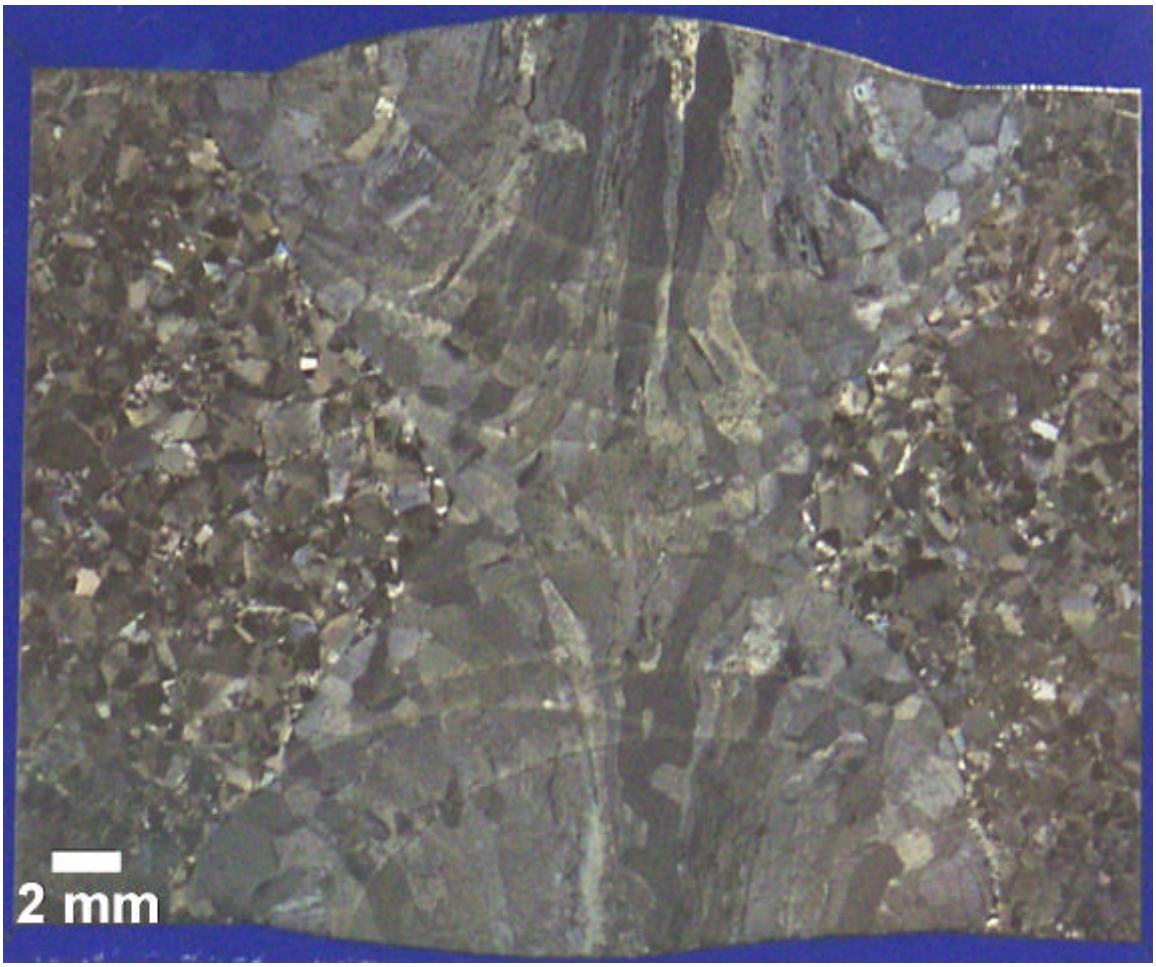

Figure 10: Weld zone macrostructure of Ti-5111 Weld 0 (matching filler). Note the long prior-β columnar grain growth that continues between weld passes and the large width of these grains, especially at the center of the weld. Very few equiaxed grains exist inside the weld FZ.

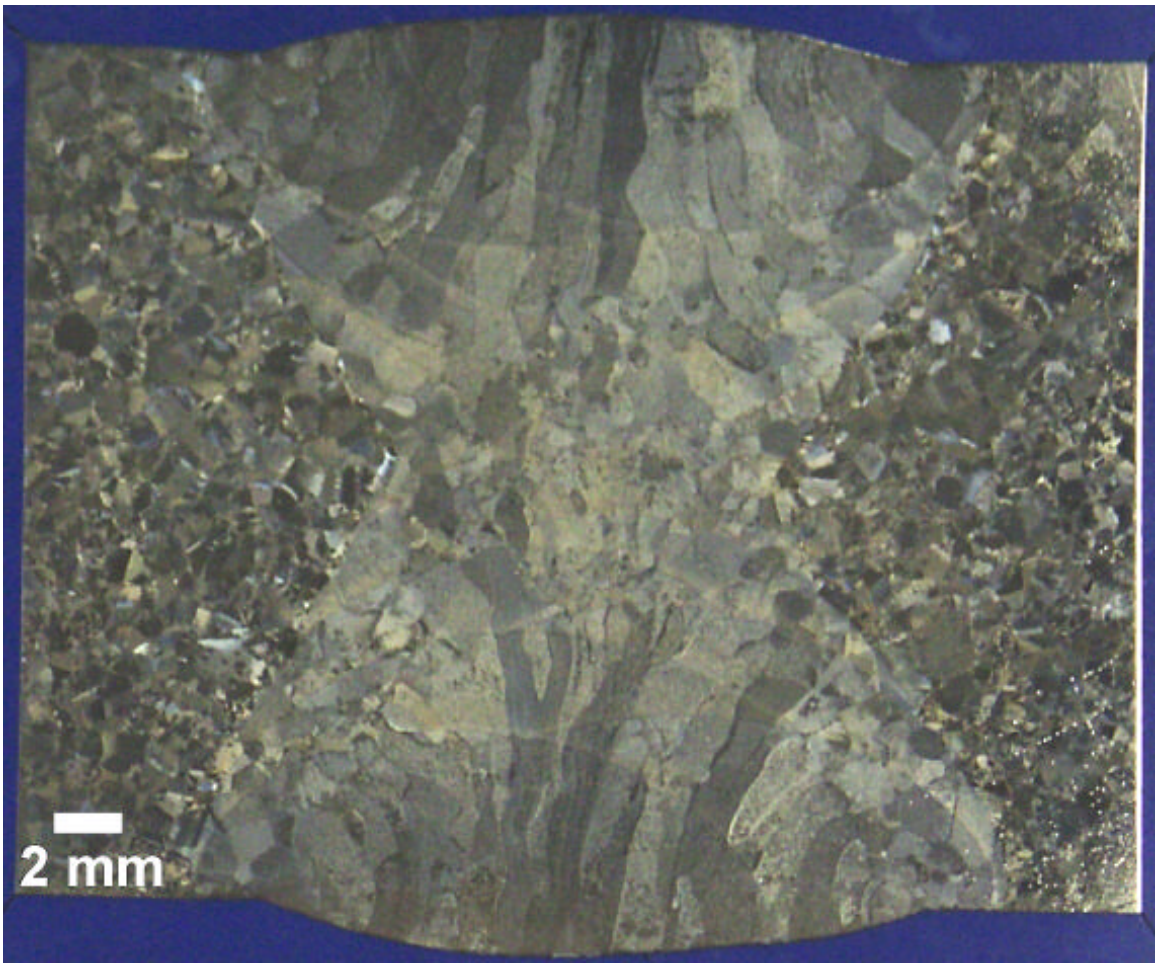

Figure 11: Weld zone macrostructure of Ti-5111 Weld 1 (50 ppm Y). Note that again there are long prior-β columnar grains that continue to grow between weld passes. Width of these grains have been reduced 15% overall and 38% at the weld center as compared to the matching filler metal weld. A few equiaxed grains were seen to be present within the weld FZ.

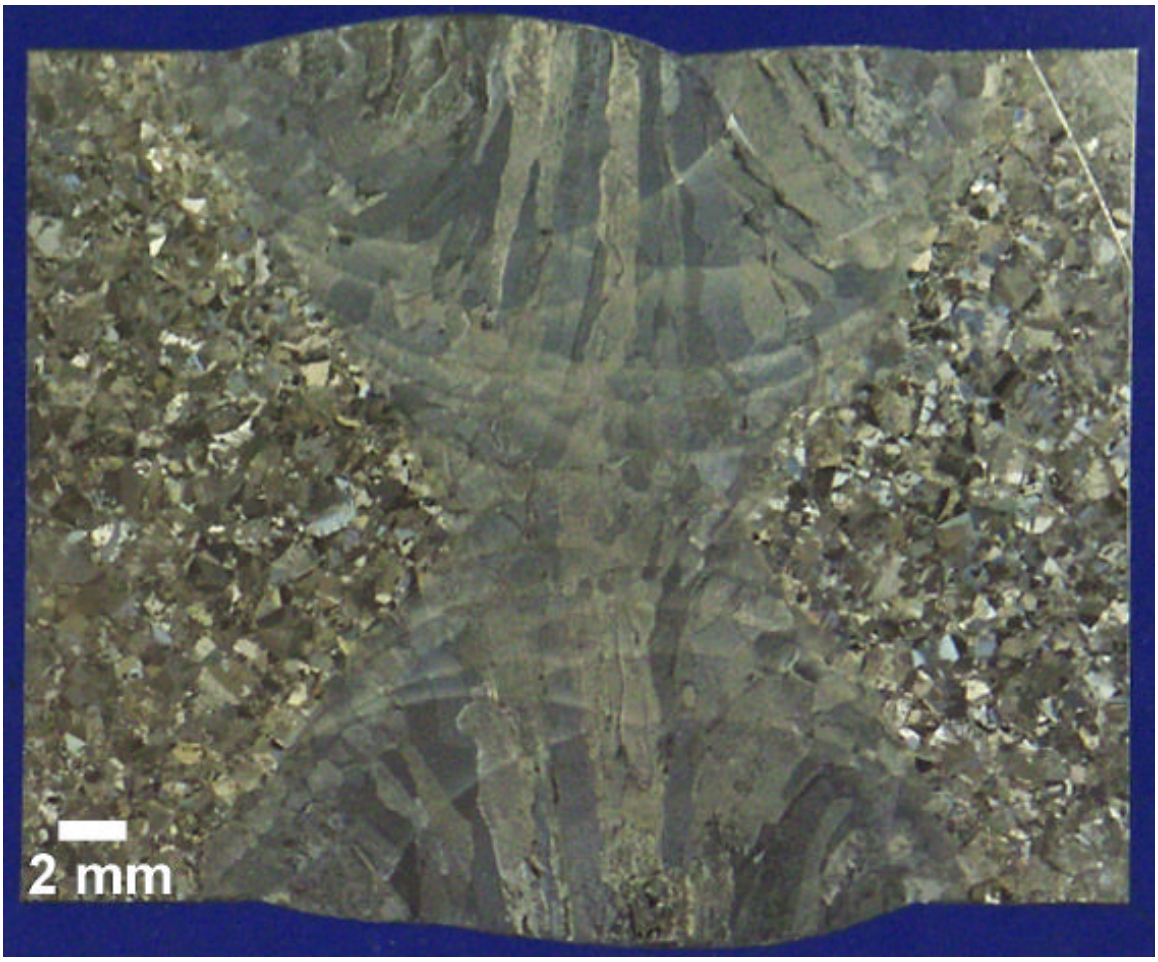

Figure 12: Weld zone macrostructure of Ti-5111 Weld 2 (200 ppm Y). Note that the long columnar prior-β grains continue to exist between weld passes. Width of these grains have been reduced a drastic 25% overall and 48% at the weld center as compared to the matching filler metal weld. A few equiaxed grains were seen to be present within the weld FZ.

Table 7: Prior-β grain sizes in fusion zone.

	Weld 0	Weld 1	Weld 2
Grain size at outer edges of weld plate (μm)	902	775	676
Grain size just outside of the root pass (μm)	738	775	735
Grain size at middle of weld zone (μm)	1041	643	539

The average width of the prior-β grain size in the fusion zone, at the outer edge of the plate, using the matching filler metal (Weld 0) was 902 μm. In the modified 50 ppm Y weld (Weld 1), this average grain size was 775 μm, while in the 200 ppm Y weld (Weld 2), this average grain size was 676 μm. The reduction in prior-β grain size from matching to modified 50 ppm Y represents an approximate 15% decrease, while from the matching to modified 200 ppm Y a 25% reduction in prior-β grain size takes place. Similar to work done by Simpson [19], a greater reduction in grain size was seen in the middle of the weld zone as compared to at the edges. A 38% reduction was seen from the matching filler metal to 50 ppm Y and a 48% reduction was seen from the matching filler metal to 200 ppm Y. This difference can be seen in Figure 13. Another interesting observation is that the average prior-β grain size in the fusion zone just outside the root pass was approximately equal in all cases at approximately 750 μm.

The reductions in prior-β grain sizes associated with yttrium additions occurred without any evidence of yttrium particle nucleation taking place when observed under optical microscopy up to a magnification of 500x. These results were not necessarily unexpected due to the very low concentrations of yttrium added. Further studies by SEM and TEM are required to be performed in order to definitively determine whether any

a)

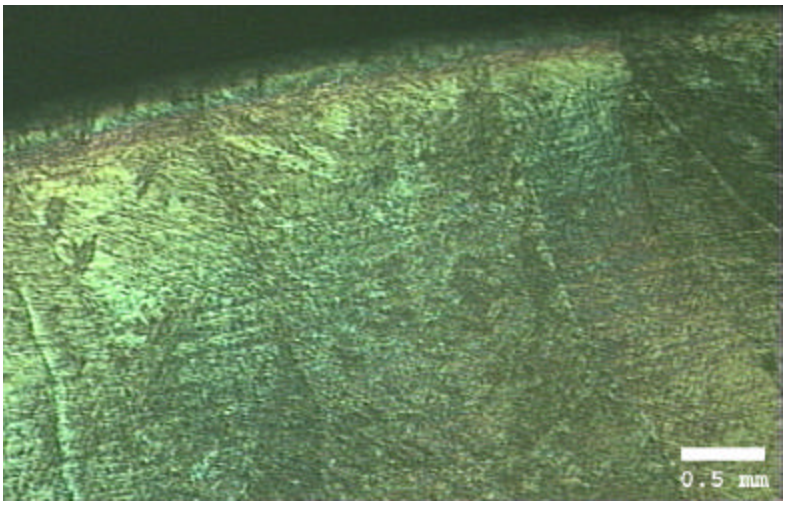

b)

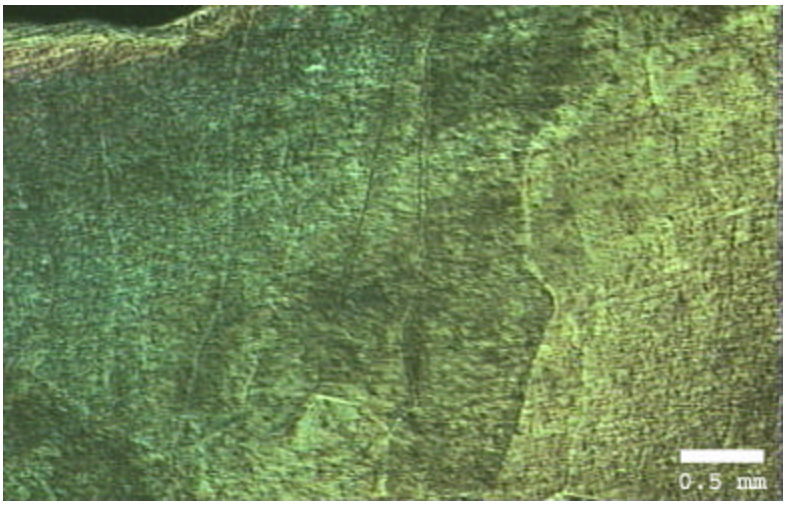

c)

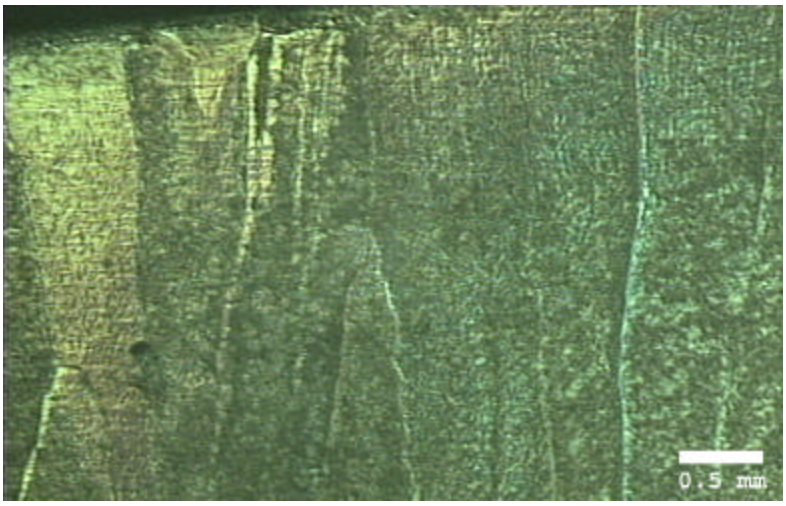

Figure 13: Ti5111 macrostructures at center of the weld zone. (a) Matching filler metal, (b) Modified 50 ppm Y filler metal, and (c) Modified 200 ppm Y filler metal. Note that prior-β grain size obviously decreases at the center of the weld zone with increasing Y concentration.

yttrium particles are present in the modified filler metal welds or not. Indirect evidence exists that there are particles forming and that they may exist as nanoparticles and will be discussed later in this paper.

IV. ROCKWELL C HARDNESS

Specimens approximately 0.635 cm in thickness were sectioned from Welds 0 and 1 after removing approximately 0.635 cm from the ends of the weld plates. These specimens were then cut to an approximate length of 7.62 cm with the weld zone in the center. The specimens were then polished on a Buehler tabletop polish unit using polishing paper to a grit of 800 and then chemically polished using a Buehler Mastermet colloidal silica polishing suspension on a Buehler Chemomet polishing pad. This polishing process produced an extremely fine mirrored surface. The surface was then etched using Kroll's reagent (88% H_2O, 10% HNO_3, and 2% HF).

Rockwell C hardness testing was performed using a Wilson Series 500 Rockwell Hardness Tester. A Brale Penetrator was used with a minor load of 10 kgf and a major load of 150 kgf. Results of testing across the weld zone from plates 0 and 1 can be seen in Figure 14. In welds, Rockwell hardness testing only gives a broad indication as to hardness results, as the penetrator covers a relatively large area of the alloy when testing. Nevertheless, it can easily be seen from Figure 14 that in the far HAZ, the hardness values in the modified filler metal are much closer to that of the base metals' as compared to the very low values of the matching filler metal. The hardness values across the near HAZ and the FZ are very similar. It is thereby suspected that the modifications are having a desired effect on mechanical properties of the weld. These results may be indicative of a reduction in time for the oxygen to diffuse from the base metal into the near HAZ. In order to determine true indicative values of hardness in the weld areas, microhardness testing must be performed. These results will be discussed later.

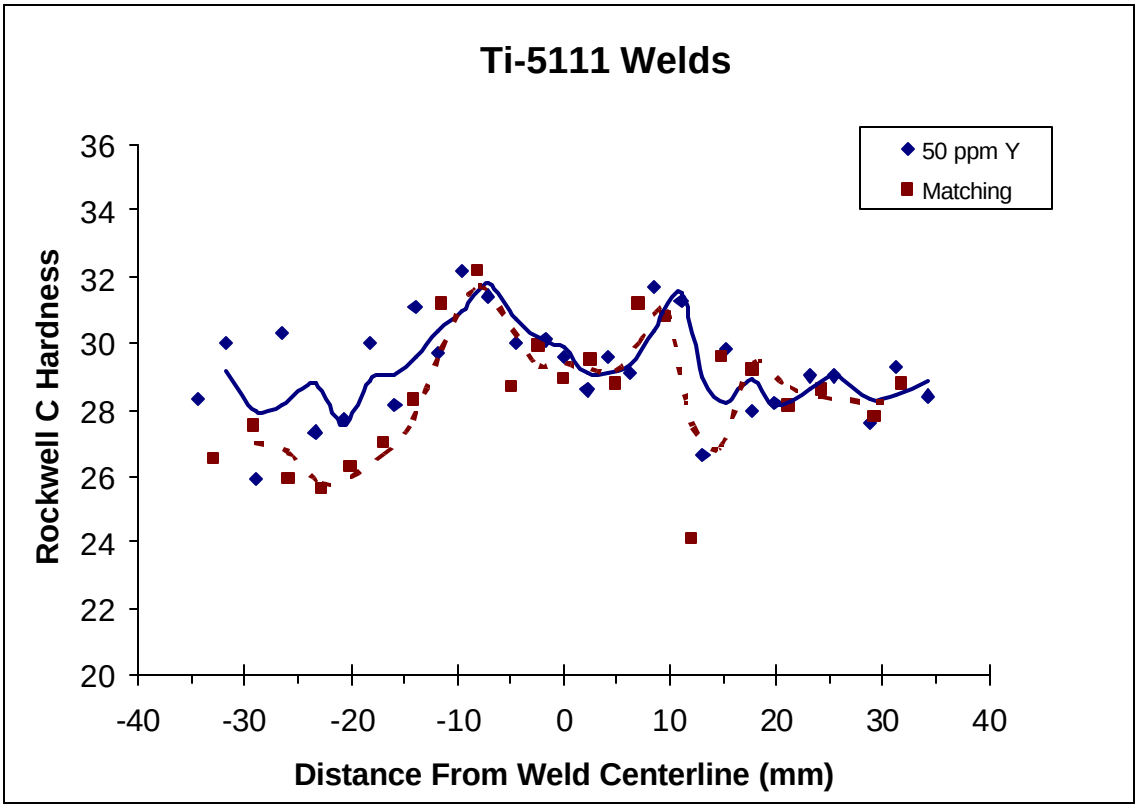

Figure 14: Rockwell C hardness values across the weld zones in Welds 0 and 1 where '0' corresponds to the center of the weld FZ's. Note that the modified 50 ppm Y filler metal weld hardness does not decrease as much as the matching filler metal's weld hardness at the edge of the far HAZ on either side of the weld. The high hardness values correspond to the near HAZ area of the welds. Note also that the FZ area inside the HAZ high hardness points decreases, but is still higher in hardness then that of the base metal.

V. TENSILE TESTING

V.1 Specimen Preparation and Procedure

Tensile testing was performed on an Instron 8502 Servohydraulic Testing System controlled by the Series IX Automated Materials Testing System. The tensile testing procedure and Instron 8502 operating instruction can be found in Appendix A. Ramp rate of the tensile test was 0.05 mm/min. Testing was conducted at a room temperature of 22°C.

Tensile tests were performed on the Ti-5111 base material, Weld 0, Weld 1 and Weld 2. Tensile specimen dimensions can be seen in Figure 15 and are in accordance with ASTM standard E 8 [27]. Specimen testing was also carried out in accordance with ASTM standard E 8 [27]. The specimen size was chosen so as to include the entire reduced section in the weld FZ, as shown in Figure 16. This was done to ensure that only the FZ metal was used for comparison between the welds and base metal in order to determine what, if any, changes are made based on filler metal composition. It should be noted that weld areas sometimes fail in the HAZ area of the base metal and that by modifying the filler metal with yttrium, this may also increase the strength of the HAZ, thereby improving overall weld properties. This was not studied in these tests however, due to the limited amount of material available for testing and will be examined instead when microhardness measurements across the weld zone are performed.

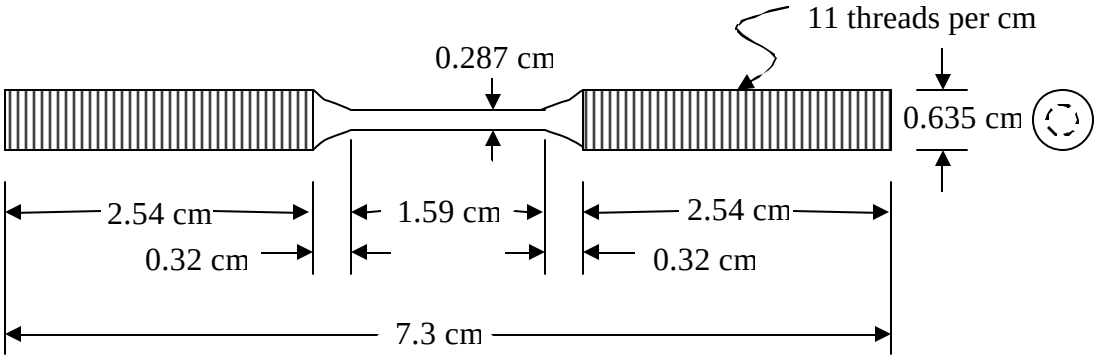

Figure 15: Tensile test specimen dimensions.

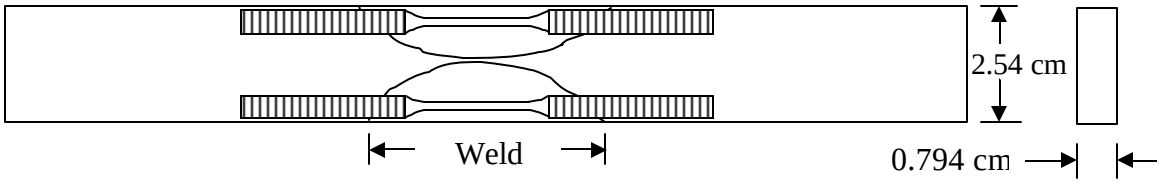

Figure 16: Diagram indicating position of where specimens were machined from in weld. Note that entire reduced section is contained within the weld fusion zone.

V.2 Results and Discussion

Four tensile tests were performed for the base metal, Weld 0 with matching filler metal, Weld 1 with modified 50 ppm Y filler metal and Weld 2 with modified 200 ppm Y filler metal. Resulting tensile testing curves for these materials can be seen in Figures 17-20 respectively. Tables 8-11 summarize the tensile testing results for each. Table 12 gives the average values for comparison.

Table 8: Summary of tensile testing results for Ti-5111 base material.

Sample	0.2YS (MPa)	UTS (MPa)	Break (%)	RA (%)	A (GJ/m^3)
B1	740.6	776.5	7.64	12.5	3.36
B2	745.4	773.5	8.27	19.9	3.69
B3	715.3	752.7	8.99	13.6	3.90
B4	736.6	772.9	8.69	14.1	3.77
Avg	**734.5**	**768.9**	**8.40**	**15.0**	**3.68**
Std Dev	**13.3**	**10.9**	**0.59**	**3.3**	**0.23**

Table 9: Summary of tensile testing results for Ti-5111, Weld 0, matching filler metal.

Sample	0.2YS (MPa)	UTS (MPa)	Break (%)	RA (%)	A (GJ/m^3)
M1	750.6	810.5	9.90	20.4	4.40
M2	728.2	795.6	7.74	16.6	3.49
M3	751.5	803.3	6.77	3.8	3.16
M4	726.4	779.6	8.87	18.2	3.98
Avg	**739.2**	**797.3**	**8.32**	**14.8**	**3.76**
Std Dev	**13.7**	**13.2**	**1.36**	**7.5**	**0.54**

Table 10: Summary of tensile testing results for Ti-5111, Weld 1, modified 50 ppm Y filler metal.

Sample	0.2 YS (MPa)	UTS (MPa)	Break (%)	RA (%)	A (GJ/m^3)
50Y1	736.7	783.7	9.36	20.1	3.99
50Y2	747.7	798.0	11.05	22.2	4.67
50Y3	783.6	821.8	8.56	20.6	3.74
50Y4	653.9	807.9	10.69	21.7	4.54
Avg	**730.5**	**802.9**	**9.92**	**21.2**	**4.24**
Std Dev	**54.8**	**16.1**	**1.16**	**1.0**	**0.44**

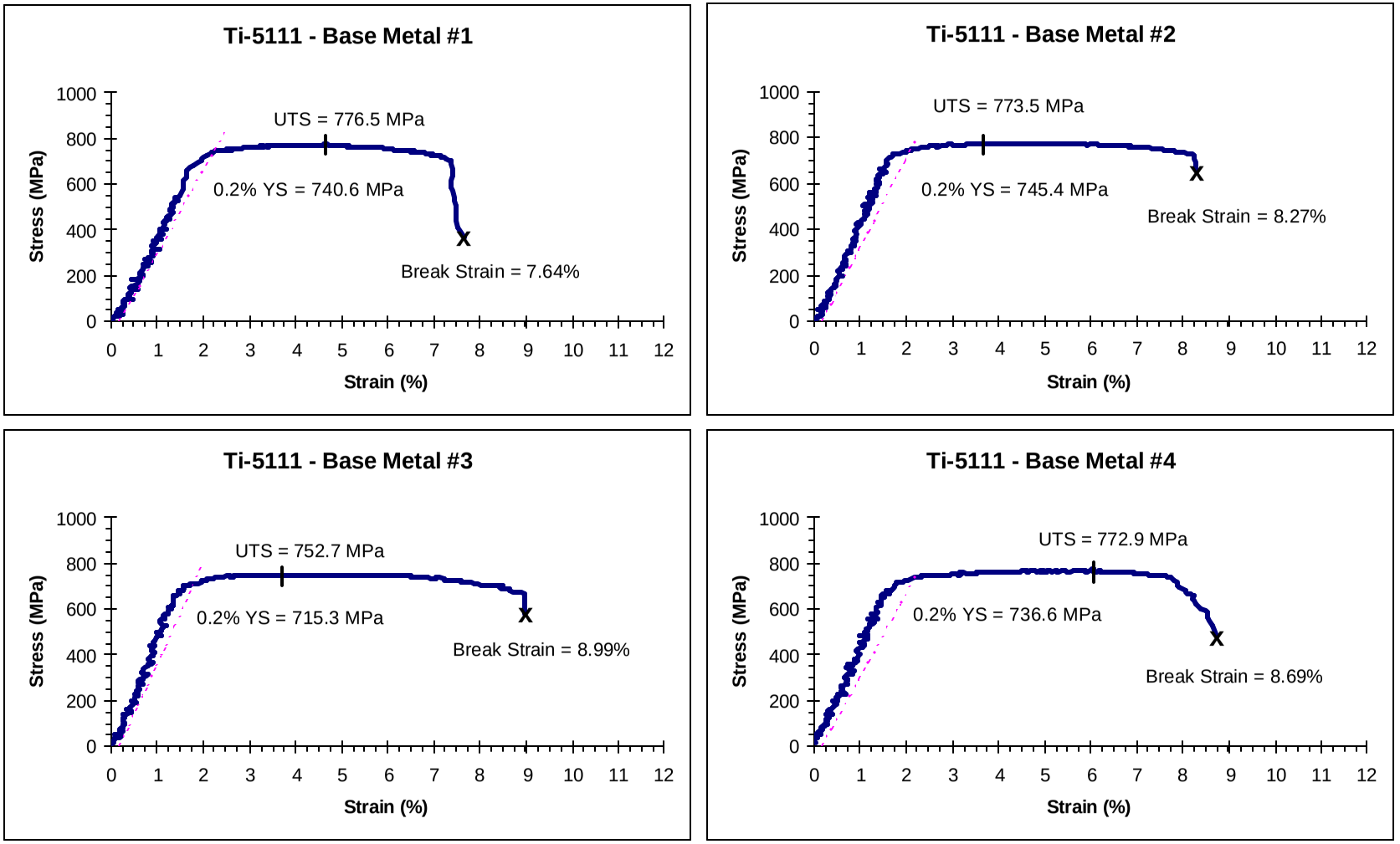

Figure 17: Tensile test curves for the Ti-5111 alloy base metal.

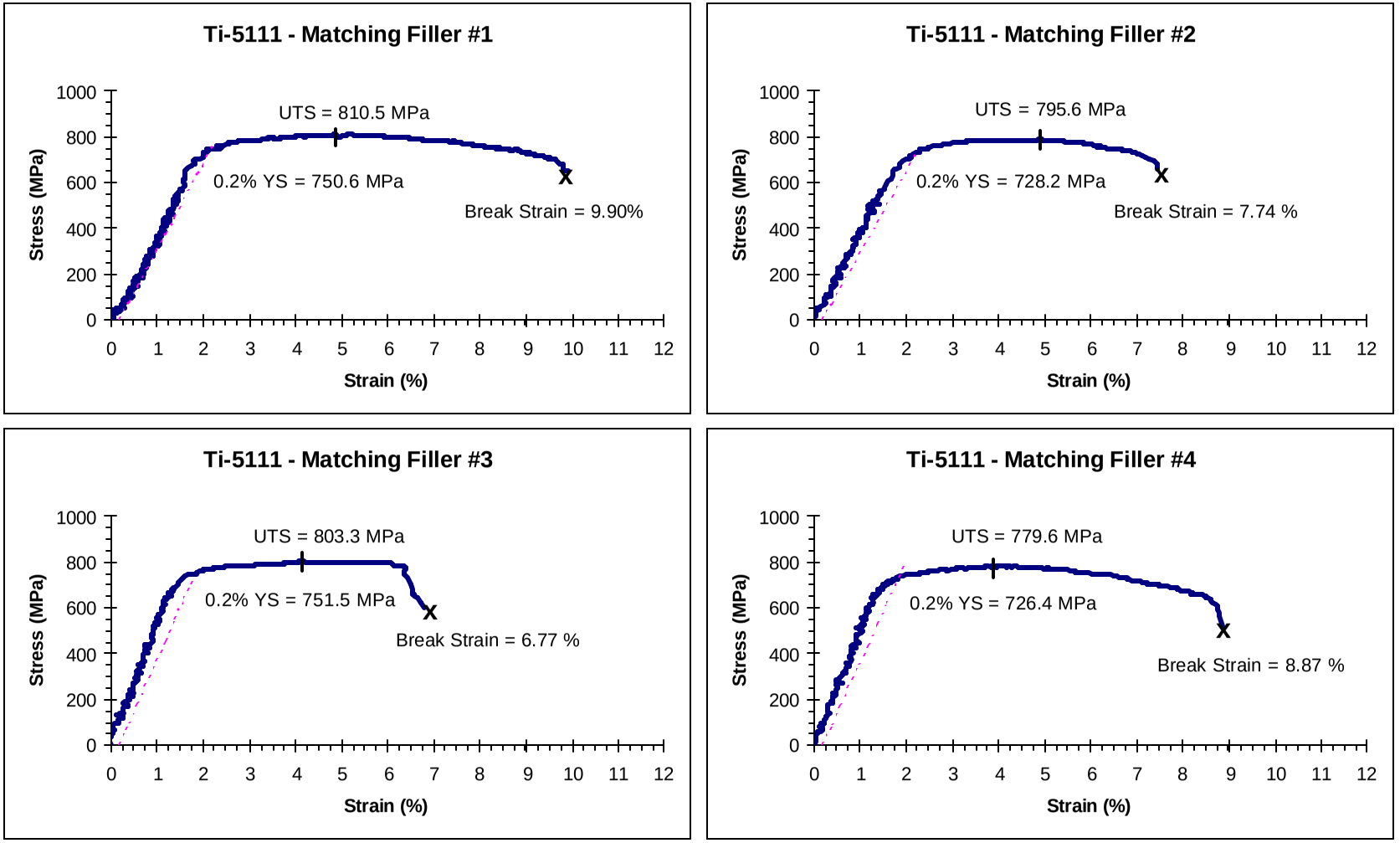

Figure 18: Tensile test curves for Ti-5111 matching filler metal welds.

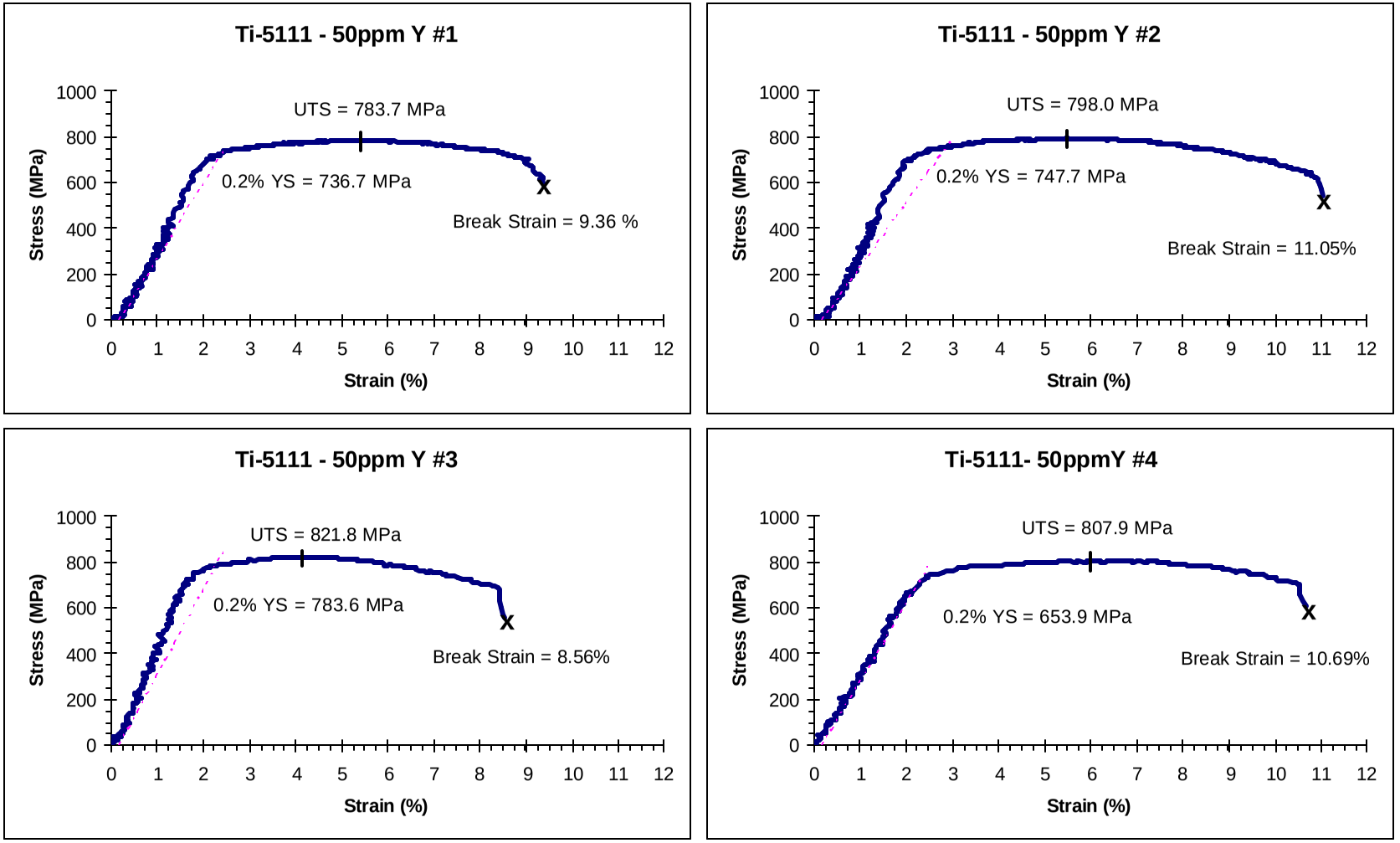

Figure 19: Tensile test curves for Ti5111 modified 50ppm Y filler metal weld.

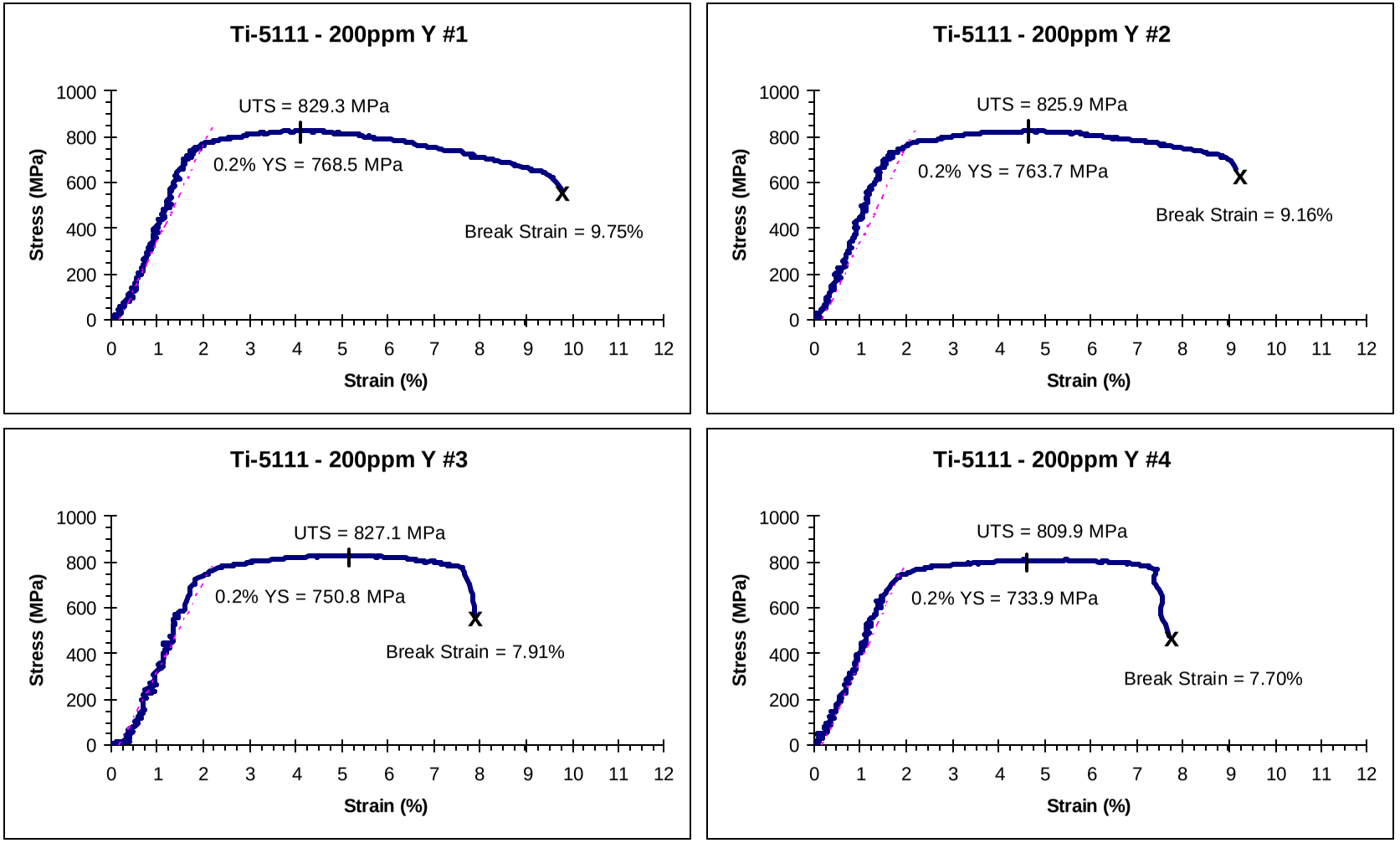

Figure 20: Tensile test curves for Ti5111 modified 268ppm Y filler metal weld.

Table 11: Summary of tensile testing results for Ti-5111, Weld 2, modified 200 ppm Y filler metal

Sample	0.2YS (MPa)	UTS (MPa)	Break (%)	RA (%)	A (GJ/m^3)
200Y1	768.5	829.3	9.75	24.6	4.40
200Y2	763.7	825.9	9.16	19.9	4.23
200Y3	750.8	827.1	7.91	15.4	3.57
200Y4	733.9	809.9	7.70	9.6	3.72
Avg	**754.2**	**823.1**	**8.63**	**17.4**	**3.98**
Std Dev	**15.5**	**8.9**	**0.99**	**6.4**	**0.40**

Table 12: Summary of tensile testing results for Ti-5111 base metal and welds.

Sample	0.2% YS (MPa)	UTS (MPa)	Total Strain (%)	Red. Area (%)	A (GJ/m^3)
Base	734.5	768.9	8.4	15.0	3.68
Matching	739.2	797.3	8.3	14.8	3.76
50 ppm Y	730.5	802.9	9.9	21.2	4.24
200 ppm Y	754.2	823.1	8.6	17.4	3.98

It is to be pointed out that the total strain of the specimens was measured by actuator displacement due to the fact that the knife edges of the strain gage caused premature failure of the specimens at the contact point of these edges when attempting to test this way. Total strain was calculated based on the gauge length of the specimen which was defined as the total length of the reduced area of the specimen minus 2D, where D is the diameter of the specimen [28]. The reduction in area (RA) for the specimens was calculated after tensile testing. The value of A in the tables is the area under the stress-strain curves and is given as a preliminary indication of expected toughness of the specimens.

Examining Table 12 for the results of tensile testing, we can see that when the matching filler metal is compared to the base metal, there is a slight increase in strength, while ductility and toughness remain approximately the same. When the modified 50 ppm Y filler metal is used, there is a slight decrease in strength, while there is a dramatic

improvement in ductility and toughness. As the yttrium concentration is increased to 200 ppm Y, it can be seen that there is a further increase in strength over the matching filler metal and we see a slight decrease in ductility and toughness from the 50 ppm Y, although they still remain above those values of the matching filler metal.

From these results, it is seen that by adding yttrium and decreasing the aluminum concentration in the filler metal, we have increased the ductility of the fusion zone in the weld while still maintaining the strength. It is further noted that continuing the addition of yttrium eventually causes a decrease in the ductility and toughness. This indicates that there is an optimum addition of yttrium that could be made between 50 and 200 ppm Y. Further research would be necessary to determine this point.

VI. FRACTOGRAPHY OF TENSILE SPECIMENS

After completing tensile testing, specimens were chosen that most closely typified that of the average results. These specimens were #2 from the base material, #2 from Weld 0, #4 from Weld 1 and #2 from Weld 2. Tensile curves for these specimens can be seen in Figures 17-20. These specimens were then examined by the Environmental Scanning Electron Microscope (ESEM) to obtain fracture surface results. A low and high magnification of these results can be seen in Figures 21 & 22 respectively. More images of the surfaces can be found in Appendix B.

Results from these micrographs indicate that the base metal and matching filler metal welds exhibit a step-like cleavage fracture surface, transgranular in nature. The matching filler metal weld surface shows a slightly more brittle aspect than the base material, as would be expected. The weld fracture surfaces [29, 30] of the modified filler metals show an increasing amount of microvoid coalescence (dimpled rupture), in addition to the transgranular cleavage, with increasing yttrium content. This increase in microvoid coalescence can explain the increase in ductility and toughness values associated with tensile testing. This microvoid coalescence may indicate the formation of yttrium particles within the grains of the welds, although no particles were seen at the bottom of the dimpled rupture surfaces. This may be indicative of nanoparticle formation.

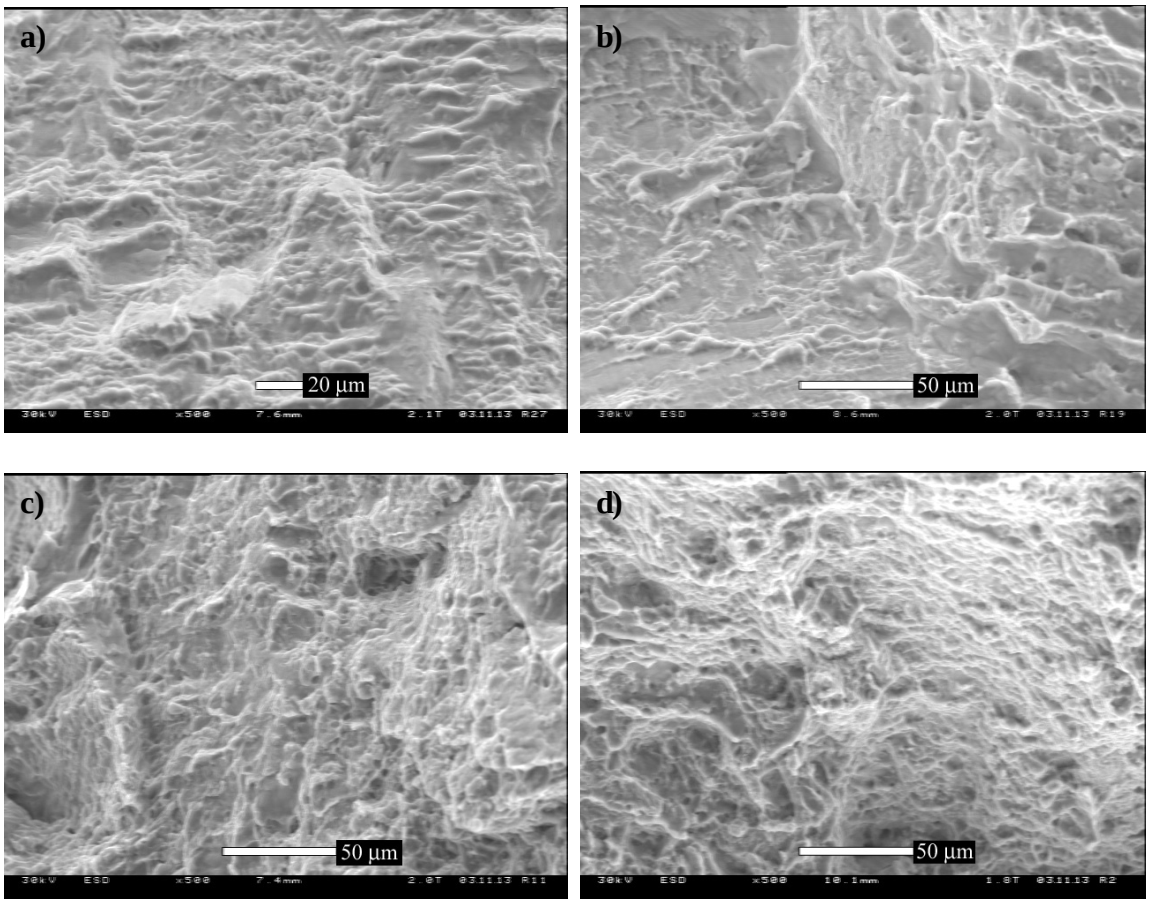

Figure 21: Fracture surfaces of tensile specimens, 500x. (a) Base metal, (b) matching filler metal weld, (c) modified 50 ppm Y filler metal weld, and (d) modified 200 ppm Y metal.

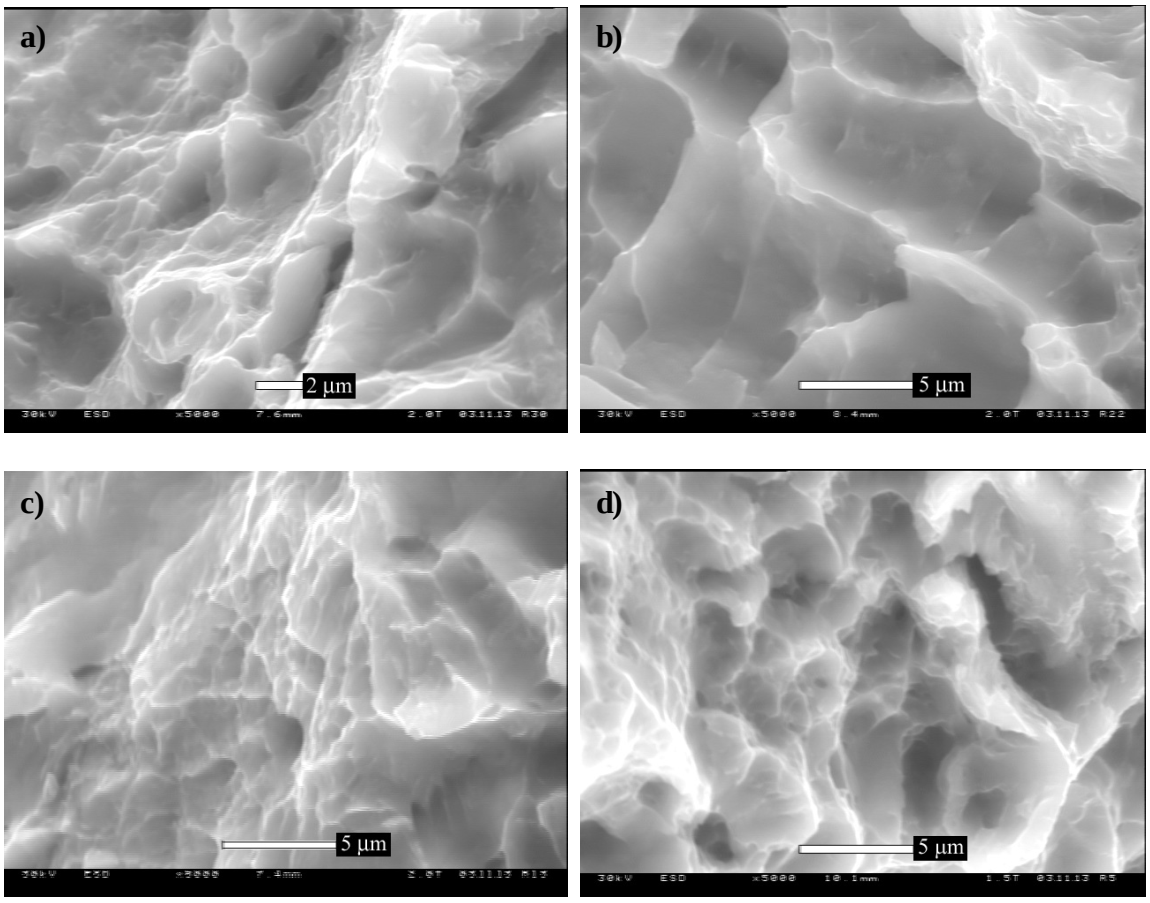

Figure 22: Fracture surfaces of tensile specimens, 5000x. (a) Base metal, (b) matching filler metal weld, (c) modified 50 ppm Y filler metal weld, and (d) modified 200 ppm Y metal.

VII. FRACTURE TOUGHNESS TESTING

VII.1 Theory

A review of the theories involved with fracture toughness testing will be provided here [31, 32]. Stresses in the vicinity of a crack tip can be given as:

$$s_{ij} = \frac{K}{\sqrt{2pr}} f_{ij}(q) \tag{1}$$

where r and θ are the cylindrical polar coordinates of a point with respect to the crack tip as illustrated in Figure 23.

The magnitude of the elastic stress field is given by a constant, K. Fracture toughness of brittle/elastically behaving materials is typically characterized by this stress intensity factor, K. The typical form of the stress intensity factor is given by:

$$K = s\sqrt{pa} * f\left(\frac{a}{W}\right) \tag{2}$$

where σ is the stress at a point ahead of the crack tip, a is the crack length, and f(a/w) is a dimensionless parameter that depends on the geometries of the specimen and crack.

Irwin [33] demonstrated that the Griffith theory for ideally brittle materials could be modified such that cracking in relatively ductile materials exhibiting limited plastic deformation was accounted for. (Note that this approach requires an ideally sharp crack and is not practical at all for slow stable crack growth.) Irwin thereby established that a critical stress intensity of either K_C (plane stress) or K_{IC} (plane strain) governs tensile fracture in theses materials. K_C values depend upon specimen temperature, thickness and constraint. For maximum constraint, the limiting value of K_C becomes K_{IC}.

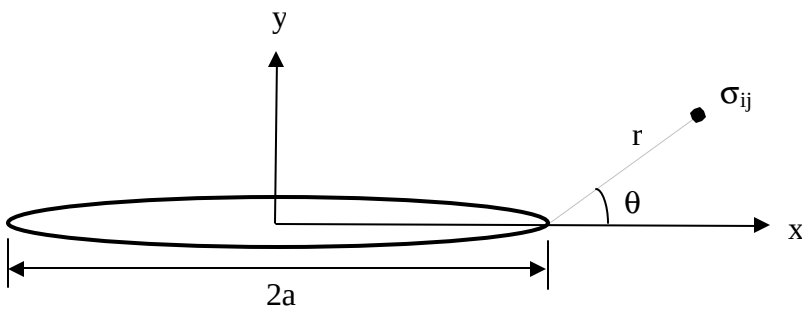

Figure 23: Stresses in the vicinity of a crack tip.

Therefore, K_{IC} may be considered a material property that characterizes crack resistance and is called the plane strain fracture toughness.

When the plastic zone is small compared to the crack size, this Linear Elastic Fracture Mechanics (LEFM) theory is perfectly valid. However, if there is significant crack tip plasticity, the problem must be treated elasto-plastically. The Elastic-Plastic Fracture Mechanics (EPFM) is not as well developed as LEFM theory though, and is complicated to understand. Some basic aspects of this theory will now be discussed.

The accepted characterizing parameter in EPFM is known as J, the crack driving energy. This constant, J, is found based on the J-integral concept, which is itself based on an energy balance approach. The energy balance is given by the Griffith Energy Balance Approach [34]:

$$U = U_O + U_a + U_g - F \tag{3}$$

where U_O is the elastic energy content of the loaded uncracked plate (constant), U_a is the change in the elastic stain energy caused by introducing the crack in the plate, U_γ is the change in elastic surface energy caused by the formation of the crack surfaces, and F is the work performed by external forces.

This equation remains valid even for nonlinear elastic behavior of a material. When U no longer increases with increasing crack length, a, and instability will occur such that:

$$\frac{dU}{da} \leq 0 \tag{4a}$$

With U_O being a constant:

$$\frac{d}{da}\left(U_a + U_g - F\right) \leq 0 \tag{4b}$$

Rearranging Equation 4b leads to:

$$\frac{d}{da}\left(F - U_a\right) \geq \frac{dU_g}{da} \tag{5}$$

Regarding Equation 5, dF/da represents the energy provided by the external work per unit crack extension and dU_a/da is the increase of elastic energy owing to the external work. Therefore, $dF/da - dU_a/da$ is the amount of energy that remains available for crack extension. The quantity dU_γ/da is the elastic surface energy of the crack surfaces. This is the energy needed for the crack to grow, or in other words, the crack resistance.

From Equation 5, a nonlinear elastic equivalent is defined such that:

$$J = \frac{d}{da}\left(F - U_a\right) \tag{6}$$

Using Equation 3, the potential energy, U_p, is defined as

$$U_p = U_O + U_a - F \tag{7}$$

Such that

$$U = U_p + U_g \tag{8}$$

where U_p takes into account all of the energy terms that contribute to nonlinear elastic behavior, and U_γ (defined previously) is irreversible.

Differentiating U_p, with U_O being constant, leads to:

$$\frac{dU_p}{da} = \frac{d}{da}\left(U_a - F\right) = -\frac{d}{da}\left(F - U_a\right) \tag{9}$$

And from Equation 6, it is seen by definition that:

$$J = -\frac{dU_p}{da} \tag{10}$$

Examining Equation 5 it is seen that dF/da is equivalent to the energy supplied by the external force over an increment of crack extension and that dU_a/da is the increase of elastic energy owing to the external work. The term dU_p/da in Equation 6 thereby represents a change in stored energy. If this stored energy decreases, there is a release of crack driving energy, J, in order to provide the energy, dU_γ/da, for an increase in crack surface by da.

For a two-dimensional body of area, A, with surface tractions, T_i, prescribed over a portion of the bounding surface, Γ, the potential energy of the body is given by [32]:

$$U_p = \int_A W dA - \int_\Gamma T_i u_i ds \tag{11}$$

where W is strain energy density, u is a displacement vector and ds is a length of surface. By differentiating Equation 11, a formal definition of J is obtained, such that:

$$J = \frac{1}{B}\int_A \frac{dW}{da} dA - \frac{1}{B}\int_\Gamma T_i \frac{du_i}{da} ds \tag{12}$$

After manipulations [35], J can be written as:

$$J = \int_\Gamma \left(W dy - T_i \frac{\partial u_i}{\partial x_i} ds \right) \tag{13}$$

This integral has the property that J = 0 on any closed contour not encircling a singularity within an elastic solid. That is, the path independency of the J integral expression allows calculation along a contour remote from the crack tip. This contour can be chosen such that it only contains elastic loads and displacements. This results in the fact that an elastic-plastic energy release rate can be obtained from an elastic calculation along a contour for which loads and displacements are known.

Some observations should now be noted when considering the derivation of J. Notably, the important property that J = 0 on a closed contour is not completely valid in

that some plastic deformation takes place, thus causing the process to be irreversible. This means that the magnitude of J may depend slightly on the integration path and the change in potential energy between crack states does not equal the energy required to form new surfaces. Also, it was assumed that there was no unloading in any part of the material. This is also not true, in that, unloading does take place at the crack tip when crack growth occurs, causing a redistribution of stress at the crack tip. While there is not a rigidly confirmed mathematical foundation to EPFM as there is in LEFM, EPFM does play an important role in the analysis and prevention of failure within its own domain of influence. When more detailed analysis is required in this elastoplastic regime, finite element analysis is performed.

It is also noted however, that there is an equivalency in the elastic regime between J and K, that is:

$$J = \frac{K^2\left(1-u^2\right)}{E} \tag{14}$$

However, a valid K analysis needs a much larger sample in order maintain predominately elastic behavior, whereas the J analysis accounts for large scale plasticity at the crack tip. It is possible to estimate K from J and apply the K analysis if the structure is predominately elastic in behavior. That is the size of the plastic zone at the crack tip must be small compared to the crack length and overall size of the sample or structure to be evaluated.

Figure 24 shows a typical J-R curve with the construction lines for data qualification. A couple of concepts are introduced here. The tearing modulus, T, is calculated from the slope of the J curve from the point at which J_Q (J_{IC}) is determined (blunting line) to the Δa_{max} limit (that is the acceptable J-values known as the R-line).

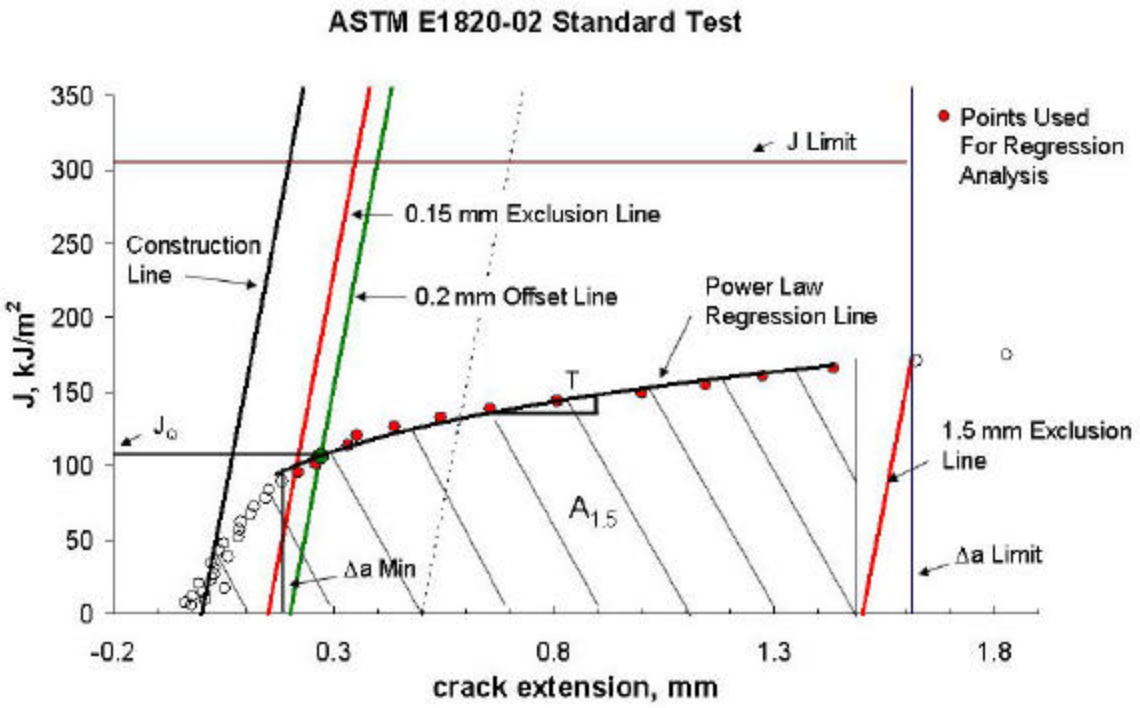

Figure 24: A prototypical J-R curve with construction lines for data qualification.

The tearing modulus attempts to describe stable crack growth under elastic-plastic conditions. The value $A_{1.5}$ describes the area under the J-R curve up to a Δa (crack extension) value of 1.5 mm. This area corresponds to the necessary energy to initiate and provide stable crack extension to the approximate maximum allowable crack extension for J_{IC} determination.

VII.2 Specimen Preparation

Compact tension specimens were prepared in accordance with ASTM standard E1820 [36]. Two compact tension (CT) specimens were machined from the base metal, matching filler metal weld and modified 50 ppm Y weld as shown in Figure 25. The specimens were machined by EDM with the dimensions shown in Figure 26. Grips and pins (known as the tension testing clevis) to hold the CT specimens were machined with the dimensions shown in Figure 27. The grips had to have a Rockwell C hardness value of at least 40 and strength of approximately 1900 MPa, in accordance with ASTM standard E1820. For this reason, Carpenter Stainless Steel alloy 440C was chosen. This alloy's typical room temperature properties with appropriate heat treatment can be seen in Table 13. Following the machining of the grips and pins, a heat treatment was necessary for hardening and then tempering. For the hardening process, the grips and pins were heated to 1311 K (1038°C) and soaked at that temperature for 1 hour in a Lindberg type 51542 furnace with automatic temperature control. The pieces were then removed from the furnace and allowed to cool in air. To obtain a Rockwell C hardness of 60, the pieces were then tempered at 450 K (177°C) for 1 hour. The pieces were again taken out of the

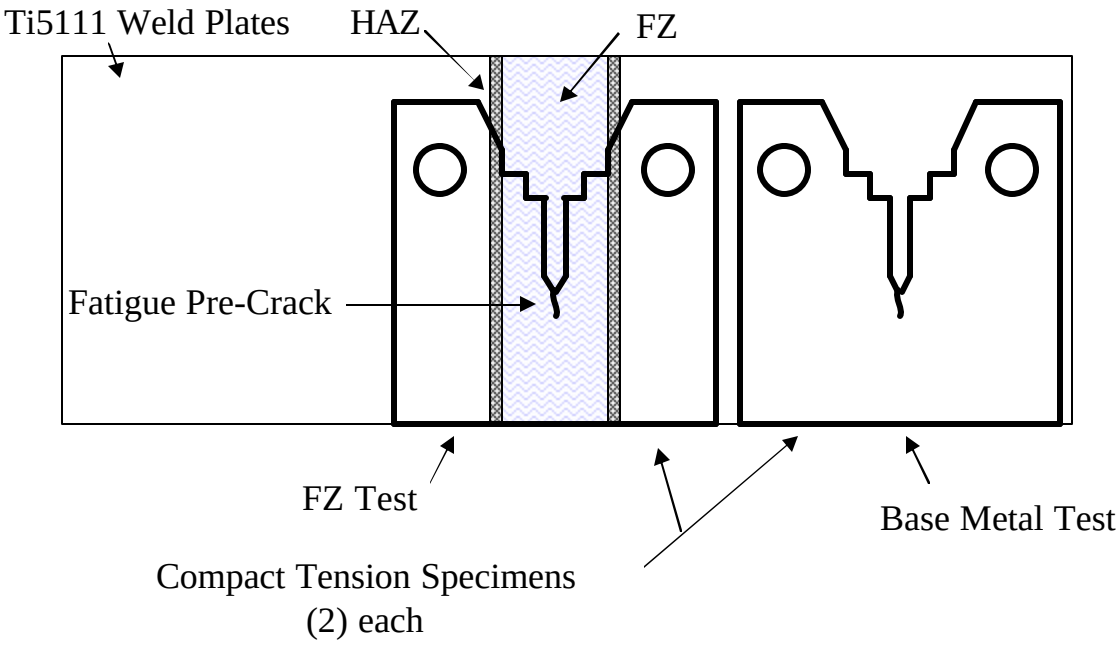

Figure 25: Schematic illustration demonstrating where CT specimens were sectioned from on the weld plates.

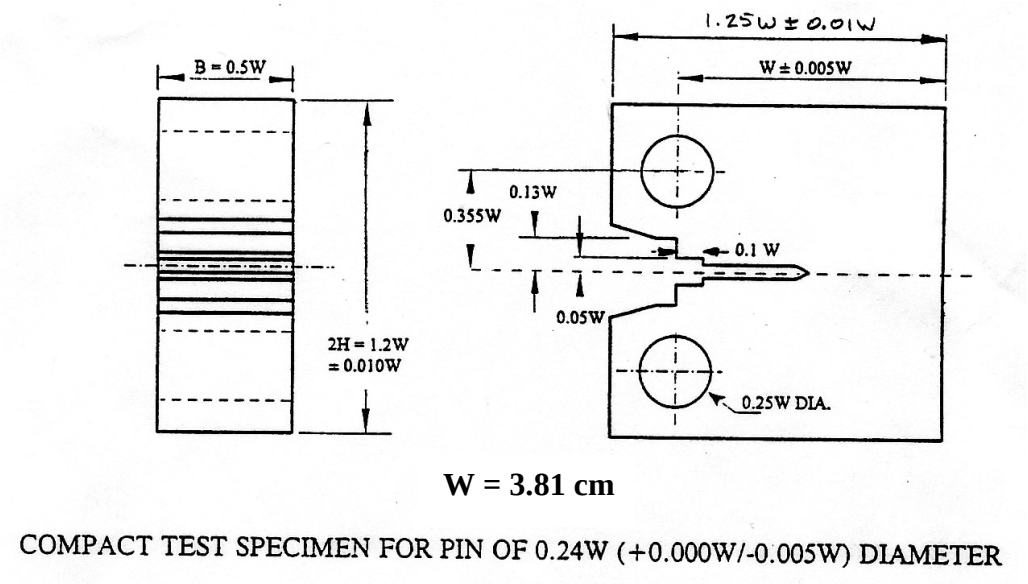

Figure 26: Schematic drawing of CT test specimen where W = 3.81 cm [36].

furnace and allowed to air cool. Once cool, the pieces were polished to remove any oxide scale that was built up during the heat treatment process.

Table 13: Typical room temperature properties of Carpenter Stainless 440C after hardening at 1311 K (1038°C) and tempering at 450 K (177°C).

0.2% YS (MPa)	UTS (MPa)	HRC
1896	1965	60

VII.3 Fatigue Precracking

It is necessary to provide a natural crack for satisfactory fracture toughness test results [36]. A machined notch is produced on the CT specimens, as seen in Figure 28, in order to obtain this crack during fatigue of the specimen. The fatigue precrack is typically produced during cyclical loading of the specimen between 10^4 and 10^6 cycles.

The fatigue crack length, which is defined as the total length of the crack starter configuration plus the fatigue crack (shown in Figure 28), must be between 0.45 and 0.70 W for J determination. For these test specimens with a W of 38.1 mm, this corresponds to a value between 17.2 mm and 26.7 mm. With a crack starter notch of 19.7 mm, this leads to fatigue crack values of 0 and 7.0 mm. The length of the fatigue crack must be a minimum of 2.5% W (1.0 mm) or 1.3 mm, whichever is greater. For these reasons a crack length of 1.5 mm was attempted to be attained.

Allowable fatigue load values are based on the load P_f as follows:

$$P_f = \frac{0.4Bb_o^2 s_y}{2W + a_o} \tag{15}$$

where B is the specimen thickness, b_o is the distance from the original crack front to the back edge of the specimen ($b_o = W - a_o$), $\sigma_y = (\sigma_{ys} + \sigma_{uts})/2$, W is the specimen width and a_o is the physical crack size at the start of testing.

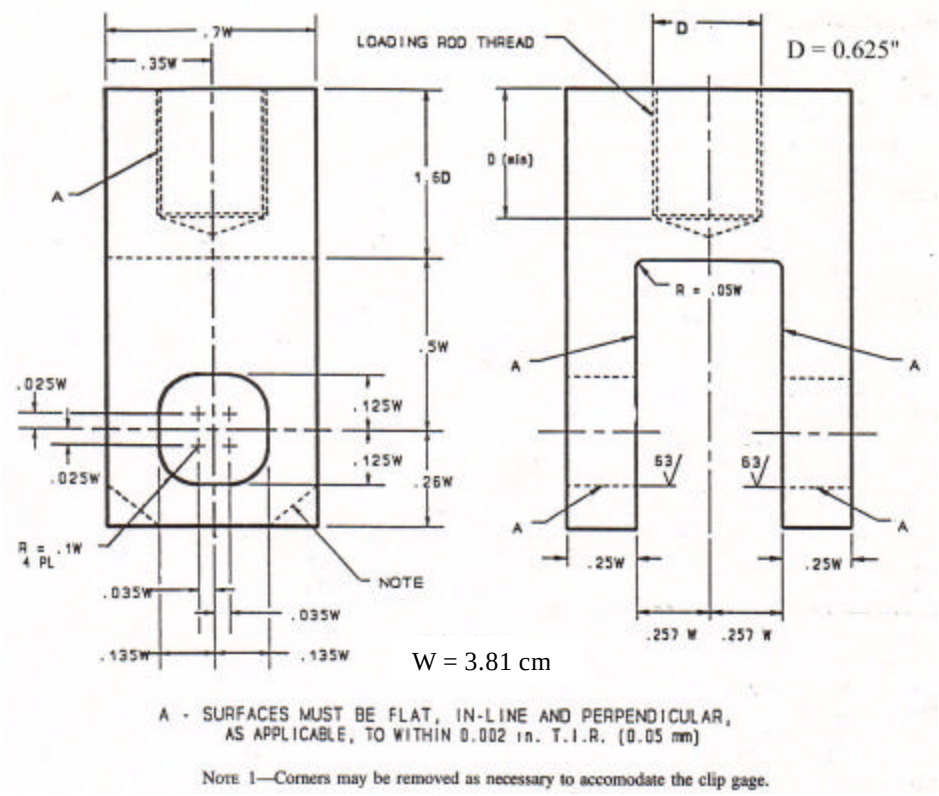

Figure 27: Schematic drawing of tension testing clevis [36].

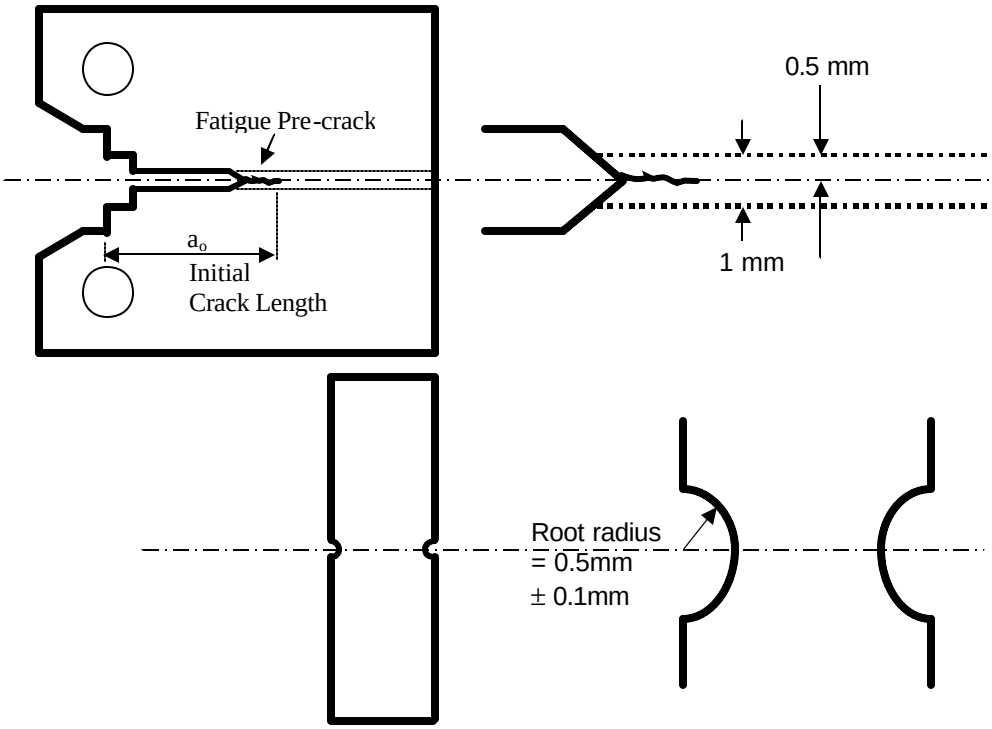

Figure 28: Schematic illustration of side grooves and fatigue crack on CT specimen.

For all specimens, B = 19.05 mm, b_o = 18.42 mm, W = 38.1 mm and a_o = 19.69 mm. For the base material, 0.2% YS = 734.5 MPa and UTS = 768.9 MPa. This leads to a σ_y value of 751.53 MN/m^2. Plugging the variables into Equation 15 leads to a P_f value of 20,254 N. For weld plate 0, 0.2% YS = 739.2 MPa and UTS = 768.9 MPa. This leads to a σ_y value of 768.42 MN/m^2. Plugging the variables into Equation 15 leads to a P_f value of 20,709 N. For weld plate 1, 0.2% YS = 730.5 MPa and UTS = 802.9 MPa. This leads to a σ_y value of 766.70 MN/m^2. Plugging the variables into Equation 15 leads to a P_f value of 20,662 N. Taking the lowest P_f value of 20,254 N, a 10% safety factor is introduced to prevent going over the maximum load, yielding a maximum fatigue load of 18,229 N. Once the fatigue crack is started, the final 1.3 mm of the crack growth should be performed at a fatigue load of 70% of the maximum load value obtained during the procedure.

The tension testing clevis was attached to the Instron 8502 mechanical testing machine previously described. The initial zero load position was recorded. The specimen was then loaded in tension to a load of 17,792 N, with the position being recorded. The specimen was then loaded in compression to a load of 17,792 N, again recording position. The CT specimen was then taken to zero load. The difference in position between the tensile load and compressive load was calculated and then divided by two, to give the peak amplitude. The Instron machine was set up to cyclically load the specimen as a sine wave at a value slightly below the peak amplitude with a frequency of 7 Hz. Once the machine is running and a steady load is reached, the peak amplitude is gradually raised until the maximum allowable load is reached (Note this will be higher than the maximum amplitude calculated due to the fact that as frequency is increased,

there is a lag in the machines response such that a higher entered amplitude is required to obtain an actual amplitude response). The machine is then run until a crack just begins to form in the specimen. The load is then reduced to a value of 70% of the maximum load achieved during the procedure. If it was noted that the crack tip front was advancing further on one side than the other, the CT specimen would be rotated in the sample holder 180° so that the crack would even out. The Instron machine is then run until a crack length of approximately 1.5 mm is achieved. The machine is then stopped and the sample is removed from the clevis device.

After precracking, the CT specimens had side grooves with a root radius of 0.5 mm machined into them alongside the crack by EDM. These side grooves are added after the fatigue crack in order to produce a straight crack front during the fracture toughness testing. The side grooves added to the specimens can be seen in Figure 28.

VII.4 Fracture Toughness Testing Procedure

Fracture toughness testing was performed on an MTS 810 system load frame with a 458 controller. Data acquisition and control was provided by an FTA-ADwin system. The software that was used to run the actual testing was an FTA NLFT (non-linear fracture toughness) package.

The CT specimen dimensions were measured using a Nikon Measuring Microscope MM-40. Knife edges were then attached to the crack tip opening along the load line using cut razor blades and an epoxy mount as shown in Figure 29. The epoxy was allowed to set and then the specimens were inserted into the clevis. The strain gage was then inserted into the crack opening. The data acquisition program was then run.

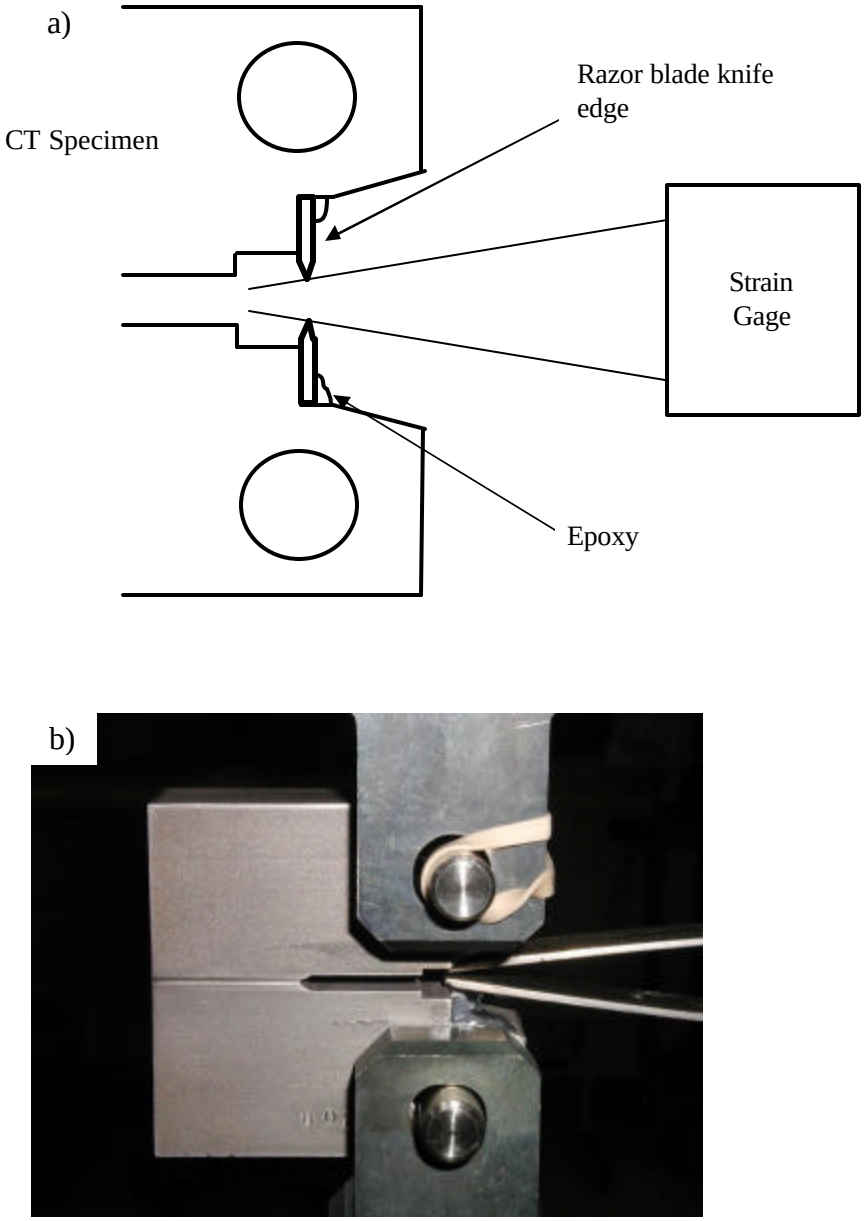

Figure 29: Knife edge setup on CT specimen (a) schematic illustration and (b) photo of the actual setup. Note how the edge of the crack opening and knife edges are directly in line with the center of the loading pins.

The compliance was measured to determine initial crack opening and then the sample was loaded to an increase in load of 2224 N or displaced a maximum of 0.0254 mm (whichever first) and then compliance measured via an unload/reload cycle. This process was repeated until 2 measurements were obtained passed the Δa_{max} endpoint. The sample was then unloaded and removed from the testing machine. The sample was then placed into an oven at 723 K (450°C) for approximately 1 hour, until a purple tint on the outside of the specimen was obtained. The samples were cooled and placed back into the testing machine in order to tear the specimen apart. Typical pictures of the torn specimen surfaces can be seen in Figures 30-32. Note in these pictures the highly ductile fracture surfaces of base metal specimens as compared to the increased brittle appearance of fracture in the welded specimens. Fatigue precrack and final crack length measurements were conducted via the Nikon Measuring Microscope MM-40 in order to check compliance validity.

Some observations have been made that would make fracture toughness testing easier. The knife edges should be machined directly into the CT specimen via EDM so that the edges are directly in line with the load line. The minimum load during the fatigue cracking procedure should be at approximately 10% of the maximum load. Finally, side grooves should be machined such that there is a total of a 10% total reduction on each side. This ensures that the crack front is kept straight.

VII.5 Results and Discussion

Two specimens were tested for each material condition. For the base material, specimens were labeled as 801 and 802. Matching filler metal weld specimens were

Figure 30: Typical compact tension specimen fracture surfaces from Ti5111 base metal. Note extensive plastic deformation leading to ductile fracture.

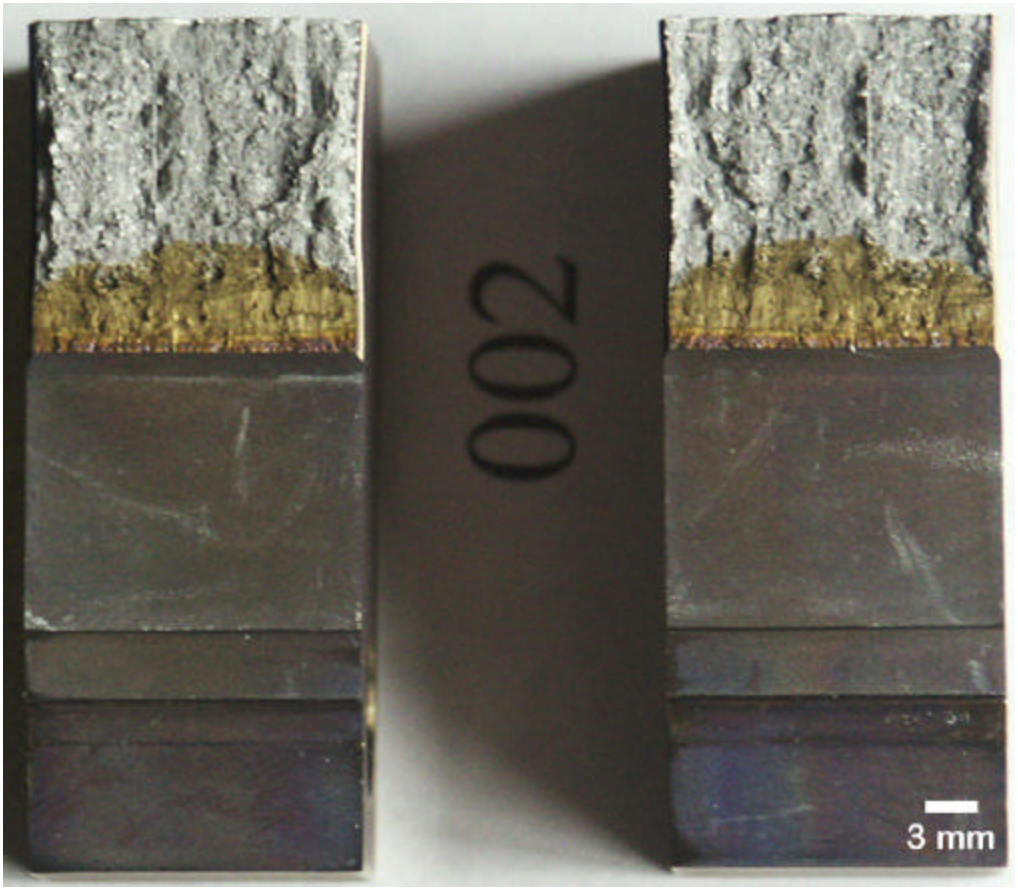

Figure 31: Typical compact tension specimen fracture surfaces from Ti5111 matching filler metal weld. Note increased aspect of brittle fracture as compared to the base material.

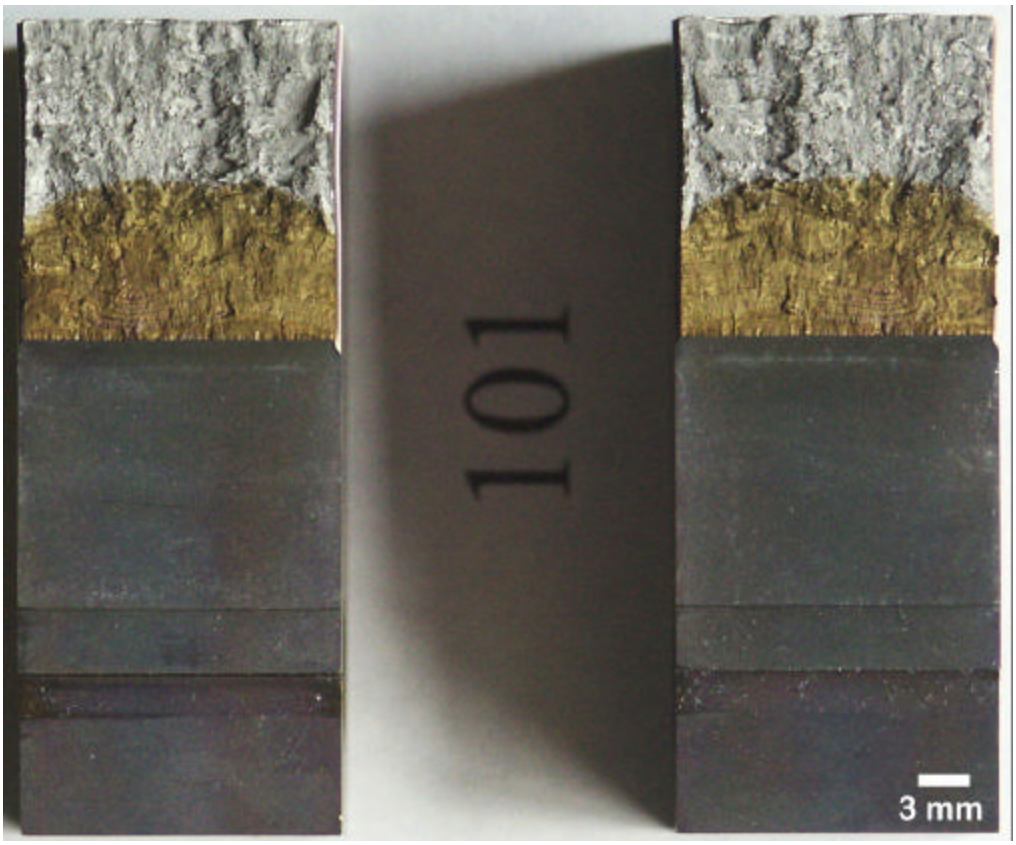

Figure 32: Typical compact tension specimen fracture surfaces from Ti5111 modified 50 ppm Y filler metal weld. Note increased aspect of brittle fracture as compared to the base metal but with a slightly more ductile aspect as compared to the matching filler metal.

labeled as 001 and 002. Modified 50 ppm Y welds were identified by the labels 101 and 102. Load vs displacement data and load vs time data can be seen in Figures 33-38. The resulting J-R curves can be seen in Figures 39-41. Fracture toughness worksheets are shown in Tables 14-19. Table 20 contains a list of the average results obtained from the J_{IC} fracture toughness testing results. Numbers in parentheses correspond to the values of standard deviation.

Table 14: Fracture toughness worksheet for sample 801.

Specimen ID	801	**Geometry**	C(T)
Description	Base Metal	**Orientation**	
Material	Ti-5111	**Yield (MPa)**	734.3
Temperature(C)	23.9	**Tensile (MPa)**	776.3
Environment	Lab Air	**Modulus (GPa)**	110.3
Specimen Dimensions			
Thickness (mm)	18.994	**Notch Depth (mm)**	19.406
Net Thickness (mm)	18.204	**Gage Length (mm)**	2.540
Width (mm)	38.039	**Alpha Ratio**	1
Pin Spacing (mm)	27.051		
Precrack Parameters			
Pmax (kN)	18.238	**Stress Ratio**	-1
Final a (mm)	22.860	**Kmax (MPa*v(m))**	55.2
Pf (kN)	18		

Initial measured crack lengths (mm)

20.930	20.625	20.810	20.752	20.706	20.731	20.762	20.894	20.902

Final measured crack lengths (mm)

20.930	22.723	24.199	25.060	24.107	25.085	23.063	21.951	22.131
x			x		x		x	x

Ave. initial crack length (mm)	20.774	**aoq (mm)**	20.755
Ave. final crack length (mm)	23.465	**Compliance Adj. Factor**	1.076
Delta a measured (mm)	2.690	**Effective Modulus (GPa)**	118.7
Delta a predicted (mm)	2.143		

Results

J_Q (E1820)	140.1 **kJ/m^2**	**Tearing Modulus (kN/m^2)**	55.2
K_{JIC}(E'*JQ)^1/2	130.3 **MPa*v(m)**		

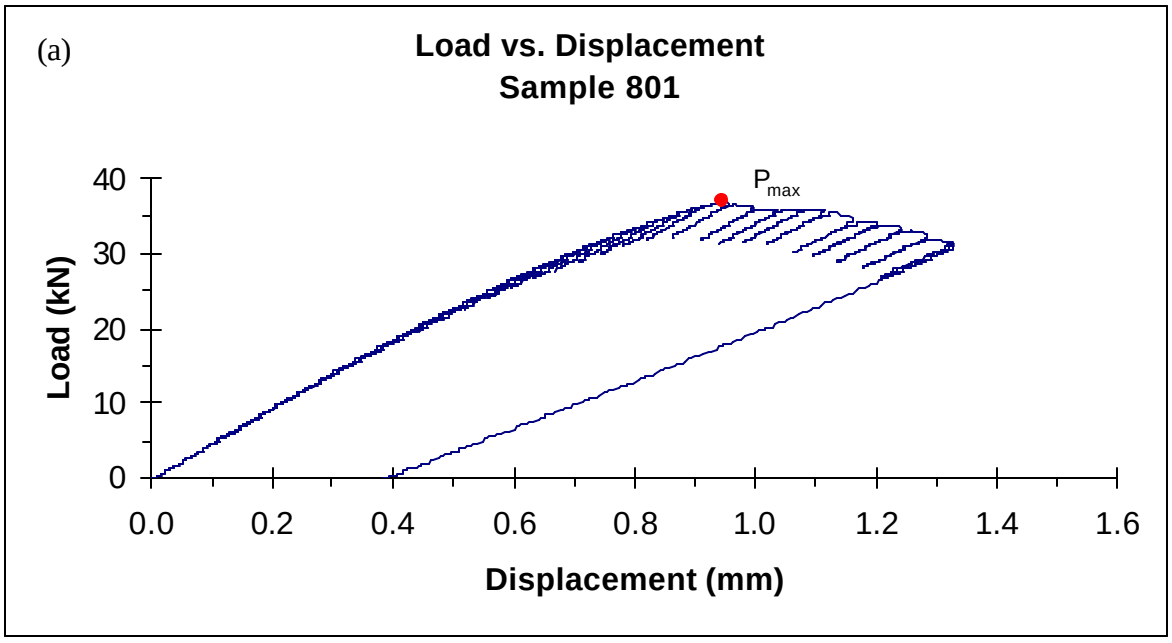

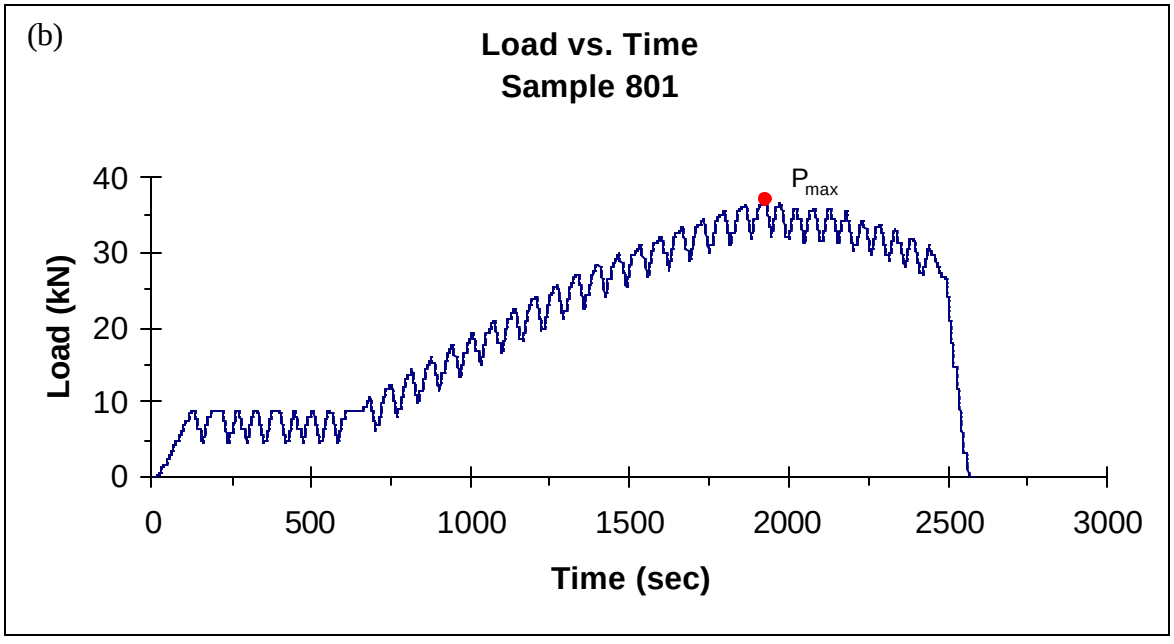

Figure 33: Ti5111 base metal #1 (sample 801); (a) Load vs. Displacement, and (b) Load vs. Time, data plots for fracture toughness testing.

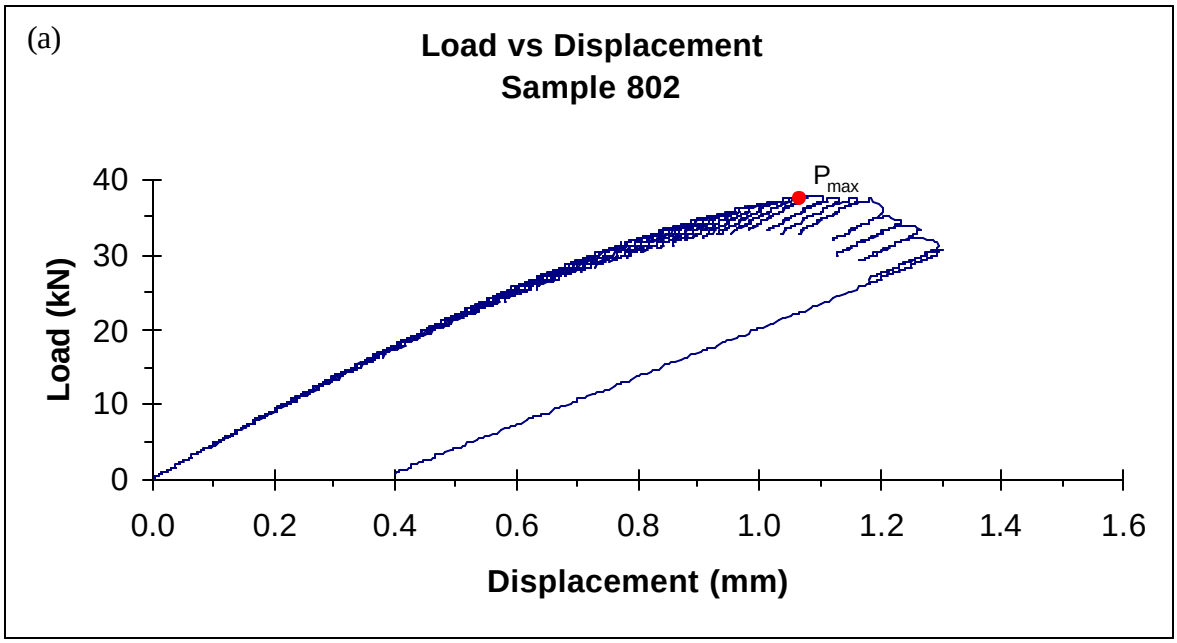

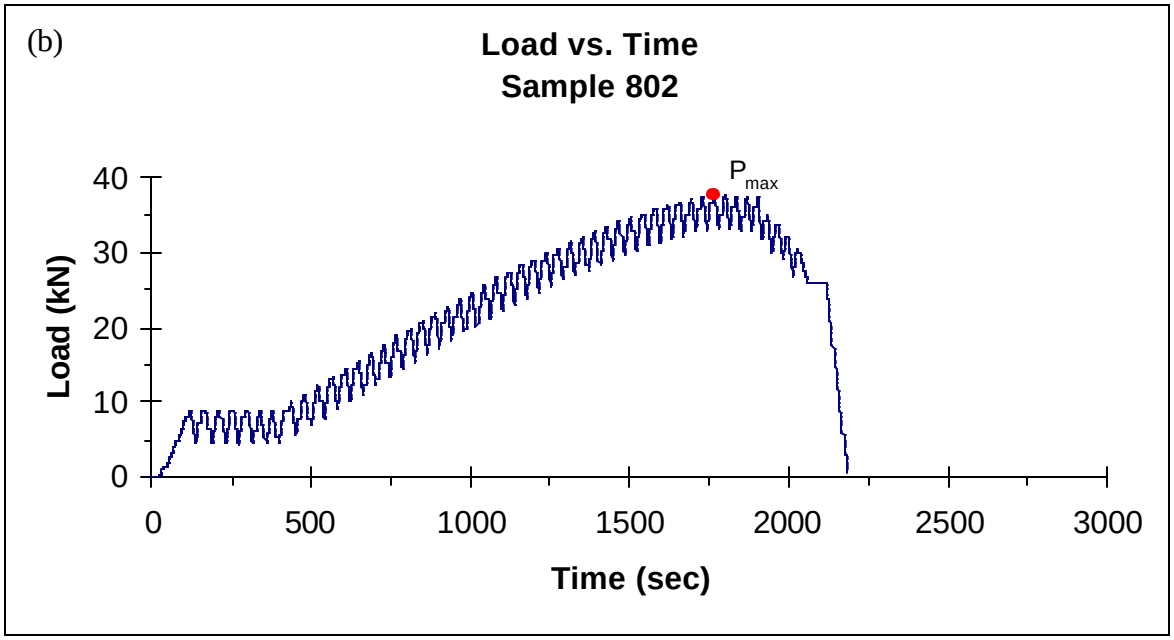

Figure 34: Ti5111 base metal #2 (sample 802); (a) Load vs. Displacement, and (b) Load vs. Time, data plots for fracture toughness testing.

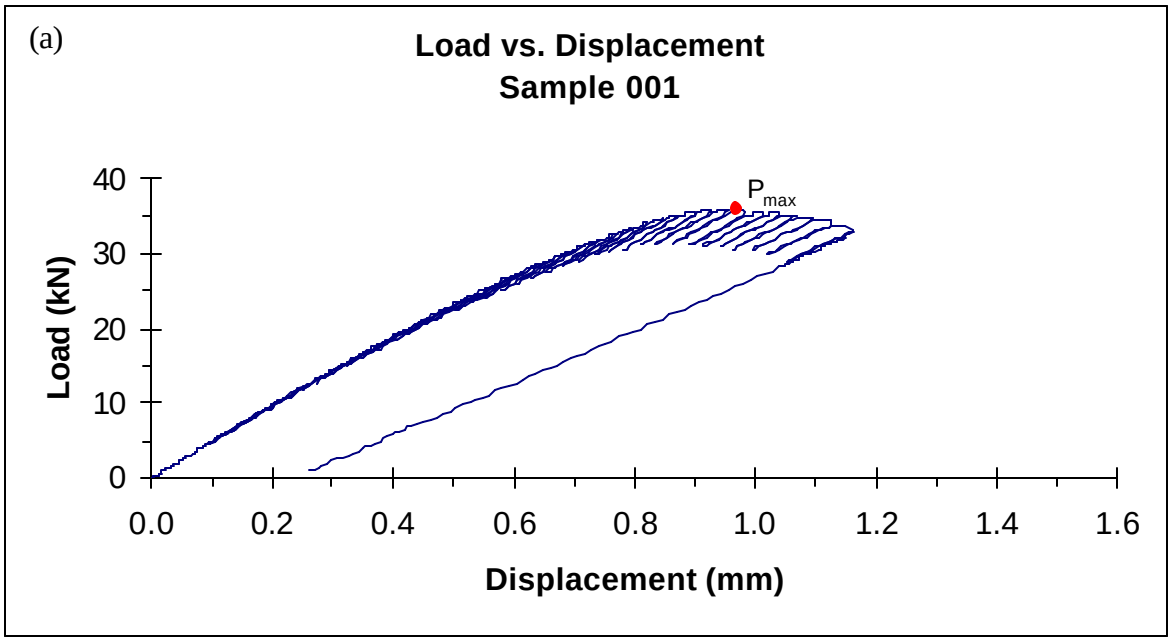

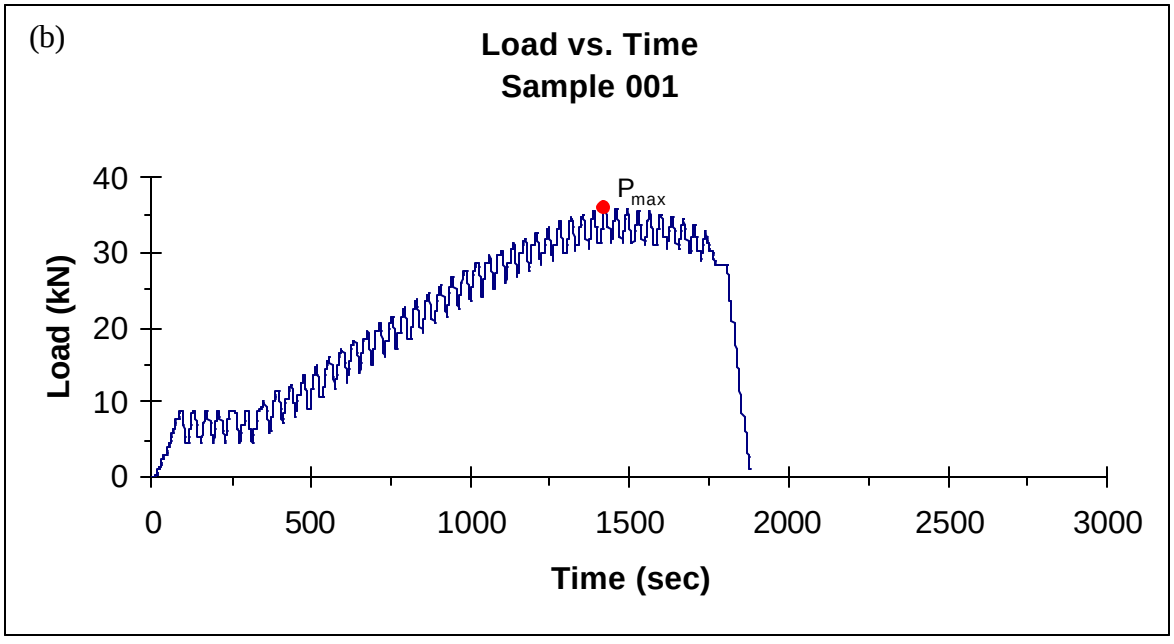

Figure 35: Ti5111 matching filler metal weld #1 (sample 001); (a) Load vs. Displacement, and (b) Load vs. Time, data plots for fracture toughness testing.

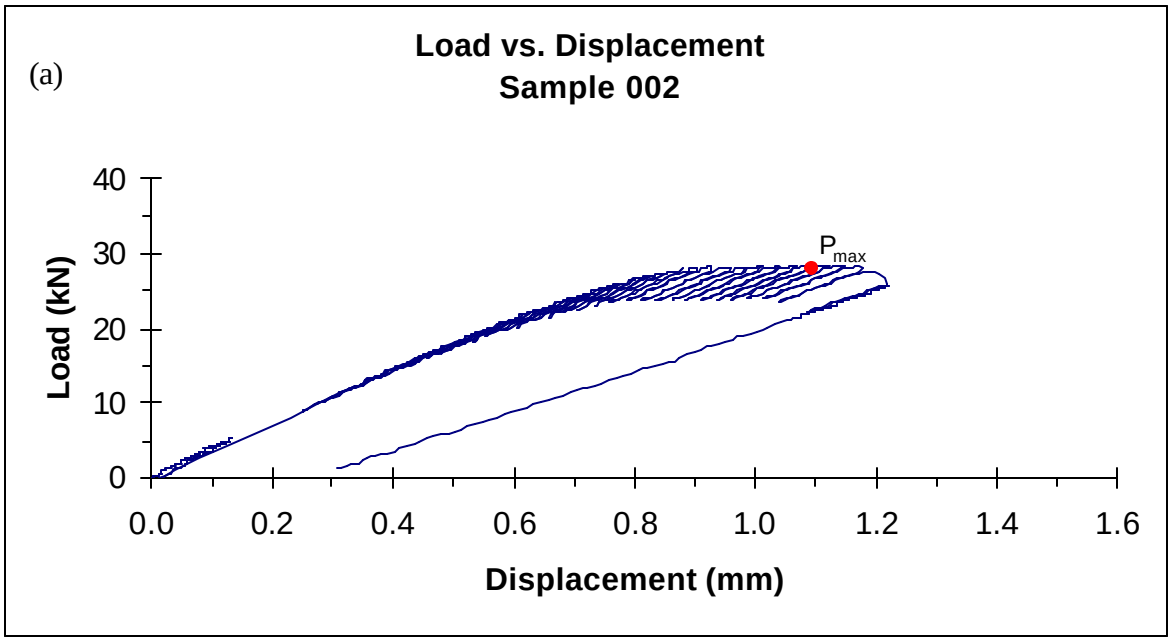

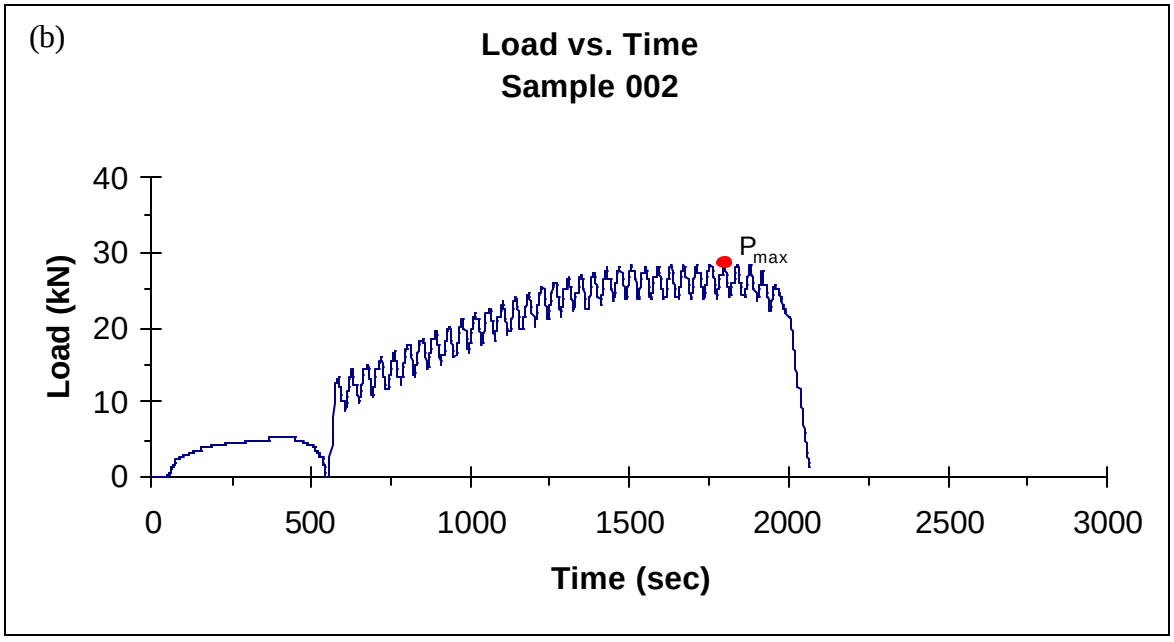

Figure 36: Ti5111 matching filler metal weld #2 (sample 002); (a) Load vs. Displacement, and (b) Load vs. Time, data plots for fracture toughness testing.

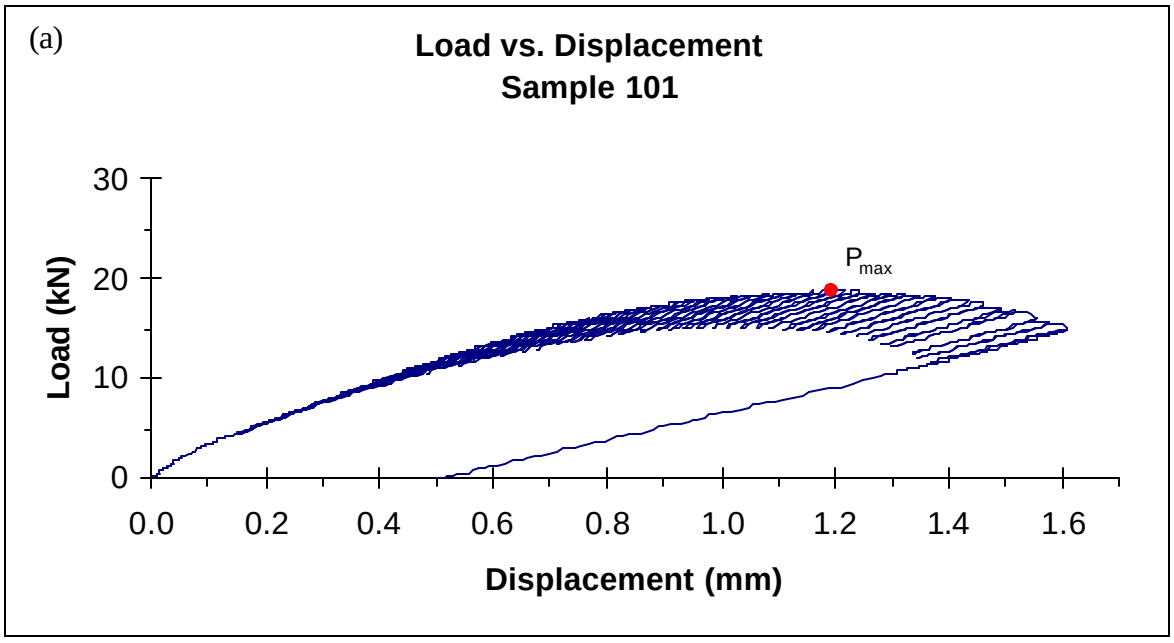

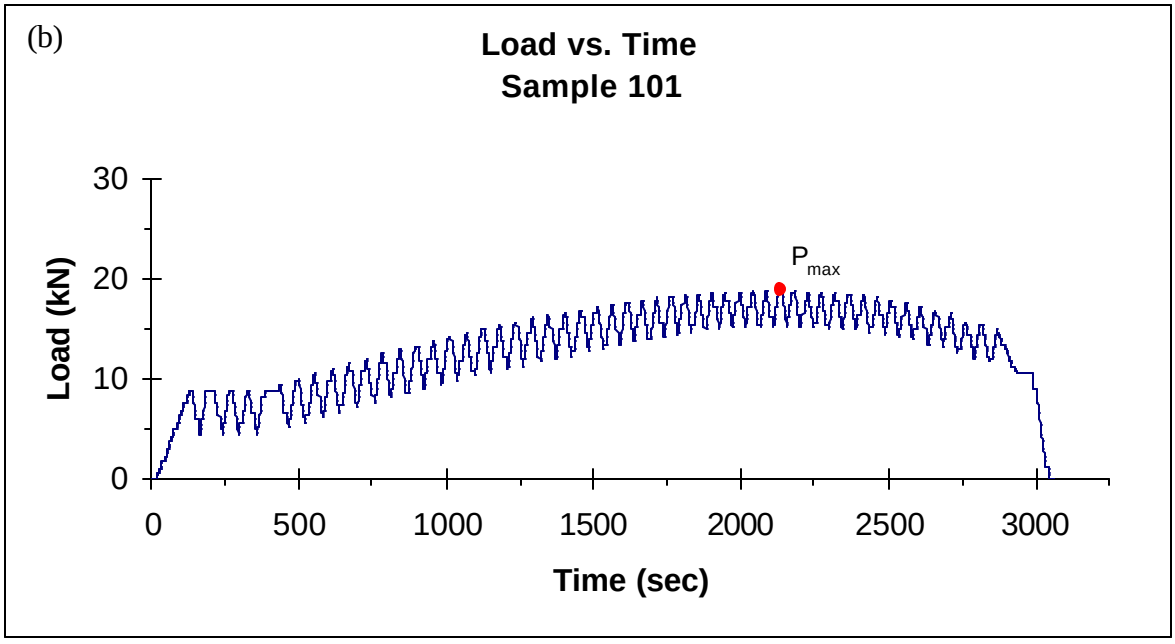

Figure 37: Ti5111 modified 50 ppm Y filler metal weld #1 (sample 101); (a) Load vs. Displacement, and (b) Load vs. Time, data plots for fracture toughness testing.

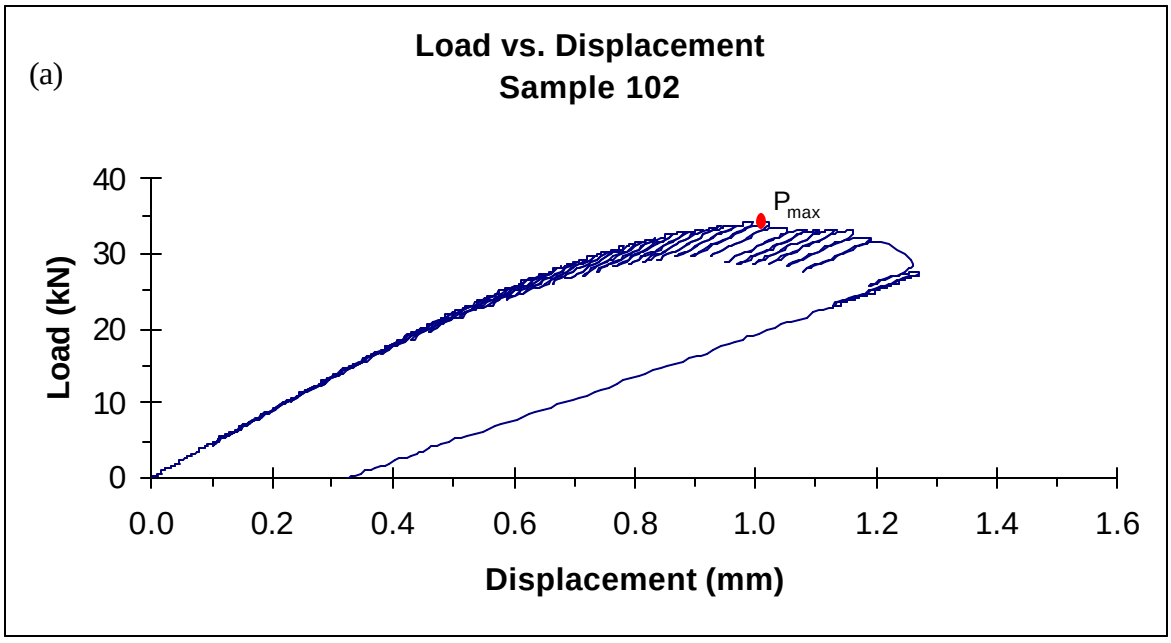

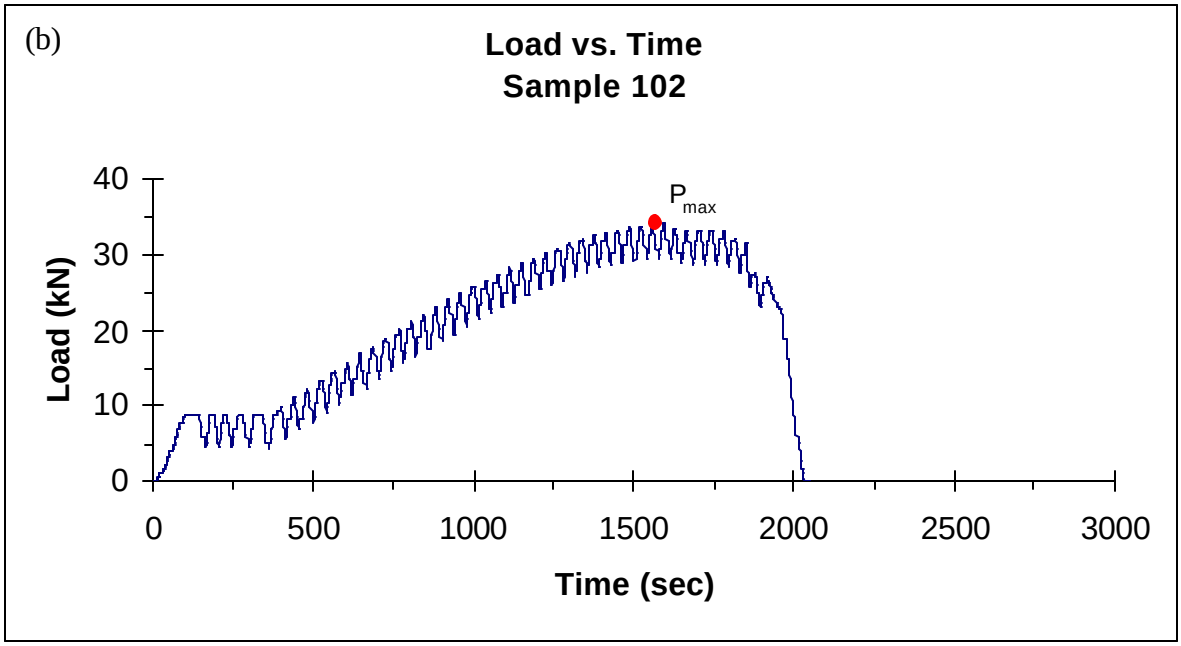

Figure 38: Ti5111 modified 50 ppm Y filler metal weld #2 (sample 102); (a) Load vs. Displacement, and (b) Load vs. Time, data plots for fracture toughness testing.

(a)

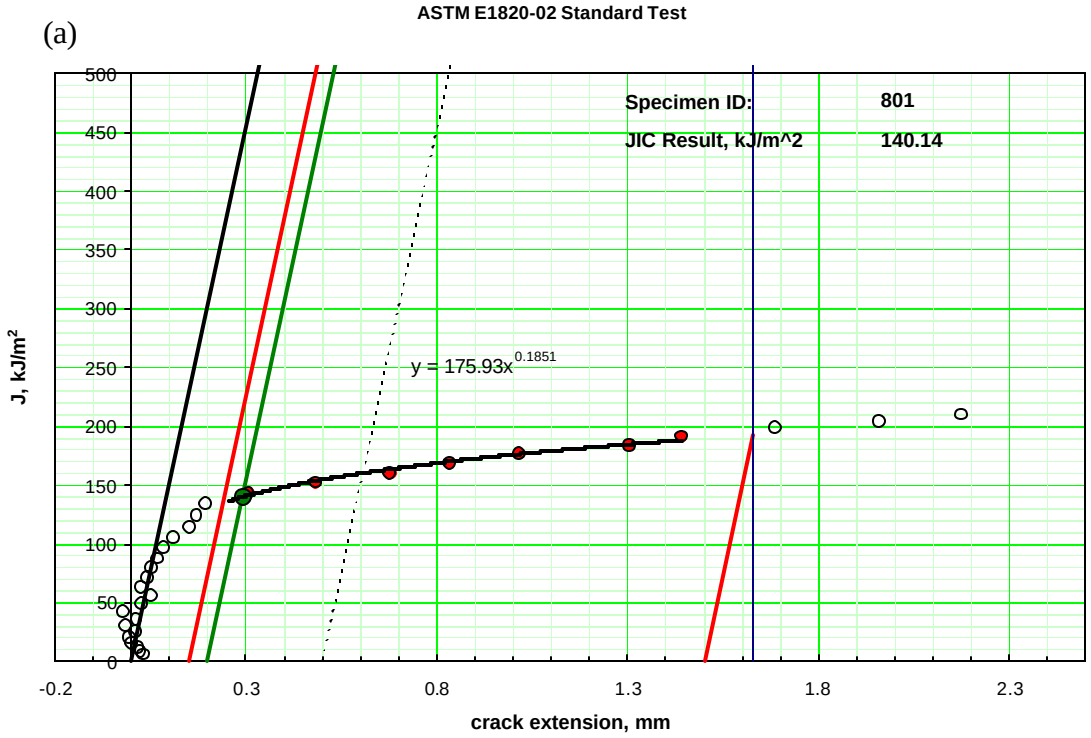

(b)

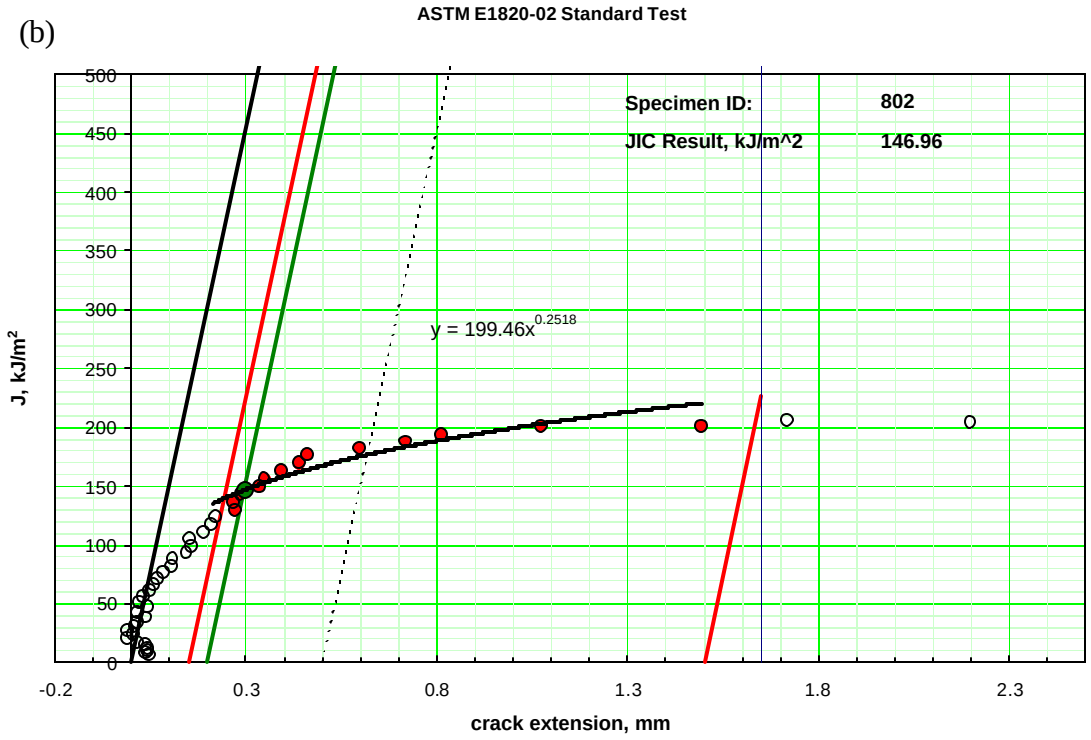

Figure 39: Resulting J-R curves for Ti5111 base metal - (a) #1 (sample 801), and (b) #2 (sample 802), CT specimens.

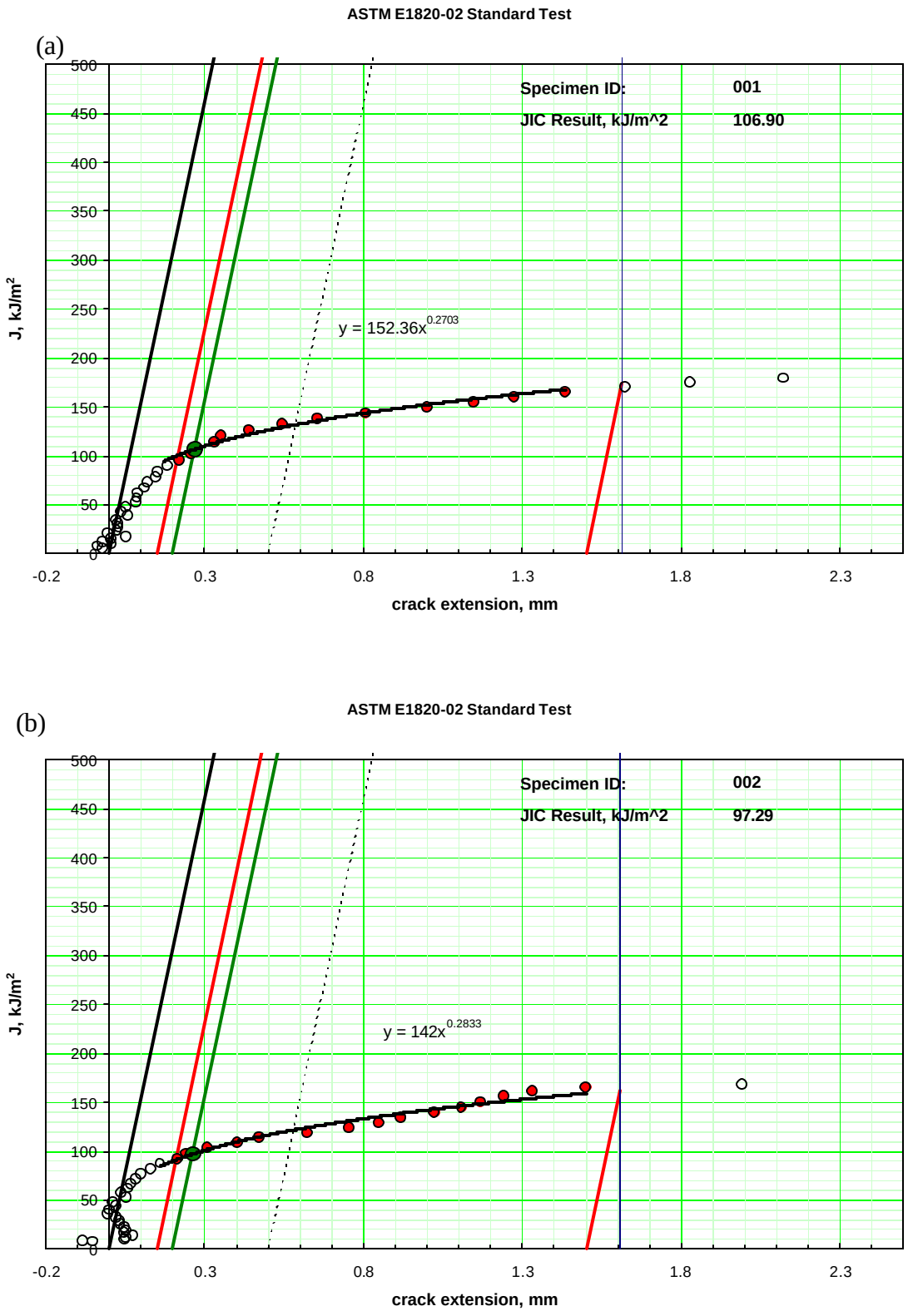

Figure 40: Resulting J-R curves for Ti5111 matching filler metal welds - (a) #1 (sample 001), and (b) #2 (sample 002), CT specimens.

(a)

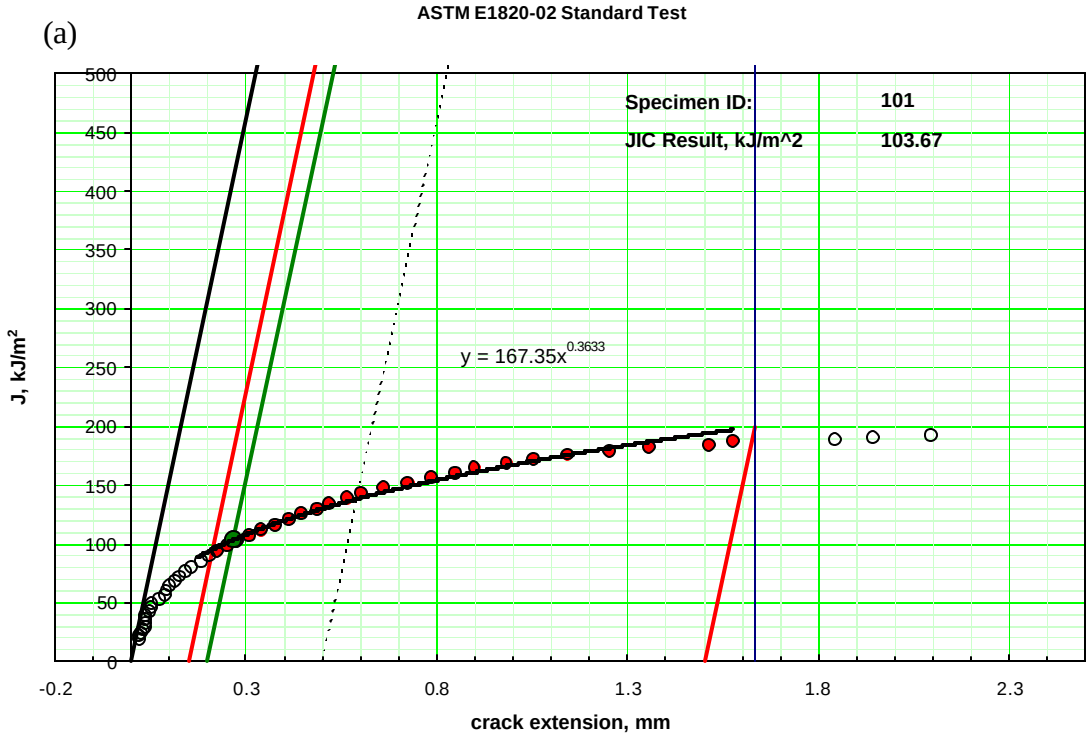

(b)

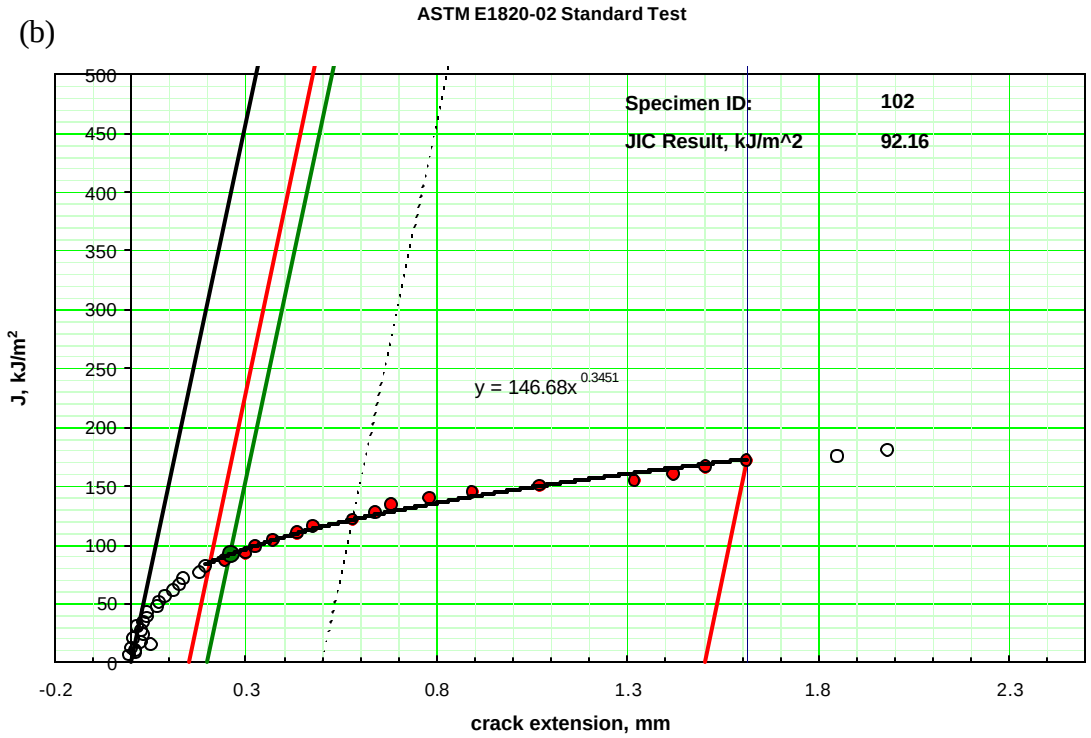

Figure 41: Resulting J-R curves for Ti5111 modified 50 ppm Y filler metal welds- (a) #1 (sample 101), and (b) #2 (sample 102), CT specimens.

Table 15: Fracture toughness worksheet for sample 802.

Specimen ID	802	**Geometry**	C(T)
Description	Base Metal	**Orientation**	
Material	Ti-5111	**Yield (MPa)**	734.3
Temperature(C)	23.9	**Tensile (MPa)**	776.3
Environment	Lab Air	**Modulus (GPa)**	110.3

Specimen Dimensions

Thickness (mm)	18.987	**Notch Depth (mm)**	19.350
Net Thickness (mm)	18.202	**Gage Length (mm)**	2.540
Width (mm)	38.011	**Alpha Ratio**	1
Pin Spacing (mm)	27.051		

Precrack Parameters

Pmax (kN)	17.348	**Stress Ratio**	-1
Final a (mm)	22.860	**Kmax (MPa*v(m))**	53.9
Pf (kN)	17		

Initial measured crack lengths (mm)

21.445	21.115	20.968	20.846	20.800	21.074	21.133	21.102	21.064

Final measured crack lengths (mm)

22.281	24.016	24.922	24.275	23.625	23.906	24.061	23.233	21.986
x								x

Ave. initial crack length (mm)	21.037	**aoq (mm)**	21.003
Ave. final crack length (mm)	23.772	**Compliance Adj. Factor**	1.098
Delta a measured (mm)	2.735	**Effective Modulus (GPa)**	121.1
Delta a predicted (mm)	2.151		

Results

J_Q (E1820)	147.0 **kJ/m^2**	**Tearing Modulus (kN/m^2)**	76.5
K_{JIC}(E'*JQ)^1/2	133.5 **MPa*v(m)**		

Table 16: Fracture toughness worksheet for sample 001.

Specimen ID	001	**Geometry**	C(T)
Description	Matching Filler Metal	**Orientation**	
Material	Ti-5111	**Yield (MPa)**	739.1
Temperature(C)	23.9	**Tensile (MPa)**	797.7
Environment	Lab Air	**Modulus (GPa)**	110.3

Specimen Dimensions

Thickness (mm)	18.984	**Notch Depth (mm)**	19.441
Net Thickness (mm)	18.072	**Gage Length (mm)**	2.540
Width (mm)	38.014	**Alpha Ratio**	1
Pin Spacing (mm)	27.051		

Precrack Parameters

Pmax (kN)	18.238	**Stress Ratio**	-1
Final a (mm)	22.860	**Kmax (MPa*v (m))**	54.5
Pf (kN)	18		

Initial measured crack lengths (mm)

21.102	20.874	20.566	20.163	20.338	20.406	20.485	20.889	21.288

Final measured crack lengths (mm)

21.354	22.281	23.432	23.246	23.508	23.401	23.106	22.588	21.803
x								

Ave. initial crack length (mm)	20.614	**aoq (mm)**	20.650
Ave. final crack length (mm)	22.893	**Compliance Adj. Factor**	1.089
Delta a measured (mm)	2.278	**Effective Modulus (GPa)**	120.1
Delta a predicted (mm)	2.145		

Results

J_Q (E1820)	106.9 **kJ/m^2**	**Tearing Modulus (kN/m^2)**	67.6
K_{JIC}(E'*JQ)^1/2	113.8 **MPa*v(m)**		

Table 17: Fracture toughness worksheet for sample 002.

Specimen ID	002	**Geometry**	C(T)
Description	Matching Filler Metal	**Orientation**	
Material	Ti-5111	**Yield (MPa)**	739.1
Temperature(C)	23.9	**Tensile (MPa)**	797.7
Environment	Lab Air	**Modulus (GPa)**	110.3

Specimen Dimensions

Thickness (mm)	18.976	**Notch Depth (mm)**	19.439
Net Thickness (mm)	18.214	**Gage Length (mm)**	2.540
Width (mm)	38.042	**Alpha Ratio**	1
Pin Spacing (mm)	27.051		

Precrack Parameters

Pmax (kN)	16.903	**Stress Ratio**	-1
Final a (mm)	22.860	**Kmax (MPa*v(m))**	60.6
Pf (kN)	14		

Initial measured crack lengths (mm)

22.451	22.964	22.944	22.629	22.111	22.258	22.212	22.776	22.431

Final measured crack lengths (mm)

22.916	24.387	25.288	25.507	25.441	25.255	24.356	24.282	22.715
x								x

Ave. initial crack length (mm)	22.542	**aoq (mm)**	22.607
Ave. final crack length (mm)	24.666	**Compliance Adj. Factor**	1.101
Delta a measured (mm)	2.125	**Effective Modulus (GPa)**	121.4
Delta a predicted (mm)	2.044		

Results

J_Q (E1820)	97.3 **kJ/m^2**	**Tearing Modulus (kN/m^2)**	71.7
K_{JIC}(E'*JQ)^1/2	108.6 **MPa*v(m)**		

Table 18: Fracture toughness worksheet for sample 101.

Specimen ID	101	**Geometry**	C(T)
Description	50 ppm Y Filler Metal	**Orientation**	
Material	Ti-5111	**Yield (MPa)**	730.1
Temperature(C)	23.9	**Tensile (MPa)**	803.2
Environment	Lab Air	**Modulus (GPa)**	110.3
Specimen Dimensions			
Thickness (mm)	18.984	**Notch Depth (mm)**	19.522
Net Thickness (mm)	18.207	**Gage Length (mm)**	2.540
Width (mm)	38.042	**Alpha Ratio**	1
Pin Spacing (mm)	27.051		
Precrack Parameters			
		Stress	
Pmax (kN)	15.569	**Ratio**	-1
Final a (mm)	22.860	**Kmax (MPa*v(m))**	82.5
Pf (kN)	8		

Initial measured crack lengths (mm)

25.258	25.997	26.350	26.640	26.231	25.682	25.451	25.809	25.387

Final measured crack lengths (mm)

26.213	27.582	28.501	28.420	28.636	28.824	28.224	27.917	26.396
x								x

Ave. initial crack length (mm)	25.935	**aoq (mm)**	25.928
Ave. final crack length (mm)	28.051	**Compliance Adj. Factor**	1.095
Delta a measured (mm)	2.116	**Effective Modulus (GPa)**	120.7
Delta a predicted (mm)	2.071		

Results

J_Q (E1820)	103.7 **kJ/m^2**	**Tearing Modulus (kN/m^2)**	90.3
K_{JIC}(E'*JQ)^1/2	112.1 **MPa*v(m)**		

Table 19: Fracture toughness worksheet for sample 102.

Specimen ID	102	**Geometry**	C(T)
Description	50 ppm Y Filler Metal	**Orientation**	
Material	Ti-5111	**Yield (MPa)**	730.1
Temperature(C)	23.9	**Tensile (MPa)**	803.2
Environment	Lab Air	**Modulus (GPa)**	110.3

Specimen Dimensions

Thickness (mm)	18.974	**Notch Depth (mm)**	19.522
Net Thickness (mm)	18.138	**Gage Length (mm)**	2.540
Width (mm)	38.085	**Alpha Ratio**	1
Pin Spacing (mm)	27.051		

Precrack Parameters

Pmax (kN)	15.569	**Stress Ratio**	-1
Final a (mm)	22.860	**Kmax (MPa*v(m))**	48.1
Pf (kN)	17		

Initial measured crack lengths (mm)

20.991	20.825	20.930	20.991	20.846	20.843	20.864	21.524	21.740

Final measured crack lengths (mm)

21.354	23.741	24.054	24.574	24.879	25.016	24.447	24.135	23.454
x								

Ave. initial crack length (mm)	21.023	**aoq (mm)**	21.042
Ave. final crack length (mm)	24.157	**Compliance Adj. Factor**	1.075
Delta a measured (mm)	3.133	**Effective Modulus (GPa)**	118.6
Delta a predicted (mm)	3.038		

Results

J_Q (E1820)	92.2 **kJ/m^2**	**Tearing Modulus (kN/m^2)**	73.1
K_{JIC}(E'*JQ)^1/2	105.7 **MPa*v(m)**		

Table 20: Average fracture toughness testing results from Ti-51111 base metal, matching filler metal and modified 50 ppm Y filler metal CT specimens.

Sample	J_{IC} kJ/m^2	K_{JIC} MPa*v(m)	T kN/m^2	$A_{1.5}$ N
Base	143.6 (4.8)	131.9 (2.3)	65.9 (15.1)	252.4 (17.4)
Matching	102.1 (6.8)	111.2 (3.7)	69.7 (2.9)	193.5 (10.3)
50 ppm Y	97.9 (8.1)	108.9 (4.5)	81.7 (12.2)	200.7 (17.8)

From the results in Table 20, it is seen that the J_{IC} values for fracture toughness in both the matching and modified filler metal welds, decrease quite a bit as compared to base metal specimens. The values of J_{IC} for the matching and modified filler metal are approximately the same and are within one standard deviation of one another. When these values are converted to the more commonly used K_{IC} values, it is more readily evident exactly how close these values are to one another. Therefore, the additions of yttrium and subtraction of aluminum to the filler metal does not have a significant effect on the fracture toughness value, as measured by J_{IC}, either one way or the other. This implies that the modifications that were made do not have a deleterious effect on fracture toughness values. This can be expected since the microstructure of the welds has not significantly been altered much by the yttrium additions.

Upon examination of Table 20 again, it is seen that there is a significant increase in the value of the tearing modulus, T and a slight increase in the value of the energy required for increasing the crack length of the specimen by 1.5 mm. The tearing modulus value actually is increased to a value above that of the base metal. These values of T and $A_{1.5}$ indicate that the modified filler metal provides a much greater resistance to cracking once a crack has already been initiated. This increase in resistance to further tearing is also evidenced by the fracture surfaces where the yttrium modified filler metal welds show an increased amount of ductile failure as compared to the matching filler metal

weld. This increased resistance to fracture is an important property in materials, in that complete failure in the modified welds would not be of a catastrophic nature, and would require more energy for failure as compared to matching filler metal welds.

VIII. MICROHARDNESS MAPPING

VIII.1 Introduction

Microhardness testing allows one to test the hardness (resistance of material to plastic deformation) of a specimen on a microscopic scale. Other macrohardness tests, such as Rockwell, result in an average reading that is not as likely to demonstrate true conditions. Microhardness testing usually takes place by statically loading a diamond indenter into a specimen with a load larger than 1 gf and no greater than 1 kgf [37]. The indenter may either be of the Vickers (square based pyramidal head) or Knoops (rhombohedral-shaped pyramidal head) variety. Conversions from microhardness to tensile strength are available for many alloys even though hardness is empirical in nature. Hardness is also an indicator of wear resistance and ductility. By using the hardness testing across many points in a weld zone, one is able to determine microstructural properties concerning the weld, based on these microhardness measurements.

Comparing indentations made with Knoop and Vickers Diamond Pyramid indenters for a given load and test material [37]:

- Vickers indenter penetrates about twice as deep as Knoop indenter
- Vickers indentation diagonal about 1/3 of the length of Knoop major diagonal
- Vickers test is less sensitive to surface conditions than Knoop test
- Vickers test is more sensitive to measurement errors than Knoop test
- Vickers test best for small rounded areas
- Knoop test best for small elongated areas
- Knoop test good for very hard brittle materials and very thin sections

In this testing process, the Vickers hardness (VH) testing method (ASTM Standard E-384 [38]) was used. There are two significant advantages in using VH: (1) Similar indentations and constant hardness measurements are obtained, regardless of the magnitude of loads applied, as long as the specimens are homogeneous. (2) Undivided hardness measurements are possible from extremely soft to extremely hard materials using the same scale.

VH correlates to a value obtained from a test load applied to a specimen from an indentation on it with a square-based pyramidal diamond indenter, which has a force angle of 136°. See Figure 42.

The VH measurement is found from the permanent indentation based on the diagonal lengths using [37]:

$$H_v = 0.102\ F/S = 0.102(2F\sin\theta/2)/d^2 = 0.1891\ F/d^2 \quad (16)$$

where H_v is the Vickers hardness, F is the test load (N), S is the surface area of indentation (mm^2), d is the average diagonal length of an indentation (mm) that equals $(d_1+d_2)/2$, and θ is the face angle of the pyramidal indenter (°).

The program set up by LECO to automatically measure the surface area of the Vickers microhardness indentation is known as the Automatic Microindentation Hardness (AMH) Testing. AMH combines the tasks of indenting the specimen, measuring the surface area of the indent, and then converting and documenting the data into one automated instrument operation. To measure the size of the indentation, the size of the indent must be defined. In order to do this, the specimen must be carefully polished to eliminate any surface scratching that may confuse the program. The specimen should also not be etched. The definition of the indent by AMH is based upon

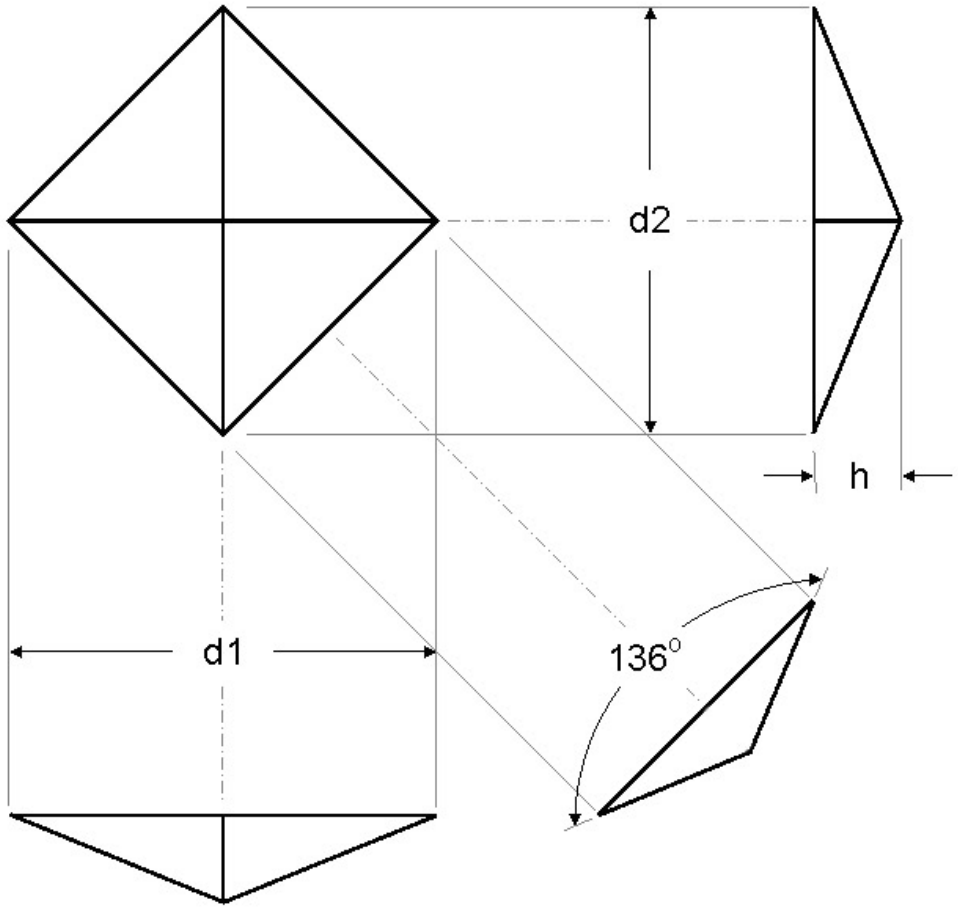

Figure 42: Schematic diagram of the Vickers pyramid diamond indenter indentation.

detection of gray levels (256 gray scale; 0 = black, 255 = white) from the surface of indent as viewed by the camera. After the sample image is obtained by the camera, the AMH system transforms this image to a 256 gray-scale image. The program then uses thresholding, which involves detecting which gray levels are present in the image of the indent and then categorizing the pixels according to a defined range, to obtain the indent surface area. Every pixel in the screen image that falls within the threshold limits is transferred to another part of system memory in order to calculate the Vickers hardness by measuring d_1 and d_2. In the AMH, the threshold pixels appear as red on the image monitor, allowing the user to manually adjust thresholding to the appropriate values. The proper thresholding occurs when the bitplane color precisely covers all of the indent's contour and surface.

VIII.2 Experimental

Specimens were cut off in 6 mm slices, after removing ~ 1.2 cm from the plate edge, from Welds 0, 1 and 2 using EDM. These specimens were then cut to approximately 76 mm in length encompassing the weld zone in the center of the specimen. The specimens were then polished using a Buehler Vibromet polishing table with polishing paper grits of 240, 320, and 400 at 300 RPM to ensure the specimens were flat and to remove the oxide layer resulting from EDM. Specimens were then cut to approximately 35 mm in length using a Buehler Isomet diamond saw, yielding a specimen of approximately 25 mm x 35 mm x 6 mm with the weld zone in the center of the specimen. This length of 35 mm ensured the specimens could be mounted into 50 mm diameter specimen holders.

The three specimens were then mounted into 50 mm diameter Diallyl Phthalate mounts using a Struers Primopress Automated Mounting Press. Approximately 60 cc of the Diallyl Phthalate was used to yield mounts approximately 20 mm in height. A mould release powder was added to the walls of the chamber and then the Diallyl Phthalate was placed around the specimen in the mounting chamber. The mount was then heated to 433 K (160 °C) at 30 kN for 10 minutes. After automatic water cooling, a hard mount was obtained for the specimens. This mount was then rounded on the edges using a polisher to eliminate excess material and sharp edges.

Polishing of the three specimens continued using a Struers RotoPol-31 and RotoForce-4 automatic polisher. The three specimens were mounted on the RotoForce and then ground again to ensure flatness using Struers MD-Piano 120, a resin bonded grinding disc for plane grinding of materials, for 2 minutes at force of 40 N with water cooling at 300 RPM. Between each polishing step, the apparatus was cleaned and the specimens were subjected to an ethanol bath and ultrasonically cleaned for approximately 1 minute to ensure the remnants of the previous polishing step were completely removed. A Struers MD-Allegro polishing disc was then used with a Struers 9 µm diamond suspension at 40 N for 10 minutes with Struers DP Blue Lube at 150 RPM. The same polishing combination was then used at 30 N for a total of 30 minutes. The specimen was removed during this time and examined under an optical microscope to ensure that the scratches from the previous step were completely removed. After this, the apparatus and specimen were again cleaned. Next a Struers MD-Allegro polishing disc was again used with a Struers 6 µm diamond suspension at 30 N and 150 RPM with Blue Lube for a total of 30 minutes. The specimens were again intermittently examined under an optical

microscope to ensure scratches from previous step were removed. After cleaning again, a Struers DP-DAC satin woven acetate polishing cloth was used with a Struers 3 μm diamond suspension at 30 N, 150 RPM, Blue Lube for a total of 15 minutes. The 3 specimens were then polished on a Struers LaboPol-5 at 300 RPM for 5 minutes with Buehler Mastermet Colloidal Silica Suspension on a Buehler Chemomet Disc. This final polishing step is a chemical-mechanical process that removes all the scratches from the relatively soft titanium specimens. For the final 30 seconds or so of polishing, water was turned on to rinse the specimens and disc. No etchant was used so as to not confuse the program as to where the tips of the indent are.

Microhardness testing was carried out on a LECO FM-7 Digital Microhardness Tester, set up by Dr. Deug Moon at the Physical Metallurgy Branch in the Naval Research Laboratories Materials Science and Technology Division headed by Dr. Edward Metzbower [39, 40], using the Vickers method. Test blocks were used to ensure proper calibration of the system. The system was set up to apply a 500 g load using the square pyramidal diamond indenter with a dwell time of 5 seconds. To make the microhardness maps, a grid was set up in the computer with spacing of rows and columns at 1 mm, thereby ensuring spacing greater than 3d between test points. For Weld 0 a grid of 31 rows x 32 columns was created leading to 992 total points to be tested. Weld 1 had 32 rows x 34 columns leading to 1088 total test points. Finally Weld 2 was set up with 32 rows x 33 columns for 1056 total test points. The testing was controlled by the program LECO AMH 32 version 2.3. The machine would first indent all programmed points and then go back to automatically read the values of d_1 and d_2 as previously discussed. Due to the specimen surface features and residual scratches, the program

would occasionally misread or be unable to read values for indent surface area. This required going back and manually measuring the values for d_1 and d_2 by sighting cross-hairs from microscope on appropriate indentation for input to determine Vickers hardness values. Approximately 50-100 manual measurements were required per specimen in order to ensure accurate results.

Hardness values were then saved as a text file and then input to the program Transform PPC that gave a map showing each individual hardness test point. The program was then used to interpolate the original image and generate the final hardness map.

After the Vickers microhardness testing, the specimens were again polished using the procedure described above. The specimens were then etched using Kroll's reagent, consisting of 88% H_2O, 10% HNO_3, and 2% HF, for approximately 20 seconds. The Kroll's reagent colors the β phase a dark brown. Macrographs of the specimens were taken using an Olympus SZH10 Research Stereo Microscope and Polaroid Digital Microscope Camera. The specimens were mounted on a labjack on top of dark felt illuminated in a dark room with a specimen light. Exposure was for approximately 50 ms at 3.5 x magnification.

VIII.3 Results and Discussion

Vickers microhardness test results and macrographs of the areas tested are shown in Figures 43-45. From these results it is immediately clear that the modified 50 ppm Y weld shows hardness values that are most homogeneous and closest to that of the base metal, although the base metal plates do show inhomogeneous spots, likely as a result

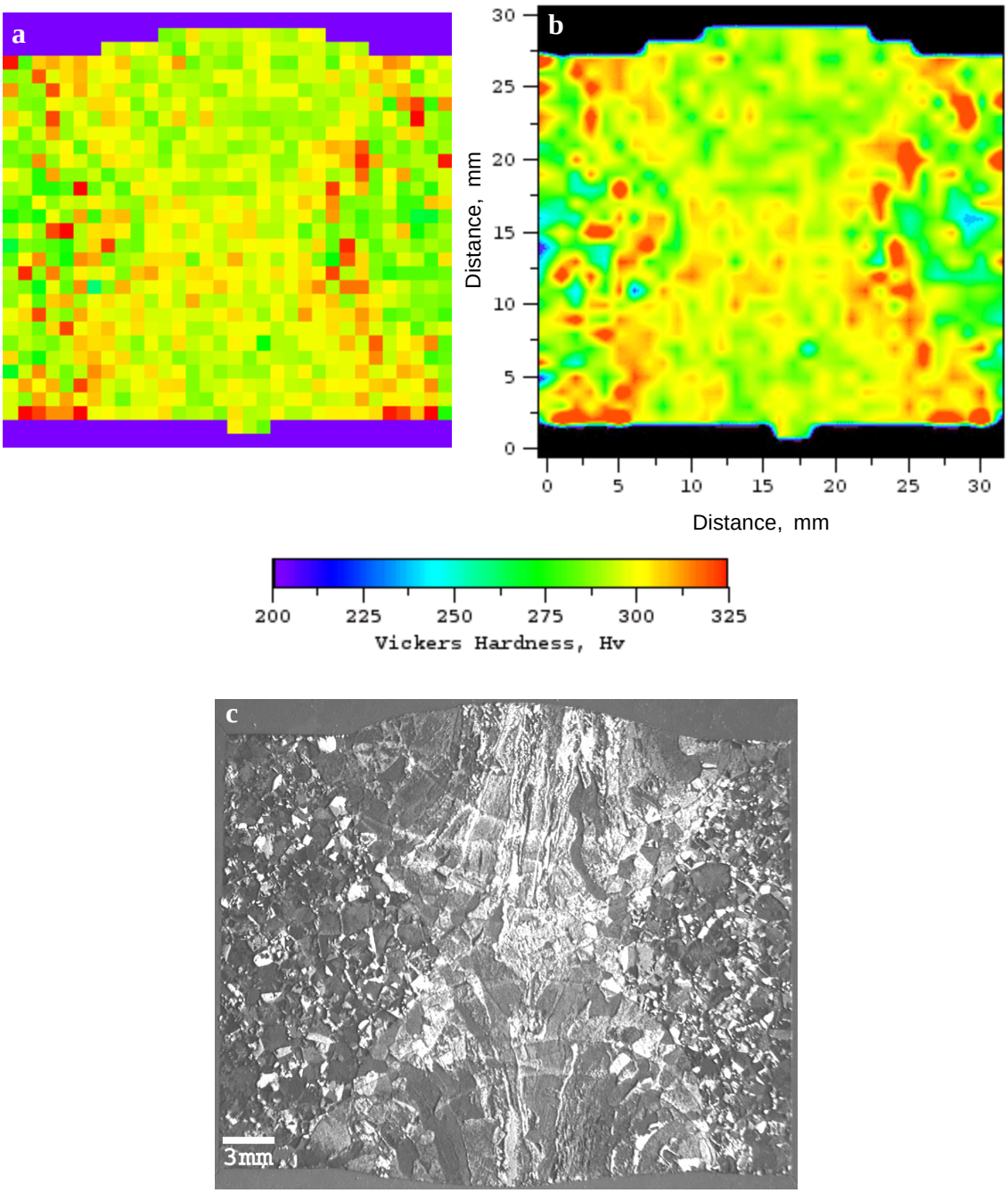

Figure 43: Ti-5111 GTAW with matching filler metal. (a) Original microhardness map. (b) Interpolated microhardness map obtained through use of the program Transform PPC. (c) Macrograph. Note the large HAZ areas and root pass' high hardness values. Also note the general overall increase in hardness values inside the FZ.

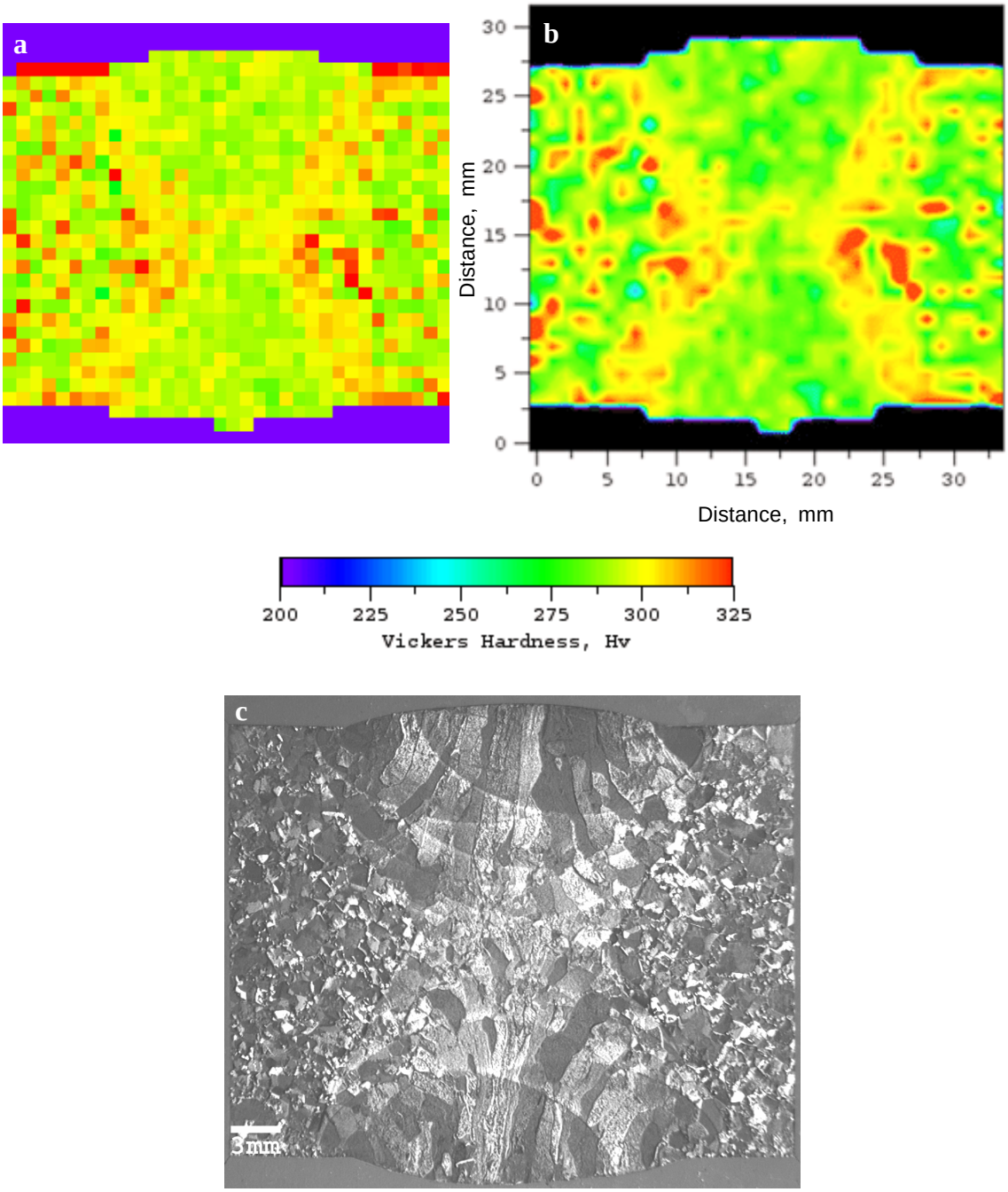

Figure 44: Ti-5111 GTAW with modified filler metal containing 4.5% Al and 50 ppm Y. (a) Original microhardness map. (b) Interpolated microhardness map obtained through use of the program Transform PPC. (c) Macrograph. Note smaller degree of high hardness areas of the HAZ and root pass as compared to the matching filler metal weld. Also note the much lower hardness values inside the FZ as compared to the matching filler metal weld zone. Hardness values inside the FZ correspond very well to the general values of the base metal area.

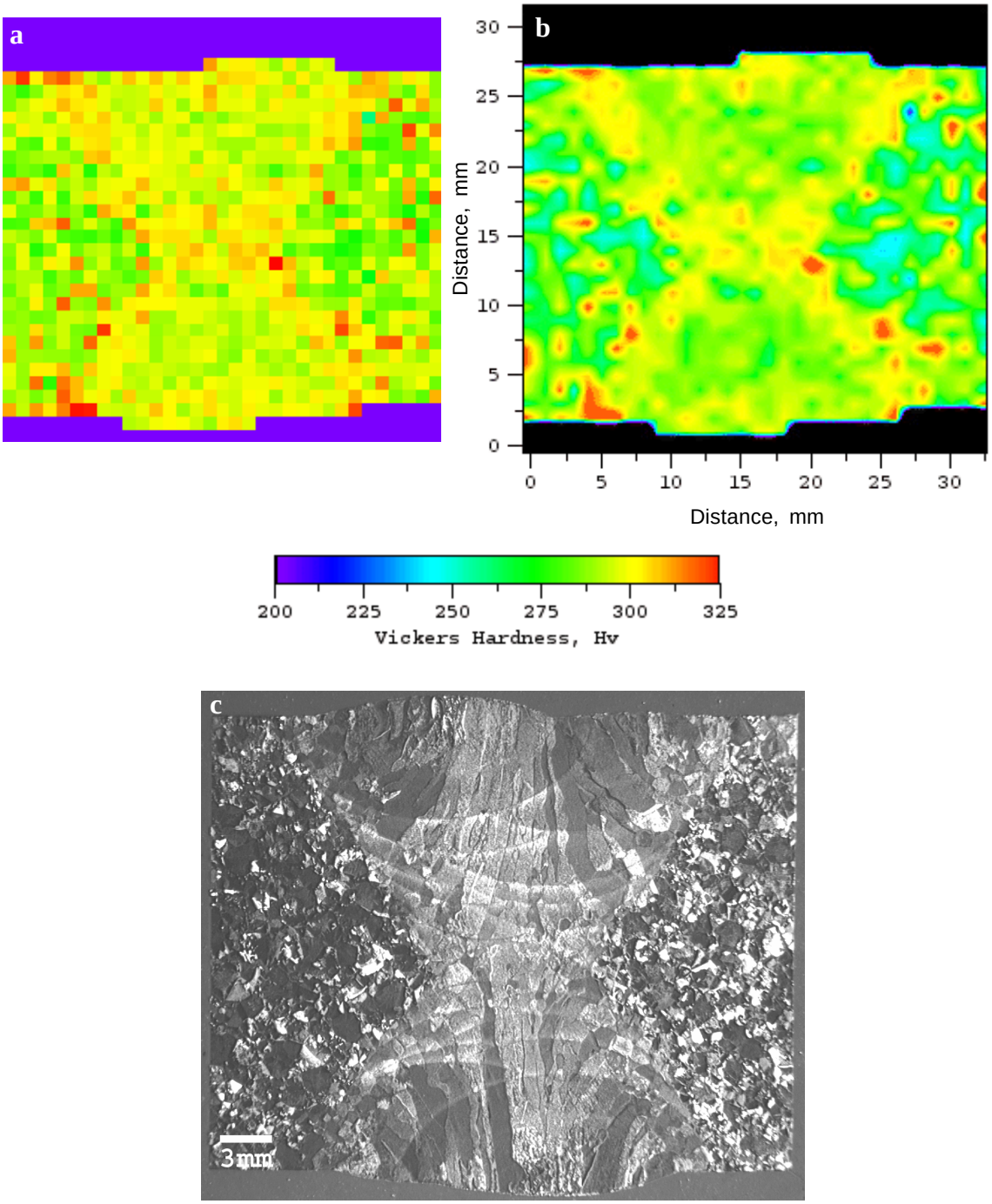

Figure 45: Ti-5111 GTAW with modified filler metal containing 4.5% Al and 200 ppm Y. (a) Original microhardness map. (b) Interpolated microhardness map obtained through use of the program Transform PPC. (c) Macrograph. Note small HAZ and root pass hardness areas. Note that the hardness values inside the FZ area are slightly higher than those of the 50 ppm Y filler metal weld but less than those of the matching filler metal weld.

from the inhomogeneous distribution of the β-phase in the near-a alloy. The matching filler metal weld shows the hardest weld zone while the modified 200 ppm Y weld showed a weld zone that is slightly harder than that of the 50 ppm Y weld. This decrease in hardness across the weld zone is believed to be due to yttrium oxysulfide particle formation in the melt, with further oxidation to yttrium oxide sulfate, thereby tying up oxygen and preventing it from interstitially filling the lattice and strengthening it. Increased hardness areas at the root pass and in areas of the FZ affected by the heat of the multiple weld passes made during welding (FZ HAZ) are likely due to microstructural differences and will be examined by ESEM and TEM. Concerning the increase in hardness from the 50 ppm Y to 200 ppm Y filler metal weld, this may be the result of increased platelet refinement and randomization or possibly the effect of oxide dispersion strengthening. Further research would be necessary to determine the exact mechanism.

Concerning the HAZ in the weld zone areas, it can be seen the matching filler metal of Weld 0 displays a very wide increased hardness area at the HAZ. This HAZ area size is decreased in Weld 1 with modified 50 ppm Y filler metal and is decreased even further in Weld 2 with the 200 ppm Y filler metal. This decrease in HAZ hardness may be the result of a decreased amount of oxygen diffusion across the HAZ, which would lead to localized increases in strength where oxygen concentrations were higher. Upon careful examination of the matching filler metal weld on the left side of the weld zone, just outside the HAZ, along most of its length, there seems to be a portion in the base metal that has a hardness value less than the average value of the base metal. This reduced hardness area may be indicative of possible oxygen diffusion into the HAZ. This

theory will be examined by performing wave-length dispersive spectroscopy across the HAZ to examine diffusion of elements in this area.

From these microhardness results it is clear that the addition of yttrium and subtraction of aluminum has a significant effect on weld zone hardness. Based on the results, it would seem to suggest that there would be an ideal amount of yttrium that one may add to the modified filler metal such that one achieves a weld zone hardness value that closely matches that of the base metal while minimizing hardening in the HAZ. More testing would be necessary to determine this amount, which would seem to lie somewhere between the 50-200 ppm Y specimens tested.

IX. WAVELENGTH DISPERSIVE SPECTROSCOPY (WDS)

IX.1 Introduction

Wavelength dispersive spectroscopy (WDS) was performed on the weld samples using a JEOL JXA-8900R scanning electron microprobe. WDS identifies and counts the impinging X-rays based upon their characteristic wavelengths. WDS is preferred over EDS for obtaining quantitative information and analysis of light or trace elements. Energy dispersive spectroscopy (EDS), which identifies and counts impinging X-rays based upon characteristic energy levels, is useful for obtaining a rapid qualitative analysis of an unknown specimen.

The WDS performed was accomplished via line scans across certain areas of the specimens. In particular, the areas chosen for study included running a relatively quick scan across the entire weld zone and then conducting a more thorough scan at the BM to HAZ to FZ area, and then conducting a scan running vertically through the center of the weld from the top of the weld through the root pass. Additionally, a high collection time line scan was run inside the FZ areas of Welds 1 and 2 to determine whether any yttrium-oxide peak correlations exist. The line scans were performed in order to study any possible elemental segregation that occurs during the GTAW process. By defining any possible elemental segregation areas in the weld, one could indicate potential failure points in the weld. Any elemental segregation could lead to areas where there is a localized change in the strength of the alloy, in that there could be either an increase in strength (and thus a harder area), or decrease in strength (or softer area). Therefore, one

could compare results of the WDS scans to microhardness maps of the welds to see if there is any correspondence. This will indeed be described later.

In addition to the WDS line scans, a few WDS maps were made on Welds 0, 1 and 2. These maps were performed on the matching and modified filler metal welds after observing results from the WDS line scans. The map areas were 1.2 mm x 1.2 mm in size with 300 x 300 points, collected at 100 ms dwell times. These map areas were performed inside the weld FZ in order to show a representation of possible particle formation.

IX.2 Results and Discussion

Line scan areas in Welds 0, 1 and 2 can be seen if Figures 46-48. Prior to scanning, the samples were cleaned in methanol and then air blown dry. Background scans can be found in Appendix C. In the line scans across the entire weld zone, a 1000 ms dwell time was used and elements analyzed for included O, S, Al and Y. This scan was performed in order to show the decrease in Al concentrations in the modified filler metal welds as compared to the matching filler metal weld and to see if any O or S peaks corresponded to a Y peak that may be indicative of yttria formation or some yttrium-sulfide/-sulfate compounds. While a clear difference in Al concentration in the modified filler metals could be seen and there were peaks of O and S, some of which coincided, it was impossible to determine if any of these peaks coincided to a Y peak. The Y scan was inconclusive due to the fact that there was such a low concentration of Y in the fusion zone combined with the fact that the K line for Y is at an energy level of 17.04 keV,

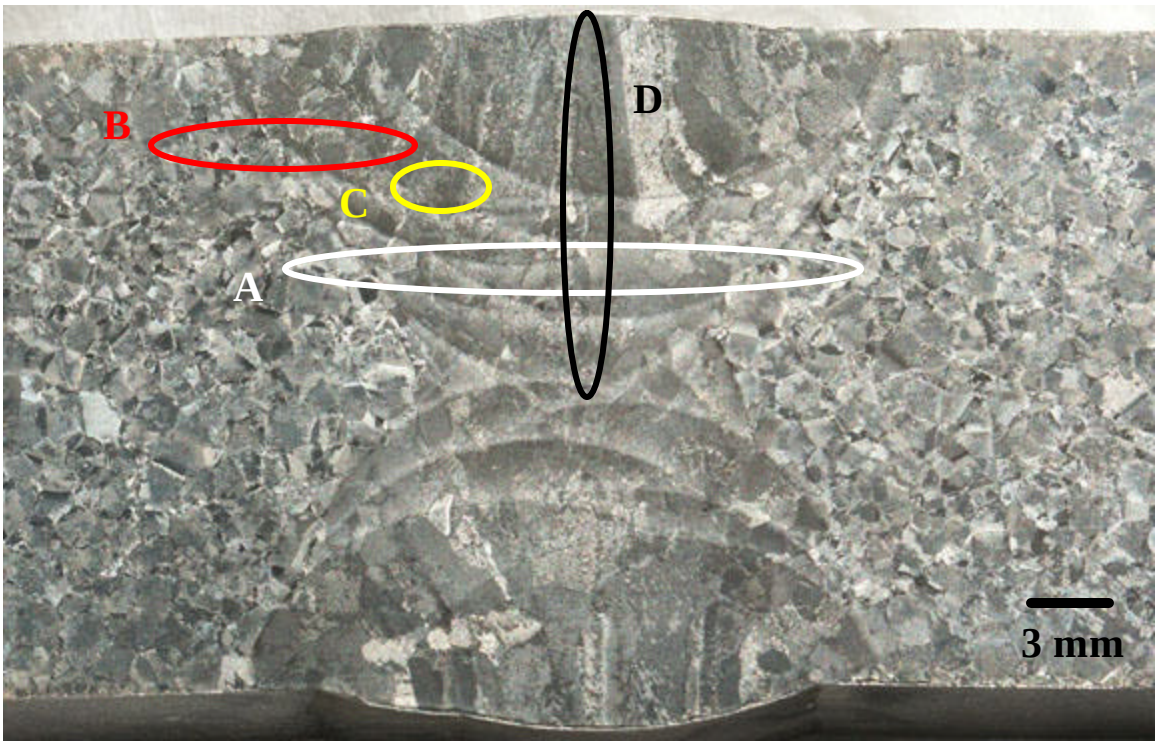

Figure 46: Weld 0 WDS line scan areas: A) across entire WZ, B) BM→FZ, C) high count WZ, and D) vertically through WZ.

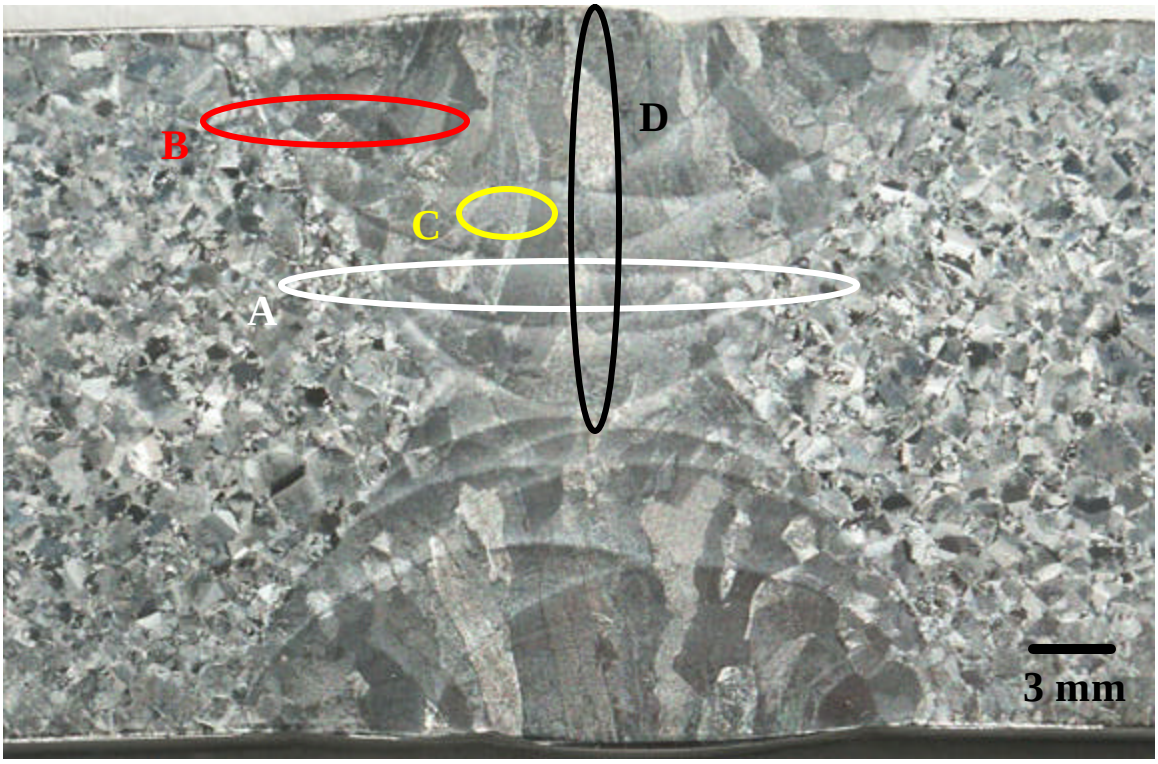

Figure 47: Weld 1 WDS line scan areas: A) across entire WZ, B) BM→FZ, C) high count WZ, and D) vertically through WZ.

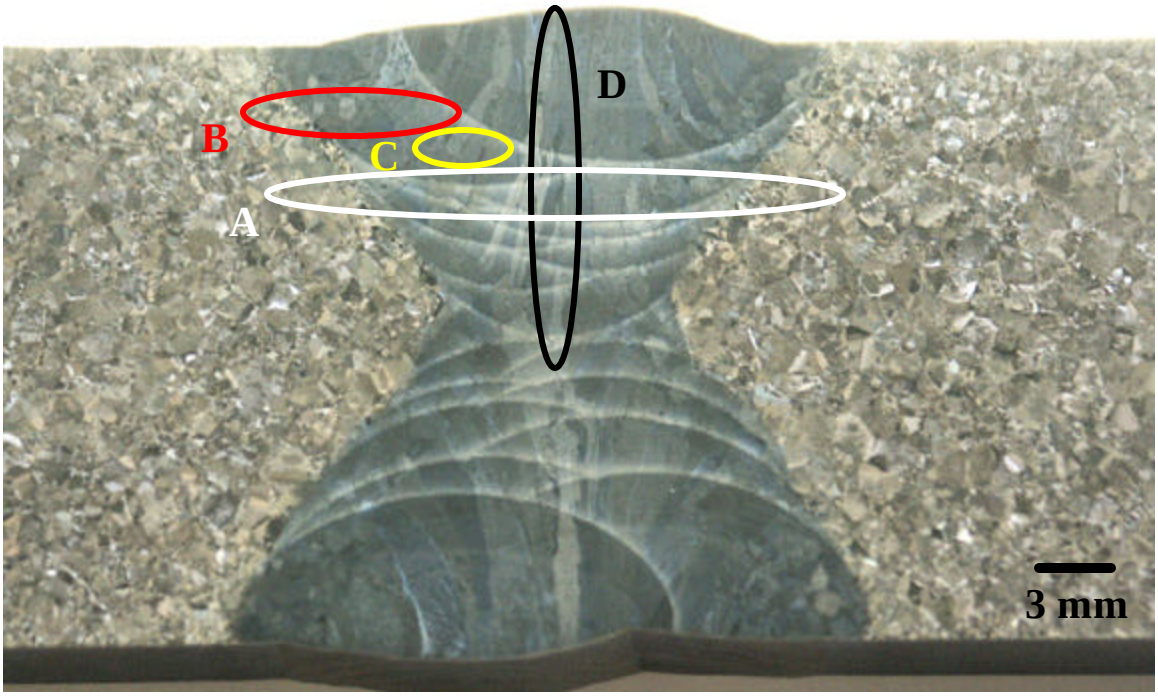

Figure 48: Weld 2 WDS line scan areas: A) across entire WZ, B) BM→FZ, C) high count WZ, and D) vertically through WZ.

while that of the L_1 line is at 2.37 keV. Typically, in order to accurately see the wavelengths of an element, a total of 3x the value of the wavelength energy is needed. The JEOL JXA-8900R is not capable of supplying that high of an energy to the specimen to accurately determine Y peaks at the very low concentrations of Y dealt with here during relatively short collection times. In addition, the L line energy of the Y is so low, that it is obscured by peaks from other elements.

In the BM→FZ scan and the vertical scan through the center of the weld, a 2000 ms dwell time was used and the elements analyzed for included all of the major alloying elements and impurities, namely, O, S, Si, Fe, Y, Al, V, Sn, Mo and Zr. These scans were performed in order to carefully analyze whether or not any elemental segregation was occurring during the GTAW process. A background scan was performed for each dwell time in the base metal of the alloy at an area far from the weld to establish a baseline for the counts on each element. A blowup of the areas scanned across the HAZ can be found in Appendix C.

Line scan results for Weld 0 can be seen in Figures 49-53. From the scan across the entire weld zone in Figure 53, it can bee seen that the Al concentration across the entire weld zone is fairly uniform. Examining Figures 50 & 51, the BM→FZ line scan, several interesting effects of the welding process can be seen. First, concerning O and Al, both α stabilizers, it can be seen that there are many more peaks and valleys in the BM as compared to the HAZ and FZ. The reasoning for this is that since the BM exists as a near-α alloy, such that some β is present, the amount of Al and O that diffuses into the α phase of the alloy is more than that present in the retained β phase. In the FZ area,

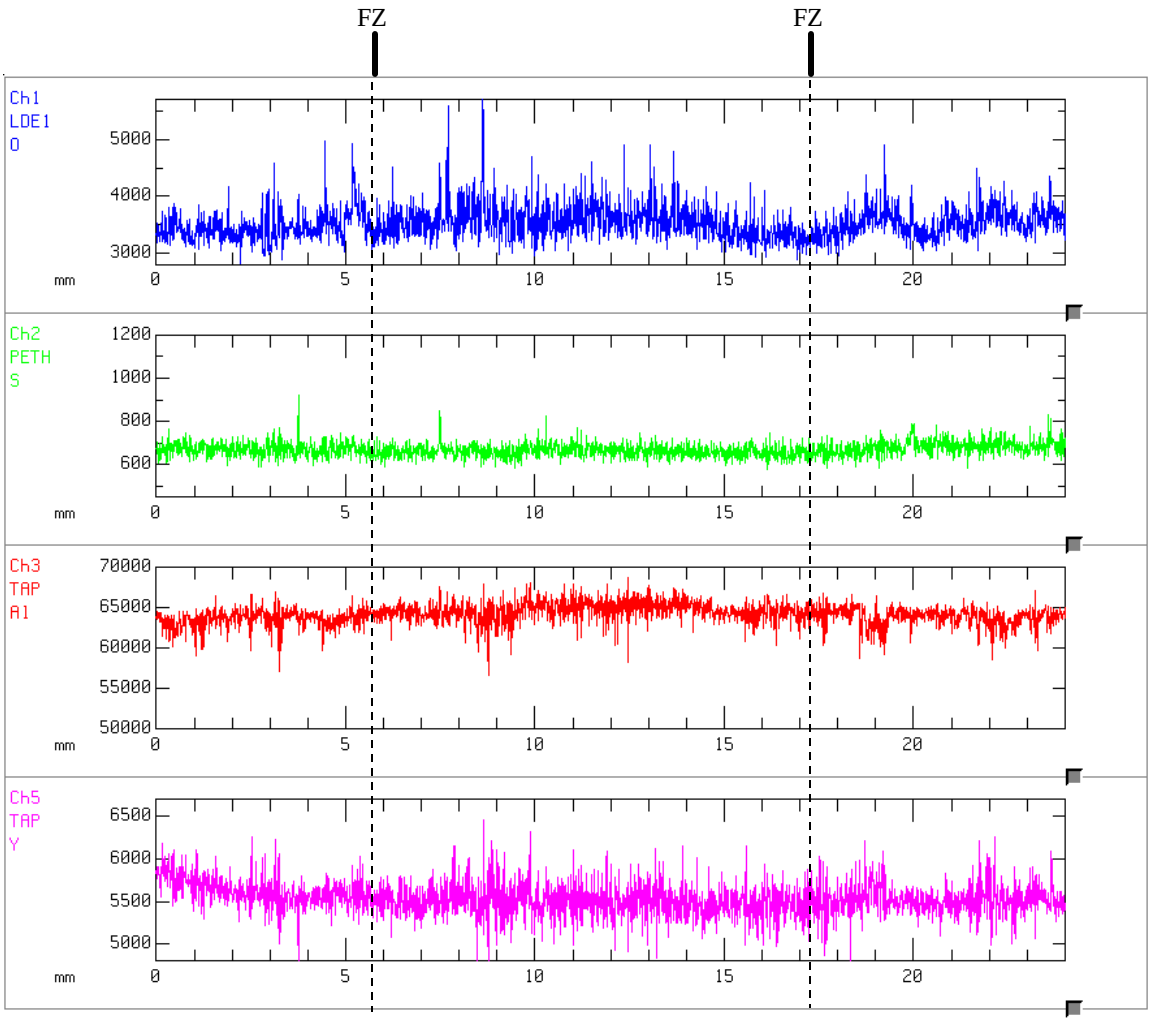

Figure 49: WDS scan of Ti5111 matching filler metal weld across entire weld zone (1000ms dwell time). Elements O, S, Al, Y. Observe how the Al concentrations remain fairly steady across the weld zone and that there are no matching peaks of O and S.

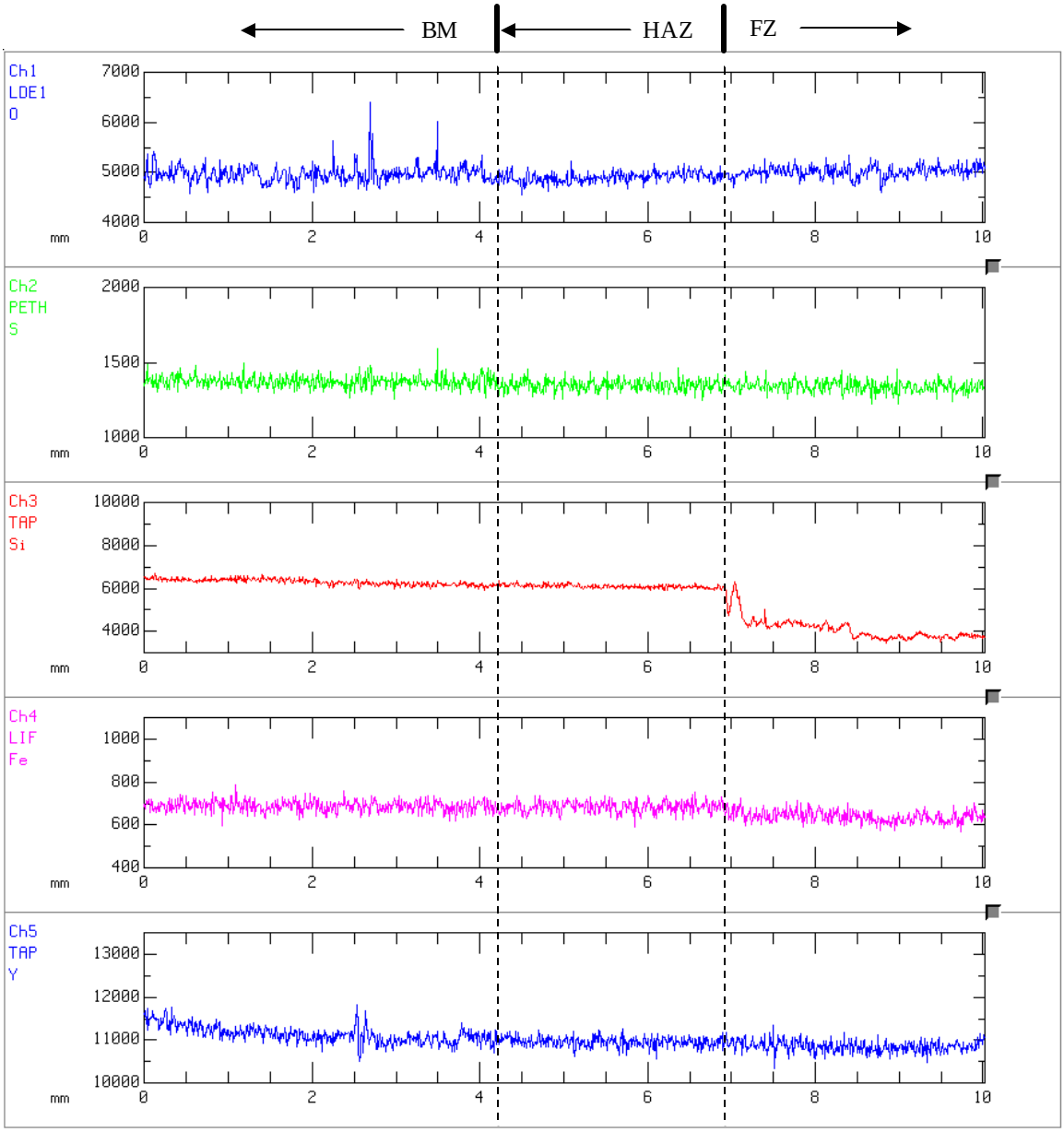

Figure 50: WDS scan of Ti5111 matching filler metal weld from BM to FZ (2000ms dwell time). Elements O, S, Y, Si, Fe. Observe that the O concentration in the BM is much more random then in the HAZ and FZ.

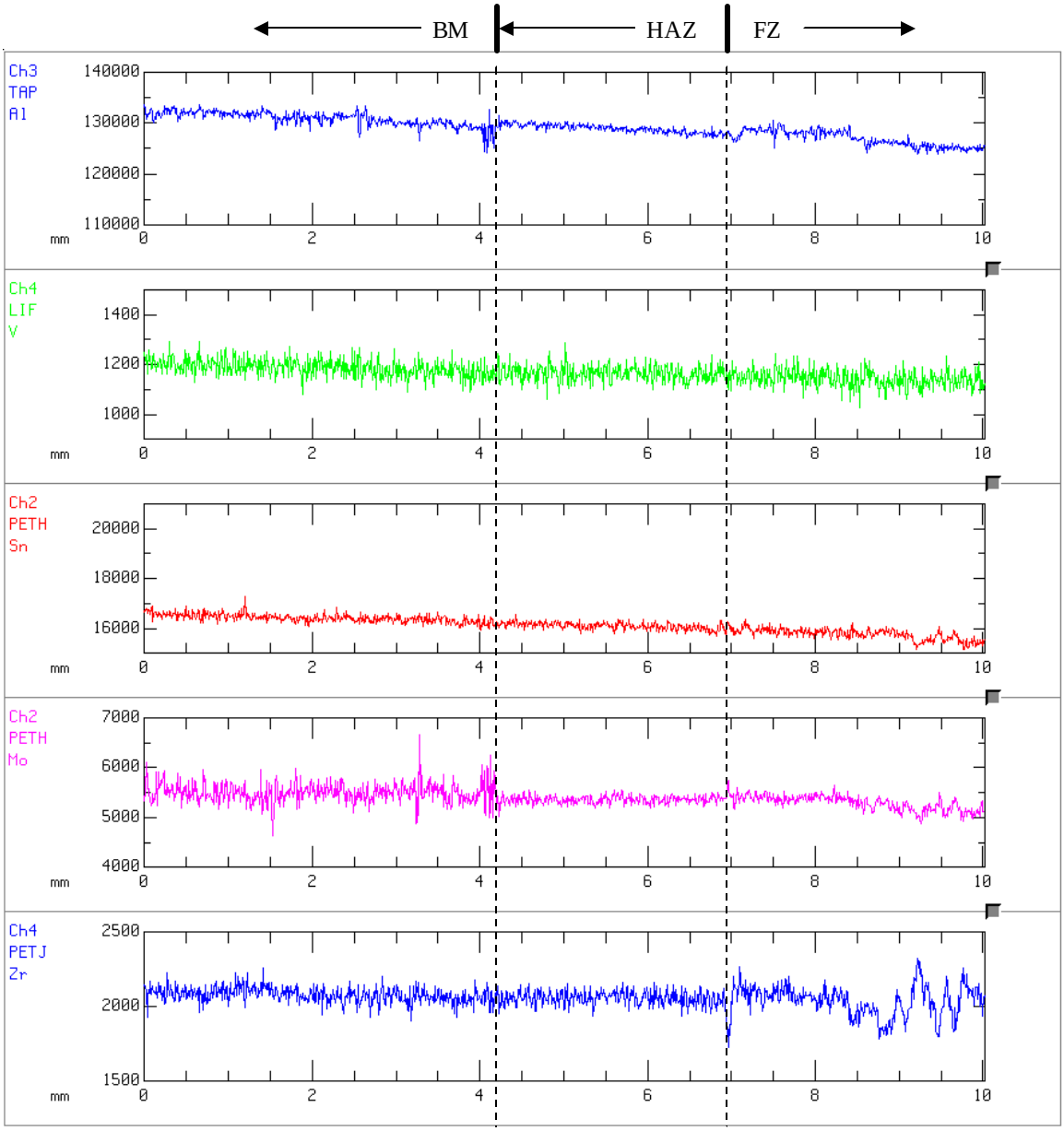

Figure 51: WDS scan of Ti5111 matching filler metal weld from BM to FZ (2000ms dwell time). Elements Al, V, Sn, Mo, Zr. Observe that he Al and Mo levels are much more random in the BM as compared to the HAZ and FZ.

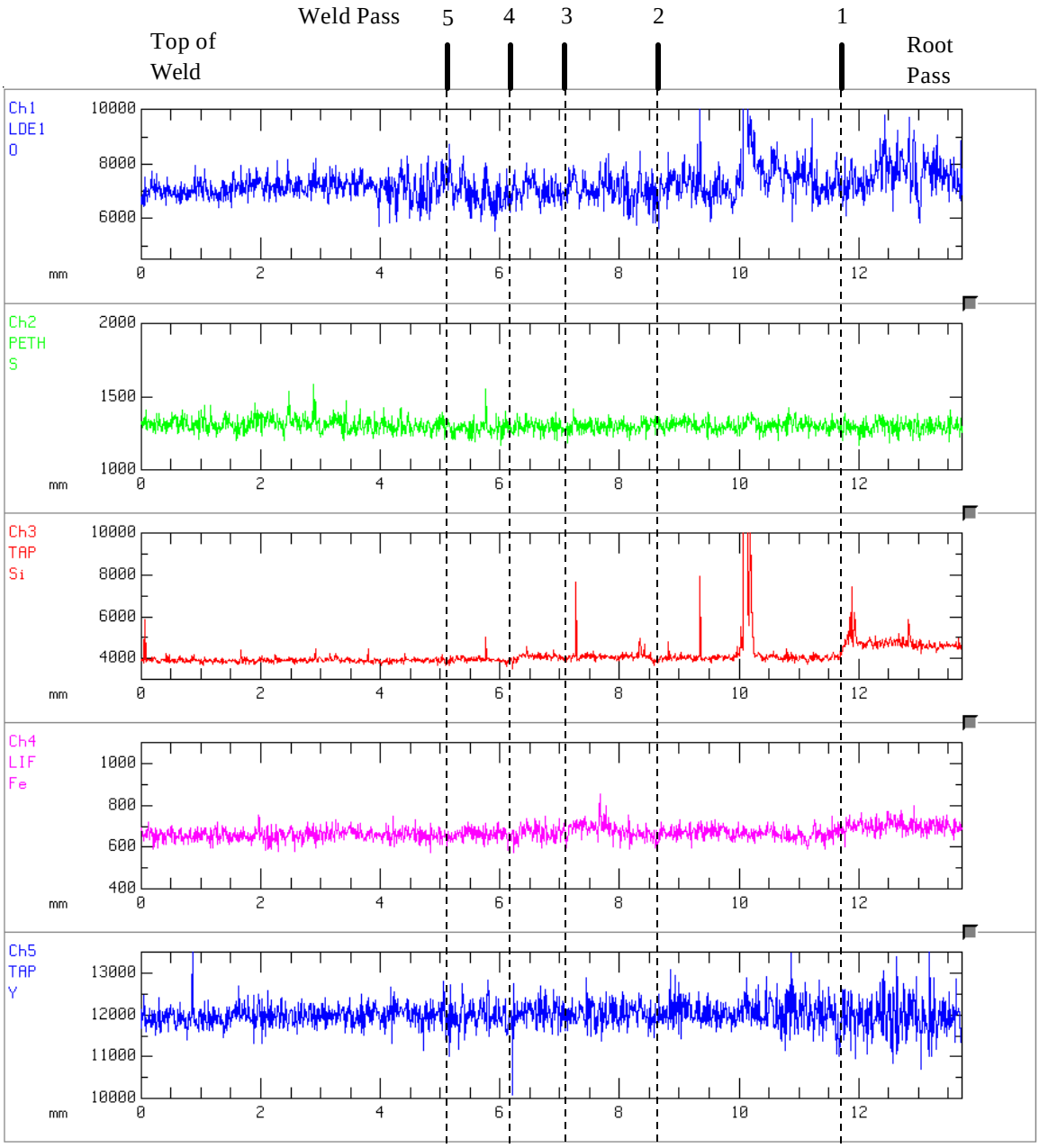

Figure 52: WDS scan of Ti5111 matching filler metal weld vertically through the weld center (2000ms dwell time). Elements O, S, Y, Si, Fe.

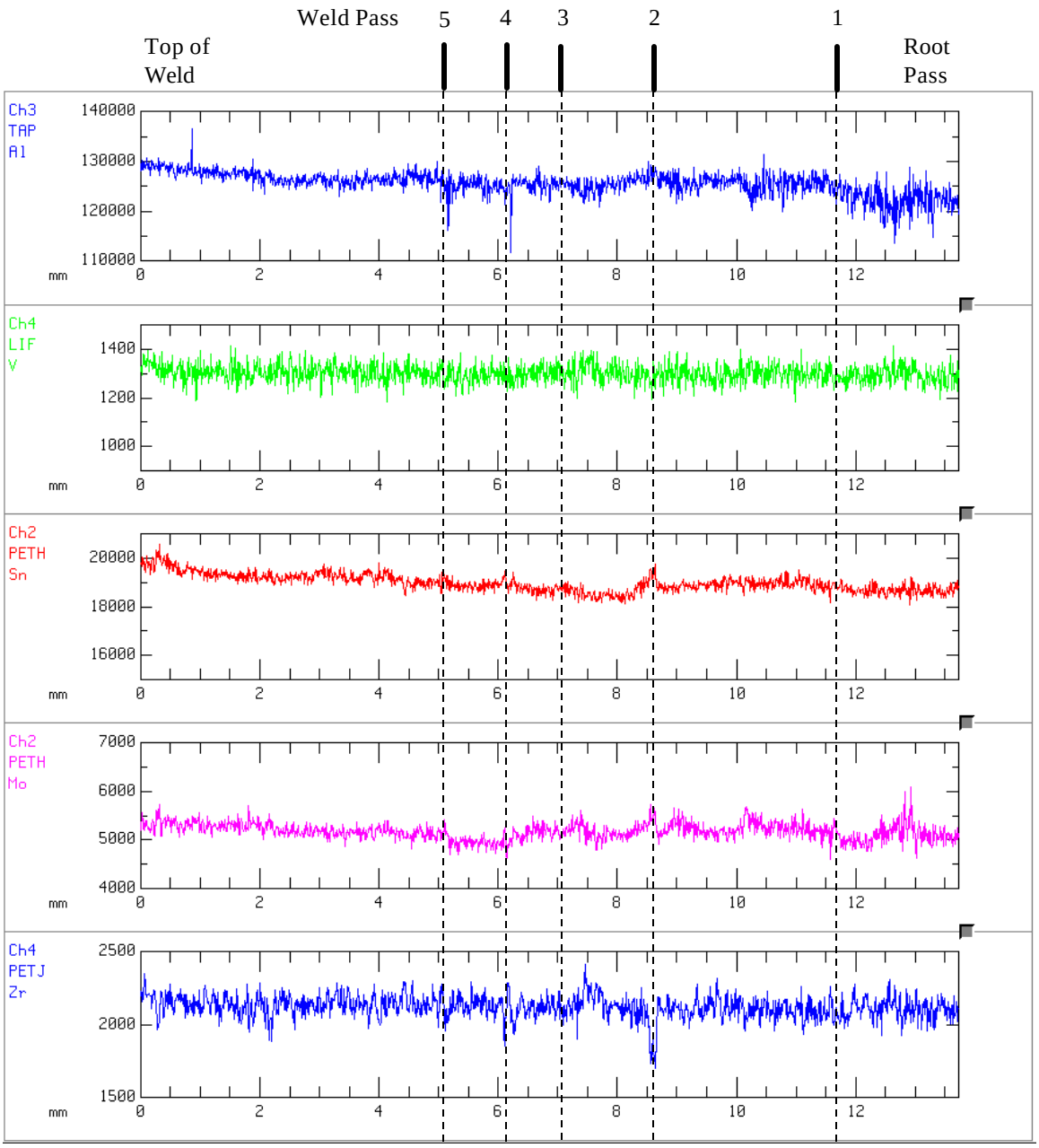

Figure 53: WDS scan of Ti5111 matching filler metal weld vertically through the weld center (2000ms dwell time). Elements Al, V, Sn, Mo, Zr.

the final structure of the lattice is predominantly an acicular Widmanstätten α. This phase transformation takes place by a rapid diffusion process, thus not allowing for a complete redistribution of the α and β stabilizers. Therefore, the transformed α phase and retained β phase in the weld zone are likely not at equilibrium concentrations.

In the HAZ, the initial near-α crystal lattice is heated above its βTT and then rapidly cooled. This again produces a Widmanstätten structure (rapid diffusional transformation), thereby resulting in a more even distribution of the Al and O in the HAZ. Close examination of the Al scan results shows that the Al concentration is steadily decreasing from the BM to the FZ. There is a sharp valley in its concentration at the BM to HAZ interface and just inside the FZ interface. The elements V, Sn and Mo also show a steadily decreasing concentration from the BM to FZ.

Molybdenum, which is a β stabilizing element, is also seen to show a greater uniformity in the HAZ and FZ as compared to the BM. Again the reasoning for this is similar to that of the Al and O. The Mo also shows a spike in concentration near the BM to HAZ boundary. This spike corresponds to the valley seen in Al and may be indicative of part of the size of the far HAZ, which would be on the order of approximately 0.25 mm. It is pointed out that it is stated as part of the size of the HAZ due to the fact that it is expected that O is affected to a greater distance. This indicates that there may be several parts to the far HAZ where mechanical properties could be affected due to the amount of elemental diffusion at various temperatures.

Oxygen concentration is slightly elevated inside the FZ as compared to the other areas. It is also seen that as the line scan passes from the BM to the HAZ, there is a spike

down in concentration just before the HAZ, then a slight spike up in concentration at the interface and then a drop-off in concentration that lasts for the first 0.6 mm inside the HAZ. After that, the O concentration again starts to rise as you get closer to the FZ. Close to the FZ, there again is a slight decrease in concentration, before rising again in the FZ. These results seem to indicate that there is indeed a diffusion of O towards the HAZ from the BM and towards the FZ from the HAZ.

The decrease in concentration of Si at the HAZ to FZ interface coincides with the difference in Si chemistry concentrations between the base plate and matching filler metal plate due to processing. Processing differences in the alloys also leads to the slight decrease in concentration of Fe seen inside the FZ as compared to the BM.

At the HAZ to FZ interface there is a spike down in Zr concentration, followed by a rise and then decrease over approximately 1.5 mm. Over the next 1.5 mm there are several spikes in concentration. These spikes are also seen in Mo and Sn over the same area and correspond to valley in Al, V and O. These spikes and valleys are likely the result of passing over one of the retained β phases inside the weld zone.

Vertical line scan results through the center of the weld can be seen in Figures 52 & 53. A few observations are pointed out. Oxygen concentration is higher towards the center of the weld and shows many peaks and valleys. The higher concentration at the weld center is probably due to the welding taking place inside a glovebox environment. The first few passes probably had a higher concentration of O available to diffuse into the molten metal. As this O left the gas, less was available to diffuse into later weld passes. The Mo typically showed a peak on one side of the weld pass and a valley on the other. The higher concentration of Mo was generally on the bottom of the pass which solidified

first. The Mo showed a decreasing trend in concentration from the root pass to Pass 5, where it again rose and leveled off in the final weld pass. Tin started at a higher concentration at the top of the weld and gradually decreased to Pass 2, where it showed a spike up. Concentration then came back down, leveling off towards the center of the weld. Aluminum showed a slightly higher concentration towards the top of the weld but remains fairly constant between the passes, although valleys were seen at Passes 4 & 5. Valleys in Zr concentration were seen at Passes 2, 4 & 5 with concentration remaining fairly constant across the weld otherwise. Silicon was fairly constant across the weld passes with a higher concentration at the center and several large spikes and small valleys at Passes 2-5. Sulfur, iron and vanadium had fairly uniform concentrations across all the passes.

Line scan results for Weld 1 can be seen in Figures 54-59. The line scan across the entire weld zone, shown in Figure 54, clearly indicates the reduction in Al content that was made to the filler metal. Corresponding peaks of O and S were present, although no correlation could be discerned between any O and Y peaks.

Again, several interesting results are pointed out from the BM→FZ line scans of Figures 55 & 56. Oxygen concentration is again higher in the FZ than in the HAZ or BM. There is a peak of O at the BM to HAZ interface, but no sharp valley exists just before the HAZ. After the peak, O concentration decreases for approximately 1 mm before increasing again (~2 mm) towards the HAZ. Silicon, iron and aluminum concentration decrease at the FZ due to chemistry differences resulting from processing and Si also decreases slightly at the BM/HAZ interface. Tin increases in concentration going towards the FZ, where it then increases quite a bit with several spikes.

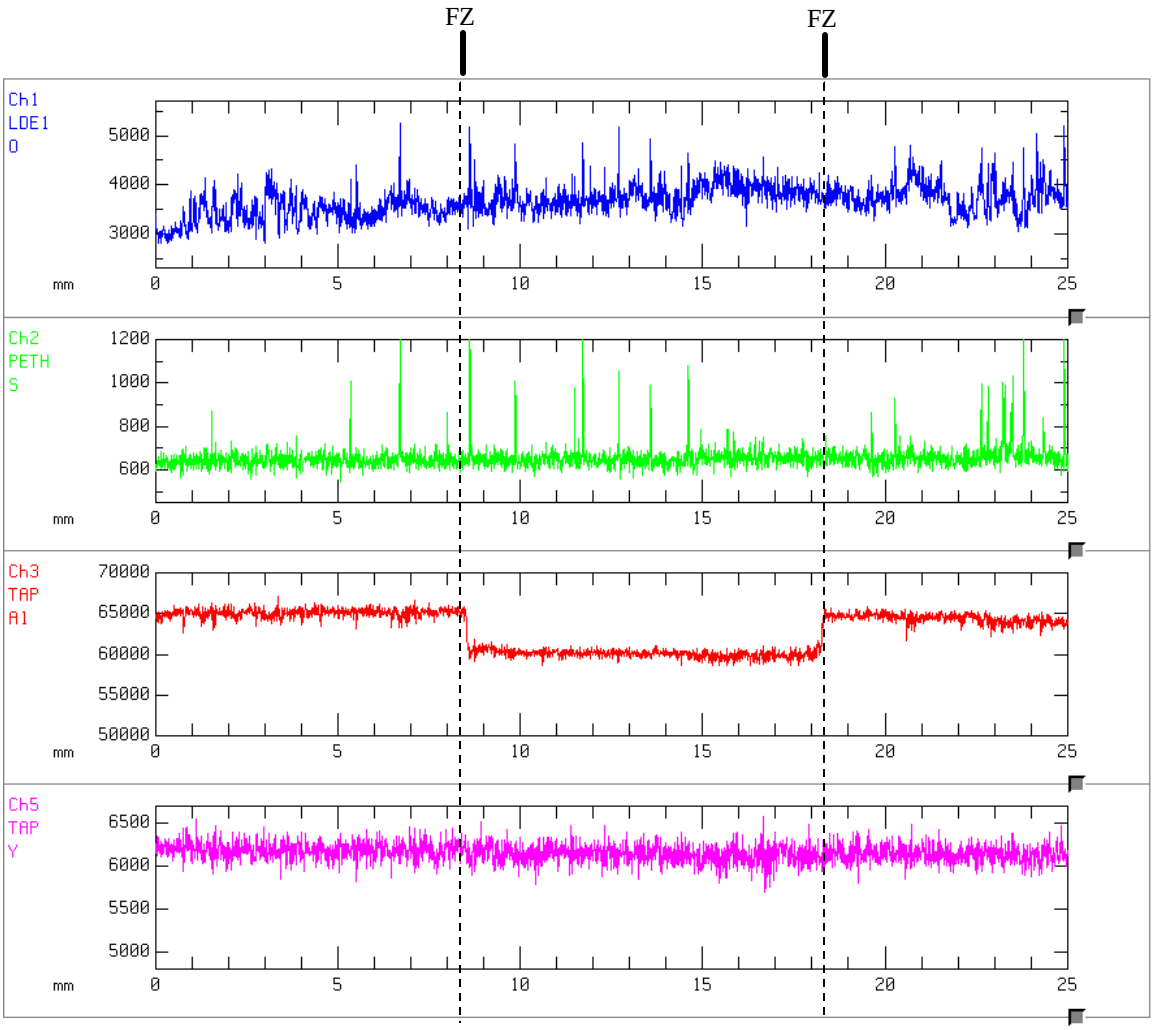

Figure 54: WDS scan of Ti5111 modified 50 ppm Y filler metal weld across the entire weld zone (1000ms dwell time). Elements: O, S, Al, Y. Note the decreased Al concentration inside the weld FZ and that there appears to be some S and O peak correlation.

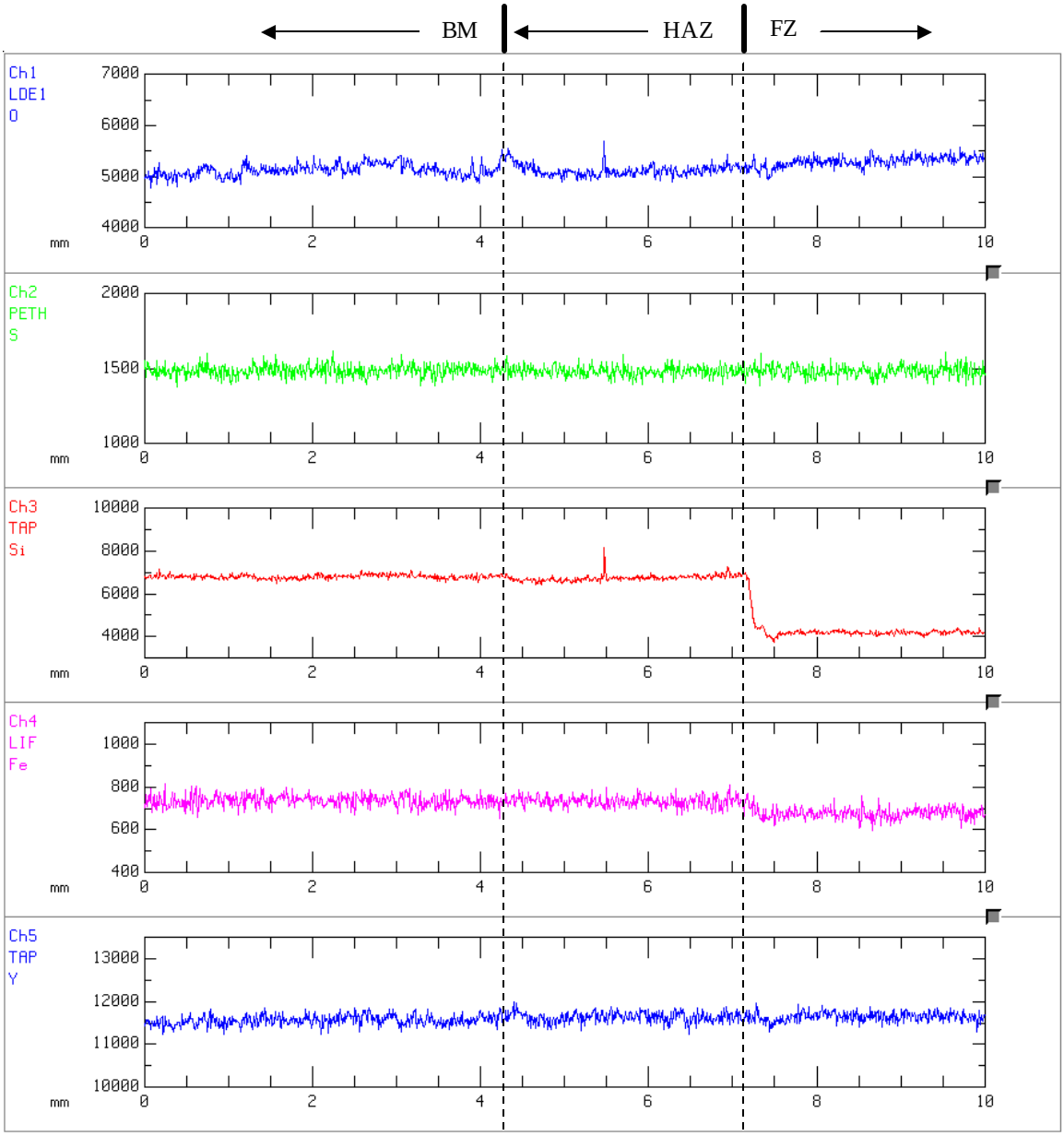

Figure 55: WDS scan of Ti5111 modified 50 ppm Y filler metal weld across the HAZ (2000ms dwell time). Elements: O, S, Y, Si, Fe.

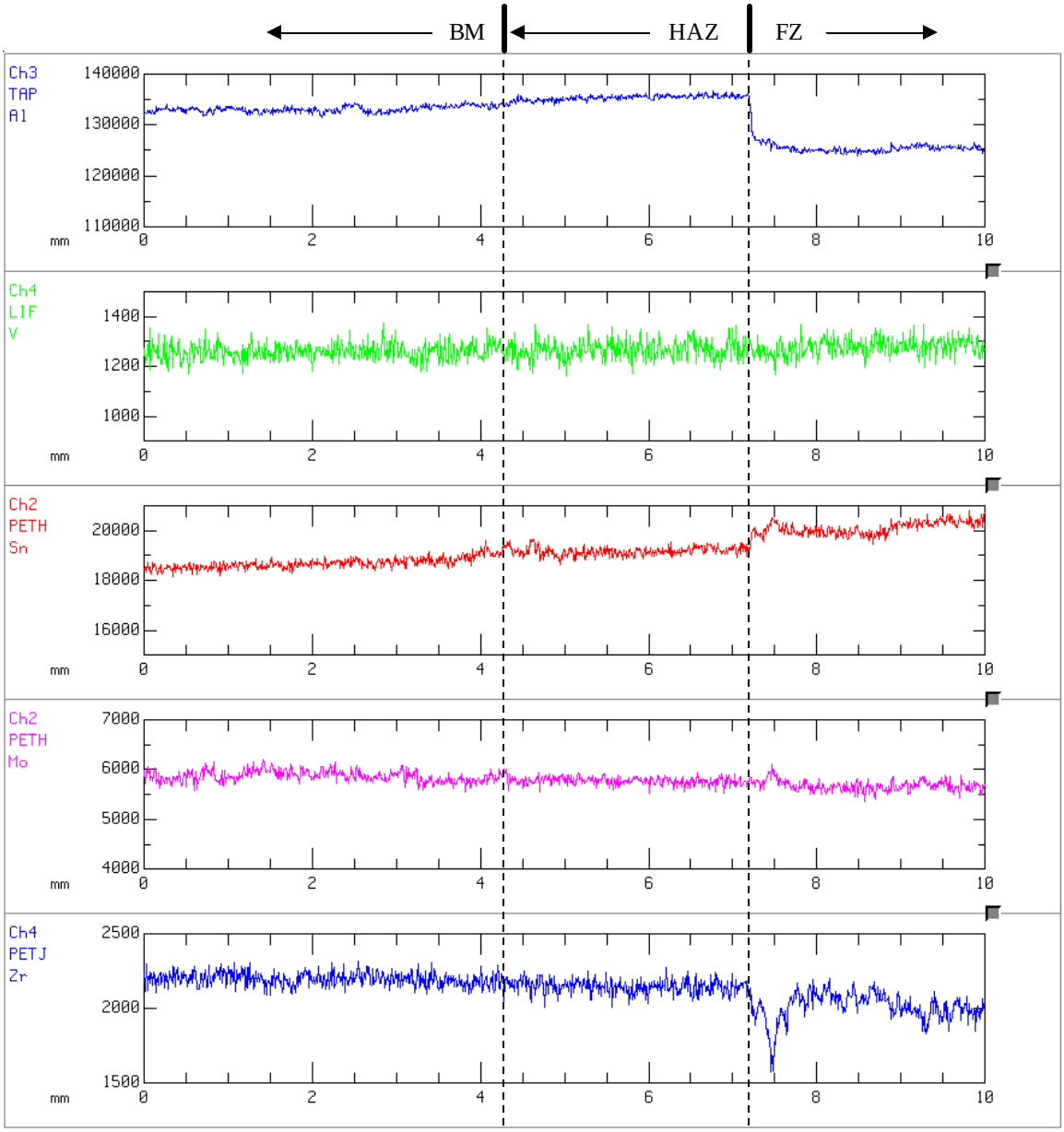

Figure 56: WDS scan of Ti5111 modified 50 ppm Y filler metal weld across the HAZ (2000ms dwell time). Elements: Al, V, Sn, Mo, Zr.

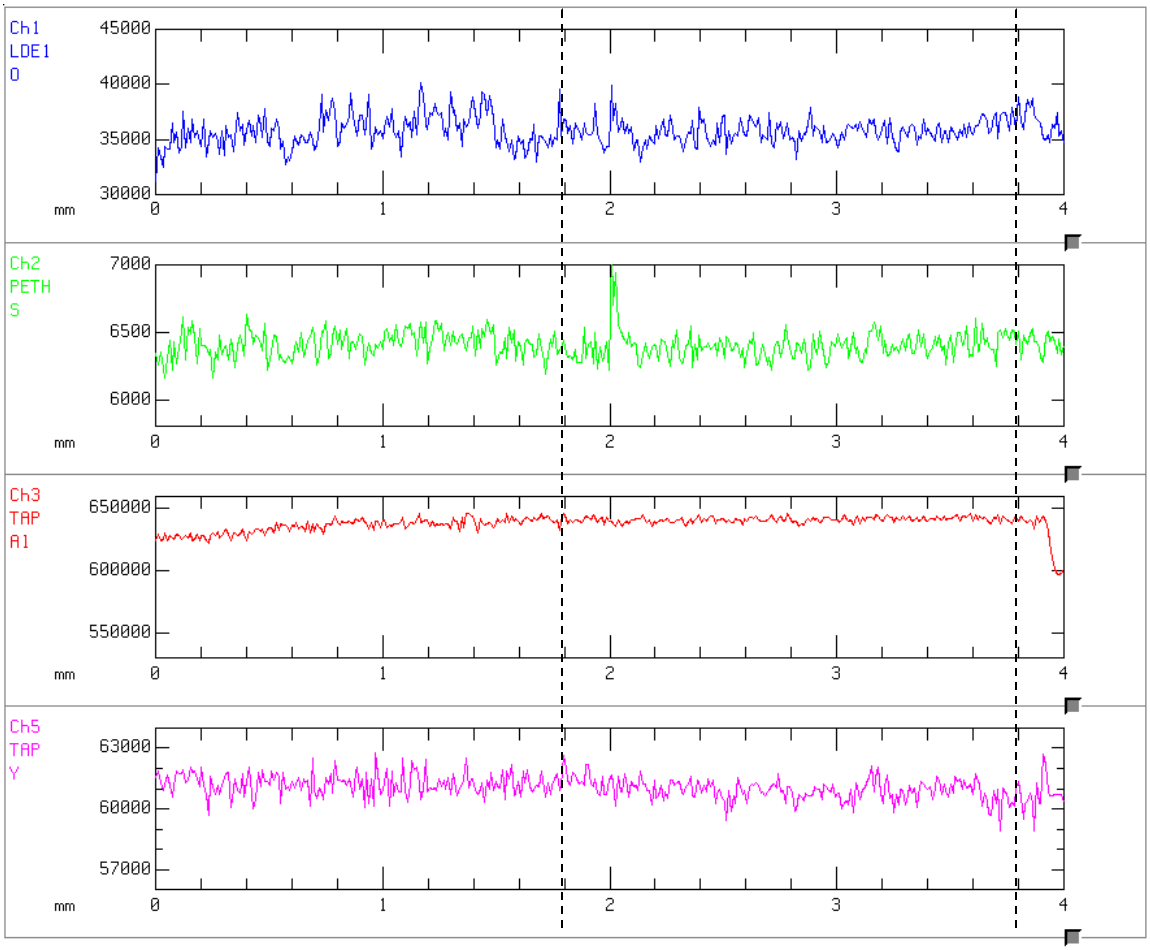

Figure 57: WDS scan of Ti5111 modified 50 ppm Y filler metal weld in weld area (10000ms dwell time). Elements: O, S, Al, Y. Dotted lines indicate where peaks of O, S and Y correspond.

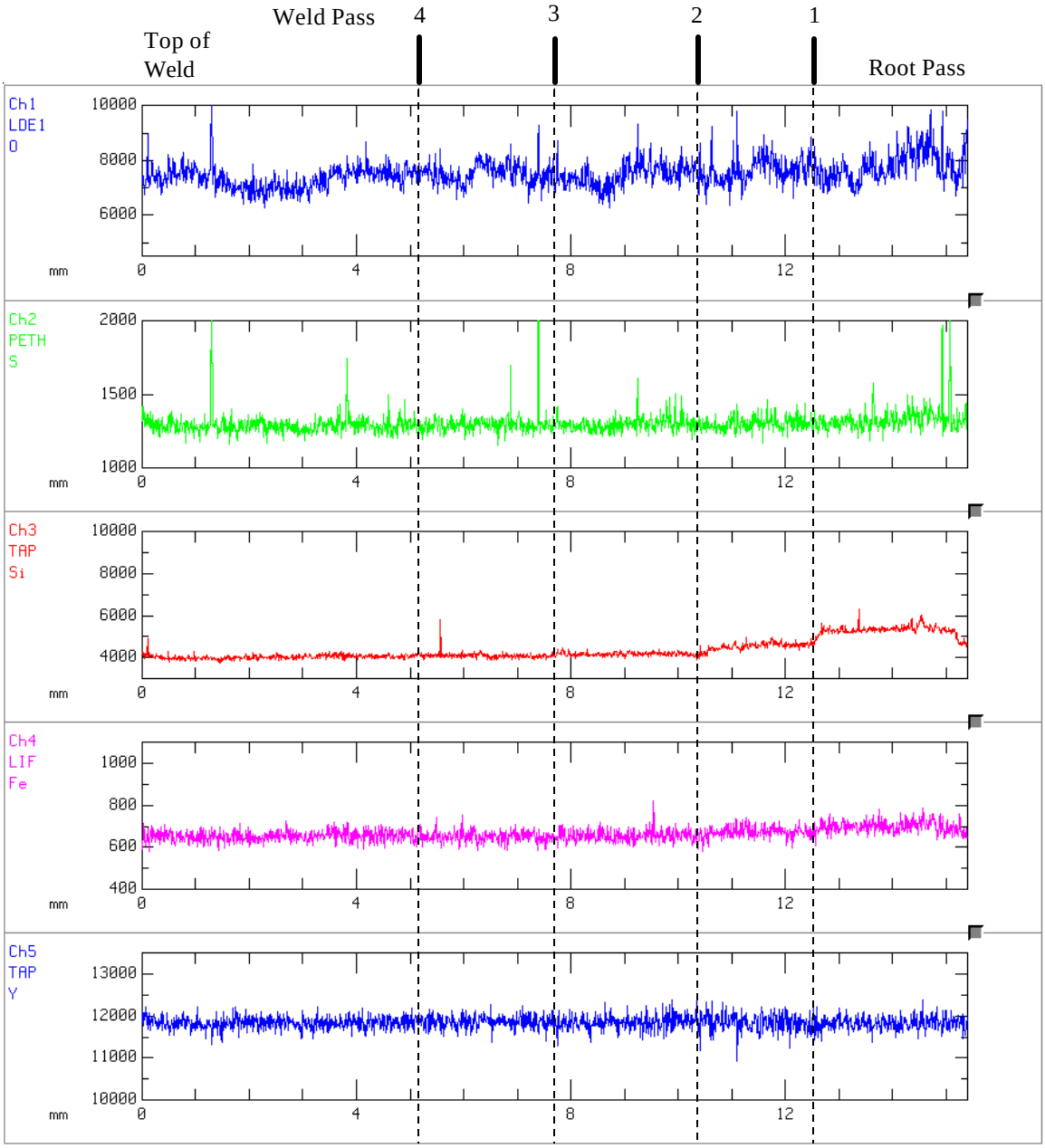

Figure 58: WDS scan of Ti5111 modified 50 ppm Y filler metal weld vertically through weld center (2000ms dwell time). Elements: O, S, Y, Si, Fe.

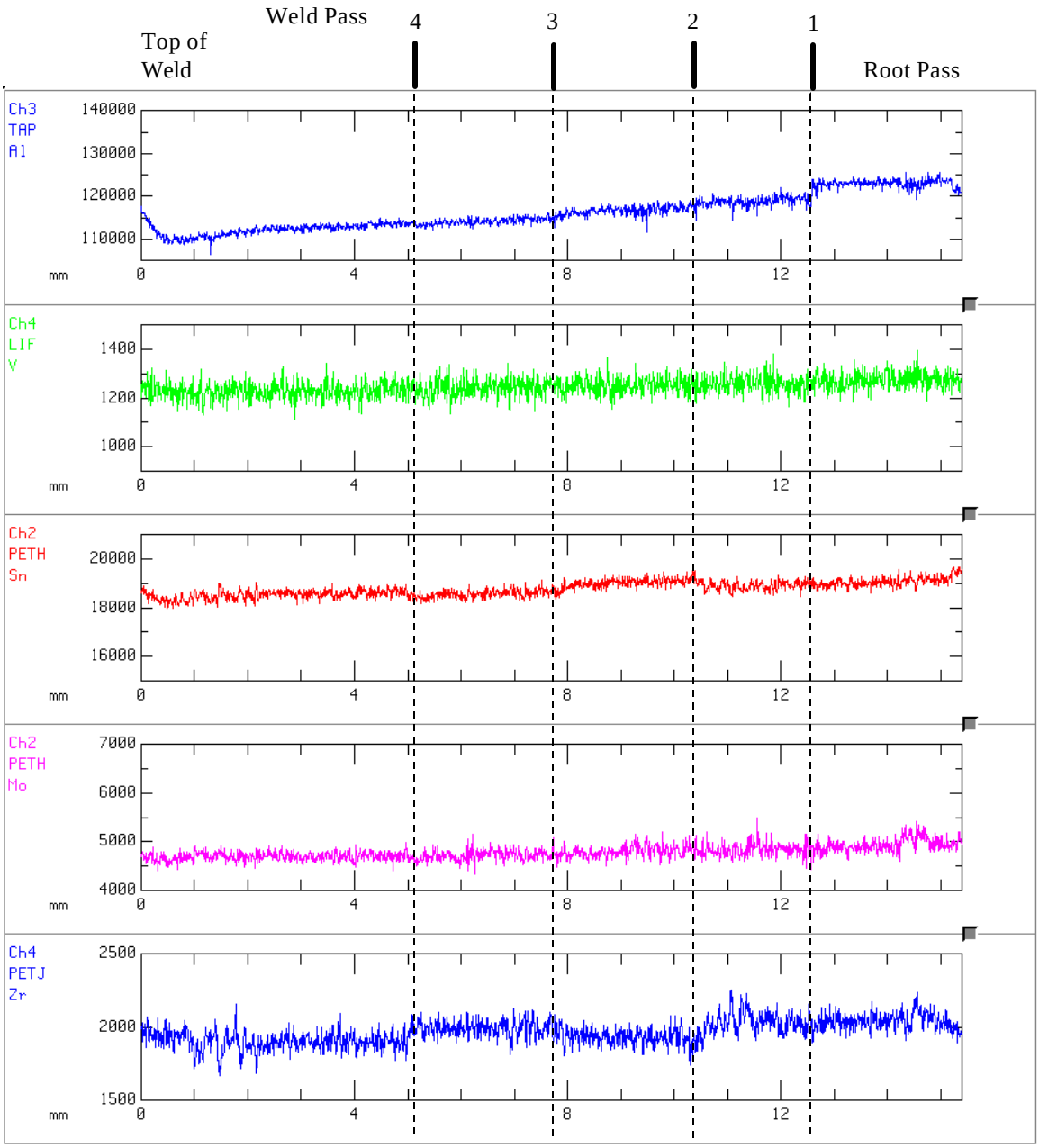

Figure 59: WDS scan of Ti5111 modified 50 ppm Y filler metal weld vertically through weld center (2000ms dwell time). Elements: Al, V, Sn, Mo, Zr.

Molybdenum spikes in concentration inside the FZ also. Zirconium again shows a valley just inside the HAZ/FZ interface.

Figure 57 shows a high dwell time count line scan inside the FZ in order to determine whether any O, S and Y peaks correspond, thereby indicating the presence of yttrium particle formation. The dotted lines in Figure 57 show where O, S and Y peaks do correspond. Clearly no conclusions can be drawn from this scan, as the few times that peaks do correspond, may be the result of pure chance versus yttria or yttrium oxysulfide formation.

The vertical weld scan is shown in Figures 58 & 59. Here again, O shows several spikes and has a higher concentration at the center of the weld vs. the top of the weld. Silicon shows increasing concentration in Pass 1 and is again highest in the root pass. Iron also shows slightly higher concentrations at the root pass. Aluminum concentration is very interesting in that it starts high at the top of the weld, drops off in concentration rapidly, and then rises steadily to the root pass. Tin and molybdenum both show slightly increasing concentrations towards the root pass. Zirconium shows several spikes in concentration and increases in concentration at Passes 2 & 4.

Line scan results for Weld 2 can be seen in Figures 60-65. The line scan across the 200 ppm Y modified filler metal weld is shown in Figure 60. Here again, it is obvious that the Al concentration was decreased in the FZ. There are also obvious corresponding peaks in the O and S concentrations that again could not be matched positively to any Y peaks.

Examining the BM→FZ line scans of Figures 61-62, several notable characteristics are pointed out. Oxygen is again higher in the FZ as compared to the BM

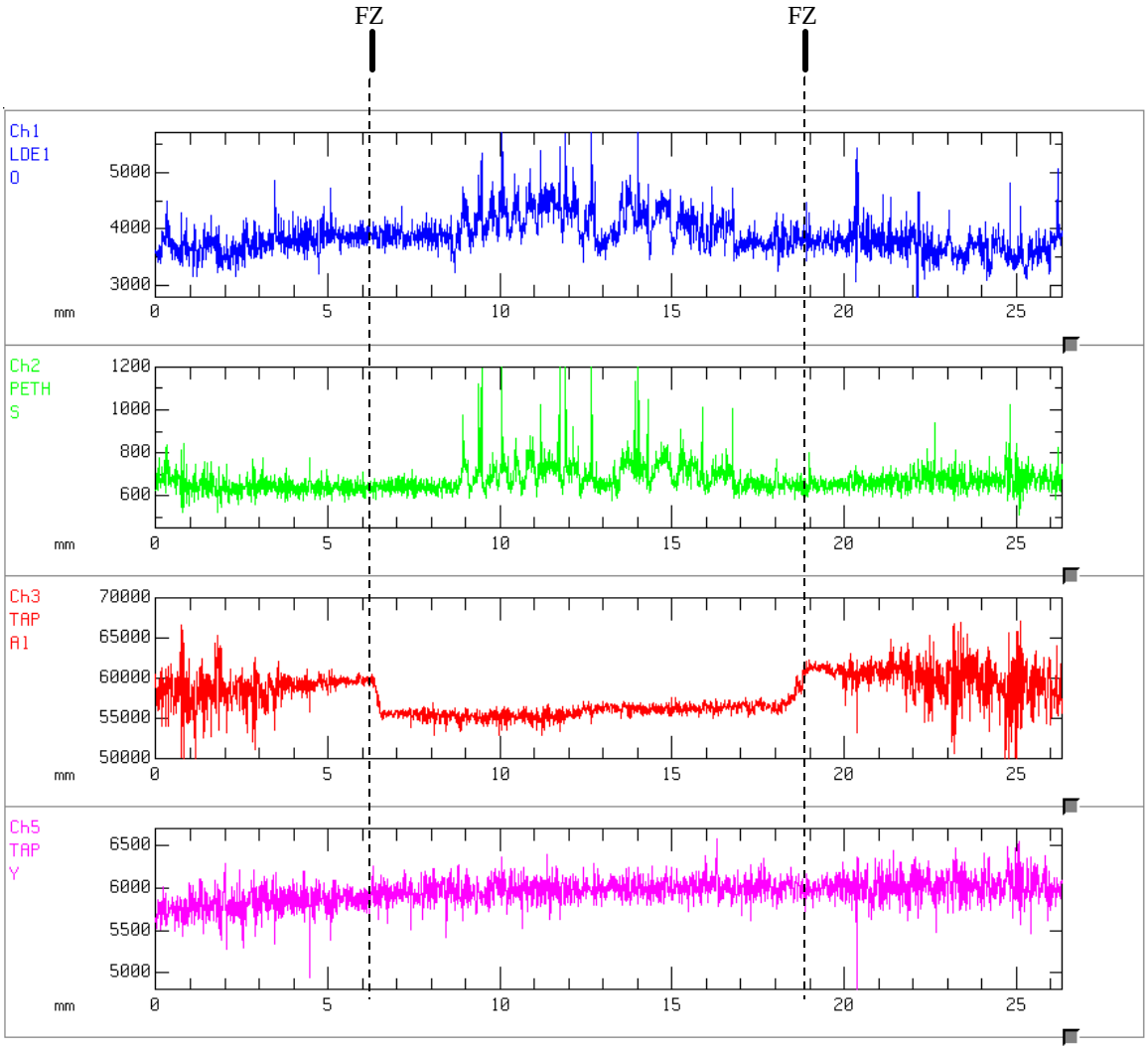

Figure 60: WDS scan of Ti5111 modified 200 ppm Y filler metal weld across the weld zone (1000ms dwell time). Elements: O, S, Al, Y. Note the decrease in Al concentration inside the weld FZ and that there are strong correlations between the O and S peaks.

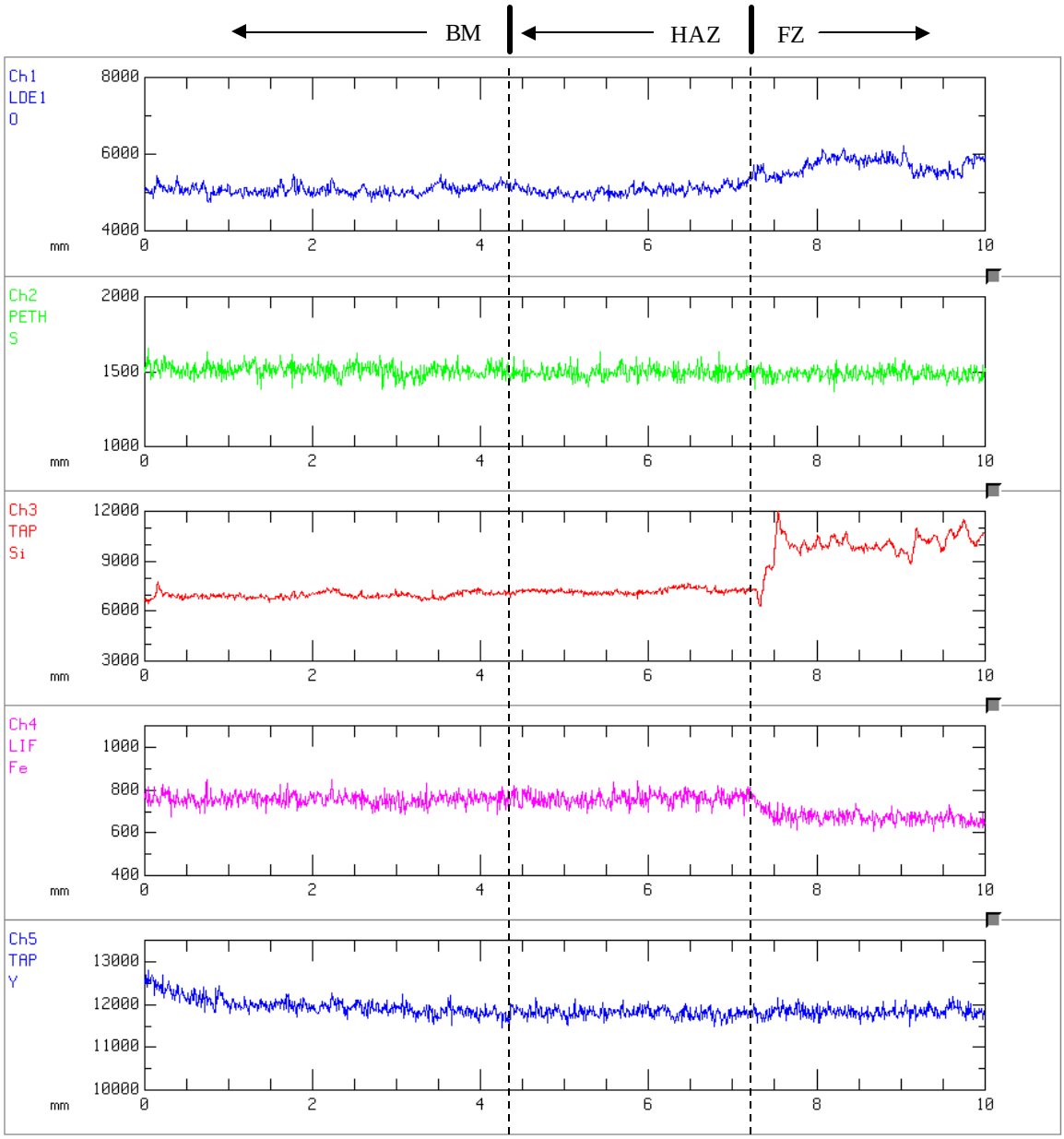

Figure 61: WDS scan of Ti5111 modified 200 ppm Y filler metal weld across the BM HAZ (2000ms dwell time). Elements: O, S, Y, Si, Fe.

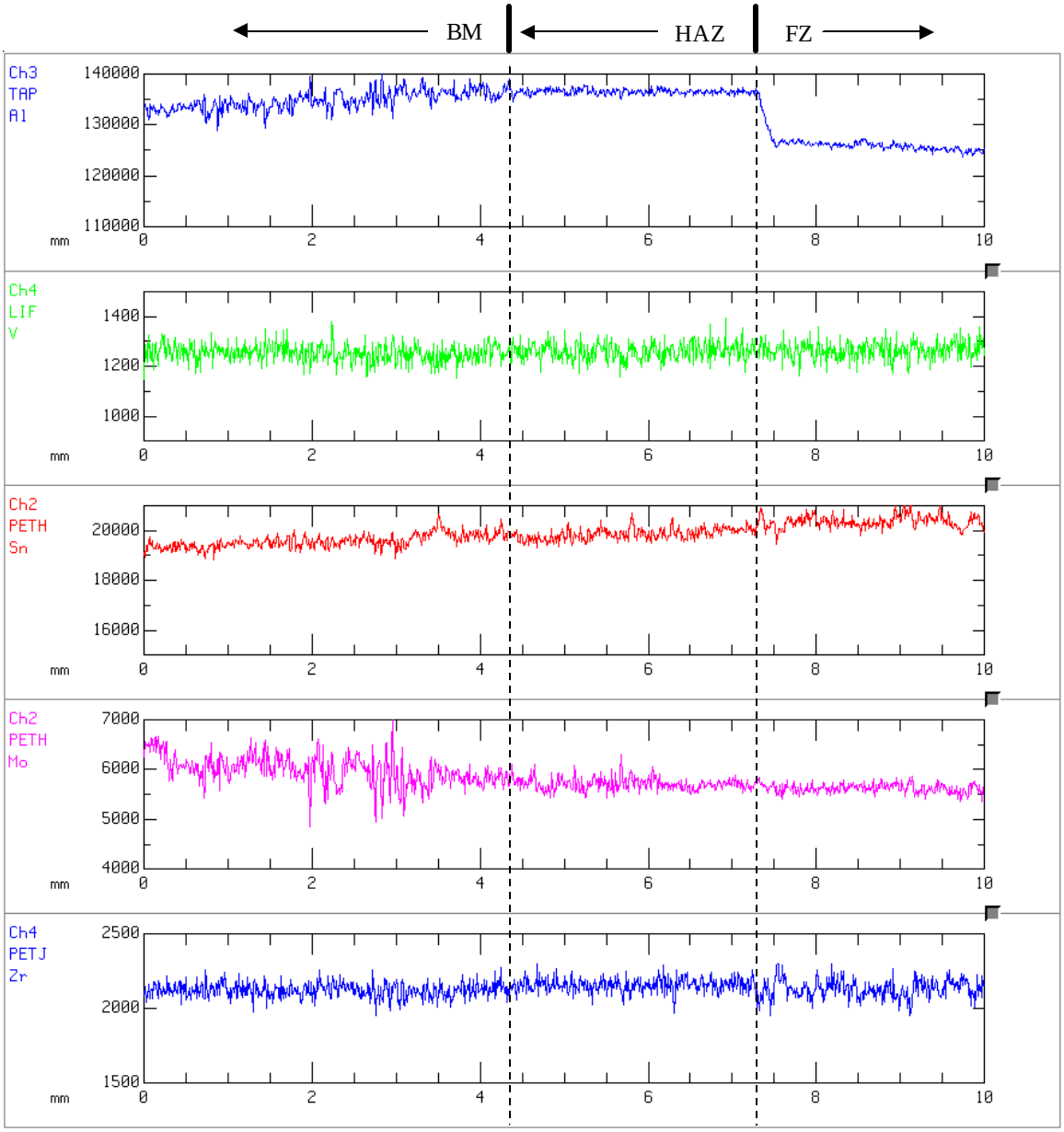

Figure 62: WDS scan of Ti5111 modified 200 ppm Y filler metal weld across the BM HAZ (2000ms dwell time). Elements: Al, V, Sn, Mo, Zr.

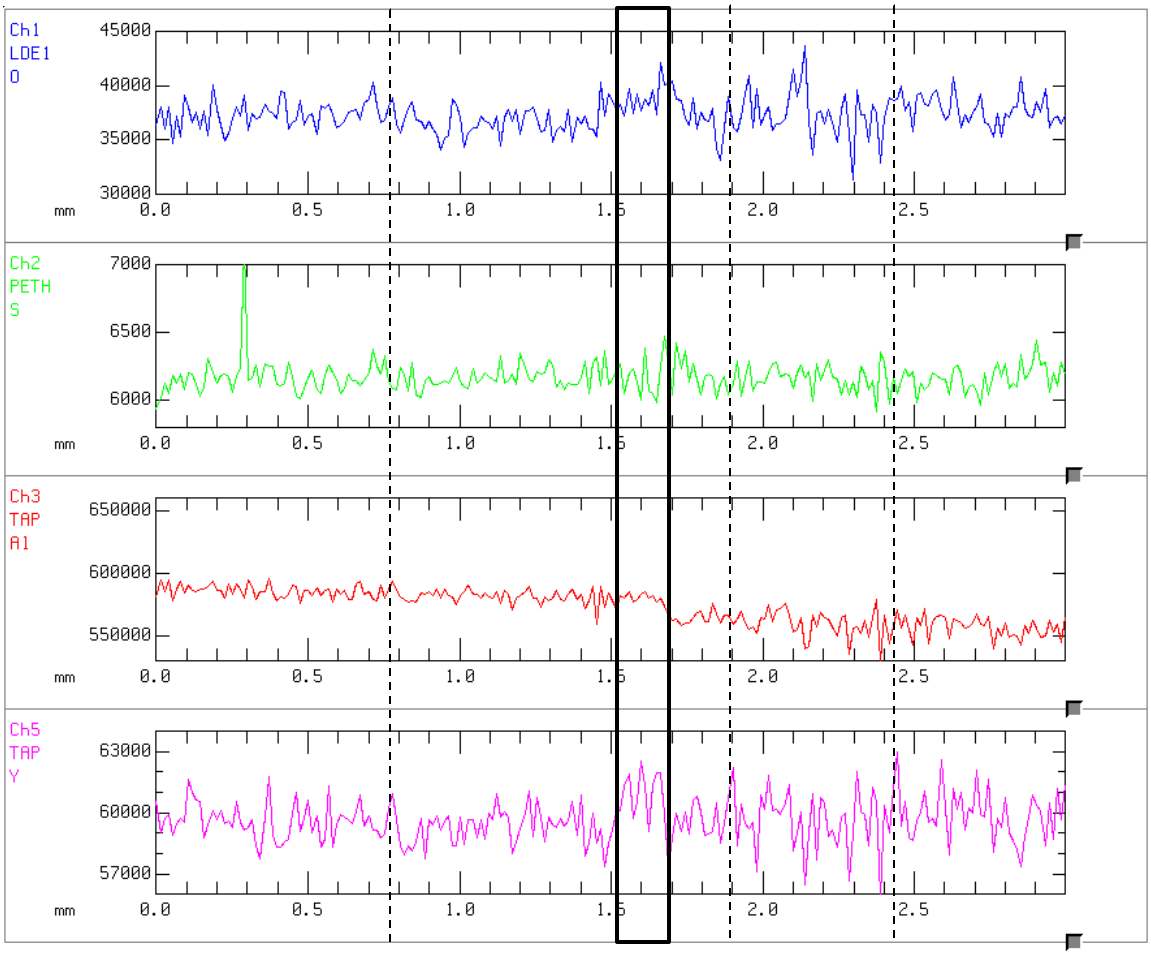

Figure 63: WDS scan of Ti5111 modified 200 ppm Y filler metal weld in weld area (10000ms dwell time). Elements: O, S, Al, Y. Dotted lines correspond to points where O, S and Y peaks correlate. The box indicates an extended area of peak correlation. The drop-off in Al concentration after this area may be indicative of the area being at a prior-β grain boundary.

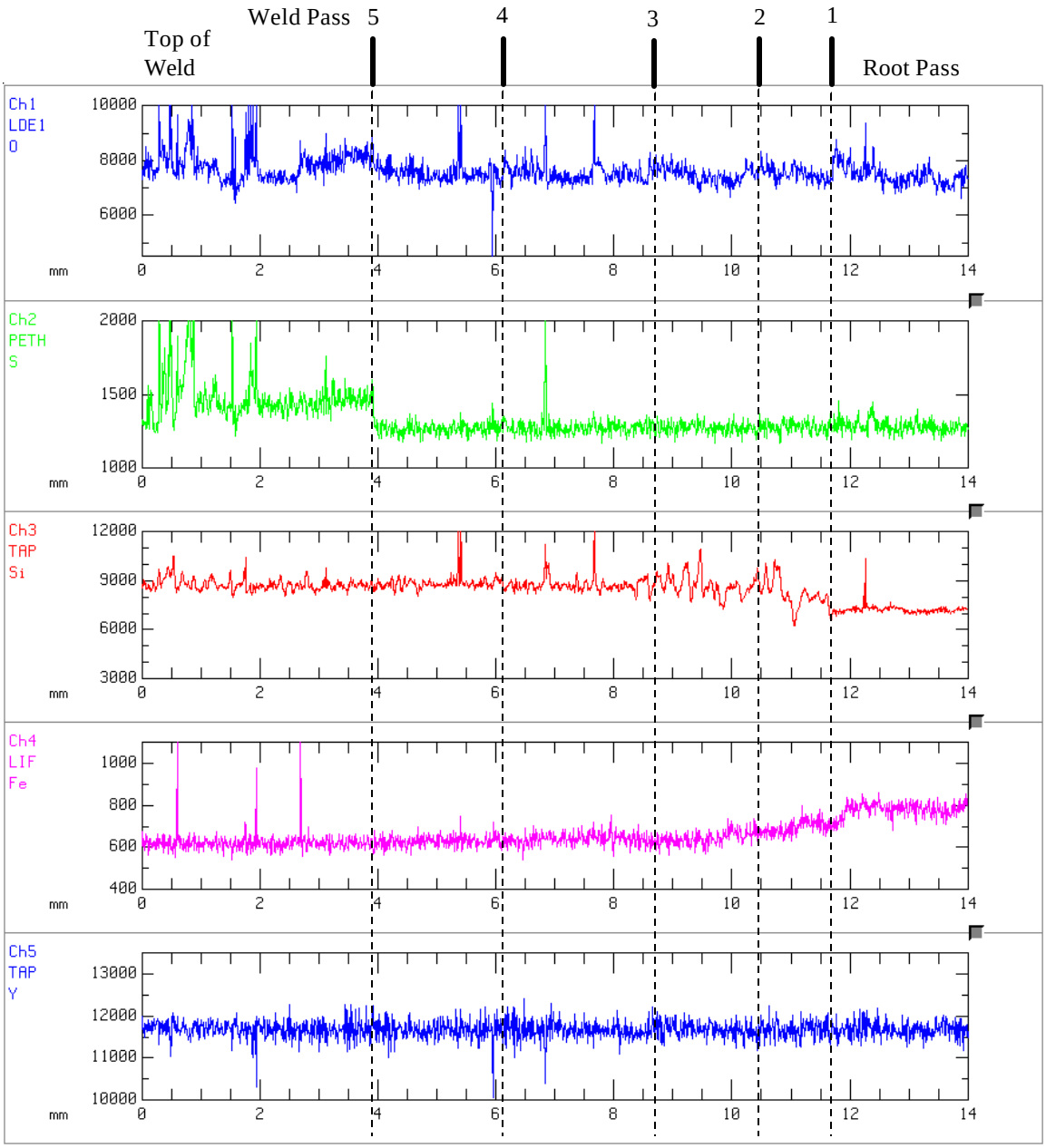

Figure 64: WDS scan of Ti5111 modified 200 ppm Y filler metal weld vertically through weld center (2000ms dwell time). Elements: O, S, Y, Si, Fe.

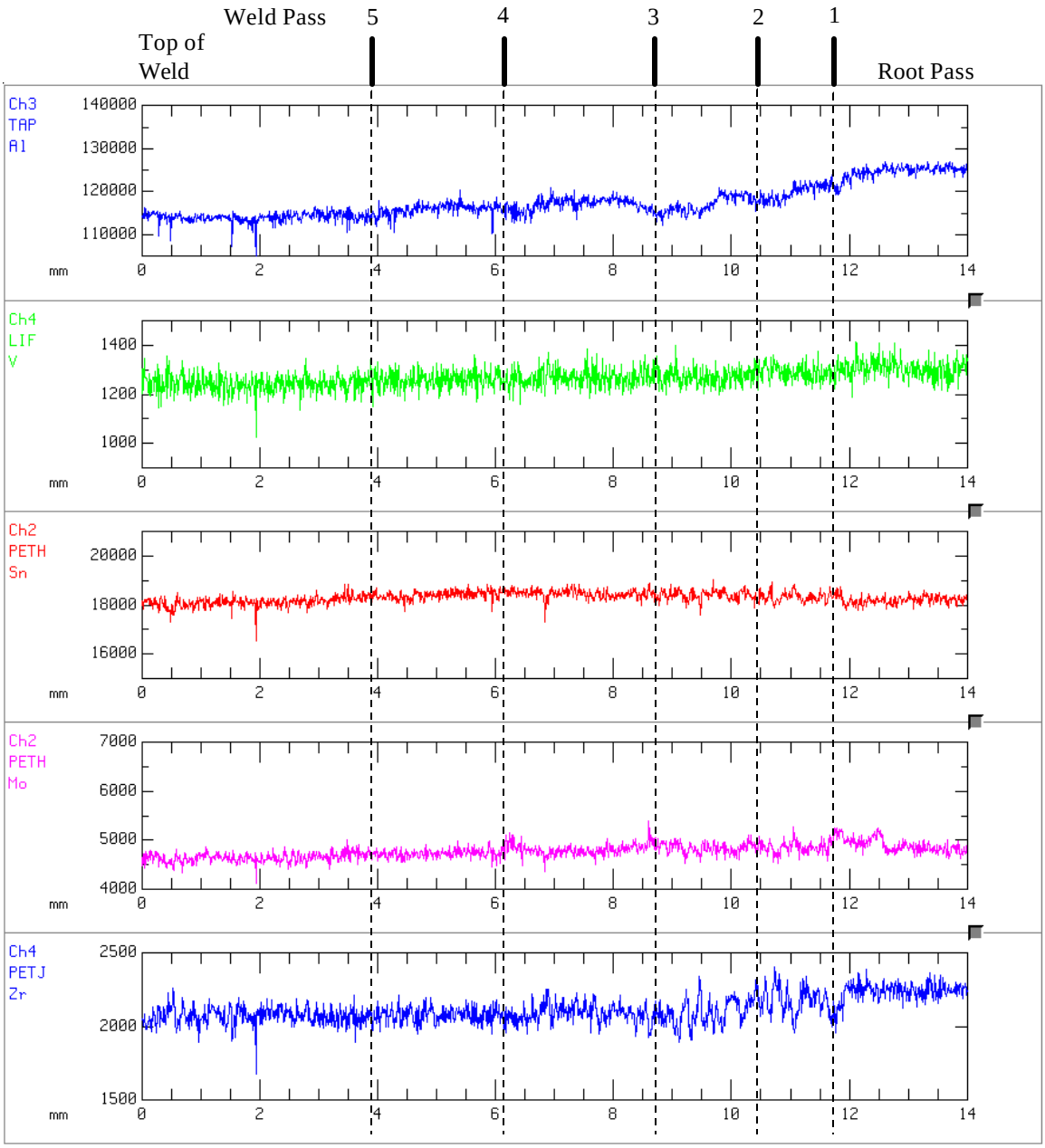

Figure 65: WDS scan of Ti5111 modified 200 ppm Y filler metal weld vertically through weld center (2000ms dwell time). Elements: Al, V, Sn, Mo, Zr.

and HAZ. There is a slight spike in O at the BM/HAZ interface, but no valley on the BM side. Oxygen decreases slightly in concentration after this peak for approximately 1 mm before increasing over the next 2 mm (approximately) towards the FZ. There is another slight peak in O concentration just inside the FZ and then a further increase in concentration inside the FZ. Silicon concentration shows a slim valley just inside the FZ followed by a large peak that comes back down again slightly but at a concentration higher than that of the BM and HAZ. Iron and aluminum both show a decrease in concentration at the HAZ/FZ interface. Tin concentration shows a steady increase in concentration from the BM to FZ and molybdenum shows a steady decrease in concentration from the BM to FZ. Zirconium concentration shows a slight valley in concentration just inside the FZ.

In Figure 63, line scan results for the high dwell time counts are shown. Dotted lines again show where some of the O, S and Y peaks correspond. In addition, the box in Figure 63 shows an area where several peaks of O and S correspond to several peaks of Y. This extended area of correspondence indicates that yttria or yttrium oxide sulfate formation is likely at this point. Examining the Al concentration at this area shows that there is a sudden slight drop-off in its concentration. This may indicate the presence of a grain boundary. This then leads to a likely conclusion that the yttrium oxide sulfate may only be significantly present at the grain boundaries inside the FZ.

The vertical line scan of the 200 ppm Y modified filler metal weld can be seen in Figures 64 & 65. Oxygen shows many spikes along this scan with each weld pass typically showing a spike. Fairly high spikes exist at the top of the weld and at the root

pass to Pass 1 interface. The O spikes at the top of the weld correspond with S spikes. Sulfur also drops off at the Pass 5 to Pass 4 interfaces. Silicon concentration is fairly steady to Pass 3 and then shows well-defined peaks and valleys as Si concentration decreases towards the root pass. These peaks and valleys correspond to ones seen in Zr and to a lesser extent in Sn and Mo. The Zr and Mo concentrations increase towards the root pass after the start of these peaks while Sn has its highest concentration at the start of Pass 4. Aluminum concentration shows increasing concentration from the top of the weld towards the root pass, where concentration begins to rise rapidly in Pass 2.

Several comments will now be made concerning diffusion of elements in the welds. First and perhaps most important, O clearly diffuses from the BM into the HAZ and from the HAZ to the FZ. A comparison of O diffusion across the HAZ's can be seen in Figure 66. That is, in all cases, there was a peak in O concentration close to the BM/HAZ interface, then decreasing O concentration over the next 1 mm or so towards the FZ and then a rise again over the next 2 mm, resulting in another peak in O concentration close to the HAZ/FZ interface. Inside the FZ, the O concentration is also clearly diffusing between weld passes with peaks possibly occurring at grain boundaries. The Al seems to be able to rapidly diffuse over larger distances to smooth out the concentration gradient. This was seen in both the HAZ of the matching filler metal and the weld passes in the modified filler metal. The α and β stabilizers are clearly diffusing such that there is a higher concentration of β stabilizers and lower concentration of α stabilizers in the retained β phase of the FZ and more α stabilizers and less β stabilizers in the Widmanstätten structure of the FZ.

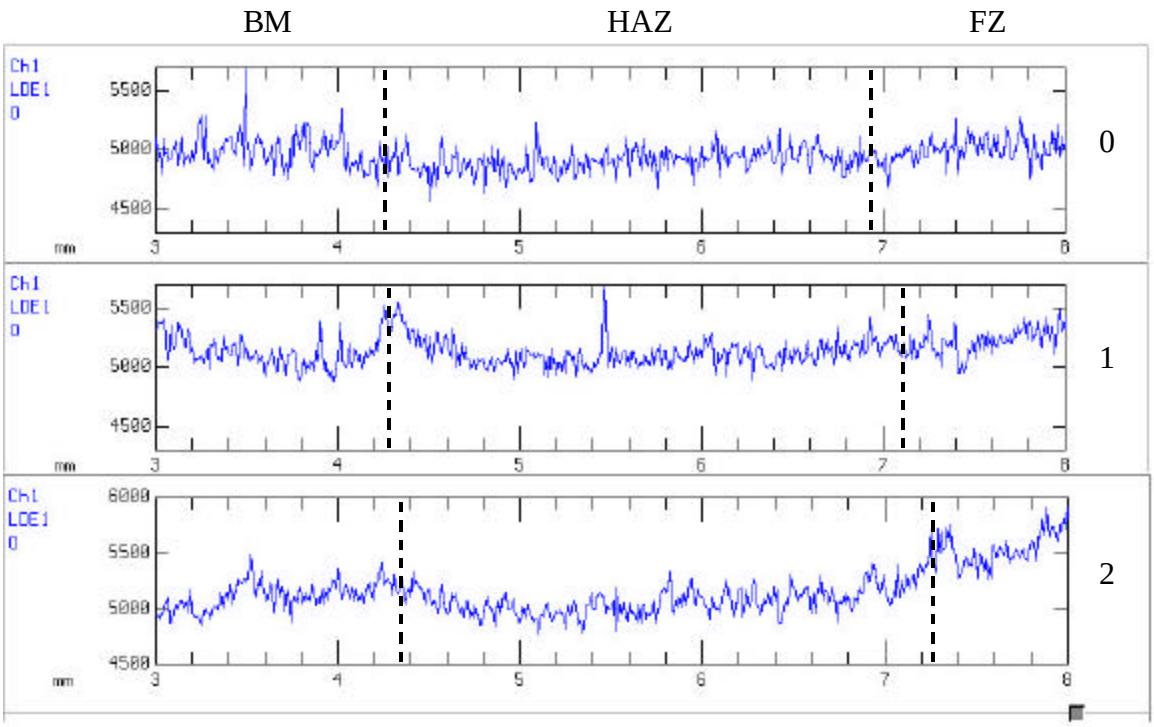

Figure 66: WDS scan for oxygen across HAZ's of Weld's 0 (matching filler metal), 1 (modified 50 ppm Y filler metal) and 2 (modified 200 ppm Y filler metal). Note decreasing O concentration after BM/HAZ interface followed by increasing O concentration towards HAZ/FZ interface in all cases.

As it was seen that sulfur and oxygen peaks often corresponded inside the weld FZ's, WDS maps were made using these elements in order to better represent possible particle formation inside the FZ. The WDS maps made can be seen in Figures 67-70. Figure 67 shows a WDS map of O and S inside the FZ in Weld 0. It can be seen that there is no real correlation between these two with the exception of some possible contamination. Figure 68 shows a map of Weld 1 FZ. Here it can be seen that there is a slight correlation between the S and O contents of the FZ, but no large clearly defined particles exist. Figure 69 shows a map of Weld 2 FZ. In this map, there is clearly a strong correlation between S and O. These two elements are clearly separating to specific regions together and it seems that larger particles are forming. However, when the samples were examined by ESEM in order to image the supposed particles, no particles were seen to clearly exist in the area mapped. Figure 70 maps a prior-β grain boundary in Weld 2 for the elements O and Y to see if any correlation exists. While there was clearly O segregation, no correlation could again be made with the Y, as was the case with the low count line scans.

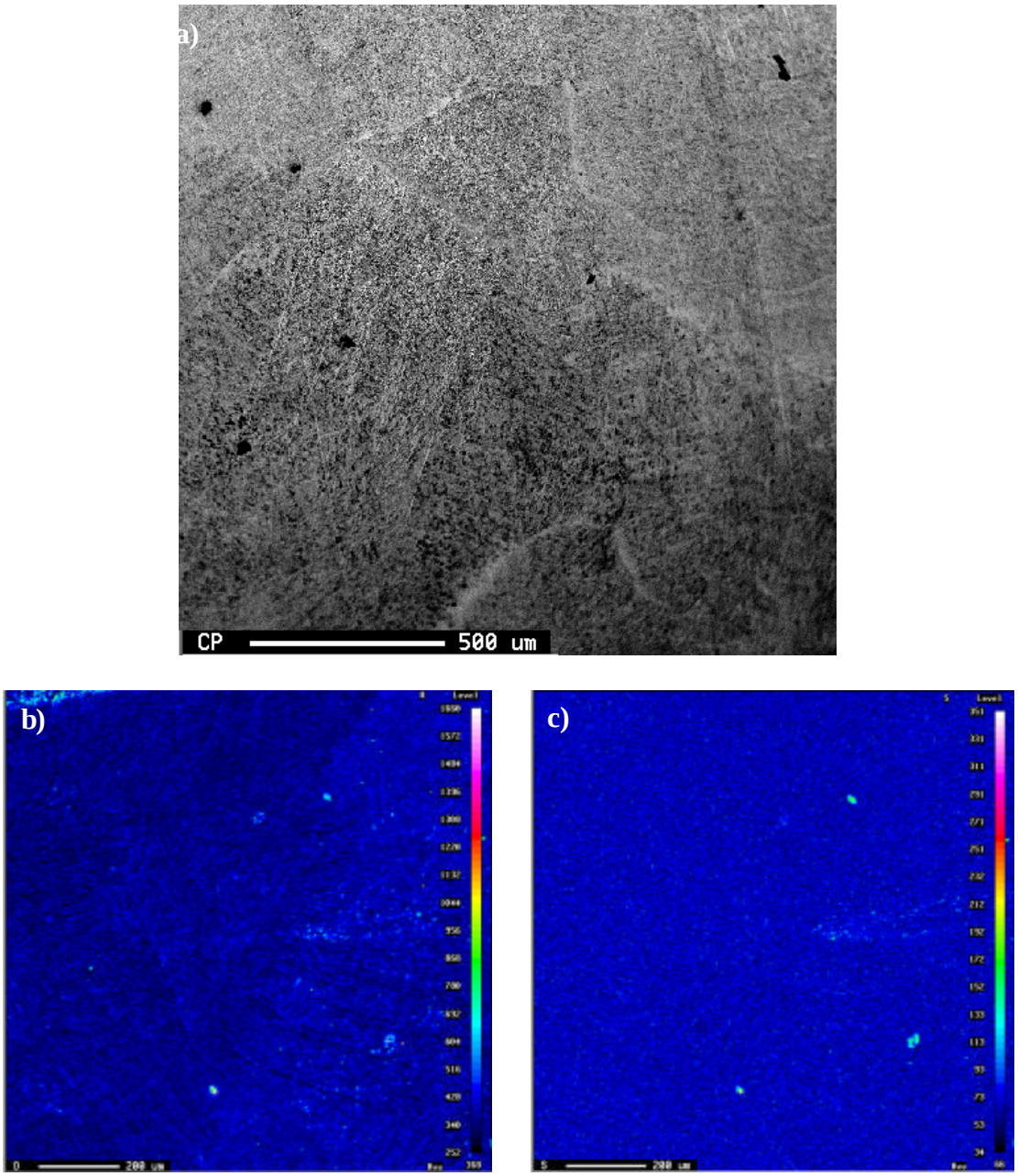

Figure 67: (a) Backscattered electron image of FZ area in Weld 0 where WDS mapping was performed. (b) WDS O map, 100 ms dwell time, 300 x 300 points over 1.2 mm x 1.2 mm area. (c) WDS S map, 100 ms dwell time, 300 x 300 points over 1.2 mm x 1.2 mm area. Note that there is no real correlation between the areas where S and O correspond except for a few areas that may be the result of contamination.

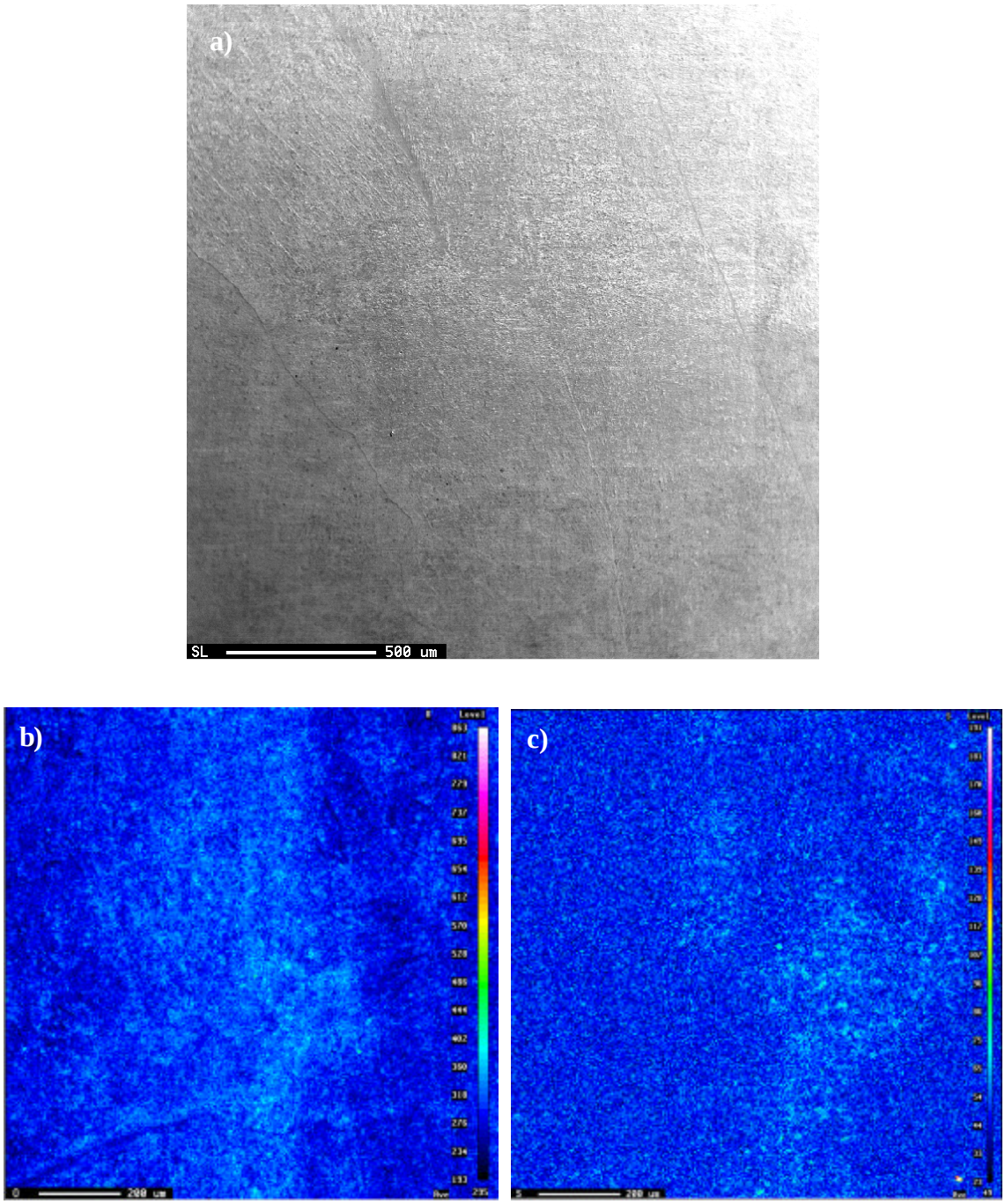

Figure 68: (a) Secondary electron image of FZ area in Weld 1 where WDS mapping was performed. (b) WDS O map, 100 ms dwell time, 300 x 300 points over 1.2 mm x 1.2 mm area. (c) WDS S map, 100 ms dwell time, 300 x 300 points over 1.2 mm x 1.2 mm area. Note that there is a slight correlation between the areas where S and O correspond.

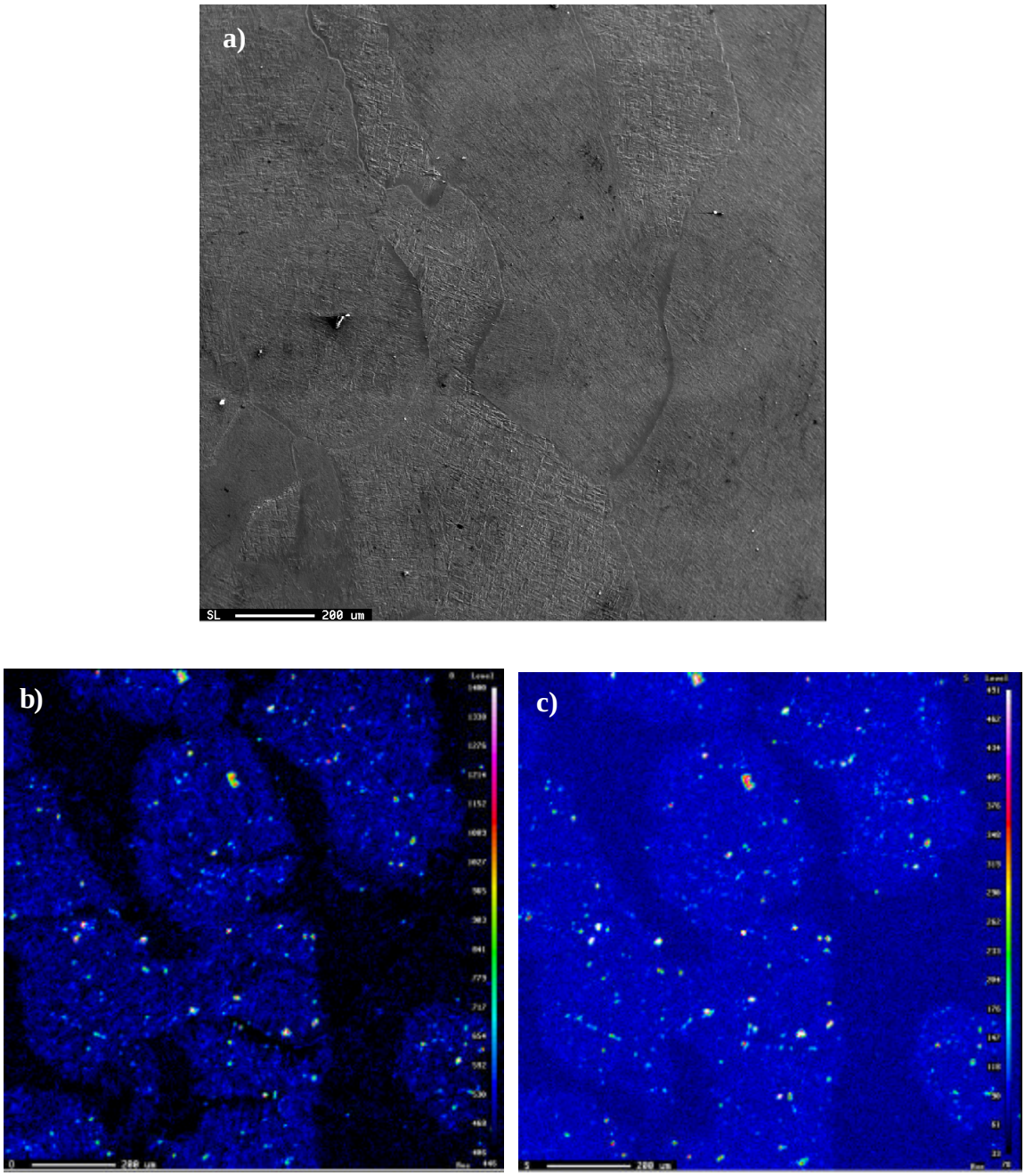

Figure 69: (a) Secondary electron image of FZ area in Weld 2 where WDS mapping was performed. (b) WDS O map, 100 ms dwell time, 300 x 300 points over 4 µm x 4 µm area. (c) WDS S map, 100 ms dwell time, 300 x 300 points over 4 µm x 4 µm area. Note that there is a strong correlation between the areas where S and O correspond.

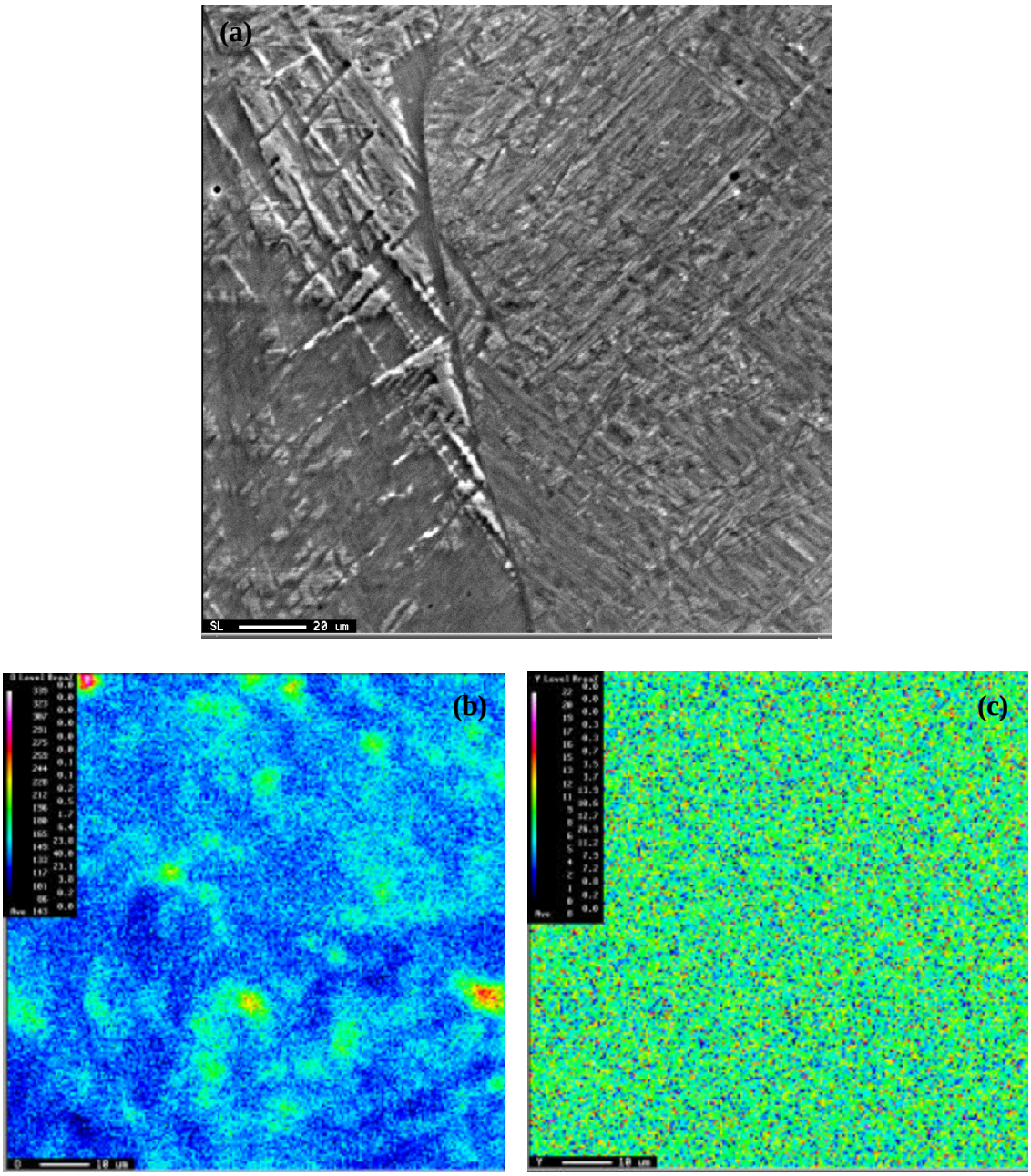

Figure 70: (a) Secondary electron image of FZ area in Weld 2 at prior-β grain boundary where WDS mapping was performed. (b) WDS O map, 100 ms dwell time, 100 ms dwell time, 300 x 300 points over 1.2 mm x 1.2 mm area. (c) WDS Y map, 100 ms dwell time, 300 x 300 points over 1.2 mm x 1.2 mm area. Note that there is no observed correlation between the areas where Y and O correspond with Y blending in with background noise.

X. WELD MICROSTRUCTURES

X.1 Introduction

The areas of specimen examined microscopically include the base metal (BM), base metal far heat affected zone (BM far HAZ), base metal near heat affected zone (BM near HAZ), unaffected fusion zone (FZ), fusion zone heat affected zone (FZ HAZ) and the root pass area. All of these areas were examined by both optical microscopy and scanning electron microscopy. The FZ and FZ HAZ were further examined by transmission electron microscopy.

X.2 Specimen Preparation and Experimental

X.2.1 Optical and Environmental Scanning Electron Microscopy (ESEM)

The same specimens were used for examination under both optical microscopy and ESEM. Specimens approximately 0.635 cm in thickness were sectioned from Welds 0, 1 and 2 after removing approximately 0.635 cm from the ends of the weld plates. These specimens were then cut to an approximate length of 7.62 cm with the weld zone in the center. The specimens were then polished on a Buehler tabletop polish unit using polishing paper to a grit of 800 and then chemically polished using a Buehler Mastermet colloidal silica polishing suspension on a Buehler Chemomet polishing pad. This polishing process produced an extremely fine mirrored surface. The surface was then etched using Kroll's reagent (88 vol.% H_2O, 10 vol.% HNO_3, and 2 vol.% HF).

Optical microscopy was performed using an Olympus BX60 optical microscope with an attached PULNiX JMC-7 digital camera. Digital pictures were captured using the program EPIX XCAP version 2.1. Magnifications used to examine the microstructures included 25x, 125x, 250x and 625x.

Environmental SEM was performed using a Philips Electroscan ESEM-E3. Digital pictures were captured using the program Image Pro Plus from an Oculus-TCX/MX image frame grabber off the ESEM video output. Magnifications used to examine the microstructure included 1000x, 2500x, 5000x and 10000x.

X.2.2 Transmission Electron Microscopy (TEM)

Microstructures of the weld fusion zones were examined through use of TEM. This TEM was performed using a 400 kV JEOL 4000FX instrument, operating at 300 kV. Areas studied microstructurally under the TEM included the FZ and FZ HAZ. The microstructural features analyzed for in these areas included what phases were present, platelet sizes and whether any particles were present.

Samples across the weld zone were cut into approximate 7 mm x 7 mm x 19 mm sections through use of the EDM. Thin sections (approximately 200 µm) from the weld zone of these samples were cut using a Buehler Isomet low speed diamond saw. Using a Gatan-659 punch, 3 mm disks were then obtained from these thin sections. The 3 mm disks were polished down to approximately 90 µm on a LECO VP-160 Mechanical Polisher using 600 micron polishing paper at 200 RPM with the technique described by Li and Salamanca-Riba [41]. These polished disks were then dimpled to approximately 20 µm using a South Bay Technology, Inc Model 515 dimpler with 6 µm diamond paste.

The dimpled disks were then placed into a Bal-Tec ion mill. The specimens were milled using argon gas at a gun voltage of 5.95 V and a current of approximately 1.2 – 1.4 mA, depending upon initial thickness, and at an angle of 15°. These specimens were milled until a hole was just detected, usually taking a few hours. After the hole was detected, the samples were further ion milled for 30 minutes at a voltage of 4.0 V and a current of 0.8 mA. This was done to remove any possible damage resulting from the higher milling voltages and currents.

X.3 Results and Discussion

The base metal of the specimens can be seen in Figures 71-74. Weld plates 0 and 1 were cut from the same sheet and are therefore only included once. Examining these figures, it can be seen that the microstructure from each of the base plates consists of equiaxed prior-β grains transformed predominantly to lamellar α. A small amount of retained β is present in all the weld plates. While weld plate 2 was from the same heat as weld plates 0 and 1, it can be seen that the lamellar α plates are slightly coarser in weld plate 2. This slight difference in microstructure is not expected to have any significant effect on weld zone properties.

The BM far HAZ microstructures can be seen in Figures 75-80. The microstructures in this section have been exposed to elevated temperatures, but the temperatures were not high enough for any significant phase transformation to take place. Slight coarsening of the microstructures can be seen as compared to the base metal's. In this area, some amount of transformation to β is likely, with a resulting transformation to α upon cooling, resulting in mixed-type microstructures.

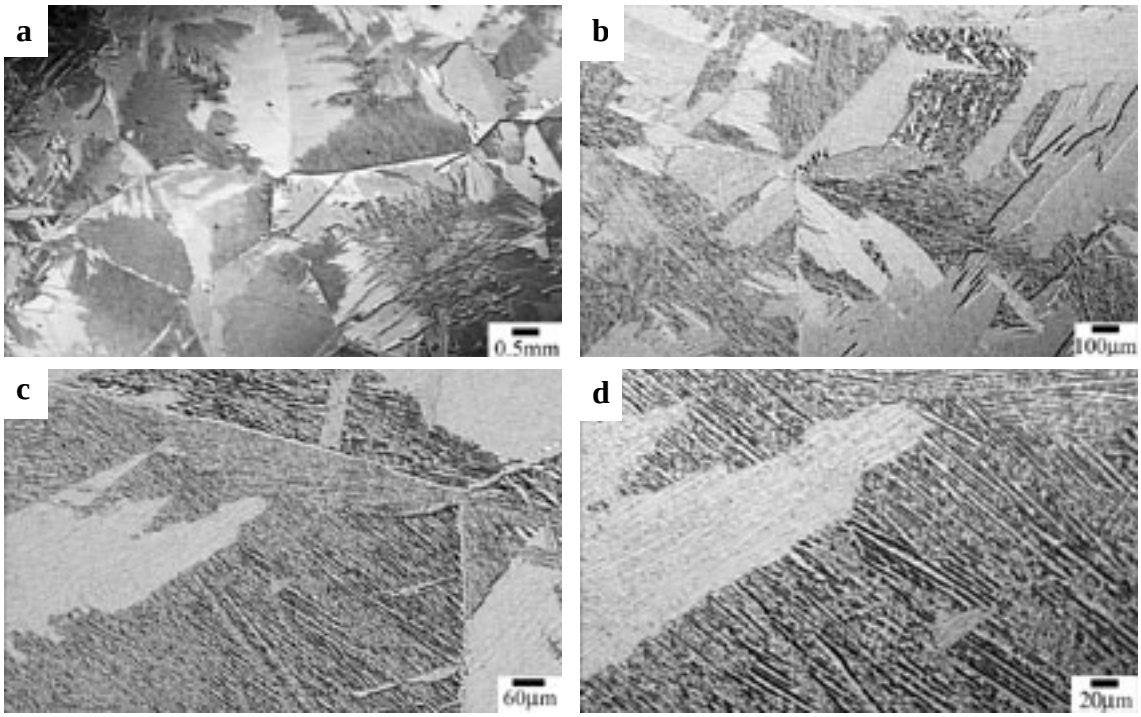

Figure 71: Optical microscopy of the base metal from weld plates 0 and 1. (a) 25x, (b) 125x, (c) 250x, and (d) 625x.

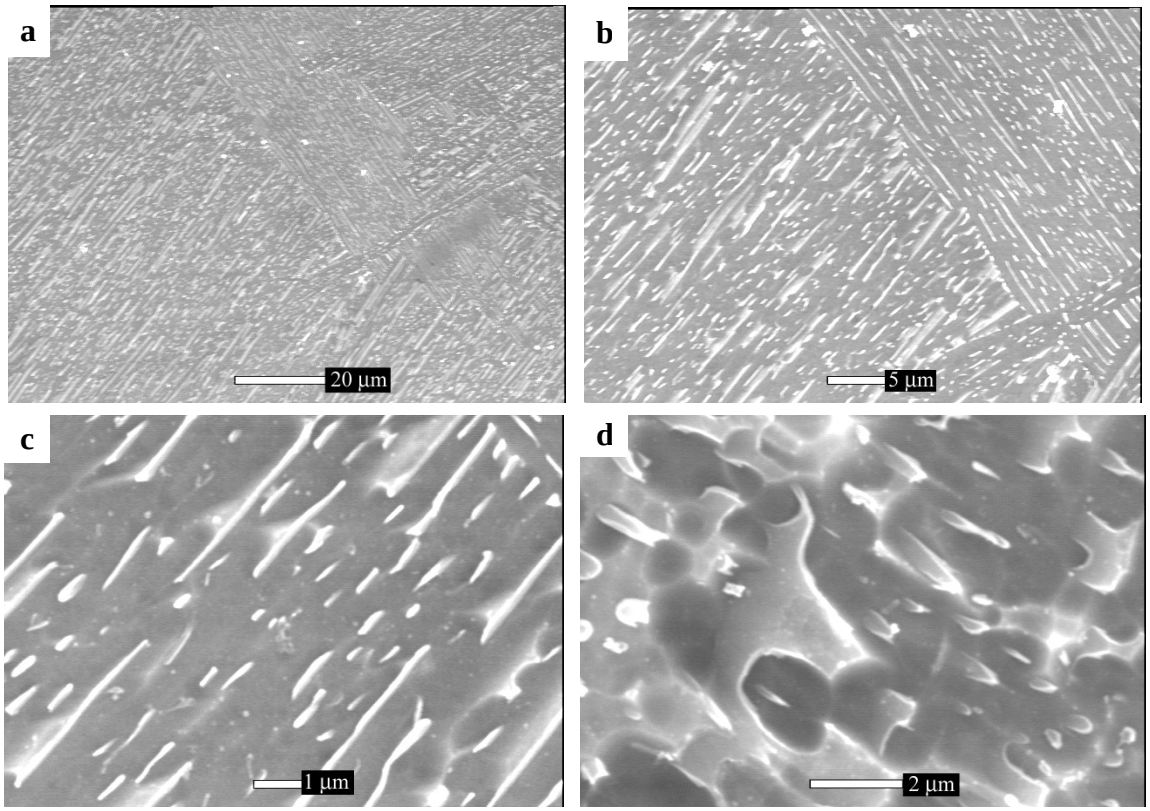

Figure 72: ESEM of the base metal from weld plates 0 and 1. (a) 1000x, (b) 2500x, (c) 10,000x, and (d) 10,000x.

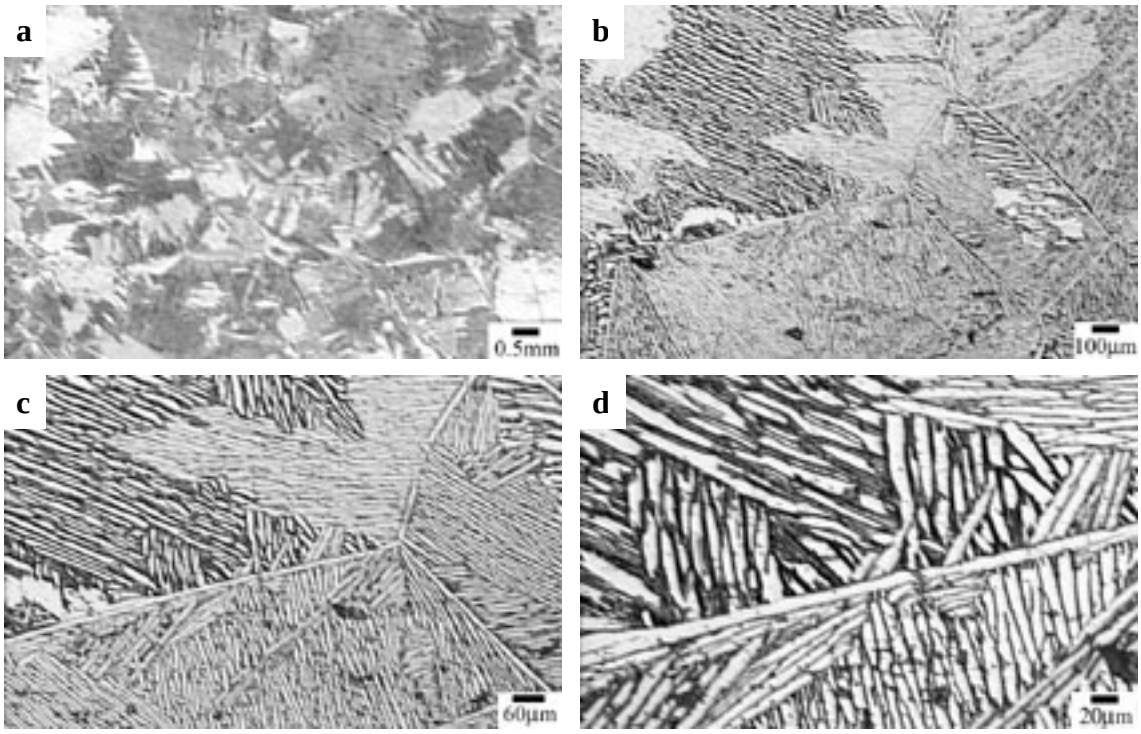

Figure 73: Optical microscopy of the base metal from weld plate 2. (a) 25x, (b) 125x, (c) 250x, and (d) 625x.

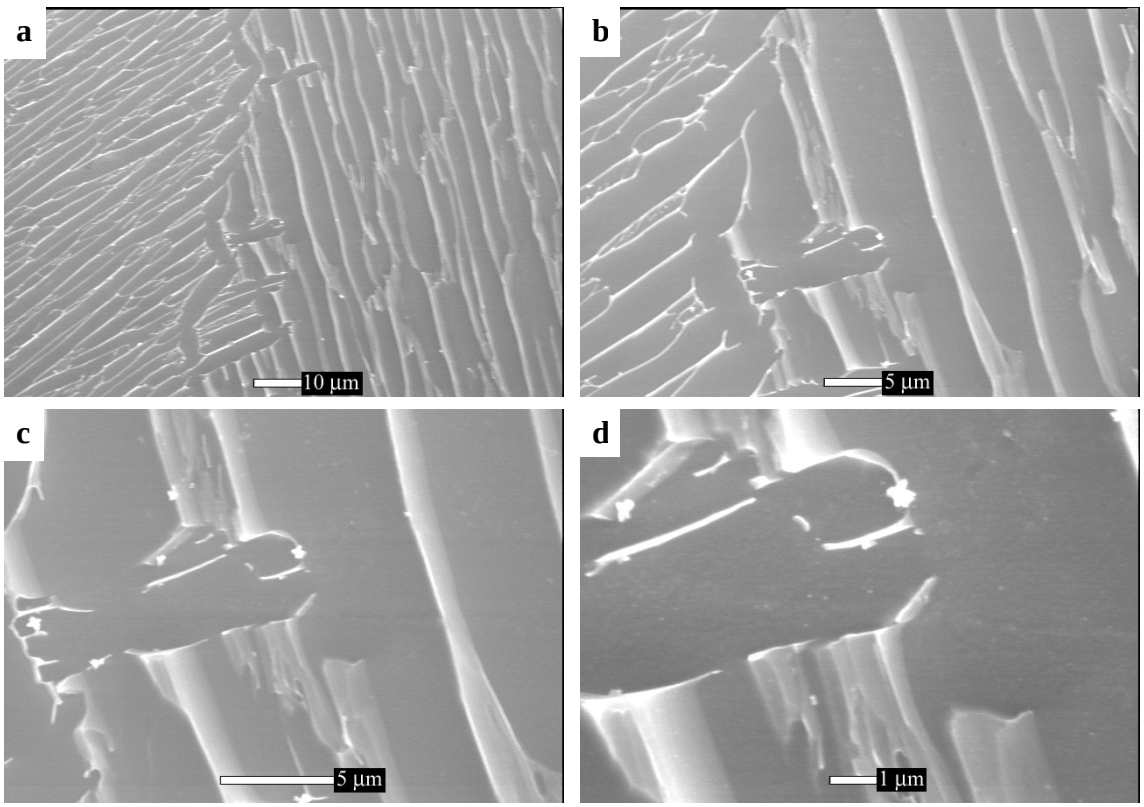

Figure 74: ESEM of the base metal from weld plate 2. (a) 1000x, (b) 2500x, (c) 5000x, and (d) 10,000x.

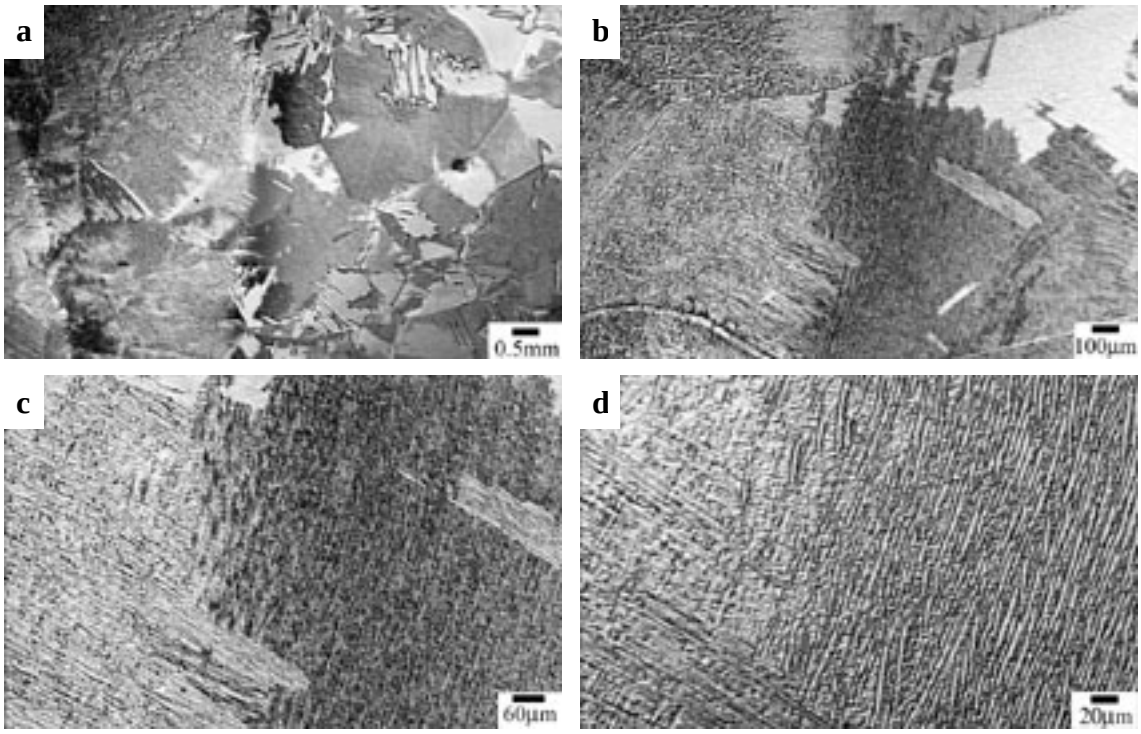

Figure 75: Optical microscopy of the near-to-far HAZ boundary area in Weld 0. (a) 25x, (b) 125x, (c) 250x, and (d) 625x.

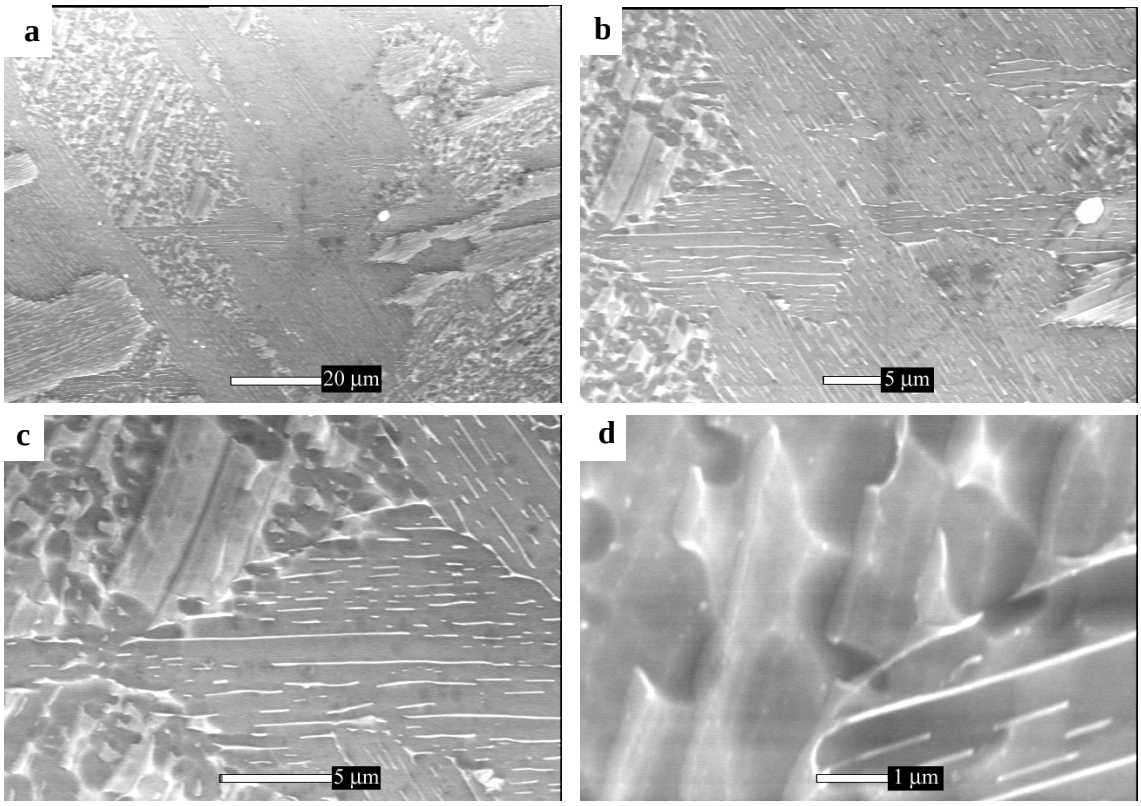

Figure 76: ESEM of the far HAZ area in Weld 0. (a) 1000x, (b) 2500x, (c) 5000x, and (d) 10,000x.

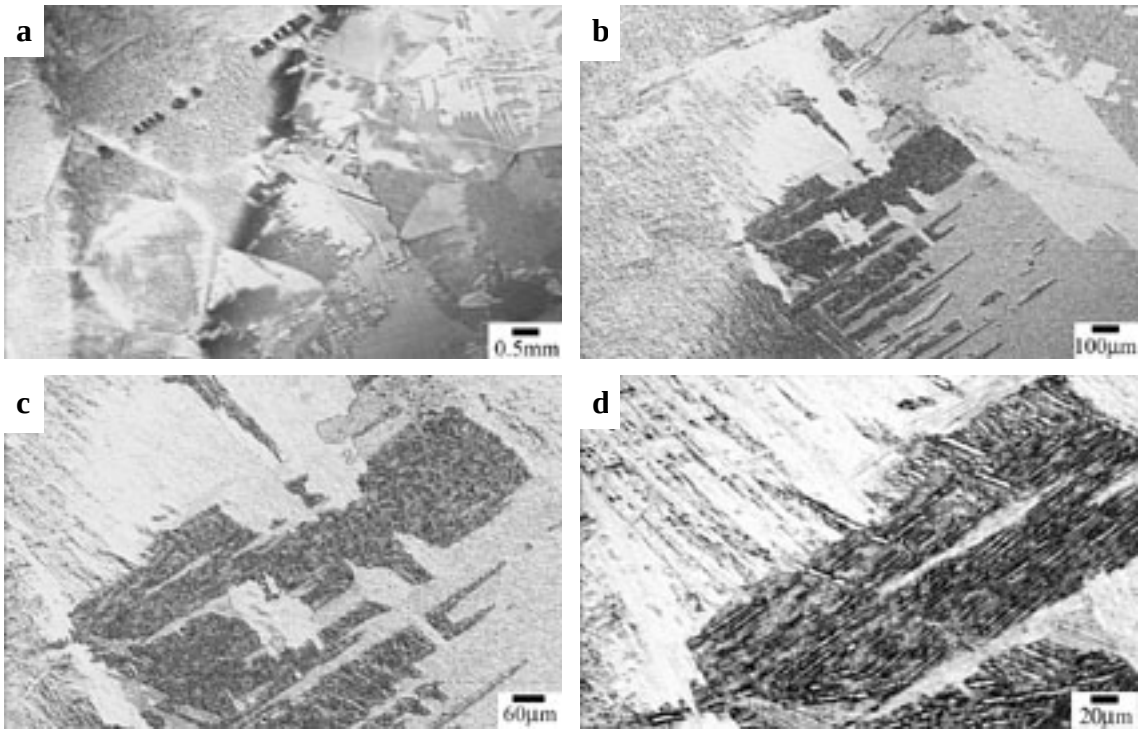

Figure 77: Optical microscopy of the near-to-far HAZ boundary area in Weld 1. (a) 25x, (b) 125x, (c) 250x, and (d) 625x.

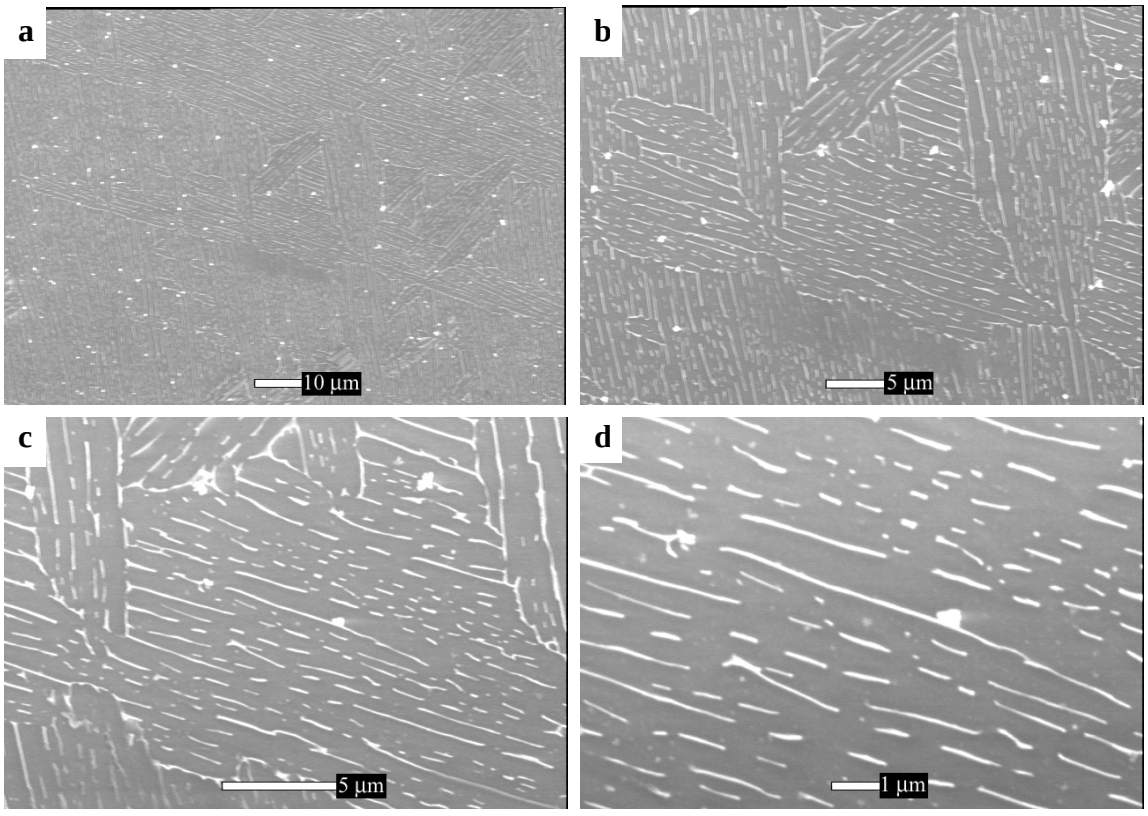

Figure 78: ESEM of the far HAZ area in Weld 1. (a) 1000x, (b) 2500x, (c) 5000x, and (d) 10,000x.

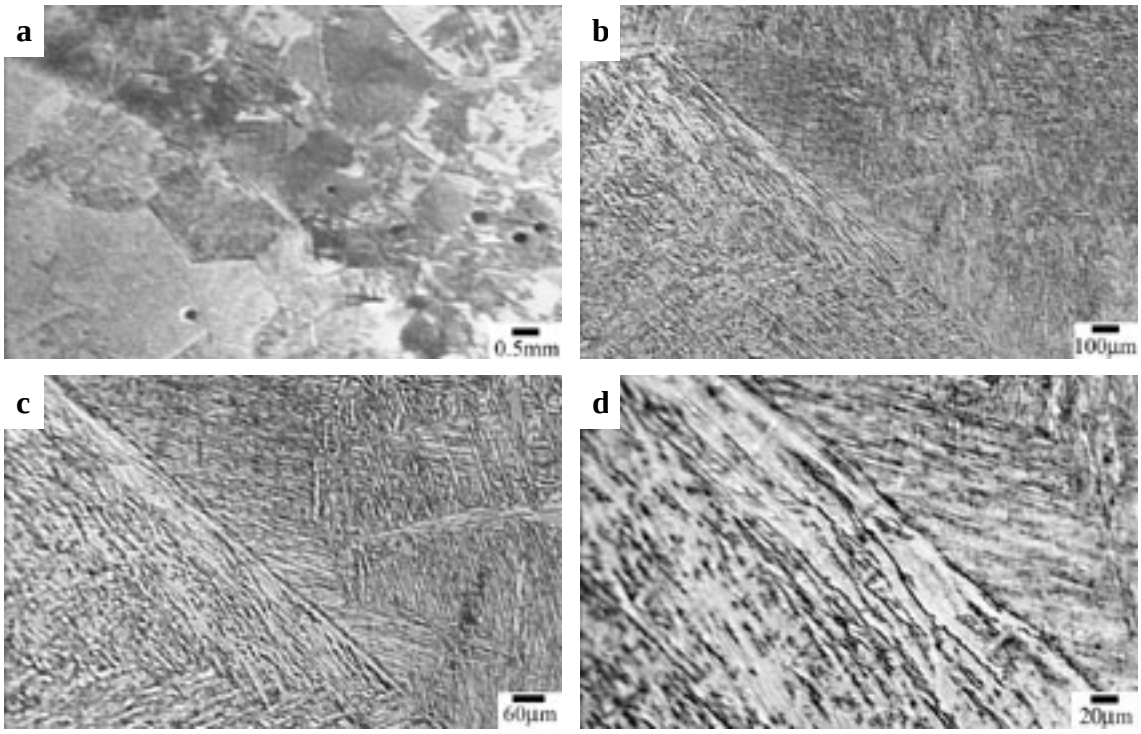

Figure 79: Optical microscopy of the near-to-far HAZ boundary area in Weld 2. (a) 25x, (b) 125x, (c) 250x, and (d) 625x.

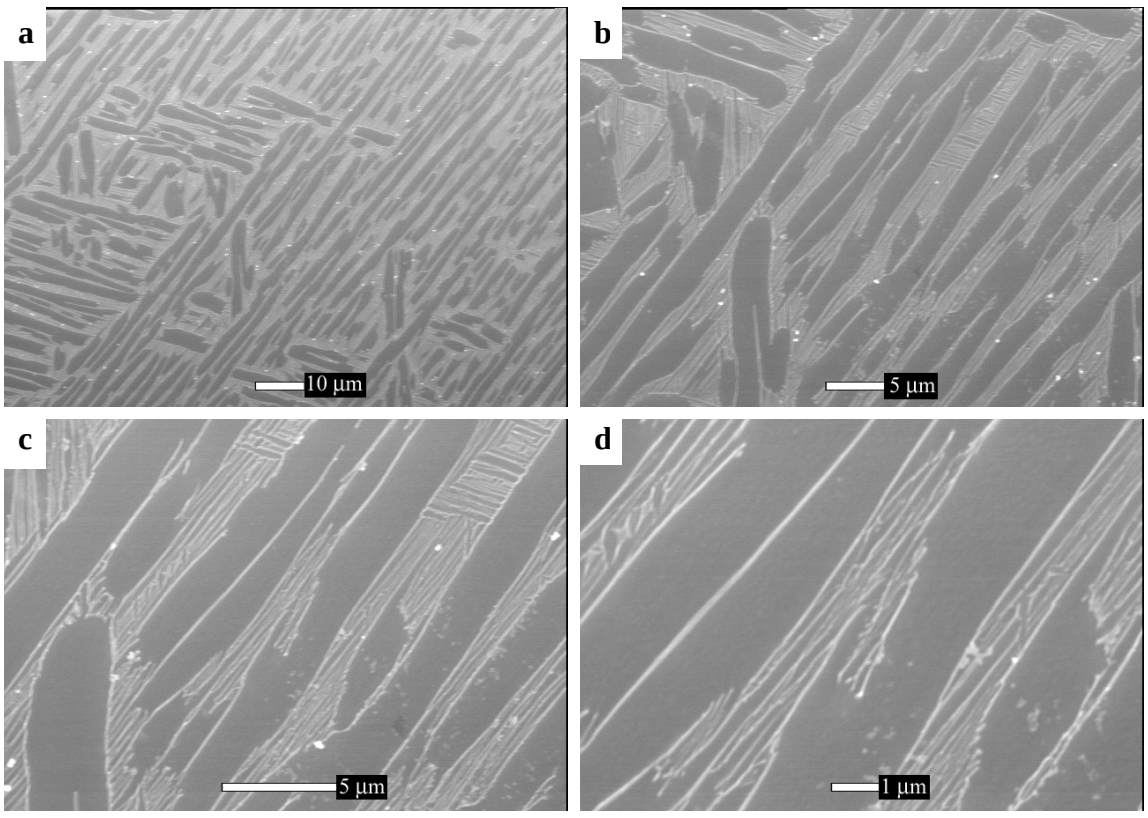

Figure 80: ESEM of the far HAZ area in Weld 1. (a) 1000x, (b) 2500x, (c) 5000x, and (d) 10,000x.

The BM near HAZ microstructures can be seen in Figures 81-86. The microstructures in this area have been exposed to temperatures high enough to cause a phase transformation from the α to β. When the rapid cooling takes place in the weld zone, the microstructure is transformed to an acicular Widmanstätten α. Prior β equiaxed grain boundaries are still present. Close to the FZ, there is a region of partially melted grains where the FZ grains epitaxially grow off of into the melt.

Unaffected FZ microstructures can be seen in Figures 87-95. The term unaffected FZ refers to the weld metal that was last laid down and was therefore not subjected to any other heating, as weld passes below the last pass are. In this area, the microstructure is predominantly a colony-type Widmanstätten α with some martensite α'. TEM performed on these weld areas, and shown for Welds 0, 1 and 2 in Figures 89, 92 and 95 respectively shows that there was some slight amount of remaining β left in the microstructure, which is indicative of a diffusional transformation to α. The low concentration of β stabilizers in the Ti-5111 alloy results in only very small amounts of the β able to become stabilized. It is often very hard to distinguish between acicular martensite α' and Widmanstätten α, with TEM or chemical analysis necessary to make the distinction. This identification is made even more difficult in welds of titanium as there are often both structures present to some degree.

Examining the unaffected FZ microstructures by TEM, it was seen that the FZ of Weld 1 had a slightly refined Widmanstätten plate size as compared to Weld 0. Average plate size in Weld 0 was approximately 425 nm while in Weld 1 the average size was approximately 375 nm. In Weld 2, while many areas had a Widmanstätten plates with a

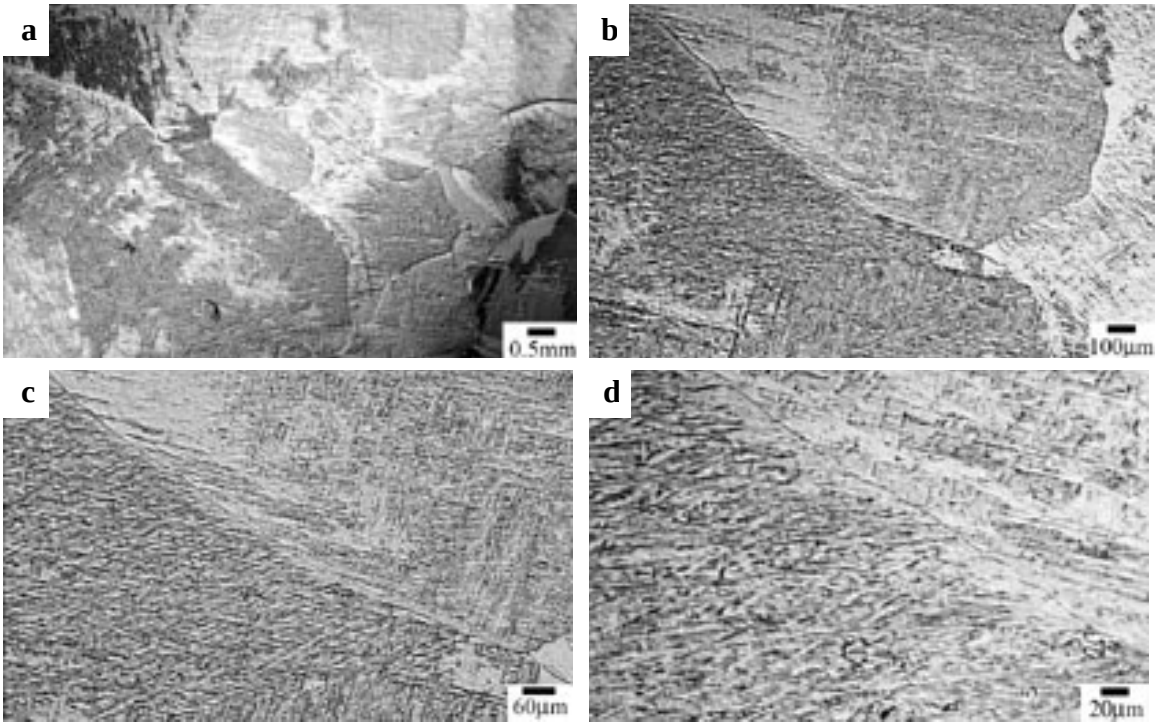

Figure 81: Optical microscopy of the near HAZ area in Weld 0. (a) 25x, (b) 125x, (c) 250x, and (d) 625x.

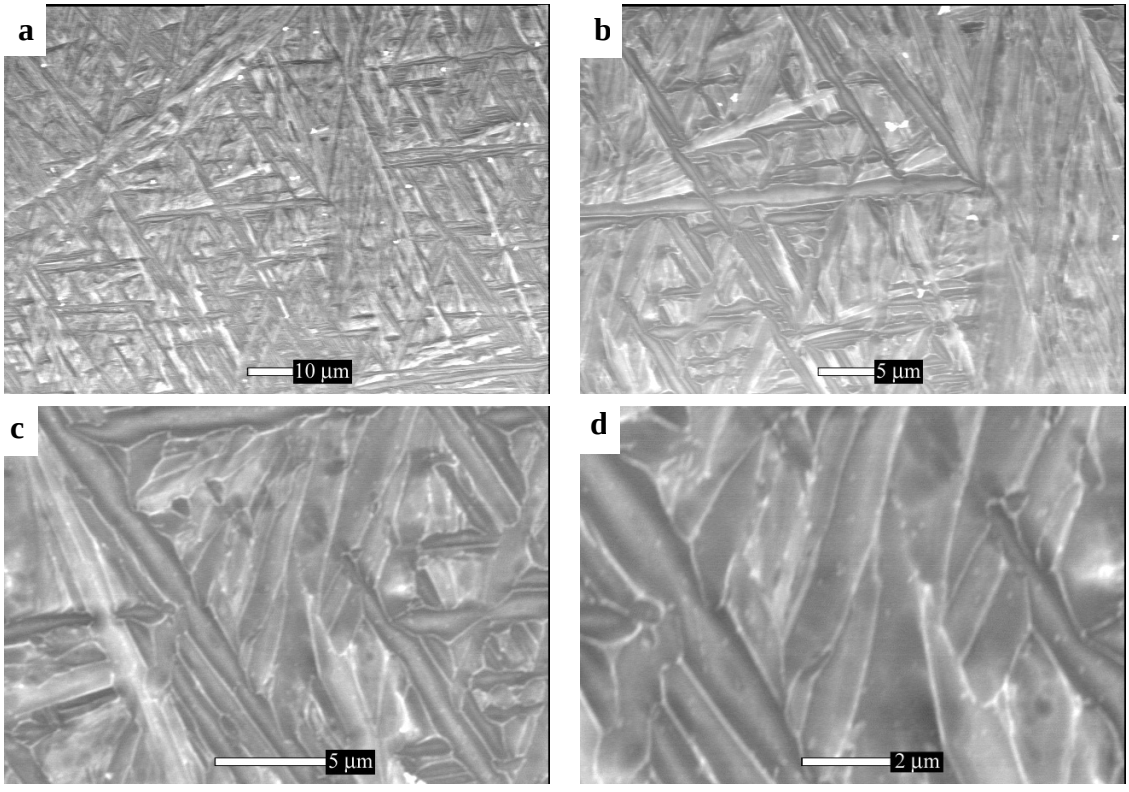

Figure 82: ESEM of the near HAZ area in Weld 0. (a) 1000x, (b) 2500x, (c) 5000x, and (d) 10,000x.

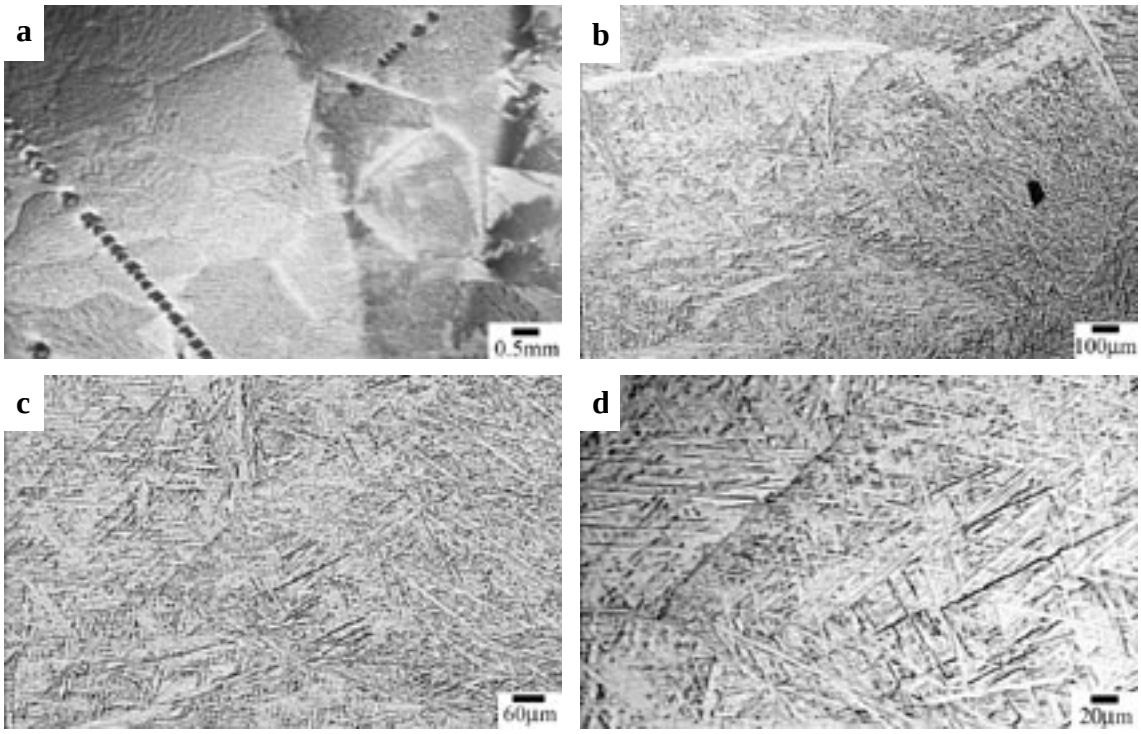

Figure 83: Optical microscopy of the near HAZ area in Weld 1. (a) 25x, (b) 125x, (c) 250x, and (d) 625x.

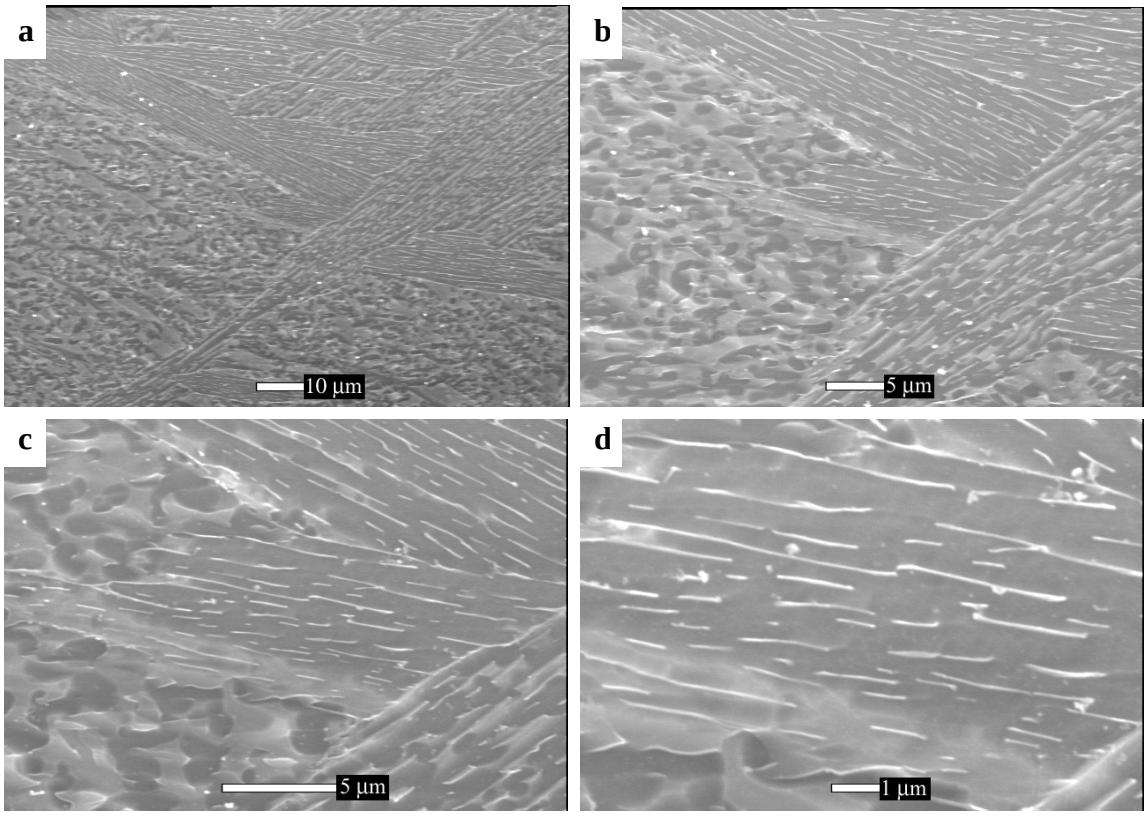

Figure 84: ESEM of the near HAZ area in Weld 1. (a) 1000x, (b) 2500x, (c) 5000x, and (d) 10,000x.

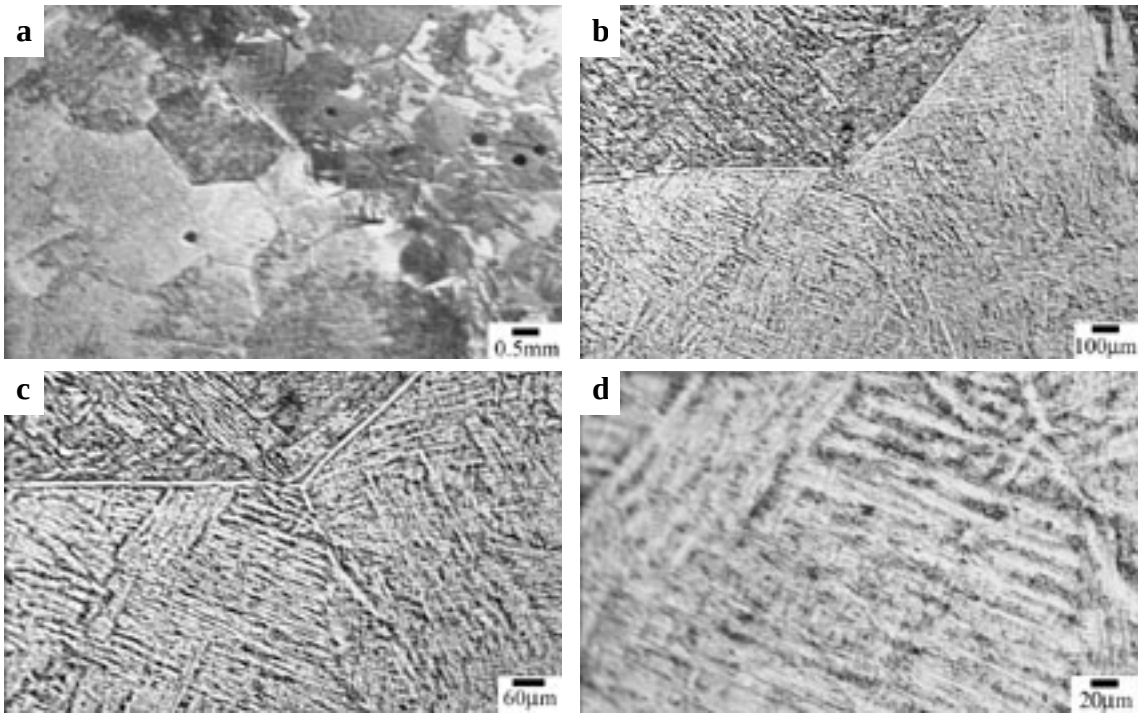

Figure 85: Optical microscopy of the near HAZ area in Weld 2. (a) 25x, (b) 125x, (c) 250x, and (d) 625x.

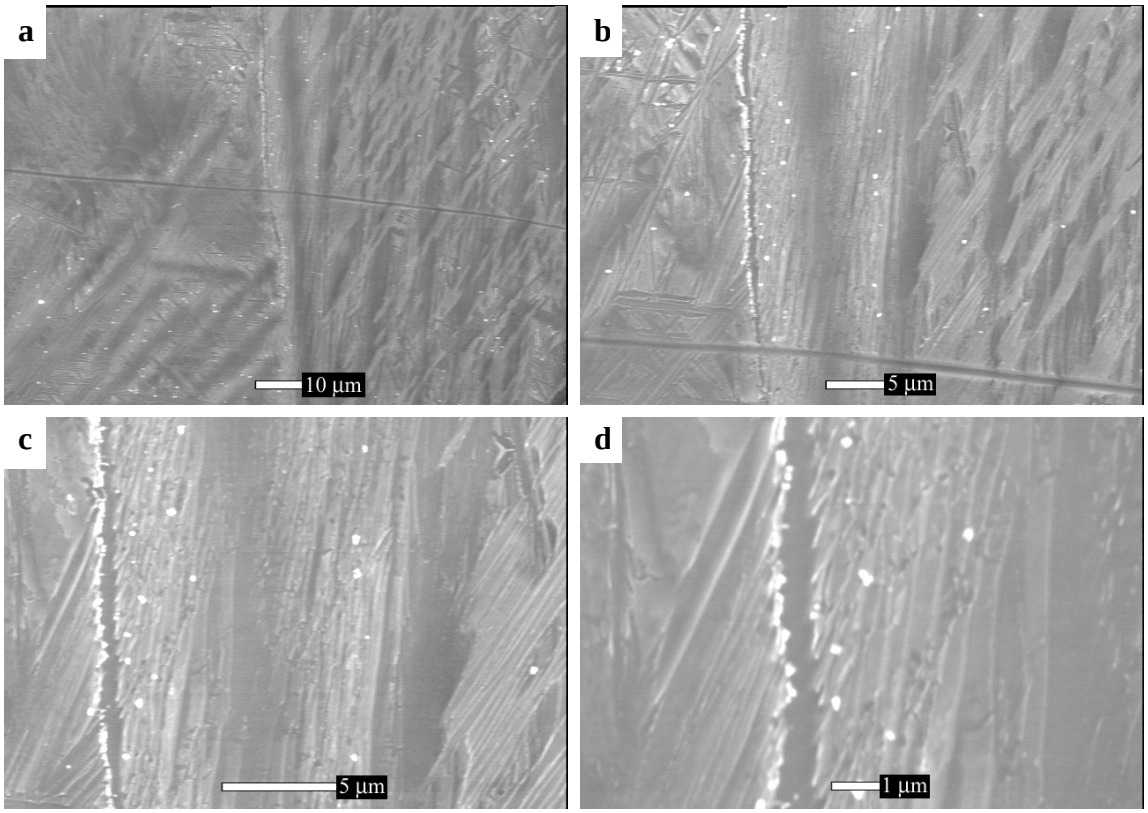

Figure 86: ESEM of the near HAZ area in Weld 2. (a) 1000x, (b) 2500x, (c) 5000x, and (d) 10,000x.

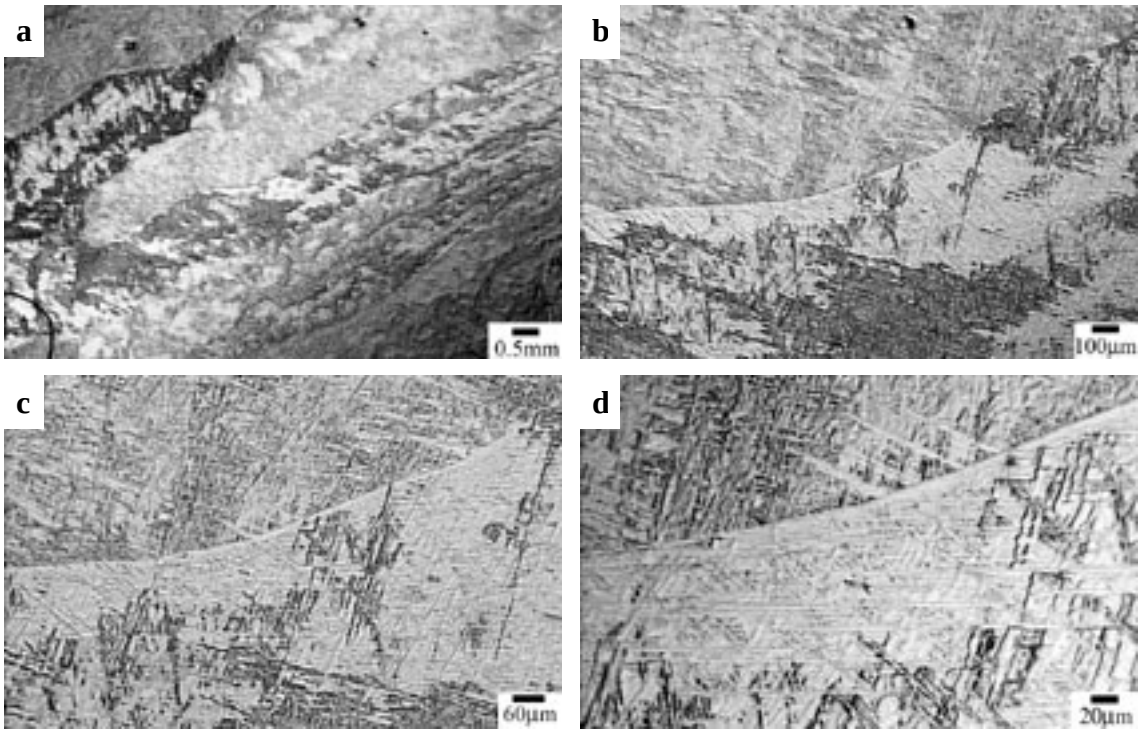

Figure 87: Optical microscopy of the FZ near the top center of the weld in Weld 0. (a) 25x, (b) 125x, (c) 250x, and (d) 625x.

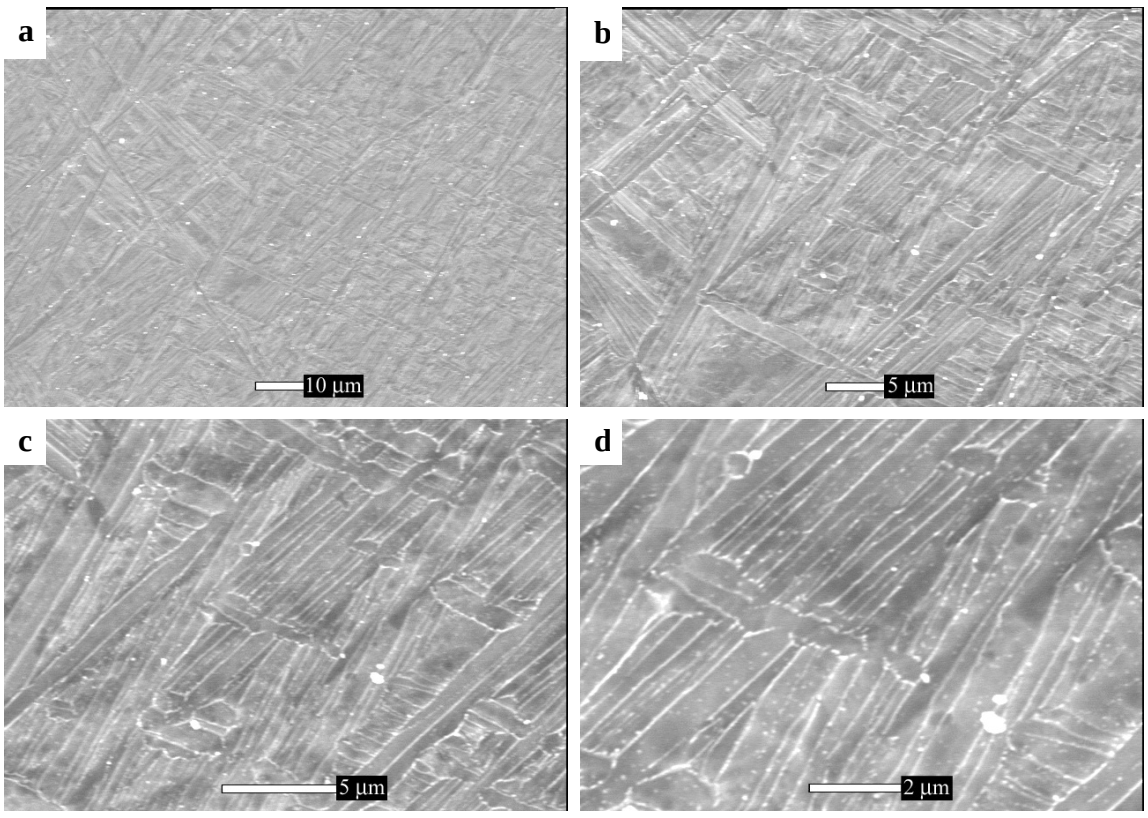

Figure 88: ESEM of the FZ near the top center of the weld in Weld 0. (a) 1000x, (b) 2500x, (c) 5000x, and (d) 10,000x.

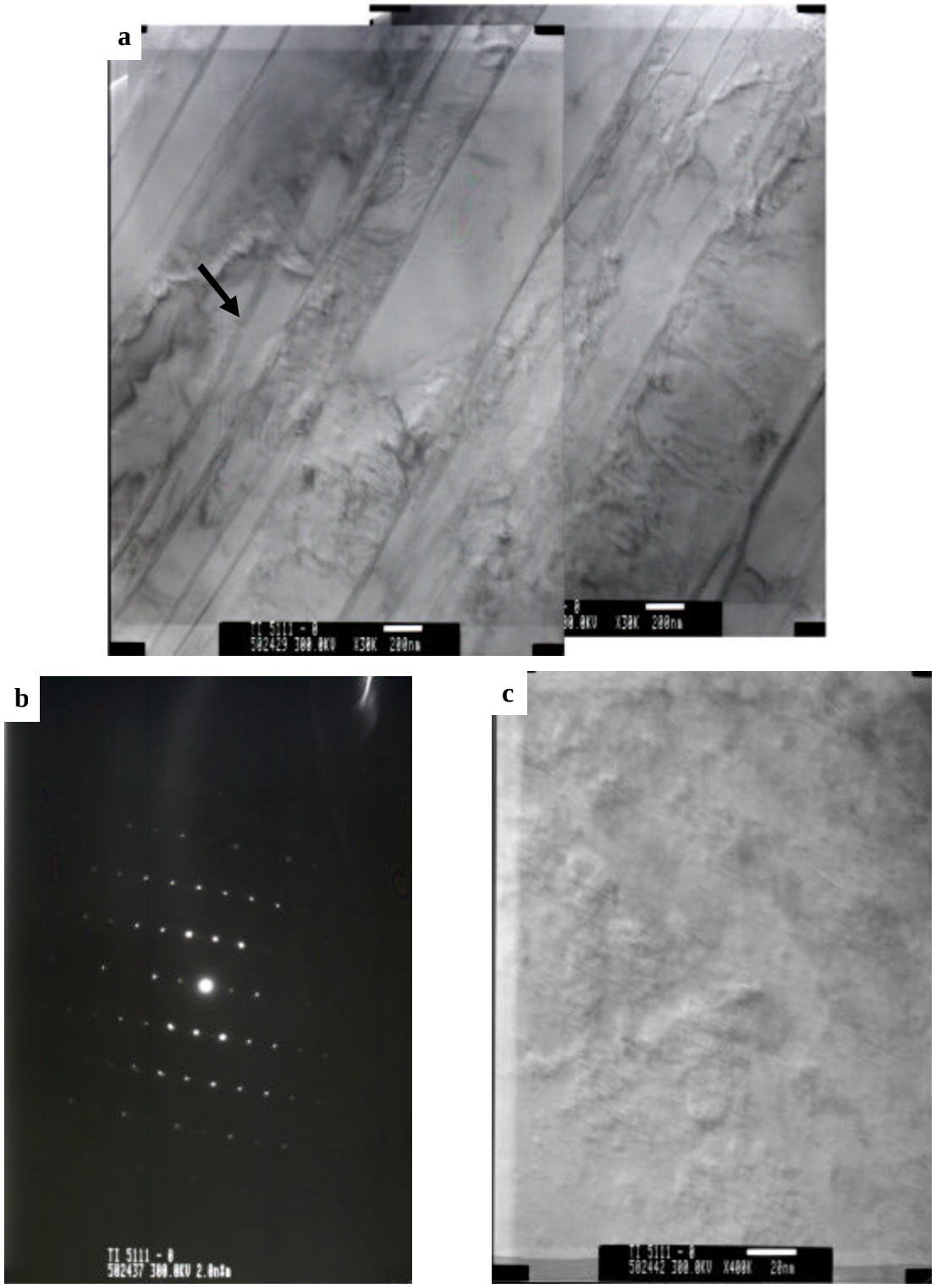

Figure 89: TEM images of FZ near the top center of the weld in Weld 0. (a) Image showing size of the parallel plates of Widmanstätten formed in the FZ. Note very thin remaining plates of β between the large α plates as indicated by arrow. (b) Diffraction pattern from area shown in (a) indicating that the microstructure is Widmanstätten α. (c) High resolution image from area (a) showing no particles exist in area.

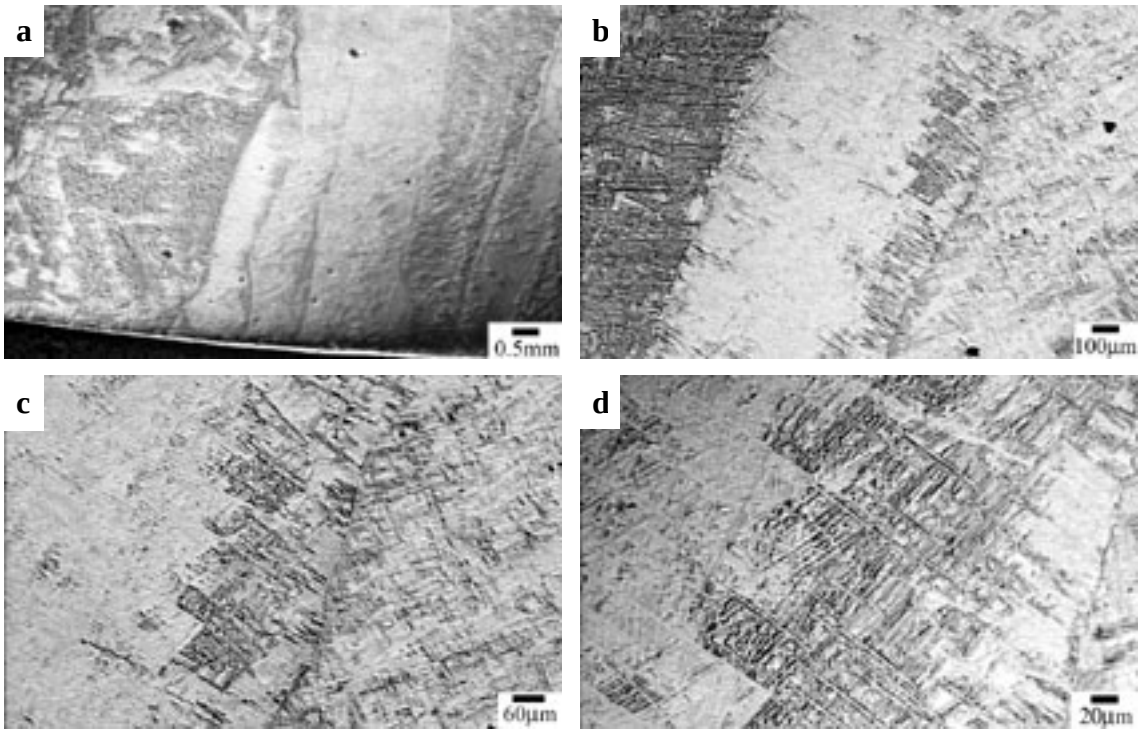

Figure 90: Optical microscopy of the FZ near the top center of the weld in Weld 1. (a) 25x, (b) 125x, (c) 250x, and (d) 625x.

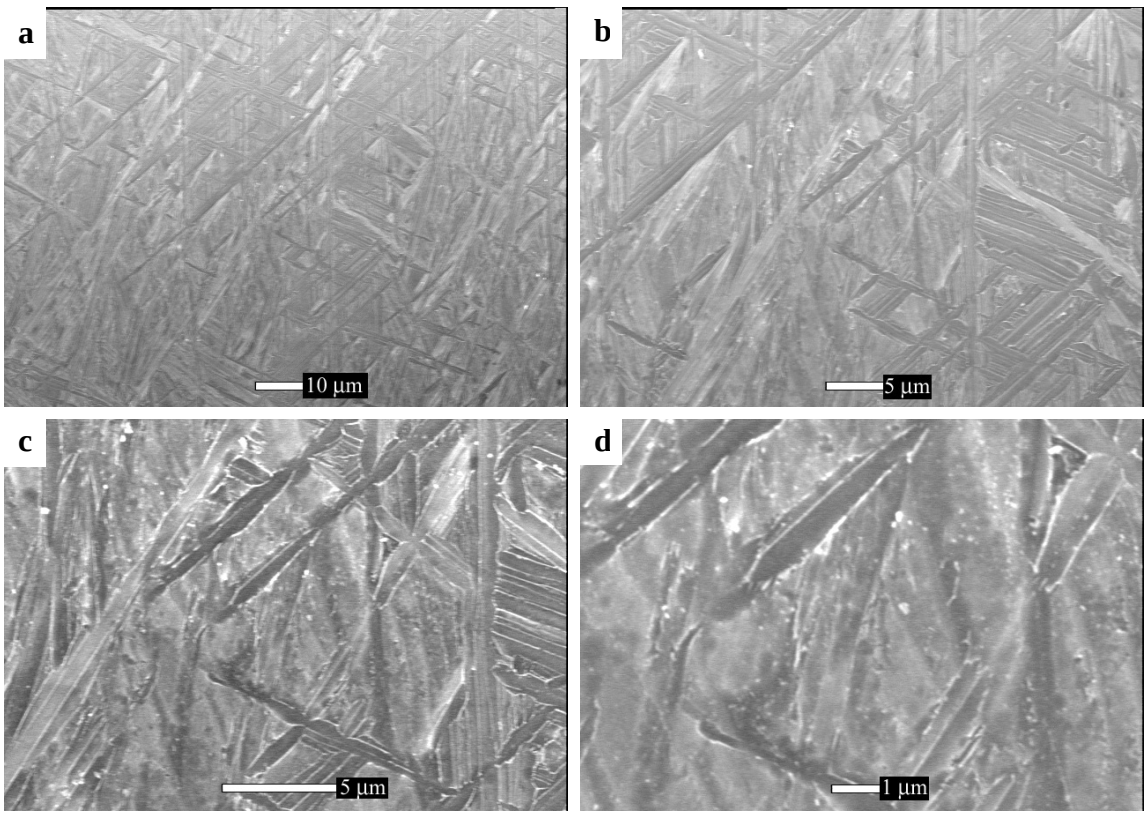

Figure 91: ESEM of the FZ near the top center of the weld in Weld 1. (a) 1000x, (b) 2500x, (c) 5000x, and (d) 10,000x.

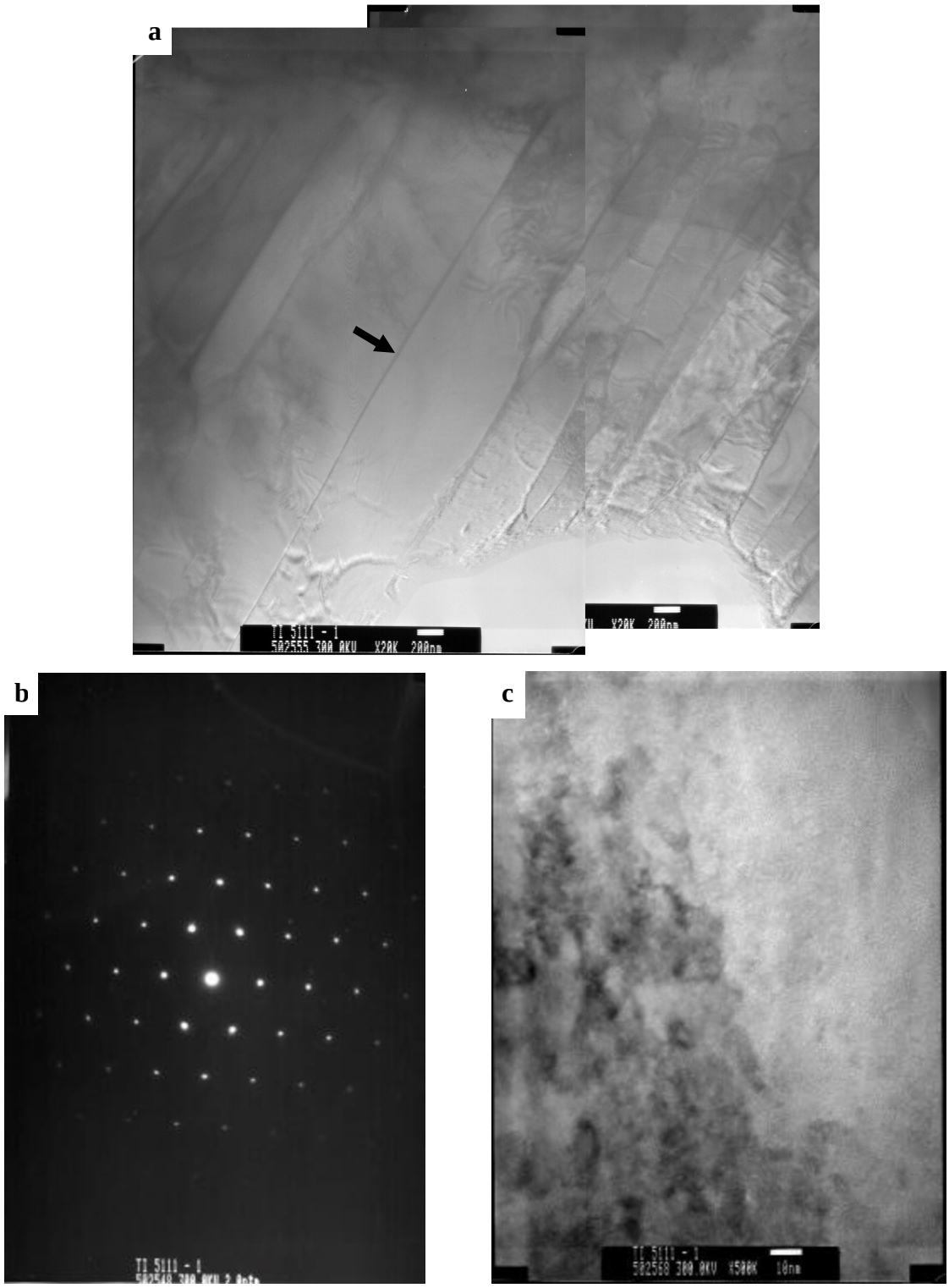

Figure 92: TEM images of FZ near the top center of the weld in Weld 1. (a) Image showing size of the parallel plates of Widmanstätten formed in the FZ. Note remaining thin β plates between large α plates, as pointed out by arrow. (b) Diffraction pattern from area shown in (a) indicating that the microstructure is Widmanstätten α. (c) High resolution image from area where particles exist.

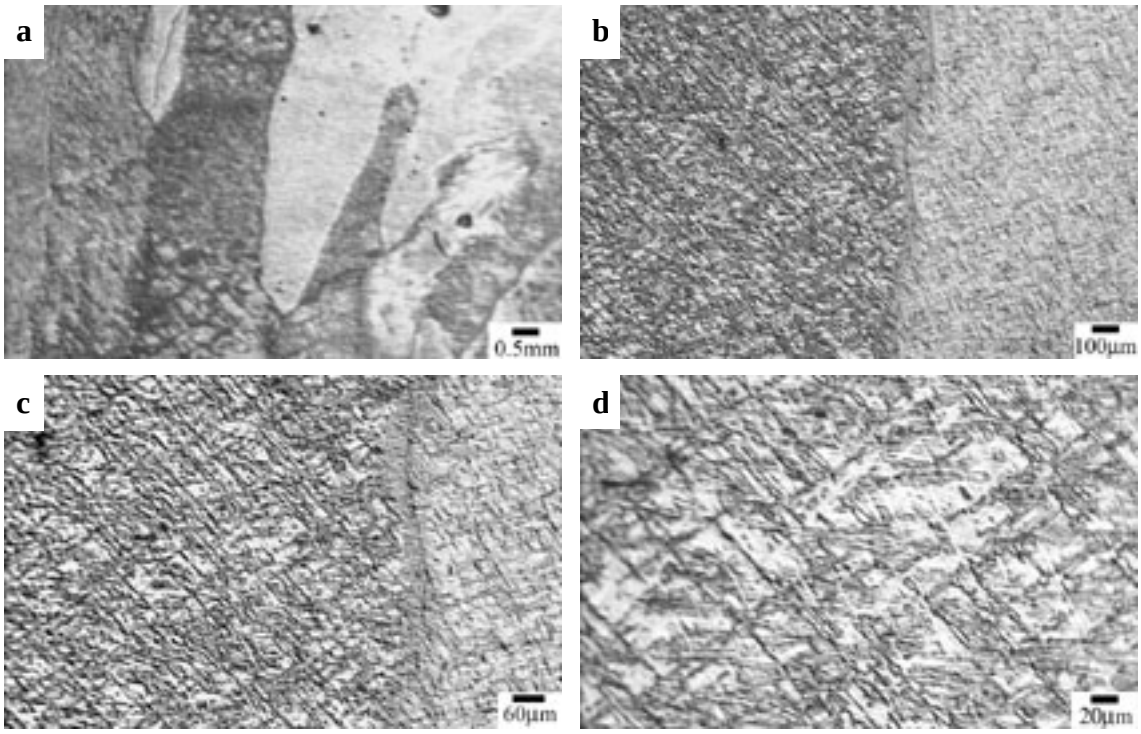

Figure 93: Optical microscopy of the FZ near the top center of the weld in Weld 2. (a) 25x, (b) 125x, (c) 250x, and (d) 625x.

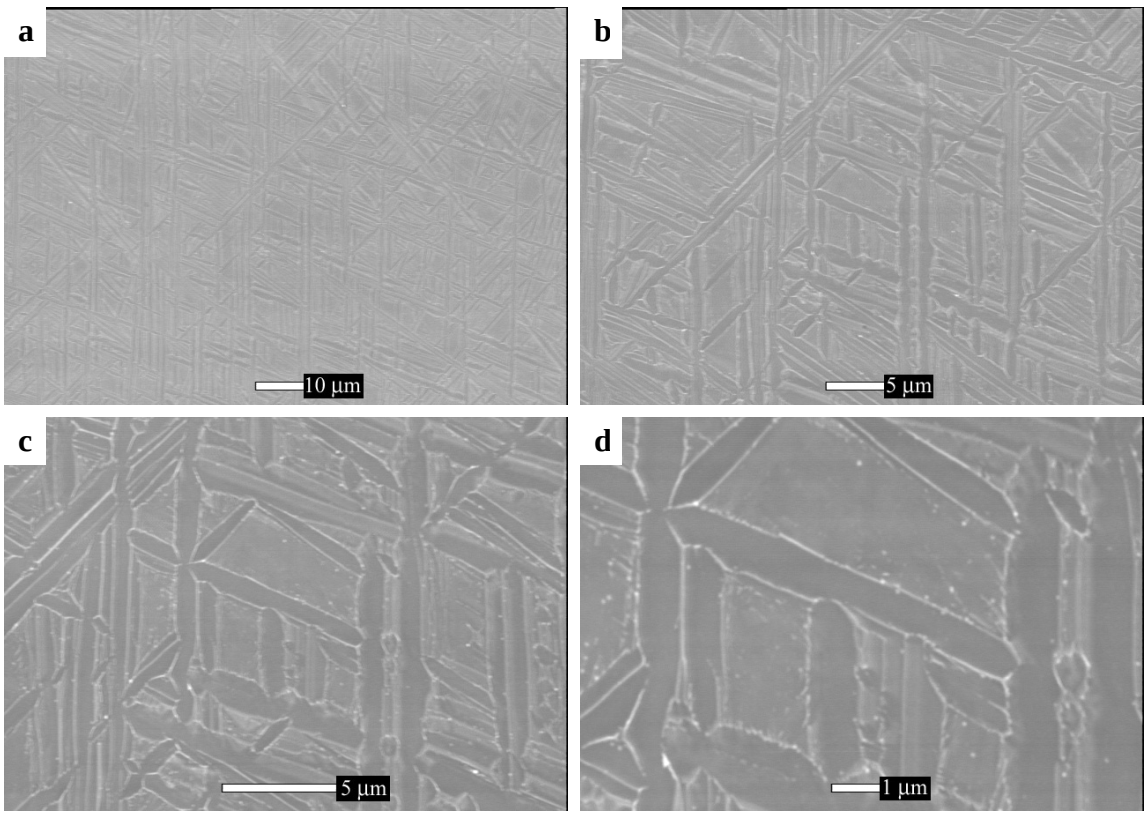

Figure 94: ESEM of the FZ near the top center of the weld in Weld 2. (a) 1000x, (b) 2500x, (c) 5000x, and (d) 10,000x.

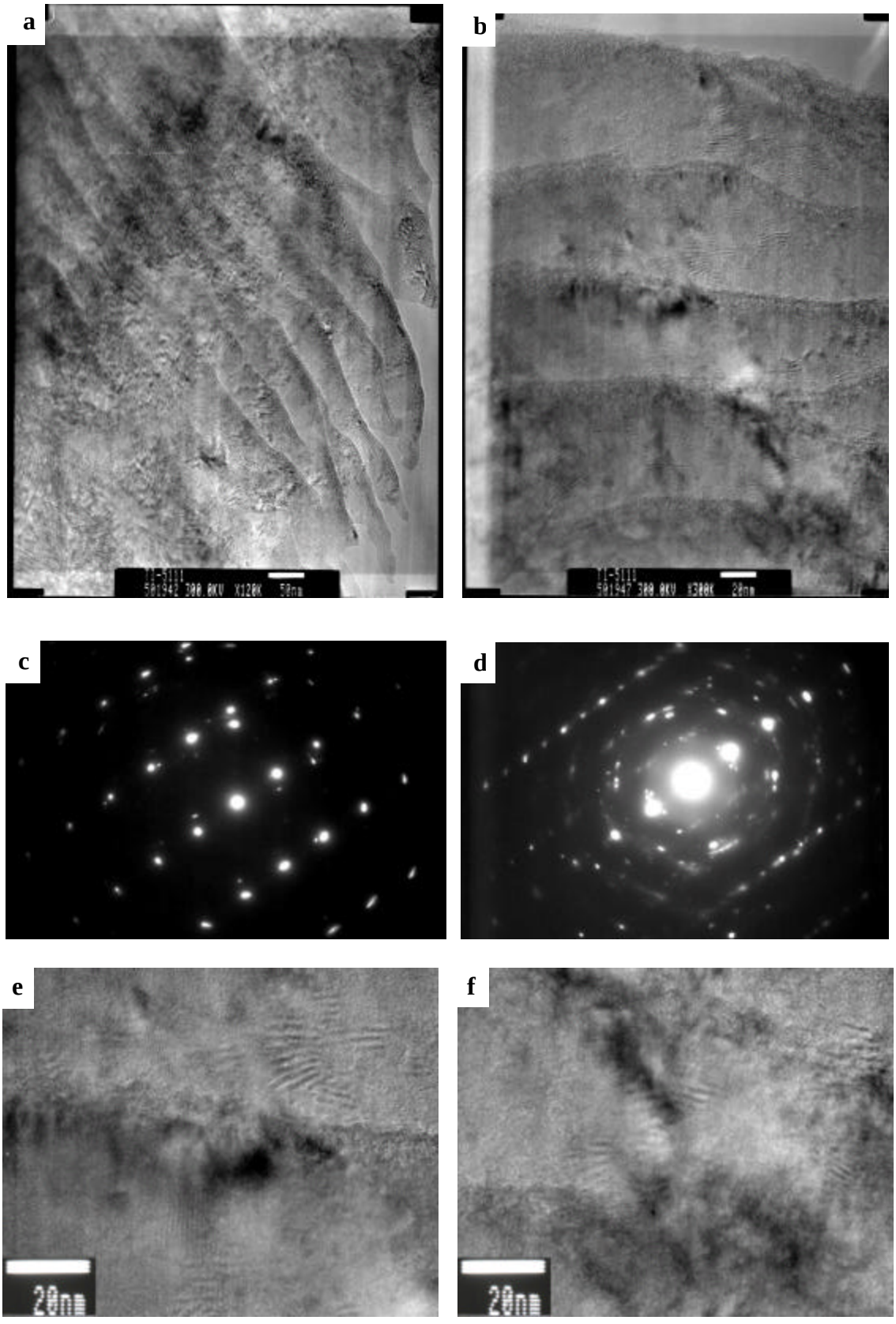
a
b
c
d
e
20nm
f
20nm

Figure 95: (previous page) TEM images of FZ near the top center of the weld in Weld 2. (a) Image showing size of the parallel plates formed in the FZ. Plates are much thinner than those in welds 0 & 1 and no remaining β phase exists between the plates indicating that the transformed structure is martensite. (b) High resolution image from area (a) where particles exist. (c) Diffraction pattern from edge of area shown in (a) indicating that the microstructure is a fully transformed martensitic α′. (c) Diffraction pattern from inside of area shown in (a) indicating that another phase exists. (d) FZ blowup of the center of (b). (e) FZ blowup of the lower right of (b).

size similar to that of Weld 1, there was also quite a few areas where martensite plates existed with their size an average approximate value of 70 nm. These thin martensite plates can be seen in Figure 95a. Note that there is no β phase present at the plate boundaries, which would indicate the presence of Widmanstätten.

Upon examining this martensite area, it was noted that very small nano-particles were present. These particles were on the order of approximately 2-3 nm in size. Occasionally it was seen that the particles seemed to clump together to form a larger particle on the order of approximately 10-15 nm. Figure 95b also shows a high resolution image of both the small and larger particles. Diffraction patterns shown in Figures 95b and 95c from these areas show that an extra phase is present, but a discernible diffraction pattern of the second phase was not able to be produced. It was suspected that the particles formed were of some yttrium containing compound. Measurements of the interplanar spacing between some of these extra spots showed these spots could be from either yttria, yttrium oxide sulfate or yttrium oxysulfide. After finding the particles in Weld 2, they were searched for more thoroughly in Weld 1. The particles were also found there, although not in as great of abundance as in Weld 2, as can be seen in the high resolution TEM image in Figure 92c. A high resolution image was also performed on Weld 0, and is shown in Figure 89c, demonstrating that the particles seen in Welds 1 and 2 are not present. Owing to the very low concentrations of yttrium added to the weld filler metals and the fact that the particles are not necessarily crystollographically aligned with the surrounding matrix, it was no surprise that the particles could not be positively identified through use of selected area diffraction in the TEM.

The FZ HAZ microstructures can be seen in Figures 96-104. Examining these

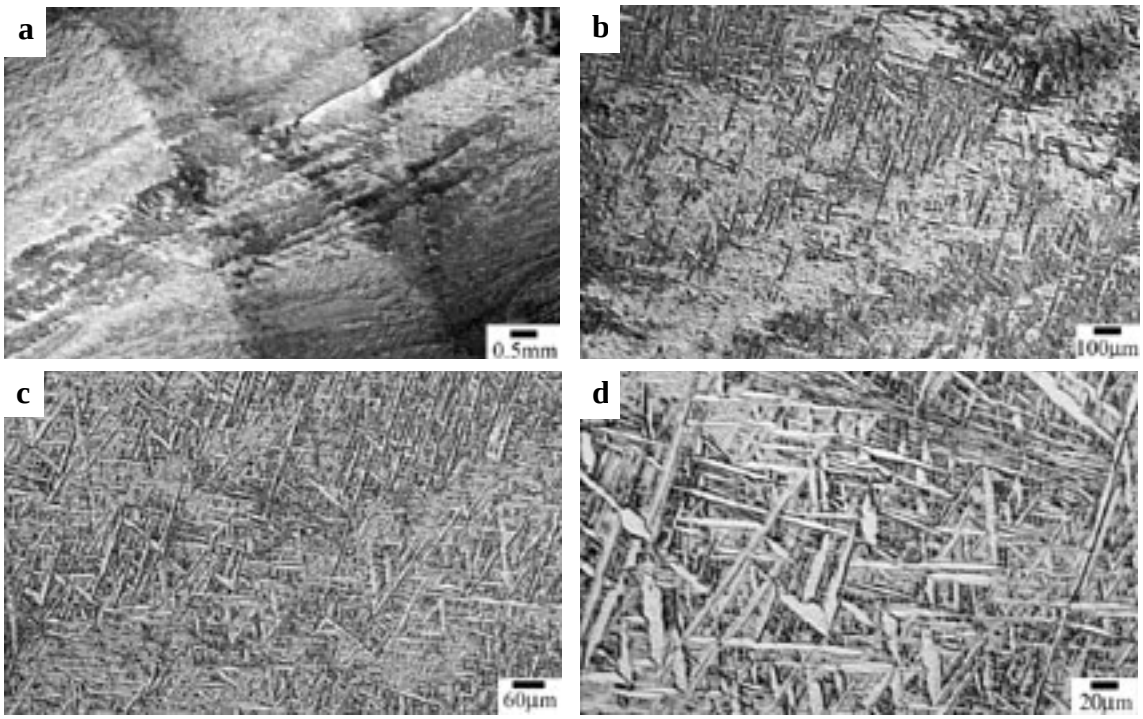

Figure 96: Optical microscopy of the FZ HAZ in Weld 0. (a) 25x, (b) 125x, (c) 250x, and (d) 625x.

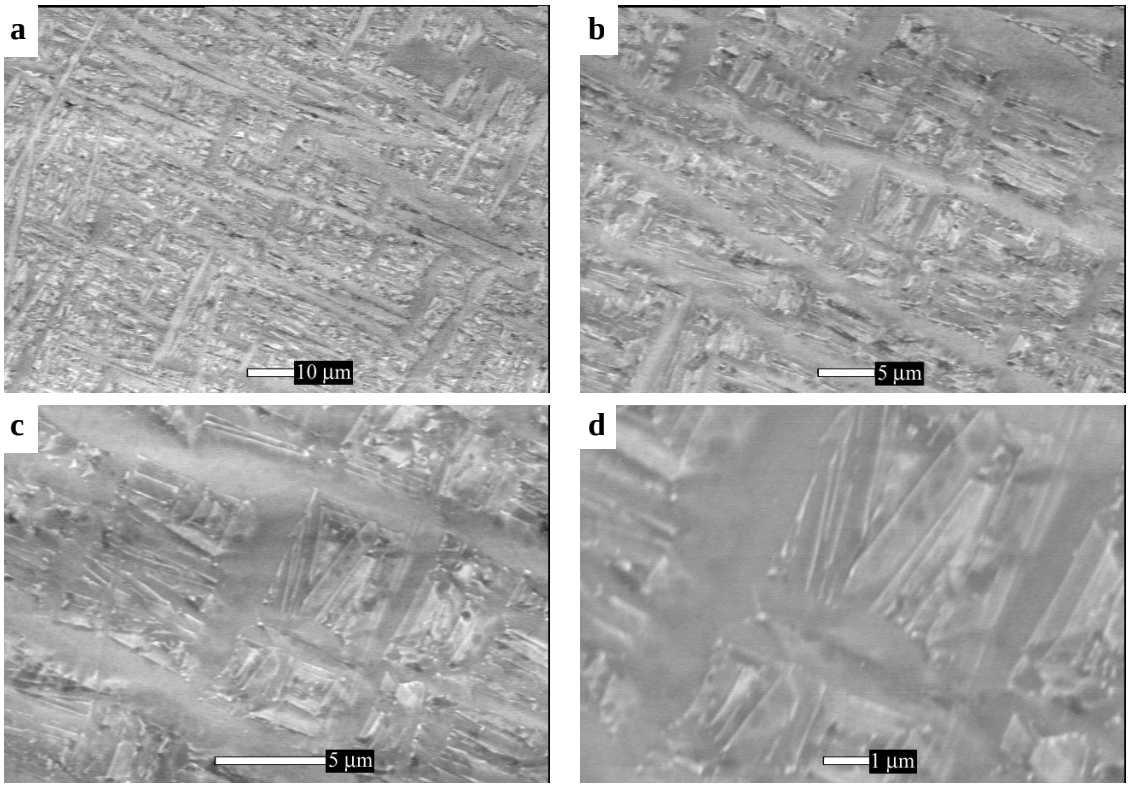

Figure 97: ESEM of the FZ HAZ in Weld 0. (a) 1000x, (b) 2500x, (c) 5000x, and (d) 10,000x.

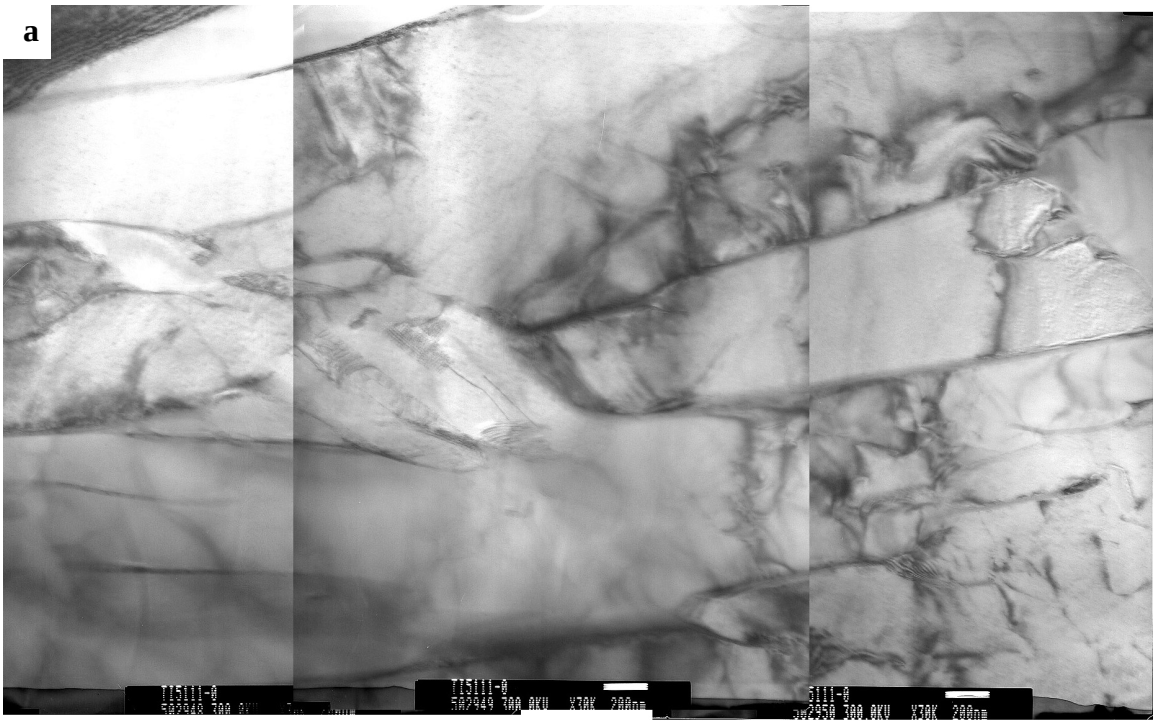

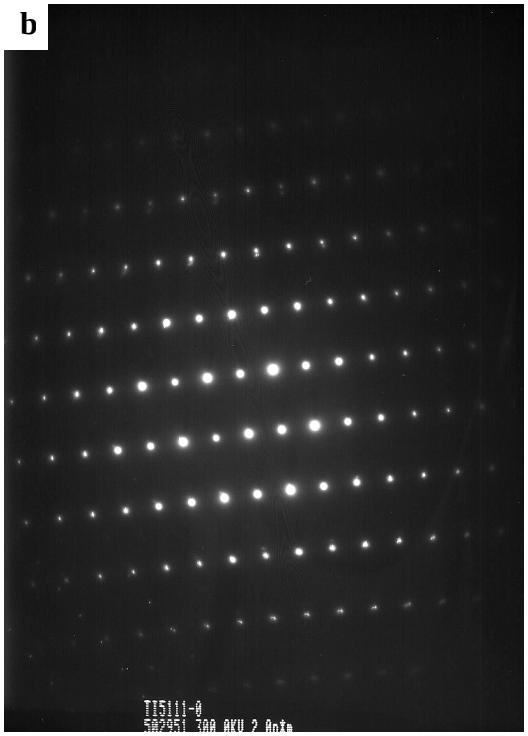

Figure 98: TEM images of Ti5111 Weld 0 FZ HAZ. (a) Image showing plate size and mixed orientation. Note presence of very thin β plates remaining between α plates. (b) Diffraction pattern from area of (a) showing Widmanstätten α structure.

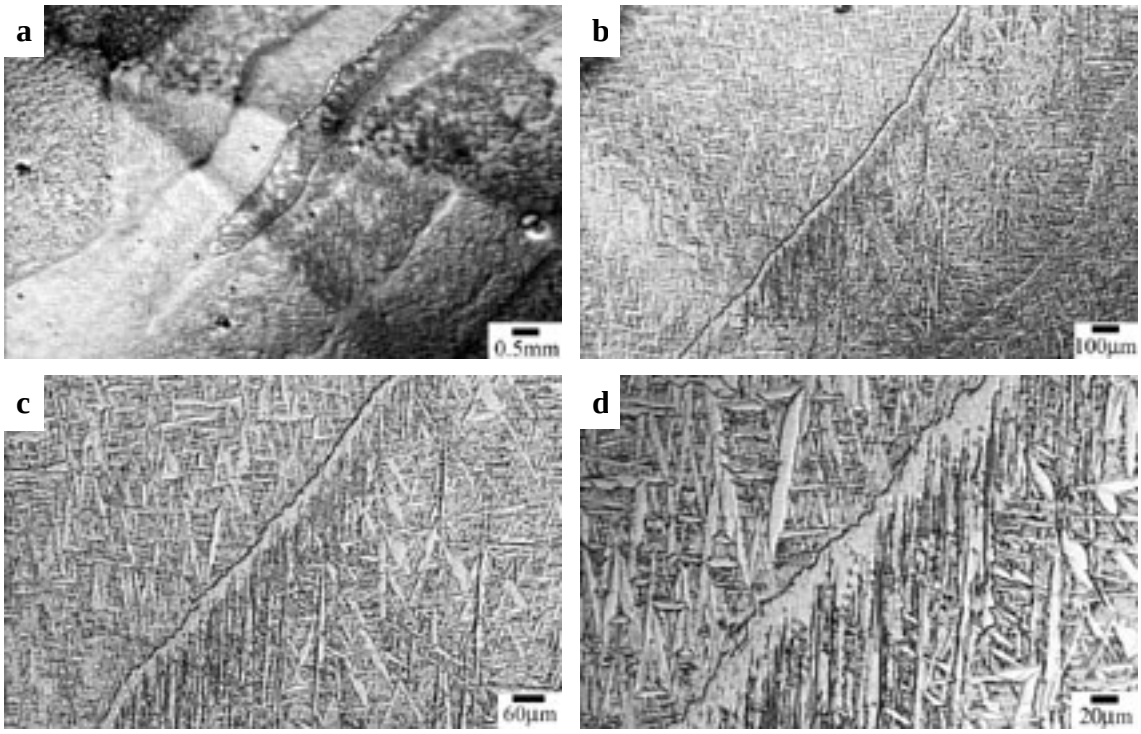

Figure 99: Optical microscopy of the FZ HAZ in Weld 1. (a) 25x, (b) 125x, (c) 250x, and (d) 625x.

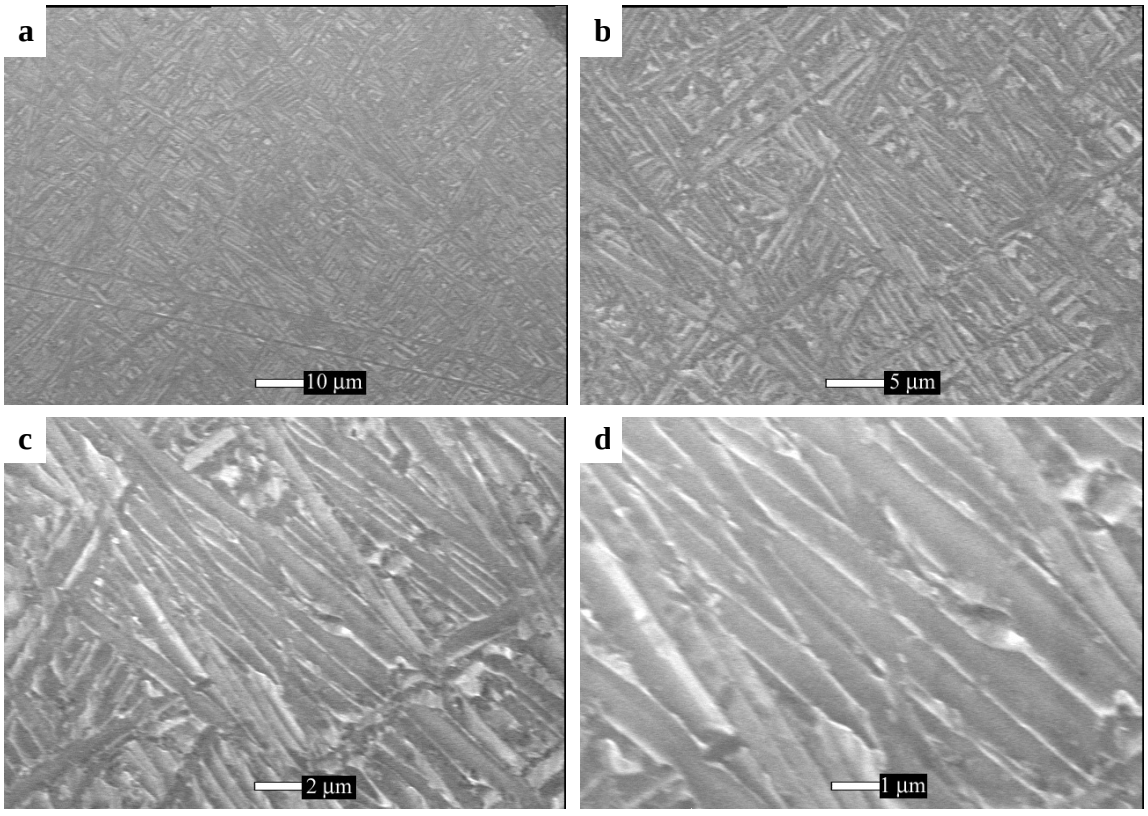

Figure 100: ESEM of the FZ HAZ in Weld 1. (a) 1000x, (b) 2500x, (c) 5000x, and (d) 10,000x.

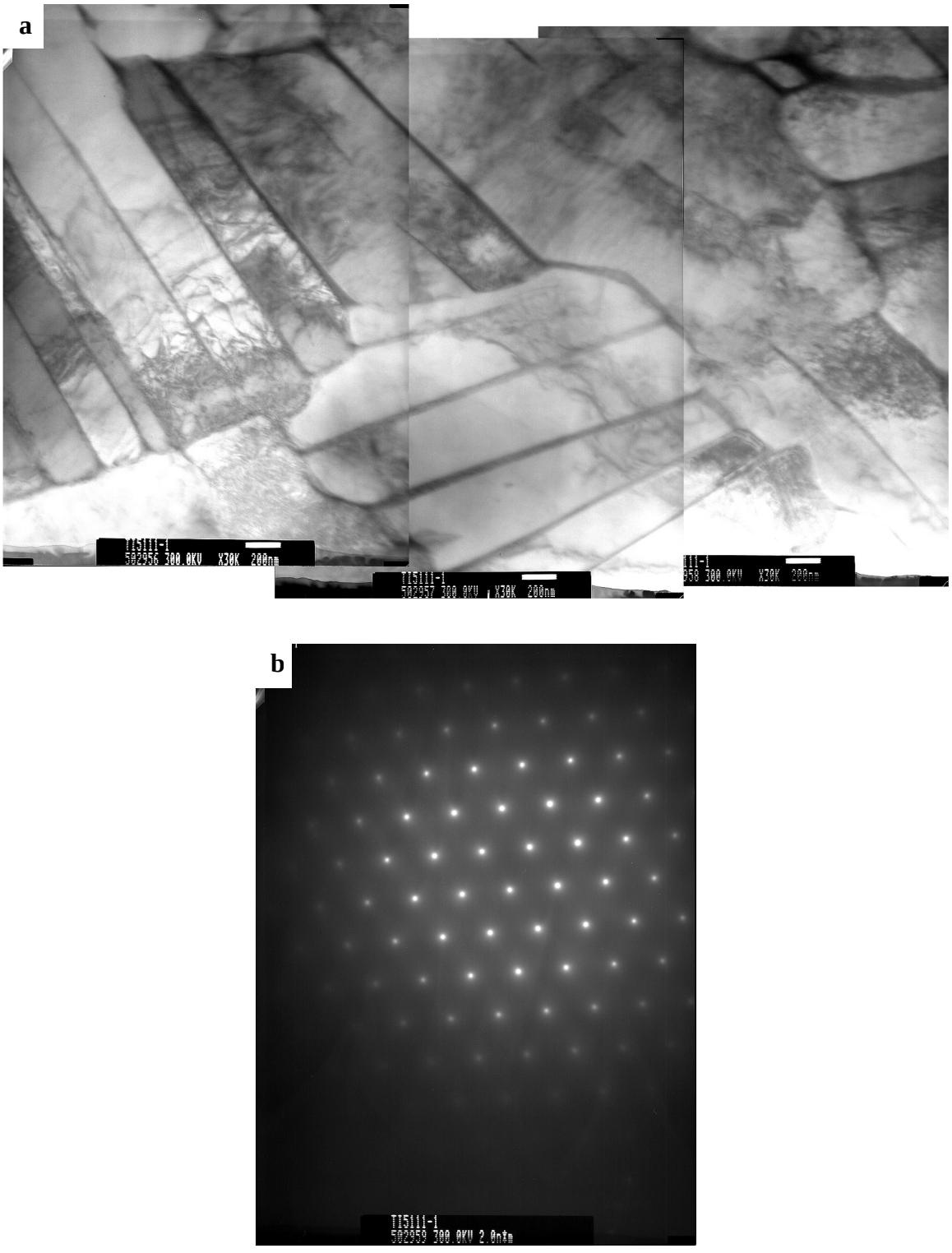

Figure 101: TEM images of Ti5111 Weld 1 FZ HAZ. (a) Image showing plate size and mixed orientation. Note presence of thin β plates remaining between α plates. (b) Diffraction pattern from area of (a) showing presence of Widmanstätten α structure.

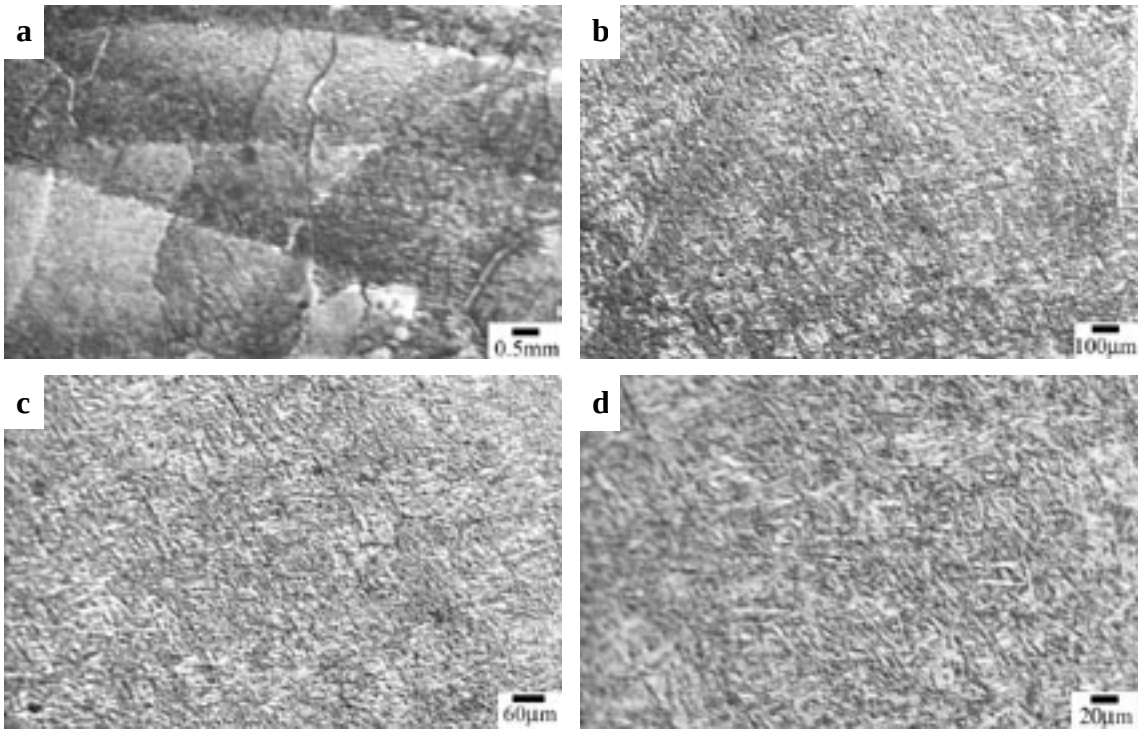

Figure 102: Optical microscopy of the FZ HAZ in Weld 2. (a) 25x, (b) 125x, (c) 250x, and (d) 625x.

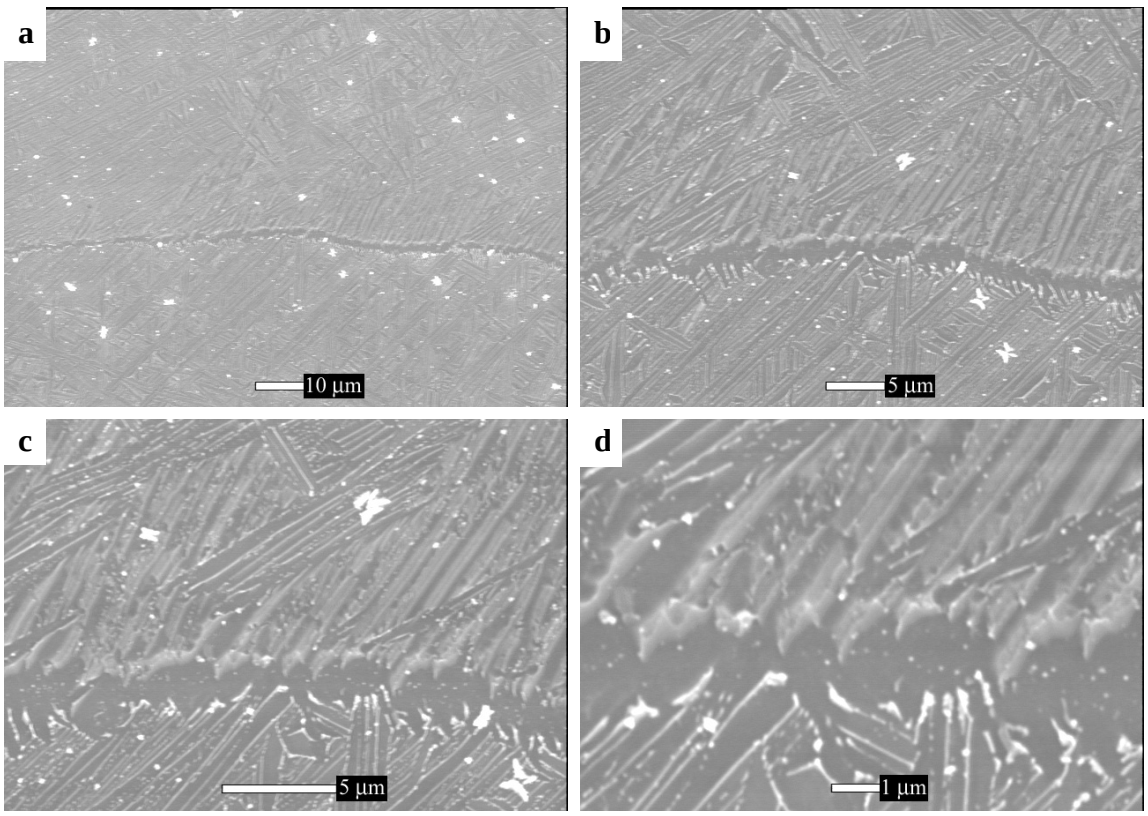

Figure 103: ESEM of the FZ HAZ in Weld 2. (a) 1000x, (b) 2500x, (c) 5000x, and (d) 10,000x. Note presence of particles at prior-β grain boundary.

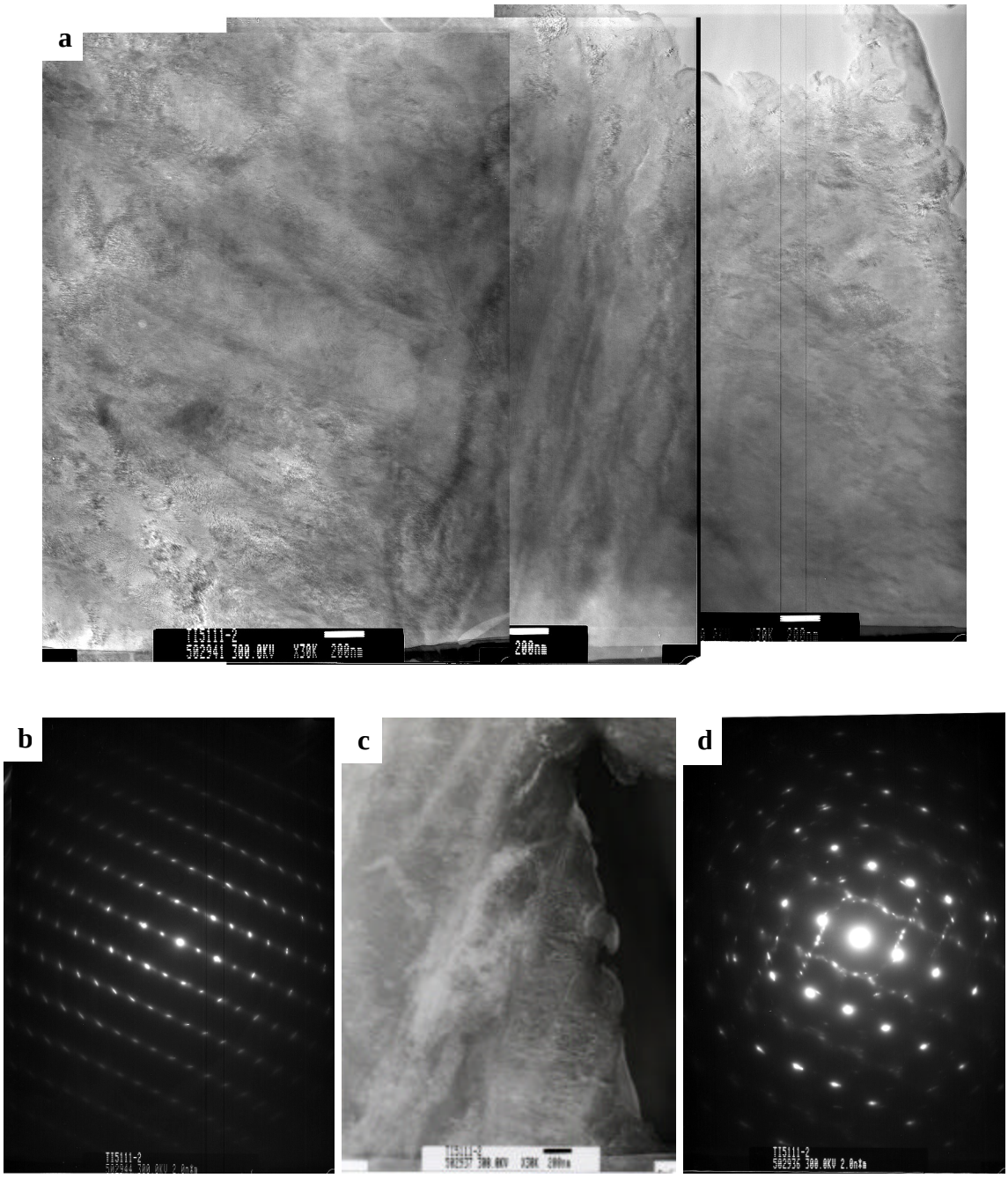

Figure 104: TEM images of Ti5111 Weld 2 FZ HAZ. (a) Image showing plate size and mixed orientation. Note no clear presence of β phase. (b) Diffraction pattern from area of (a) showing martensite α′ presence. (c) Area where small nanoparticles are present. (d) Diffraction pattern from area of (c) showing extra diffraction spots.

figures, it can be seen that the FZ HAZ microstructure is again an acicular basket-weave type Widmanstätten with a slight coarsening of the plates. Imaging by TEM of this area for Welds 0, 1 and 2 can be seen in Figures 98, 101 and 104 respectively. Again a Widmanstätten α structure was found. Particles in the matrix were seen for both Weld 1 and Weld 2, as illustrated in Figure 123c and 123d. The TEM images in Figures 98a, 101a and 104a demonstrate the mixed orientation of the plates as compared to the unaffected FZ and they show the refinement in plate size with increasing yttrium concentration of the welds.

Observing Figure 103, a prior-β grain boundary inside the weld FZ of Weld 2 can be seen. At higher magnifications in the ESEM, a collection of particles could be seen at and around this grain boundary. These particles were much larger than the ones seen inside the weld matrix under TEM. The particles were on the order of approximately 150 nm and were not seen anywhere other than right at and around the prior-β grain boundaries. These particles were not observed in Weld 0, and are therefore believed to be yttrium containing compounds.

The weld microstructures for the root pass can be seen in Figures 105-110. The root pass in a weld is where the weld plates are initially formed together and are therefore subjected to many heat treatments with overlaying passes. Examination of these figures shows a strong basket-weave acicular Widmanstätten α structure. The size of the platelets was approximately the same in all cases, with no noticeable effects of refinement due to yttrium additions. The platelet size did not seem to be as coarsened as the typical FZ HAZ's.

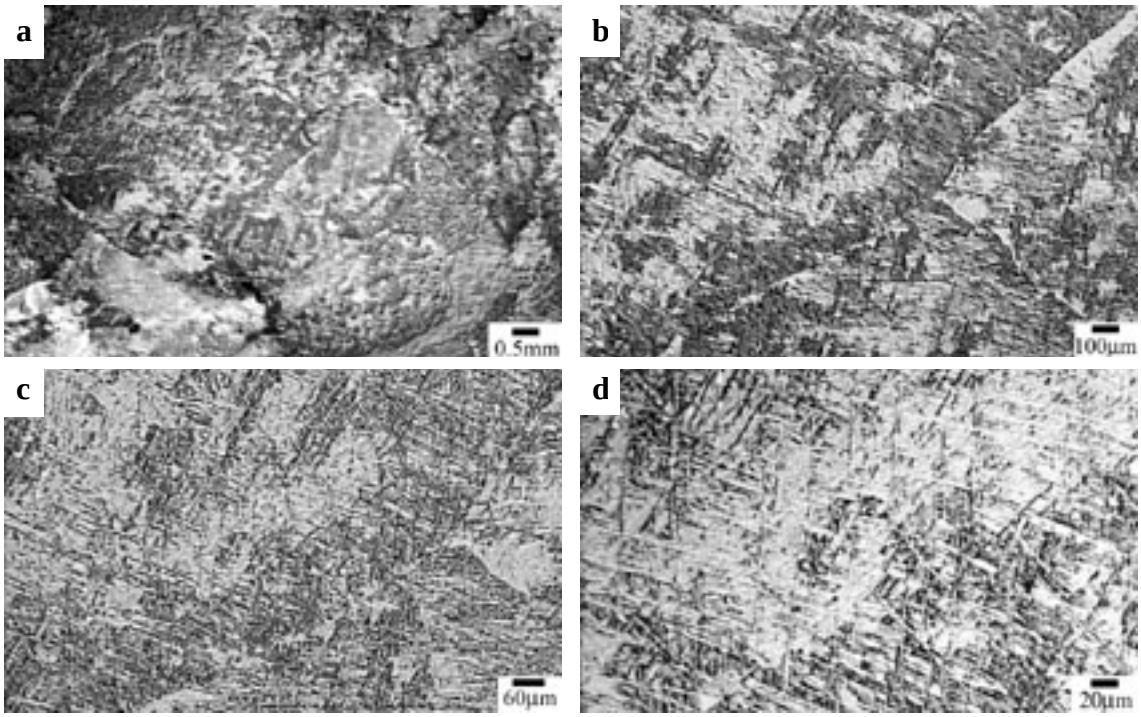

Figure 105: Optical microscopy of the FZ root pass in Weld 0. (a) 25x, (b) 125x, (c) 250x, and (d) 625x.

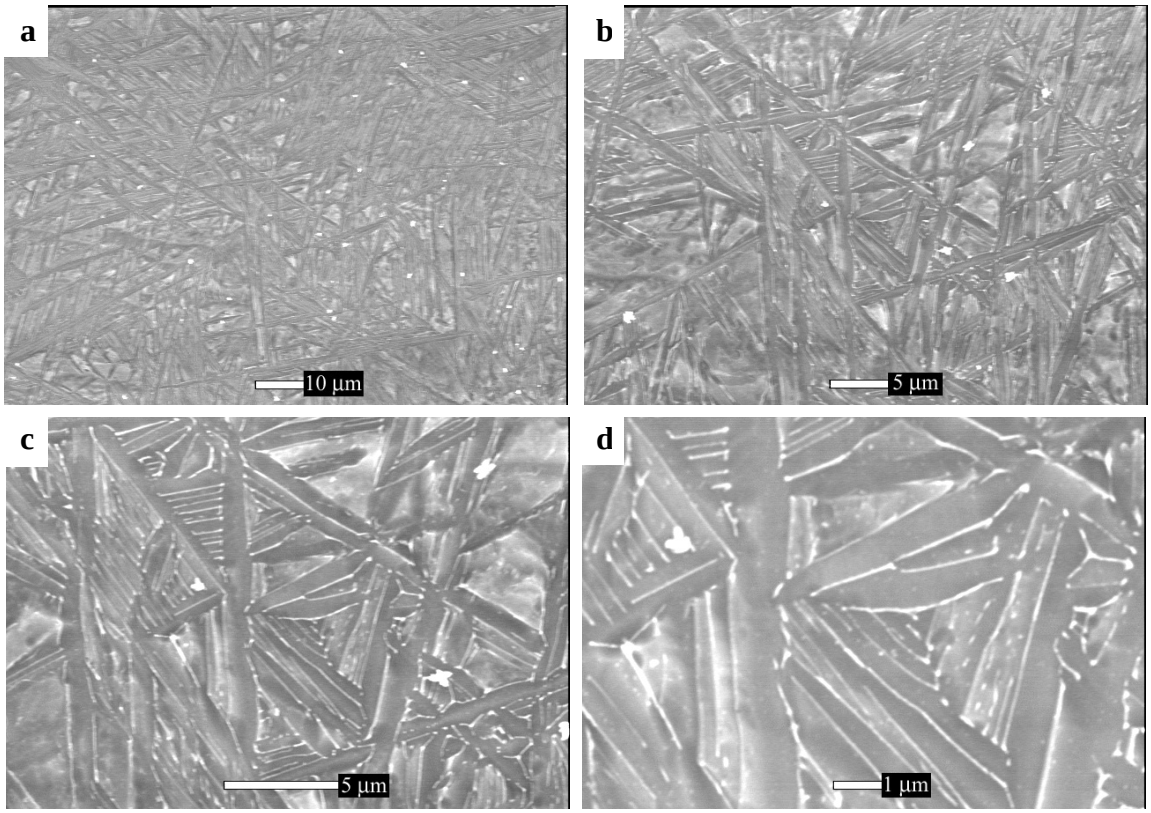

Figure 106: ESEM of the FZ root pass in Weld 0. (a) 1000x, (b) 2500x, (c) 5000x, and (d) 10,000x.

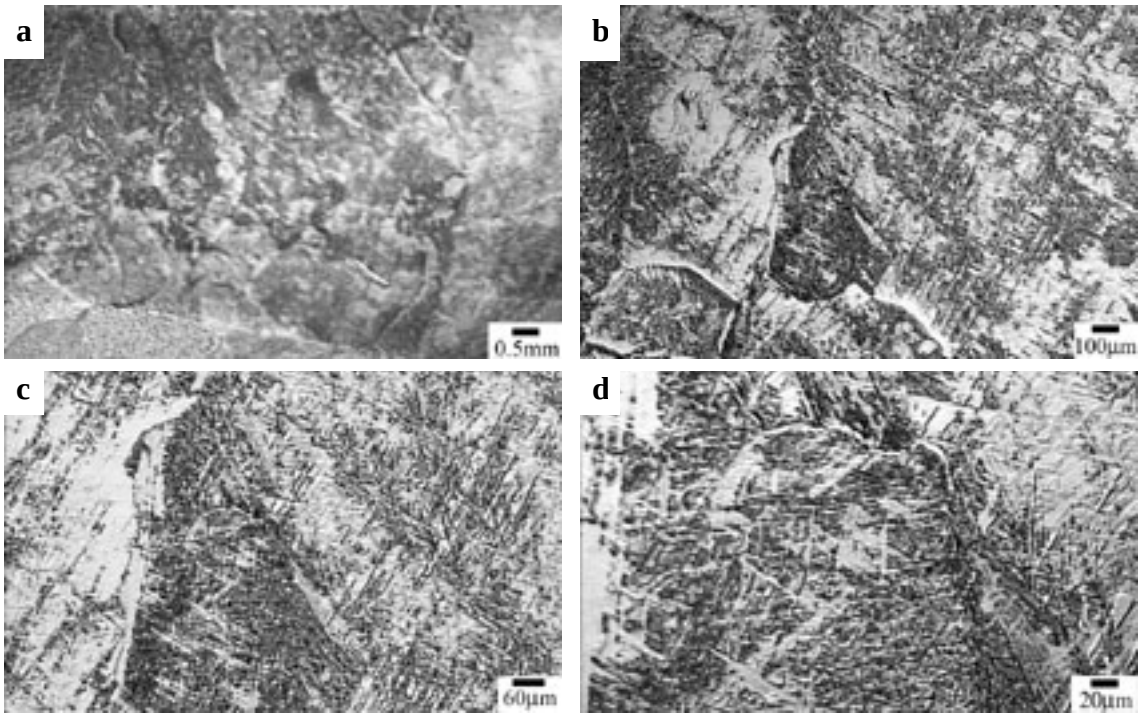

Figure 107: Optical microscopy of the FZ root pass in Weld 1. (a) 25x, (b) 125x, (c) 250x, and (d) 625x.

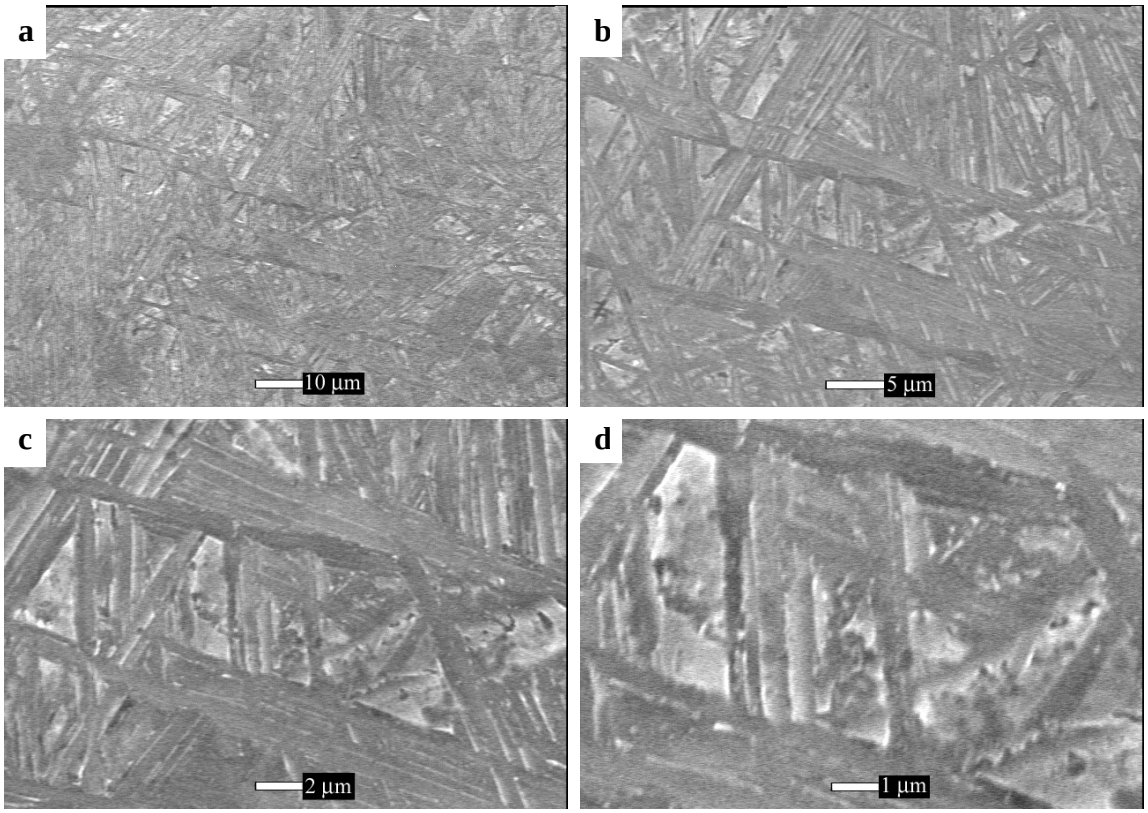

Figure 108: ESEM of the FZ root pass in Weld 1. (a) 1000x, (b) 2500x, (c) 5000x, and (d) 10,000x.

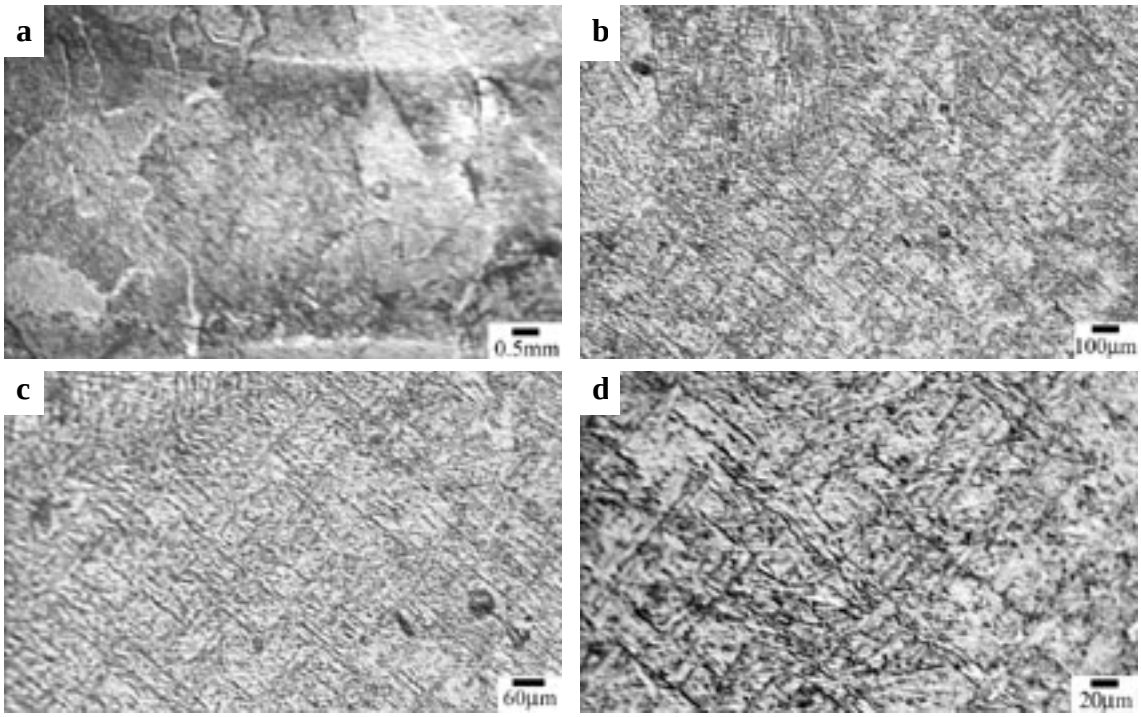

Figure 109: Optical microscopy of the FZ root pass in Weld 2. (a) 25x, (b) 125x, (c) 250x, and (d) 625x.

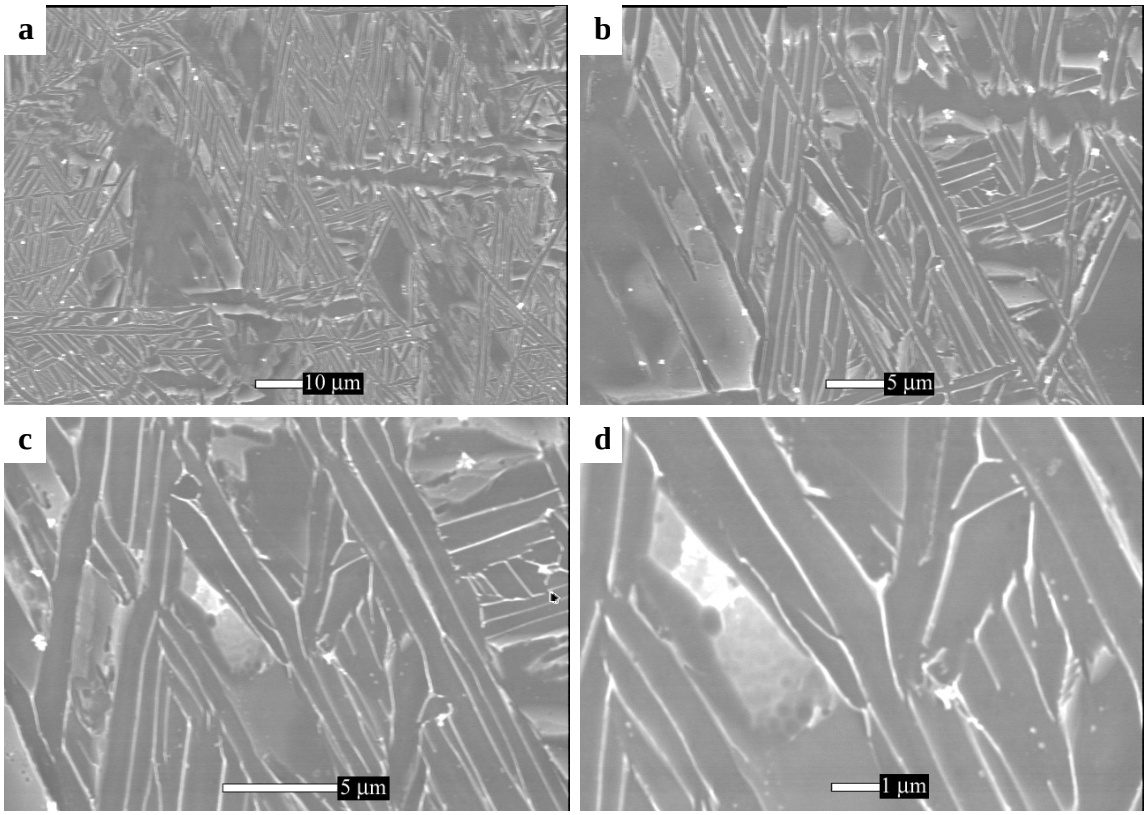

Figure 110: ESEM of the FZ root pass in Weld 2. (a) 1000x, (b) 2500x, (c) 5000x, and (d) 10,000x.

When we compare the microstructures with the microhardness mapping done in Chapter IX, we can see some correlations. The harder areas of the weld exhibit the basket-weave Widmanstätten structure. Where the hardest areas are often seen at the root pass, the most random, tight, basket-weave martensite was found. Other hard areas of the weld including the BM near HAZ and FZ HAZ exhibited a more pronounced degree of basket-weave Widmanstätten, as compared to the unaffected HAZ and BM. The basket-weave Widmanstätten is believed to be formed due to the fact that more nucleation sites are available in the BM and lower portion of the weld zone as compared to the upper portions of the weld zone. This increased opportunity for nucleation in the solid phase results in a mixed orientation acicular Widmanstätten structure. These mixed orientation structures are thereby able to resist deformation to a higher degree than the areas of the weld where the plates exist in colony-type structures. This leads to increased values of hardness and strength. Heat from each weld pass will also have an effect on the microstructure through coarsening effects.

XI. X-RAY PHOTOELECTRON SPECTROSCOPY (XPS)

XI.1 Introduction

X-ray photoelectron spectroscopy (XPS) was performed on Welds 1 & 2 in order to determine whether the small particles seen using TEM were yttria particles inside the weld FZ or some other species. The XPS was performed using a highly sensitive Kratos AXIS 165 spectrometer that is fully computer controlled and capable of imaging with Windows based Vision software.

XPS is a technique that uses x-rays to knock electrons out of inner shell orbitals in an atom. The kinetic energy (E_e) of these photoelectrons is determined based on the photon energy ($h\nu$), the binding energy of the electron (E_B) and a very small correction factor based on recoil energy of the photoelectron (r_e) and a work function (w) based on the type of material the spectrometer is constructed from [42]. This equation is expressed as:

$$E_B = h\nu - E_e - [-w + r_e] \quad (17)$$

That is, the binding energy for a given orbital, either molecular or atomic, is the difference in total energy between the initial and final states of the system that results from one electron having been removed from that orbital. These electron binding energies are dependent upon the chemical environment of the atom, thereby making XPS useful to identify oxidation states and ligands of an atom.

XI.2 Results and Discussion

The XPS scans performed on Welds 1 & 2 can be seen in Figures 111-117. Overall spectrum scans for Welds 1 & 2 are shown in Figures 111 and 114 respectively. The binding energy ranges where yttrium (Y) 3d 5/2 (binding energy ~ 156 eV [43], yttria (Y_2O_3) 3d 5/2 (double peaks at ~ binding energies of 157 and 158.6 eV [43]) and yttrium sulfate ($Y_2(SO_4)_3$) 3d 5/2 (binding energy of ~ 159 eV [43]) and 2p 3/2 (binding energy ~ 170 [43]) peaks should be located are shown in Figures 112 and 115 for Welds 1 & 2 respectively. Examining these figures, it can be seen that there are clearly peaks associated with the yttrium sulfate and no clear peaks for yttria. Deconvolution of the data shows peaks at ~156 eV and ~170 eV, clearly a result of Y and Y-SO_4 binding energies respectively. It may be that there is a Y-O peak associated with the hump at ~157 eV, but this is uncertain. The peak for yttrium itself can be seen to be combined with a peak of SiO_2, but nonetheless is definitely present. In order to confirm this, the yttrium 3p 3/2 (binding energy ~ 299 eV [43]) peak was examined for and was found to clearly exist, as shown in Figures 113 and 116 for Welds 1 & 2 respectively. Yttrium sulfate peaks obtained in this study were compared to those obtained by Vasquez [44] and were found to favorably compare. The O1s peak obtained for Weld 2 can be seen in Figure 117. Although there may be many oxides present, the tail end of the peak from 530 to 535 eV seems to correspond with what Vasquez saw for a peak when only analyzing for $Y_2(SO_4)_3$. Deconvolution of the data does show a peak at 533 eV, which corresponds to Y-SO_4.

Based on the results of XPS, it is concluded that instead of the expected yttria particles, some type of yttrium sulfate was present. It is believed that the particles are likely that of yttrium oxide sulfate ($Y_2O_2SO_4$) and will be discussed more fully in the

final discussion of results section. As a note however, the Gibbs energy of formation at 300 K for yttrium sulfate is -3626.5 kJ/mole [45]. This is compared to the Gibbs energies of formation for yttria and titanium dioxide at 300 K, which are -1816.6 and -884.5

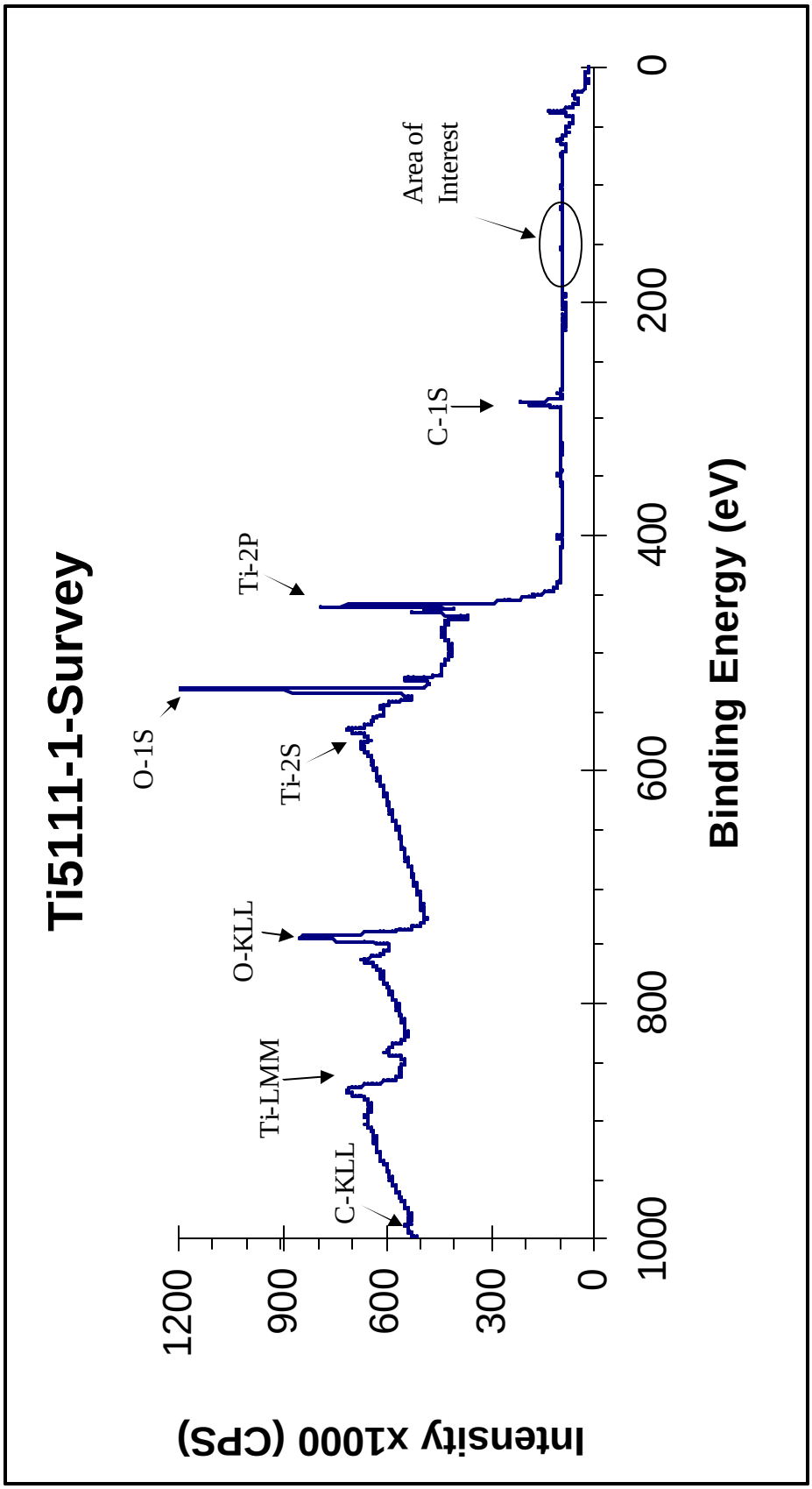

Figure 111: XPS scan of Weld 1 FZ showing overall spectrum.

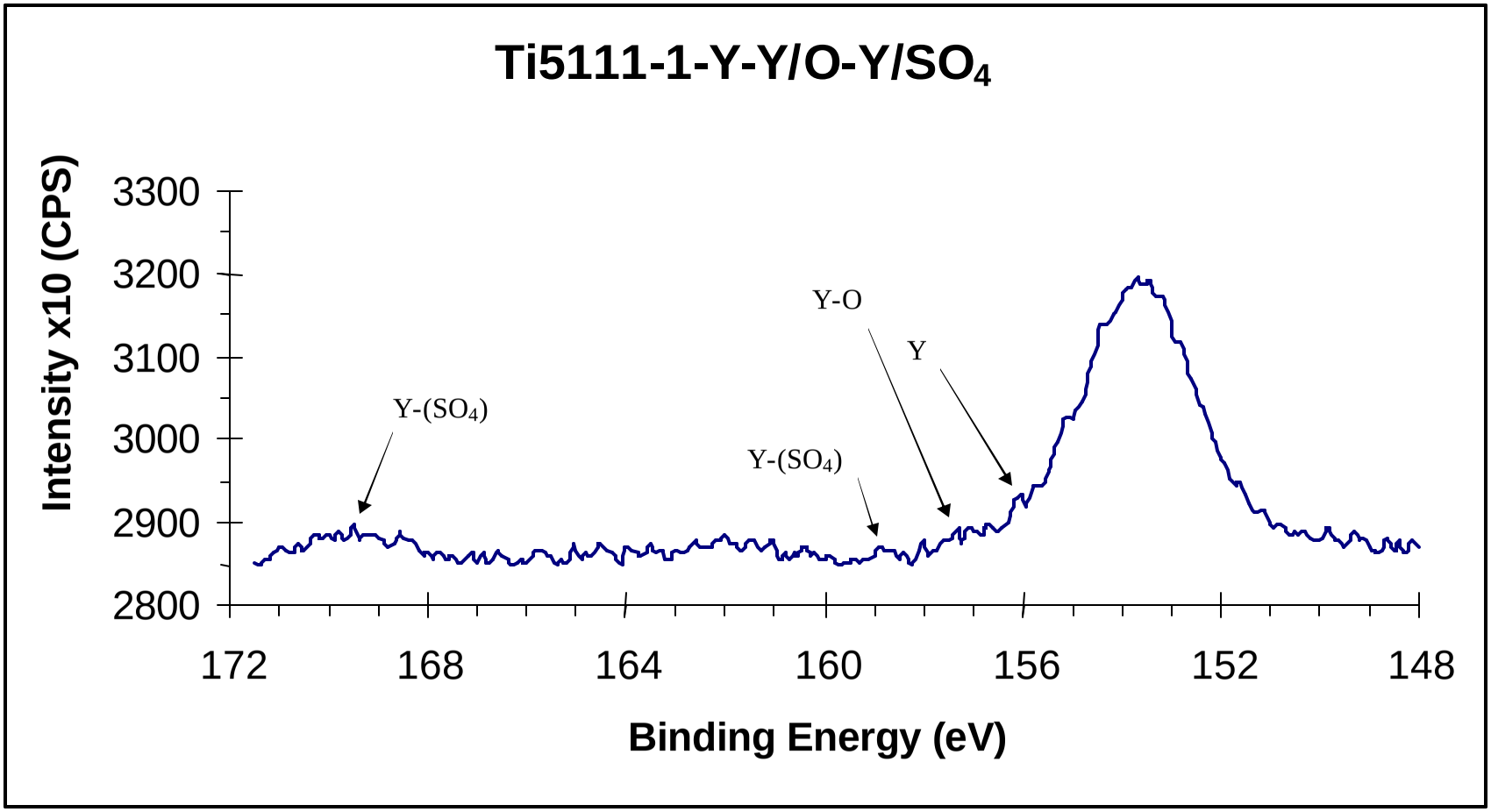

Figure 112: XPS scan of Weld 1 FZ showing the area where the Y 3d 5/2 and $Y_2(SO_4)_3$ 3d 5/2 and 2p 3/2 peaks are located. No clearY_2O_3 peaks were detected, but there may be a Y-O peak association at ~157 eV. Note background counts subtracted.

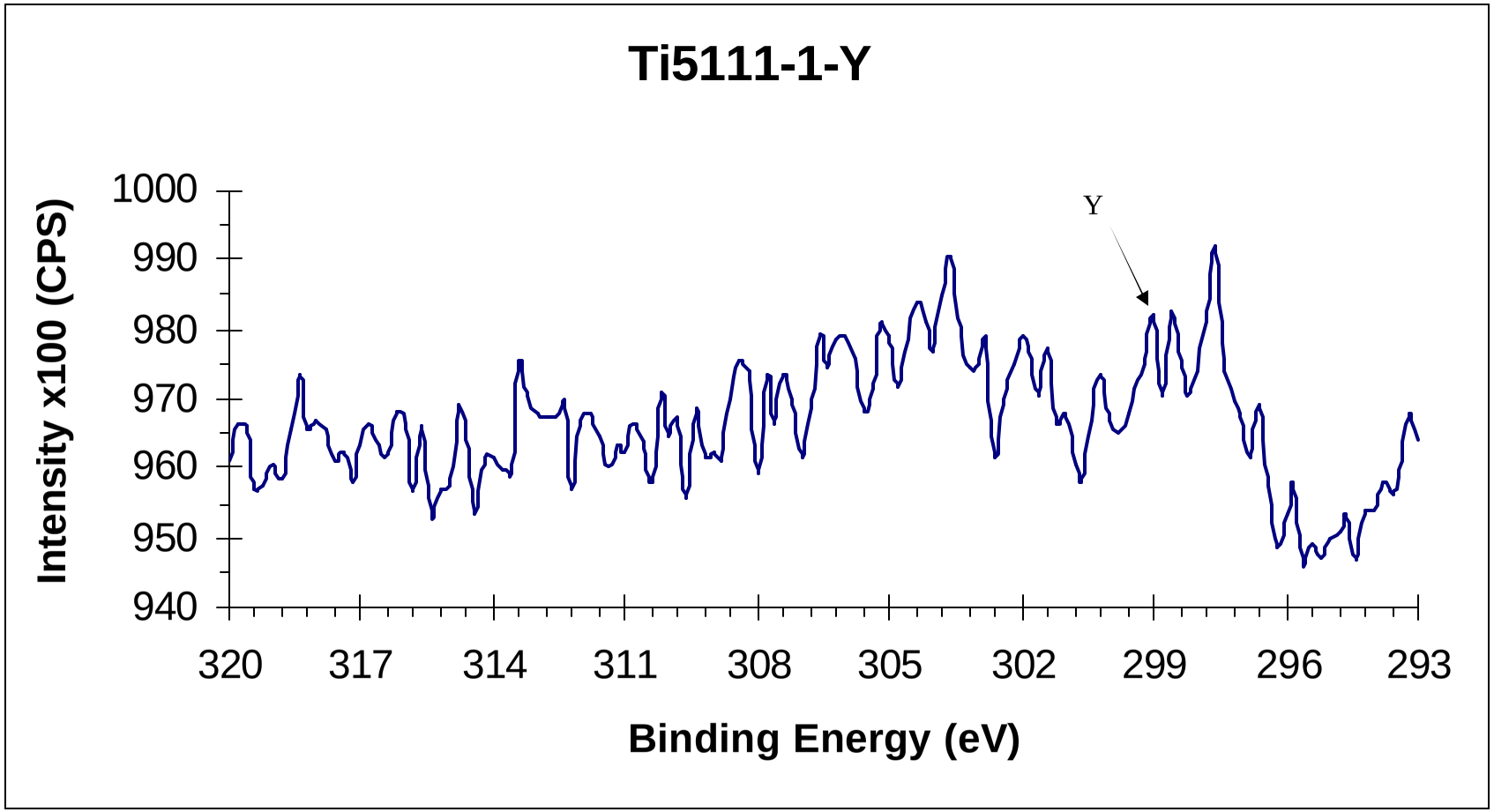

Figure 113: XPS scan showing enlargement of area in Figure 83 where the Y 3p 3/2 peak is present. Note background counts subtracted.

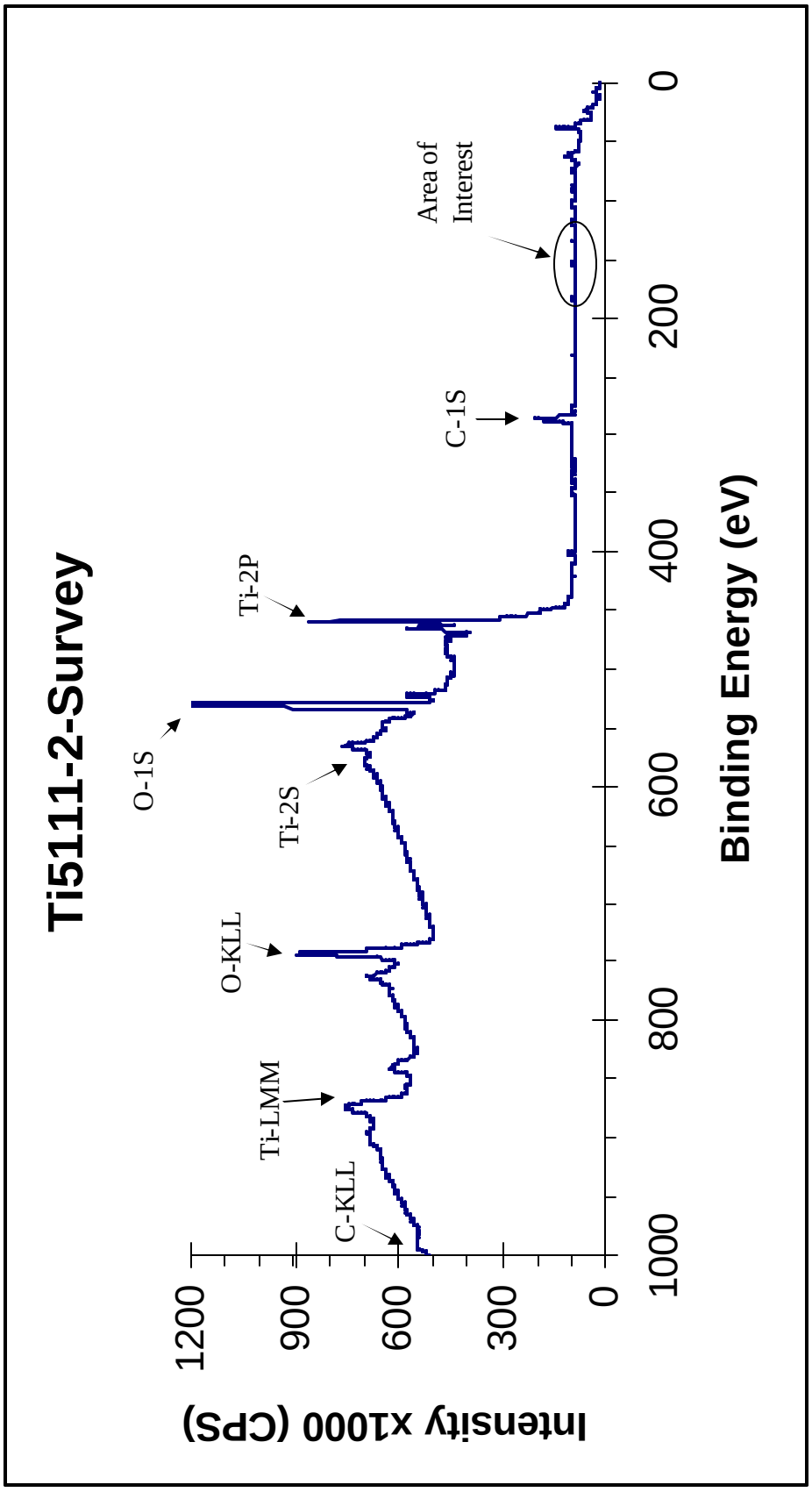

Figure 114: XPS scan of Weld 2 FZ showing overall spectrum.

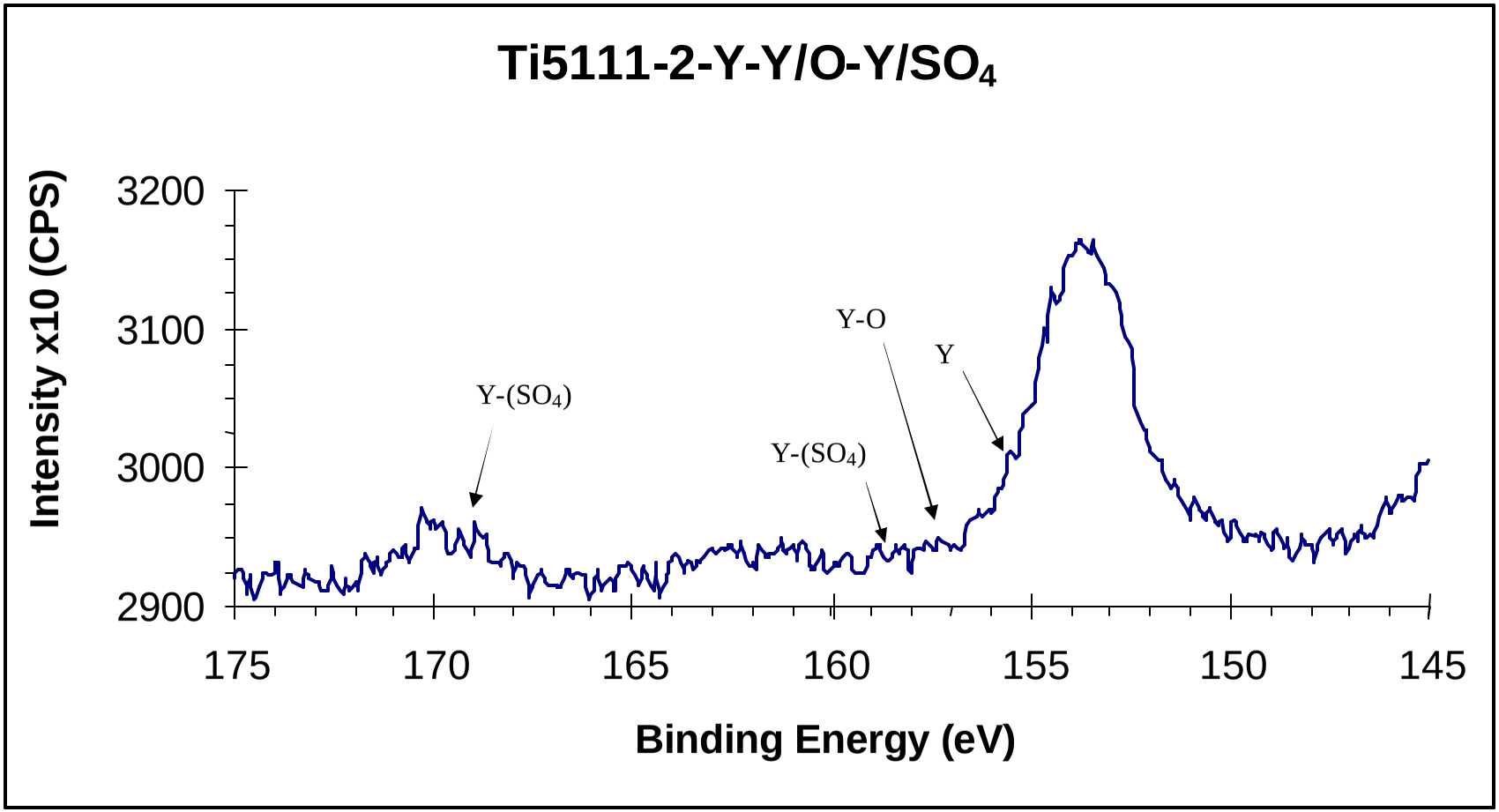

Figure 115: XPS scan of Weld 2 FZ showing the area where Y 3d 5/2 and $Y_2(SO_4)_3$ 3d 5/2 and 2p 3/2 are located. No clear Y_2O_3 peaks were detected, but there may be a Y-O peak association at ~157 eV. Note background counts subtracted.

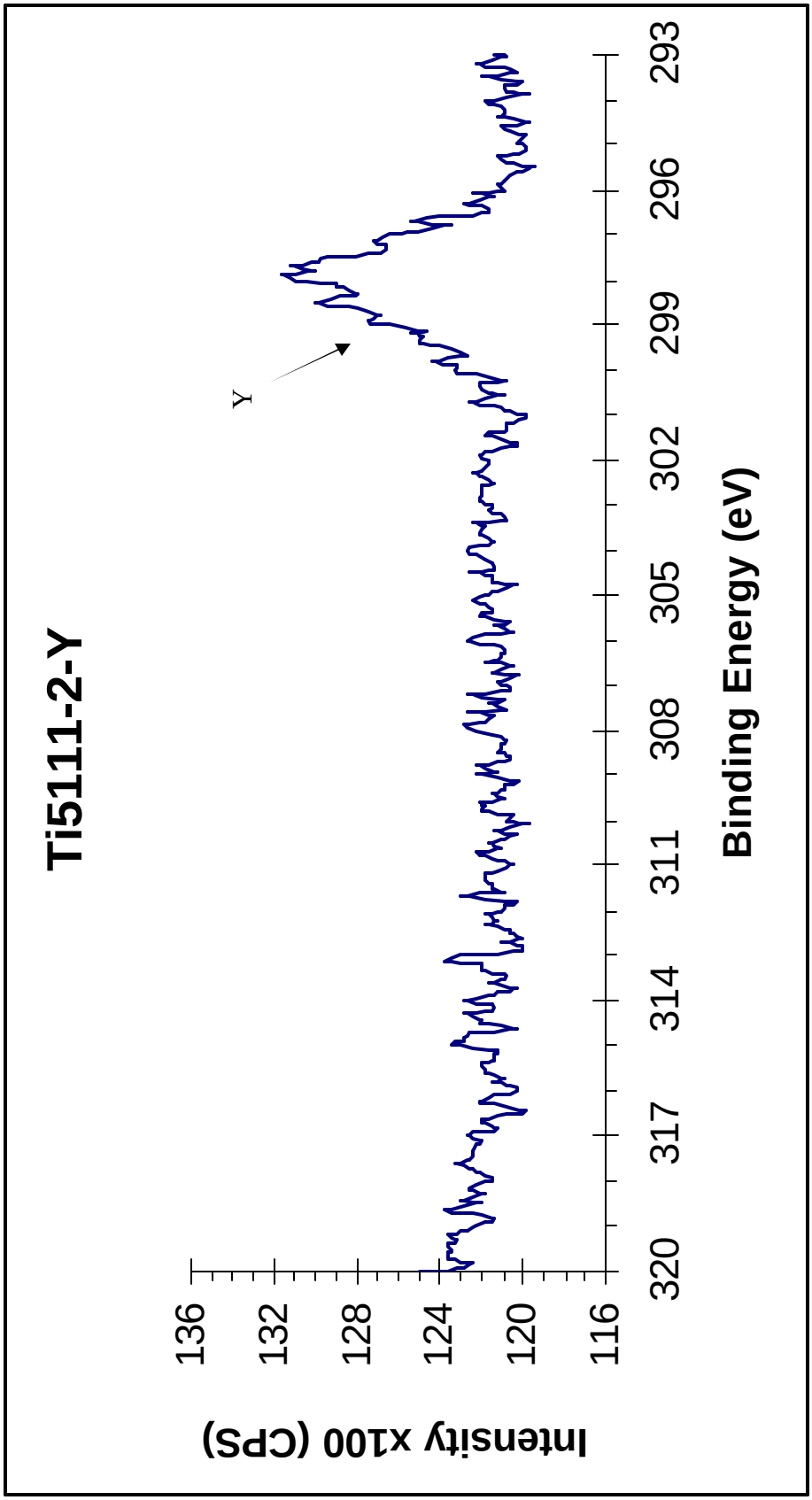

Figure 116: XPS scan of Weld 2 FZ showing the area where the Y 3p 3/2 peak is present. Note background counts subtracted.

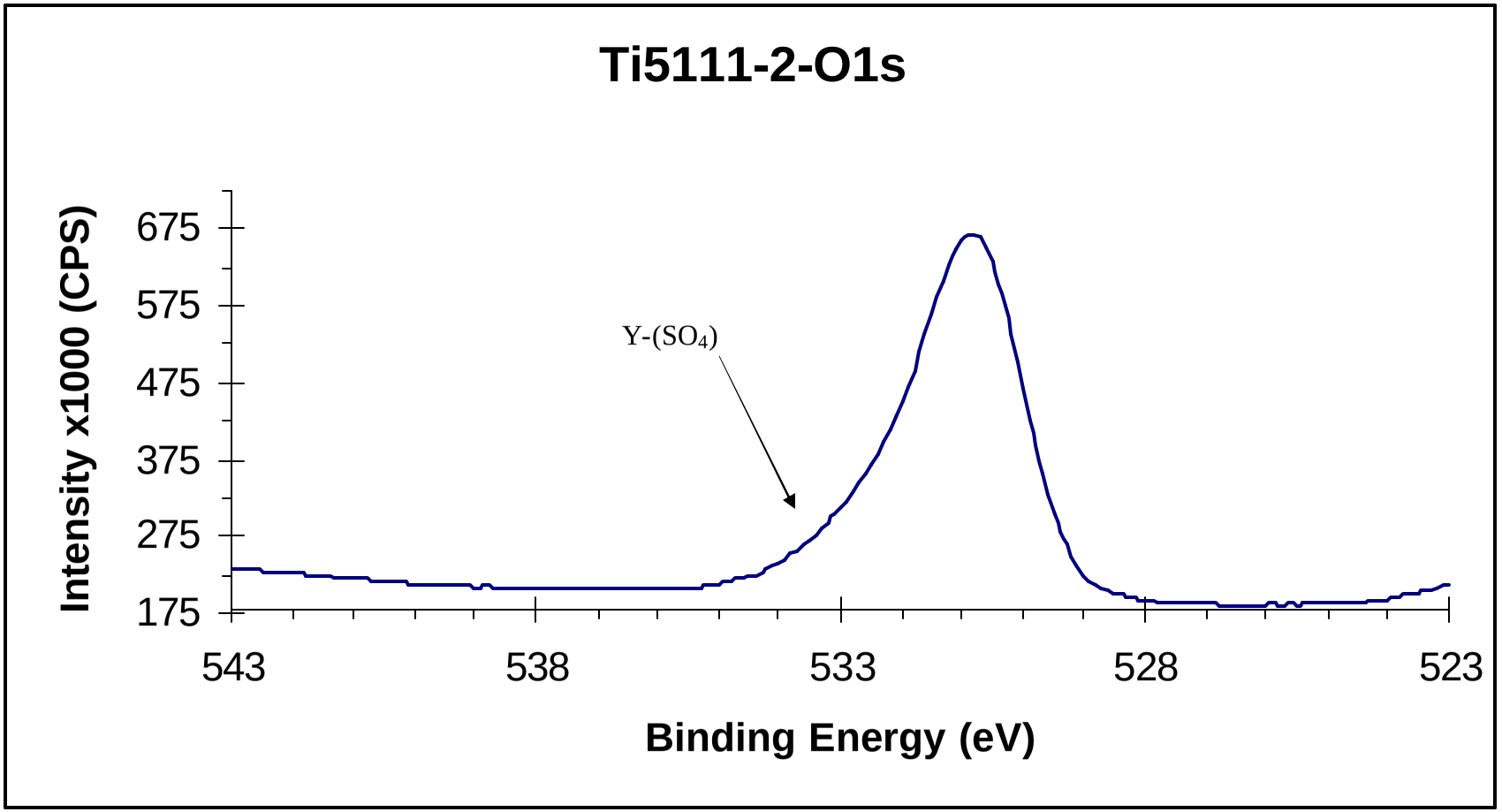

Figure 117: XPS scan of Weld 2 FZ showing the area where the O1s peak is present. Note extended tail region from 532 to 535 eV, believed to be a result of the yttrium oxide sulfate particles present. Note background counts subtracted.

kJ/mole respectively [45]. The formation of yttrium sulfate is clearly more favorable at these conditions. While, at higher temperatures, yttrium sulfate is not likely to form, the Gibbs energy of formation for yttria is at 1800K is -1302.3 kJ/mole [46] and for titanium dioxide the Gibbs energy of formation is -590.3 kJ/mole [47, 48]. As yttrium oxide sulfate was believed to be the resultant product in the weld, it can be concluded that its Gibbs energy of formation at elevated temperatures is more favorable than that of the other possible oxide or sulfide products. The results of yttrium oxide sulfate formation will be discussed more fully in the discussion of results section in Chapter XII.

XII. DISCUSSION OF RESULTS

XII.1 Weld Zone Beta Transition Temperature

In Chapter II, it was stated that the Al concentration of the modified filler metal was reduced. Since O and Al both act as α-stabilizers, the expected pickup of O during the welding process will be offset by this Al reduction. This is expected to maintain the beta transition temperature (βTT) and keep the β-to-α ratio in the FZ similar to that of the base metal. Here the expected βTT of a typical Ti5111 alloy is calculated, along with actual alloy compositions of base metal and weld filler metal, using Multiple Regression Analysis (MRA) coefficient results as determined by Ankem et al [49].

In the MRA, the relationship between the dependent variable, Y, and the independent variables, X_1, X_2, …, X_n, is determined through the use of equation:

$$Y = a + b_1X_1 + b_2X_2 + \ldots + b_nX_n \quad (18)$$

where a is a constant and b_1 through b_n are partial regression coefficients. These partial regression coefficients give the effect of various alloying elements, in this case, on βTT. These coefficients have been established by Ankem et al [49] for a near-α Ti alloy, similar to the one studied here. Their relevant results are provided in Table 21.

Table 21: Results of Multiple Regression Analysis [49].

"a"	Alloying Elements	Ti	Al	Sn	Zr	V	Mo	Fe	Si	O
	Range (wt. %)	89 - 95	4 - 6	0 - 1	0 - 2	0 - 3	0 - 2	0.01 - 0.41	0 - 0.12	0.1 - 0.19
-1866.4	T_β (K)	30.6	48.7	27.6	22.6	11.2	16.6	0.66	-24	155.9

Using the coefficients from Table 21 and Equation 18, the βTT for a typical Ti5111 alloy can be expected to be on the order of 1241.70 K. For the base metal plates used in this study, a βTT of 1247.25 K is obtained. For the matching filler metal plate, a βTT of 1252.23 is obtained, and when that filler metal is used to obtain a weld, with an expected oxygen pickup of 0.01 wt.%, a βTT of 1253.48 K results. The modified 50 ppm Y filler metal plate has a βTT of 1241.25 K and post-weld expected βTT of 1242.50 K. The modified 200 ppm Y filler metal plate has a βTT of 1234.18 K and a post-weld expected βTT of 1235.43 K. From these results, it is clear that by reducing the Al concentration, the desired effect of maintaining the βTT close to that of what is expected in this Ti5111 alloy is obtained.

XII.2 Weld Pool Convection Effects

The yttrium modified filler metals produce a deeper penetration during welding, and cause a rippled surface of the weld when it is cooled. These ripples increase in depth with increasing Y concentration in the filler metal. These observations and the fact that others [21, 22] have also noticed that yttrium additions cause agitation of the weld pool and surface rippling in the solidified weld, leads to the conclusion that either yttrium is acting as a surface active element or yttrium enhances the surface active elements sulfur and/or oxygen in the GTA weld process.

Heiple and Roper [50] developed a theory postulating that variable weld penetration stemmed from changes in the direction of the surface flow produced by the surface tension gradient across the pool. The flows that are created by these surface tensions are known as Marangoni convections. By custom, temperature produced

gradient flows are known as thermocapillary while concentration gradients are known as diffusocapillary. Heiple and Roper [50] stated that the change in surface tension, γ, resulted from a temperature gradient established between the center and edge of the weld pool.

The critical factor for Heiple and Roper [50] in understanding the variable weld penetration was the temperature coefficient of the surface tension, $d\gamma/dT$. When there was a small amount of surface active elements present, the outer edge of the pool had a lower temperature than that of the center. This means that the surface tension at the edge of the pool is higher than at the center, thus causing a radially outward thermocapillary flow. This results in hot liquid being carried to the outer edge of the weld pool and causing melt back at the solid-liquid interface, thus increasing the width of the weld pool. In contrast, when there is a high concentration of surface elements present, the surface tension will be highest at the center of the weld pool and will cause the surface flow to be directed radially inward. This will induce a downward flow in the center such that the melt back will occur at the bottom of the weld pool solid-liquid interface, thereby resulting in a deeper weld.

In a review paper by Mills and Keene [51] on the factors affecting weld penetration, it is stated that rippling on a weld surface is related to the surface properties of the melt. Surface agitation and coarse frozen ripples superimposed on a background of fine ripples are associated with a low surface tension and a positive temperature coefficient. A still fluid surface combined with very fine ripples on the solidified weld surface would indicate a high surface tension and a negative temperature coefficient. The yttrium modified filler metal welds in this research demonstrate a more highly rippled

surface than that of the matching filler metal weld, thereby indicating a positive temperature coefficient and less surface tension at the center of the weld, leading to deeper penetration, as was observed. These observations clearly indicate that yttrium, or perhaps the yttrium oxysulfide that forms in the melt, does indeed act as a surface active element in the weld pool.

The governing equations for the flow inside a weld pool are the two-dimensional, incompressible Navier-Stokes equations:

$$\frac{Dr}{Dt} + r\nabla \cdot \vec{v} = 0 \tag{19}$$

$$r\frac{D\vec{v}}{Dt} = \nabla \cdot \vec{T} + r\vec{f} \tag{20}$$

$$r\frac{D}{Dt}\left(u + \frac{v^2}{2}\right) = \nabla \cdot (\vec{w} - \vec{q}) + r\left(r + \vec{v} \cdot \vec{f}\right) \tag{21}$$

where t is the time, ρ is the fluid density [mass/volume], $\vec{v}$ is the fluid velocity [length/time], $\vec{T}$ is the stress tensor [force/area], $\vec{f}$ is the body force density [force/mss], u is the internal energy [energy/mass], v is the magnitude of the velocity vector [length/time], $\vec{w} = \vec{T}\vec{v}$ which is the power vector [energy/(time·area)], $\vec{q}$ is the heat flux vector [energy/(time·area)], and r is the volumetric energy supply [energy/(time·mass)]. Using the proper boundary conditions, these complex equations can be used to fully describe weld pool convection. This is often done through the development and application of mathematical models and computer simulation techniques such as ones developed by Matsunawa and Yokoya [52], or Zacharia et al [53], which describe weld penetration in stationary arc welds. More recently, Wang et al [54] have developed a model to study the effects of surface active elements on flow patterns and weld

penetration. They found that there is a complicated interaction between the electromotive force and the surface tension and that depending upon sulfur concentration in 304 steel, multiple vortices could be formed, flowing in various directions.

If we take a simplistic approach to the inside of a weld pool, there are four different driving forces for convection [55]. Three of these have external origins while one arises from within the weld pool. These forces include:

(1) Buoyancy or gravity force,

(2) Electromagnetic or electromotive force (emf) or Lorentz force,

(3) Impinging or friction force, and

(4) Surface tension gradient or Marangoni force.

The surface tension gradient force is the one force that is not external in origin, but rather emanates from within the weld pool due to temperature gradients or composition gradients acting to complicate temperature effects. Ignoring the effects of the external forces, the surface tension gradient exerts a force, $\left(\vec{f}_g\right)$, given by [55]:

$$\vec{f}_g = -\frac{dg}{dT}\nabla T \tag{22}$$

where γ is the surface tension of the molten metal, T is the temperature, and ∇T is the temperature gradient at the weld pool surface. Thus, according to Heiple's model as previously discussed, and illustrated in Figure 118, if the γ-T curve has a negative slope, the flow takes place from the center to the edges, while if the γ-T curve has a positive slope (as is the case with surface active elements), fluid flow takes place from the weld edges to the center, causing greater penetration. Much more needs to be learned about

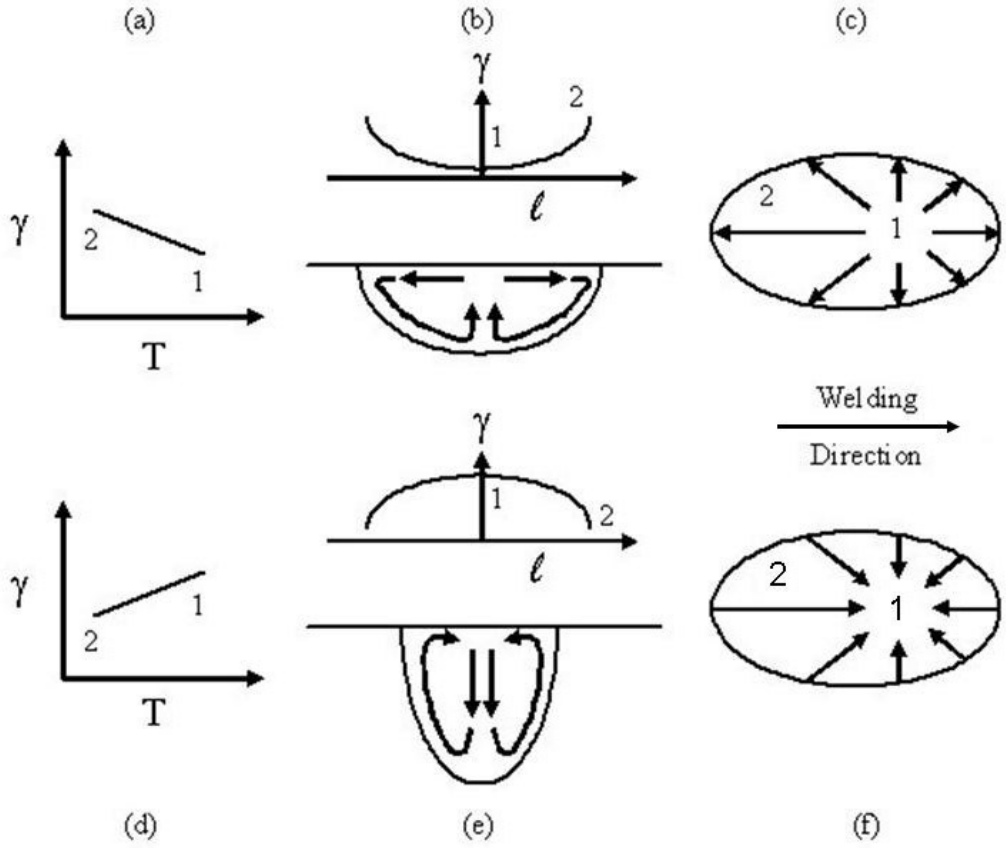

Figure 118: Schematic illustration of Heiple's model for Marangoni convection in a weld pool. (a-c) Low or no surface activant pool. (d-f) High surface activant pool. Note that in (a-c), the liquid metal with the higher temperature and lower surface tension is at the center of the pool and is pulled outward by the cooler liquid metal of higher surface tension at the pools outer edge. In (d-f), the cooler liquid metal with lower surface tension is at the edge of the pool and is pulled inward by the higher temperature liquid metal with higher surface tension near the center of the pool. The heat flow pattern in (b) favors convective heat transfer to the sides of the weld pool thus causing a wider weld. The heat flow pattern in (e) favors convective heat transfer to the bottom of the pool thus causing a deeper weld penetration.

the effects of yttrium acting as a surface active element or enhancer in titanium alloys and how a change in convection current in the weld pool affects weld zone microstructure and thereby mechanical properties.

XII.3 Formation of Yttrium Particles in the Weld

Additions of yttrium to the weld filler metals in Ti-5111 refine the prior-β columnar grains in the weld FZ. This refinement is believed to be due to the formation of yttrium oxysulfide (Y_2O_2S) particles in the melt. Nanoparticles were seen inside the matrix by examination under TEM. Larger particles were seen at prior-β grain boundaries inside the FZ under examination by ESEM. These particles were initially seen to contain both sulfur and oxygen through the use of WDS analysis. Examination by XPS showed that these particles contained yttrium sulfate and possibly contained an yttrium-oxygen bond. Identification of the particles under TEM was not possible due to the extremely low concentrations of the particles, along with the fact that the particles were not necessarily in any crystallographic orientation within the alpha phase matrix.

While XPS analysis of the particles shows that they contain yttrium and sulfate, it is believed that the particles are actually yttrium oxide sulfate ($Y_2O_2SO_4$). Evidence of a Y-O peak did exist at approximately 157 eV and the XPS signature of the yttrium oxide sulfate would be very similar to that of the yttrium sulfate. The formation of yttrium sulfate at the high temperatures of the titanium alloy melt would not be likely, as decomposition of yttrium sulfate to yttrium oxide sulfate begins to occur at 1193 K (920°C) and is complete at 1397 K (1124°C) [56]. The yttrium oxide sulfate will decompose to yttria beginning at a temperature of approximately 1400 K (1127°C) and

be complete at a temperature of 1521 K (1248°C) [56]. Temperatures in the melt are believed to be between approximately 1943K (1670°C) to 2273 K (2000°C).

While there clearly hasn't been much research done concerning the use of rare earth metals (REM's) in titanium alloy welding, REM's have been used for deoxidation and desulfurization control in steels, especially in China and Russia. Wells [57] studied the common phases resulting from addition of mischmetal (Ce ~50%, Nd ~15%, Pr ~7%, other REM's ~3%) to low alloy molten steel (Note mp of steel ~ 1673 K or 1400°C). Wells [57] found that the most common phase found was that of the oxysulfide (RE_2O_2S), with a crystal structure very similar to that of the hexagonal oxide phase (RE_2O_3). The oxide phase was only found if the oxygen content was abnormally high or the sulfur content was abnormally low. The sulfide phase RE_2S_3 would also be seen, especially as a globular ring around the oxysulfide particles while RES was only rarely present.

Ting and Longmei [58] conducted research on interactions between Y, O and S at 1873K (1600°C) in liquid iron. Their X-ray diffraction of the equilibrium products in melts of Fe-Y-O, Fe-Y-S, and Fe-Y-S-O showed these products to be Y_2O_3, YS and Y_2O_2S respectively. Their construction of a phase diagram showed that the Y_2O_3 and Y_2O_2S could exist at equilibrium over a range of oxygen and sulfur activities. Free energies of formation for Y_2O_3 and Y_2O_2S in liquid iron were determined to be:

$$\Delta G^{o}_{Y_2O_3} = -1792680 + 658.48T(^{\circ}C)[J/mol] \quad (23)$$

and

$$\Delta G^{o}_{Y_2O_2S} = -1521520 + 536.55T(^{\circ}C)[J/mol] \quad (24)$$

Findings similar to these were found by Longmei and Ting [59] for Y-O-S in liquid nickel at 1873 K (1600°C). Their free energies of formation for Y_2O_3 and Y_2O_2S in liquid nickel were determined to be:

$$\Delta G^{o}_{Y_2O_3} = -814920 + 148.16T(^{\circ}C)[J/mol] \quad (25)$$

and

$$\Delta G^{o}_{Y_2O_2S} = -634460 + 73.69T(^{\circ}C)[J/mol] \quad (26)$$

High temperature thermodynamics of the La-O-S system were conducted by Kay et al [60]. Equilibrium equations resulting from their work included:

$$La_2O_2S(s) + 2O_2(g) \leftrightarrow La_2O_2SO_4(s) \quad (27)$$

$$\Delta G^{o}_{(27)} = -219860 + 77.82T(1100 - 1500K)[cal] \quad (28)$$

and

$$La_2O_3(s) + \tfrac{1}{2}\, S_2(g) \leftrightarrow La_2O_2S(s) + \tfrac{1}{2}\, O_2(g) \quad (29)$$

$$\Delta G^{o}_{(29)} = 17507 - 2.32T(1080 - 1350K)[cal] \quad (30)$$

Jacob et al [61] also studied the equilibrium oxygen potentials for the oxidation of rare earth oxysulfides to oxysulfates between temperatures of 900 and 1480 K (1173 - 1753°C). It was seen that at a constant temperature, the oxygen potentials for the oxidation of oxysulfide to oxysulfate were seen to increase monotonically with the atomic number of the REM.

Yang et al [62] studied the effects of rare earth oxides on inclusions of hardfacing metal and of medium-high carbon steel. Their results showed that the RE oxide was reduced to the REM through an interaction with carbon. The REM can then react with oxygen and sulfur to form the RE oxide, RE sulfide and RE oxide sulfide in the

hardfacing molten pool, thereby decreasing the harmful effects of sulfur. The RE oxide could also react directly with sulfur to form the RE oxide sulfide.

It is therefore believed that the following process takes place when yttrium metal (melting point 1795 K (1522°C)) is introduced into the titanium alloy melt. The yttrium will combine with O and S to form an yttrium oxysulfide (Y_2O_2S). The yttrium oxysulfide melting temperature is approximately 2473 K (2200 °C), somewhat higher than the expected temperature of the weld melt. Small amount of yttria (melting temperature of 2683 K (2410°C)) may also form in the melt, but is probably converted to the oxysulfide via the reaction:

$$Y_2O_3(s) + ½\ S_2(g) \leftrightarrow Y_2O_2S(s) + ½\ O_2(g) \quad (31)$$

As the temperature of the melt cools to below it's freezing temperature (~1941 K (1668°C)), and reaches the temperature range of approximately 1400-1500 K (1127-1227°C), the oxysulfide is converted to the oxysulfate by the oxidation reaction:

$$Y_2O_2S(s) + 2O_2(g) \leftrightarrow Y_2O_2SO_4(s) \quad (32)$$

The final particle in the solid is thus yttrium oxide sulfate (or yttrium oxysulfate) ($Y_2O_2SO_4$) as is identified via XPS analysis.

XII.4 Effect of Yttrium Additions on Weld FZ Mechanical Properties

The results of this investigation show that the addition of yttrium and the subtraction of aluminum to the weld filler metal results in an improvement of weld ductility. The modified 50 ppm Y filler metal weld shows drastic improvements in weld ductility while still maintaining strength close to that of the matching filler metal. Ultimate strength of both the matching filler metal and modified 50 ppm Y filler metal is

higher than that of the base metal, as expected. The modified 200 ppm Y filler metal weld has a ductility higher than that of the matching filler metal, but is below that of the 50 ppm Y filler metal. The ultimate strength of the 200 ppm Y filler metal weld is significantly higher than that of both the matching filler metal weld and modified 50 ppm Y filler metal weld. The reason for the increase in ductility is due to the refinement of the prior-β grains inside the weld FZ and the subtraction of oxygen interstitials inside the weld FZ due to formation of yttrium oxysulfide particles in the melt, followed by further oxidation to yttrium oxide sulfate. It is not clear why further additions of yttrium over the 50 ppm concentration leads to decreasing ductility, but it is most likely due to the build-up of yttrium oxide sulfate particles at the prior-β grain boundaries and in the matrix. This higher concentration of the particles at the grain boundaries leads to increased intergranular fracture and hence, lowers ductility.

Weld hardness was examined by Vicker's microhardness mapping with results indicating that the modified 50 ppm Y filler metal weld has values of hardness that are most similar to that of the base metal. The matching filler metal weld has very high values of hardness as compared to the base metal, while the modified 200 ppm Y filler metal weld has values of hardness slightly higher than that of the 50 ppm Y filler metal weld, but less than that of the matching filler metal weld. As stated previously, it is expected that the decrease in hardness values (increase in ductility) is due to the formation of yttrium oxysulfide particles in the melt, which remove the available oxygen atoms that would typically go to interstitial positions in the matrix. Furthermore, oxidation of the yttrium oxysulfide to yttrium oxide sulfate serves to remove even more oxygen available to the matrix. The more oxygen interstitials present in the matrix, the

harder (and stronger) the weld typically is, with resulting decrease in ductility. By tying up these potential oxygen interstitials as particles, the modified 50 ppm Y filler metal weld was able to exhibit a much more ductile failure, as compared to both the matching and modified 200 ppm Y filler metal welds. The higher hardness of the 200 ppm Y weld over the 50 ppm Y weld is believed to be due to either the enhanced platelet refinement combined with the increased randomness of the platelets or due to oxide dispersion strengthening. More research would be necessary to determine the exact cause.

Fracture toughness testing indicates that all of the welds experience a drastic decrease in fracture toughness values, as measured by J_{IC}, as compared to the base metal. The values of the matching filler metal weld and modified 50 ppm Y filler metal weld are approximately the same. This is not unexpected as both of these weld FZ's have the same type of microstructure and are thereby expected to start to cracking at the same point. What was drastically improved in the modified 50 ppm Y filler metal weld, however, was the tearing modulus. The tearing modulus may be thought of as how much energy is required to continue crack growth after it has been initiated, or can also be viewed as a measure of the ability of the material to resist crack propagation. The modified 50 ppm Y filler metal weld's increase in tearing modulus can likely be attributed again to the formation of yttrium oxysulfide particles in the melt, with improvement resulting from either a decrease in the prior-β grain size and an increased mixed orientation of alpha colonies in the presence of yttrium oxide sulfate particles or possibly from dislocation pinning at these nanoparticles. While the fracture toughness values are not increased, the increase in the tearing modulus can be very important in

itself. This increase in tearing modulus will enhance the capability to detect a crack before a component can fail catastrophically.

XII.5 Fusion Zone Grain Nucleation

Since fusion zone grain nucleation in the weld pool is so critical when considering the refinement of grain size, a review of nucleation will be given here [63, 64]. For crystal growth in an alloy to take place, the temperature must be less than the melting temperature, T_f. The undercooling of the interface provides the driving force to bias the kinetic process in the direction of freezing. The greater the amount of interface cooling, the greater the driving force for crystal growth.

Assuming that the material nucleates as a solid sphere of radius r upon solidification from a liquid metal, the free energy of nucleation depends upon the change in free energy associated with creating the unit volume, ΔG_{vol}, of the new phase, and the energy required to create an interface with interfacial energy, γ, of the new phase in liquid metal. The ΔG_{vol}, which is dependent upon the volume of the sphere ($4/3\pi r^3$) must be negative for nucleation to take place. Interfacial energy, which is dependent upon the surface area of the sphere ($4\pi r^2$), will always have a positive value. Therefore, the free energy change associated with nucleation can be given as:

$$\Delta G_{nuc} = \frac{4}{3}\pi r^3 \Delta G_{vol} + 4\pi r^2 \gamma \tag{33}$$

Since:

$$\Delta G_{vol} = \Delta H_{vol} - T\Delta S_{vol} \tag{34}$$

and at the melting point, T_f, of the liquid, $\Delta H_{vol} = -L_{fvol}$ (latent heat of fusion per unit volume) and $\Delta S_{vol} = -L_{fvol}/T_f$, cooling the liquid metal below T_f to temperature, T, gives:

$$\Delta G_{nuc} = \frac{4}{3}\pi r^3[-L_{fvol} - T(\frac{-L_{fvol}}{T_f})] + 4\pi r^2\gamma \quad (35)$$

$$= \frac{4}{3}\pi r^3[L_{fvol}(\frac{T - T_f}{T_f})] + 4\pi r^2\gamma \quad (36)$$

Defining the degree of undercooling as $T - T_f = \Delta T$, we have:

$$\Delta G_{nuc} = \frac{4}{3}\pi r^3 (\frac{L_{fvol}\Delta T}{T_f}) + 4\pi r^2\gamma \quad (37)$$

There is a critical radius, r_{crit}, such that any sphere with a radius below this value, will be thermodynamically impossible to nucleate and a sphere with a radius above this will be thermodynamically stable, thus promoting growth. At this critical radius, the gradient of the ΔG_{nuc} curve will be zero. Therefore, differentiating ΔG_{nuc} and solving for r yields:

$$r_{crit} = \frac{2gT_f}{\Delta T L_{fvol}} \quad (38)$$

It can therefore be seen that by increasing the degree of undercooling, ΔT, and decreasing the interfacial energy, γ, between the liquid metal and the nucleating phase, nucleation is favored by reducing the critical radius size.

Homogeneous nucleation, which is nucleation within the parent phase, has in general, a high value of γ, and thus requires a larger critical radius for nucleation. The rate of homogeneous nucleation can be expressed as:

$$\text{rate} \propto \exp(\frac{-\Delta G^*_{nuc}}{RT}) \quad (39)$$

where ΔG^*_{nuc} is the free energy of activation (E_A) for nucleation and T is the temperature to which the melt is cooled. By decreasing T, ΔT is increased, thereby decreasing the critical radius size for nucleation and the free energy of activation for nucleation, leading to an increase in the rate of nucleation.

For heterogeneous nucleation to take place, the third phase must have crystallographic dimensions similar to that of the nucleating phase. The rate of heterogeneous nucleation in metals and alloys can be given as [65]:

$$N_{het} = \nu N_v \exp\left(\frac{-\Delta G^*_{het}}{RT}\right) \exp\left(\frac{-Q_d}{RT}\right) \quad (40)$$

where ν is the vibration frequency factor, N_v is the total number of heterogeneous nucleation sites per unit volume, ΔG^*_{het} is the energy barrier against nucleation, Q_d is the activation energy for atomic migration across the nucleus/matrix interface, T is the temperature and R is the universal gas constant.

By examining this equation, it is seen that there exists a balance between the diffusivity of elements at a given temperature and the thermal driving force acting to overcome the energy barrier to nucleation. Higher temperatures induce a higher diffusion rate but give a low thermal driving force, thereby giving a low rate of nucleation. The opposite is true for low temperatures. A temperature must therefore be found where these competing influences on the kinetics of reaction are optimized such that a high rate of nucleation is induced [65].

Having discussed homogeneous and heterogeneous nucleation, it is important to distinguish between the two processes. In homogeneous nucleation, undercooling is not obtainable by slow cooling. In a liquid, no long-range order exists. There is a probability

however, that some atoms will cluster together into small regions having the same crystal structure of the solid phase, for a time long enough for nucleation to commence. These small clusters are known as embryos and must have a radius greater than r_{crit} to have the potential to promote solidification.

In the liquid, the higher the temperature, the smaller the largest size embryos would be due to the increased amplitude of atomic vibrations at higher temperatures. This leads to a smaller probability of homogeneous nucleation commencing. There is however, a temperature, T*, at which nucleation will commence spontaneously in a liquid. This is called the homogeneous nucleation temperature, and $0.20T_f$ gives its approximate value.

Another factor affecting homogeneous nucleation is the volume of liquid present. A larger amount of liquid leads to a greater probability of an embryo existing with a radius greater than r_{crit}. This means that there exists a greater probability for homogeneous nucleation.

Heterogeneous nucleation typically involves the presence of foreign solids in a liquid (or the presence of dendrite break-off), serving to nucleate solids at a temperature considerably greater than the homogeneous nucleation temperature. This means that heterogeneous nucleation is energetically more favorable than homogeneous nucleation since it happens at a higher temperature.

In homogeneous nucleation, the critical nucleus size is entirely dependent upon the radius of the embryo and has nothing to do with the atoms per embryo. The probability of these atoms attaining a certain size is however, almost entirely dependent upon the number of atoms in the cluster and hardly dependent at all upon on geometric

arrangement of the atoms in the cluster. Therefore, if the atoms in the embryo can be aggregated into the shape of a stable spherical cap on a solid substrate, as seen in Figure 119, this would be the same as a spherical nucleus with r*, from a nucleation standpoint. In heterogeneous nucleation, it can be seen that fewer atoms must locally fluctuate into their solid configuration, in order to obtain viable crystal nuclei.

The solid foreign particle will act as a nucleation catalyst by stabilizing the crystalline spherical cap through provision of low energy sites to situate its lowest plane of atoms. The measure of the stabilizing power of this solid substrate on the crystal nucleus is given by its magnitude of the contact angle, θ, seen if Figure 119. This angle is also known as the wetting angle. A small θ means that the seeded material will act as a good heterogeneous nucleation catalyst, while a large θ provides a poor nucleation catalyst. The interface energy, γ, between the various phases can be given as:

$$\gamma_{LS} = \gamma_{CS} + \gamma_{LC} \cos\theta \tag{41}$$

where γ_{LS} is the interface energy between the liquid and substrate, γ_{CS} is the interface energy between the crystal and the substrate, γ_{LC} is the interface energy between the liquid and the crystal, and θ is the wetting angle. This energy balance is illustrated in Figure 119. The wetting angle will have a dramatic affect on the free energy of formation. The free energy change associated with forming a cap shaped nucleus of critical radius on a planar substrate can be given as [66]:

$$\Delta G^* = \frac{4p g_{LS}^{\ 3}}{3\Delta G_V^{\ 2}} (2 - 3\cos\theta + \cos^3\theta) \tag{42}$$

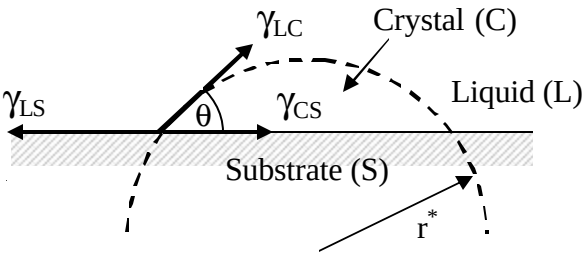

Figure 119: Schematic illustration representing heterogeneous nucleation and energy balance at the solid-liquid-substrate junction.

From this equation, it is seen that if $\theta = 0^o$, no free energy barrier to nucleation exists thereby causing nucleation to occur automatically without any undercooling. This is the case in fusion welding where the base metal grains will act as a substrate for nucleation. Since the weld metal in the weld pool completely covers these substrate grains with direct contact, $\theta = 0^o$, the crystals will nucleate on this surface without difficulty. This nucleation process results in epitaxial growth where the grains grow in a columnar structure from the partially melted grains at the S/L interface.

In addition to the epitaxial growth of the grains seen in this study, occasional heterogeneous nucleation of grains is also observed in the yttrium-modified filler metal welds. This result's from the fact that a competitive process exists between the heterogeneous nucleation sites and the epitaxial nucleation at the fusion line as to what type of grains are grown inside the weld fusion zone. This process was described by Misra et al [21]. Whether or not heterogeneous nucleation is favored is based on the concentration of the yttrium oxysulfide particles in the melt. If the concentration of these particles is high, there is a great probability that the particles will come close enough together such that the critical radius for nucleation is exceeded, thereby resulting in formation of an equiaxed grain. If this happens at many places in the weld, very rapidly, an equiaxed grain structure would result, as seen in the research by Misra et al [21]. If the yttrium concentration is not high, as in our case, and in the research by Simpson [19], Nordin et al [22] and Misra et al [21], then the epitaxial growth process will be dominant. A schematic illustration of this process can be seen in Figure 120. The amount of yttrium necessary in order for heterogeneous nucleation to predominate is undetermined.

XII.6 Fusion Zone Grain Growth

While the fusion zone microstructure was composed of long columnar prior-β grains, a refinement in width of these grains is seen with the addition of yttrium to the melt. This refinement has also been seen by other researchers [19, 21, 22], with different attempts made by each researcher to explain this refinement. Theories offered to explain this refinement have included:

1. Yttrium particle concentration at the solid/liquid (S/L) interface can build-up causing a greater undercooling as the temperature ahead of the S/L interface decreases, thereby resulting in an increased tendency for heterogeneous nucleation [19].
2. Yttrium additions affect the weld pool fluid flow (surface tension) and heat extraction from the pool, thereby causing increased undercooling at S/L interface, resulting in increased heterogeneous nucleation at S/L interface [22].
3. Increased heterogeneous nucleation throughout weld pool due to yttria particle formation in the melt and a decreased critical degree of supercooling [21].

Concerning the first two theories, both result in the fact that increased heterogeneous nucleation occurs at an undercooled S/L interface. This undercooling is a result of composition changes at the S/L interface and is referred to as constitutional supercooling [67]. If an increased amount of heterogeneous nucleation at the initial S/L interface was indeed the case, the grain size at the bottom of the weld would be more refined in the case of yttrium additions as compared to the matching filler metal. This was not

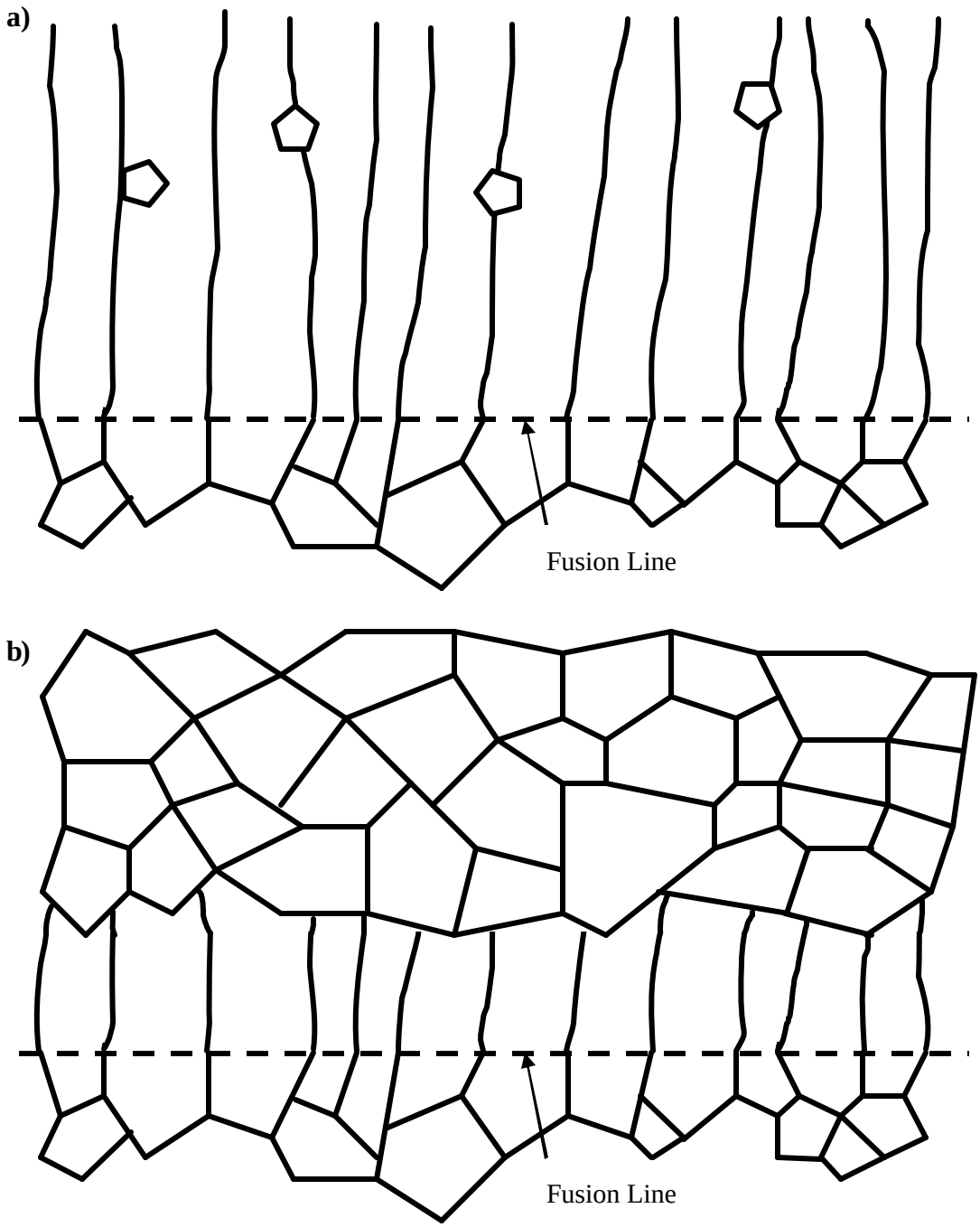

Figure 120: Schematic of yttrium modified epitaxial growth process plus competing heterogeneous nucleation sites. (a) Low yttrium concentration leads to few heterogeneous nucleation sites. (b) High yttrium concentration leads to many heterogeneous nucleation sites which blocks epitaxial growth process.

observed in this investigation, where the grain size just above the weld bottom was approximately equal in all cases at 750 μm. In addition, if heterogeneous nucleation were occurring at this interface, it would continue to occur at the interface of various weld passes, resulting in a weld that was predominantly of equiaxed grains. The heterogeneous nucleation would disrupt the epitaxial growth process which results in long columnar grains. This was clearly not seen in this investigation and was also not seen in work by Misra et al [21]. In both investigations, grain growth was seen to occur in a continuous epitaxial manner.

Concerning the third theory, Misra et al [21] developed a competing nucleation and epitaxial growth theory that results in heterogeneous nucleation sites blocking the growth of epitaxial growth grains. A schematic representation of this can be seen in Figure 120 taking into account varying amounts of yttrium. They postulated that if the added yttrium decreases the critical degree of supercooling necessary for heterogeneous nucleation, weld microstructure would depend on whether the time to grow an epitaxial grain across a weld pass was higher or lower than that to grow a heterogeneous equiaxed grain. If the time for heterogeneous nucleation was less than that of epitaxial grain growth across the weld pass, an equiaxed microstructure would result. If the times were reversed, a long columnar grain microstructure would result. This theory does not address the refinement of prior-β columnar grain width, but can be used to explain why there were some instances of heterogeneous nucleation in the welds of this study.

Epitaxial growth grains tend to grow in easy-growth directions [68, 69]. In BCC (β) titanium, this is along the <100> direction. These grains also tend to grow fastest when their easy growth direction is parallel to the maximum thermal gradient. The

maximum thermal gradient is typically in a direction perpendicular to the S/L interface at the rear of the molten metal puddle produced from welding [69]. At the S/L interface, any grains that happen to be randomly oriented with a <100> direction parallel to this maximum temperature gradient will most likely grow and expand in cross-section at the cost of other less favorably oriented grains. This process is known as the competitive growth process [69] and a schematic illustrating the process can be seen in Figure 121a.

The competitive growth process in welds is affected by the addition of yttrium metal to the weld filler metal as illustrated in Figure 121b. It is believed that as the dendrites grow into the melt from the S/L interface, yttrium oxysulfide particles are encountered that then create a drag force on the solidification front, thereby slowing the front down. This process is illustrated in Figure 122. The particles in the melt may either be small enough such that they are easily engulfed by the solidifying front and thereby locked in as part of the matrix, or they may be large enough such that they are pushed ahead of the solidification front creating the drag force mentioned, with these particles existing in higher concentrations at the grain boundaries.

This drag force on the particles may be expressed by the equation:

$$D = C_D * r * A * \frac{\vec{v}^2}{2} \tag{43}$$

where C_D is the drag force coefficient that takes into account the viscosity and compressibility of the melt and the shape of the particles, ρ is the density of the melt, A is the reference area of the particles and v is the velocity of the particles, which depends on the growth rate (or solidification rate) of the advancing S/L interface, which in turn depends upon the degree of supercooling at the S/L interface and the solvent-solute

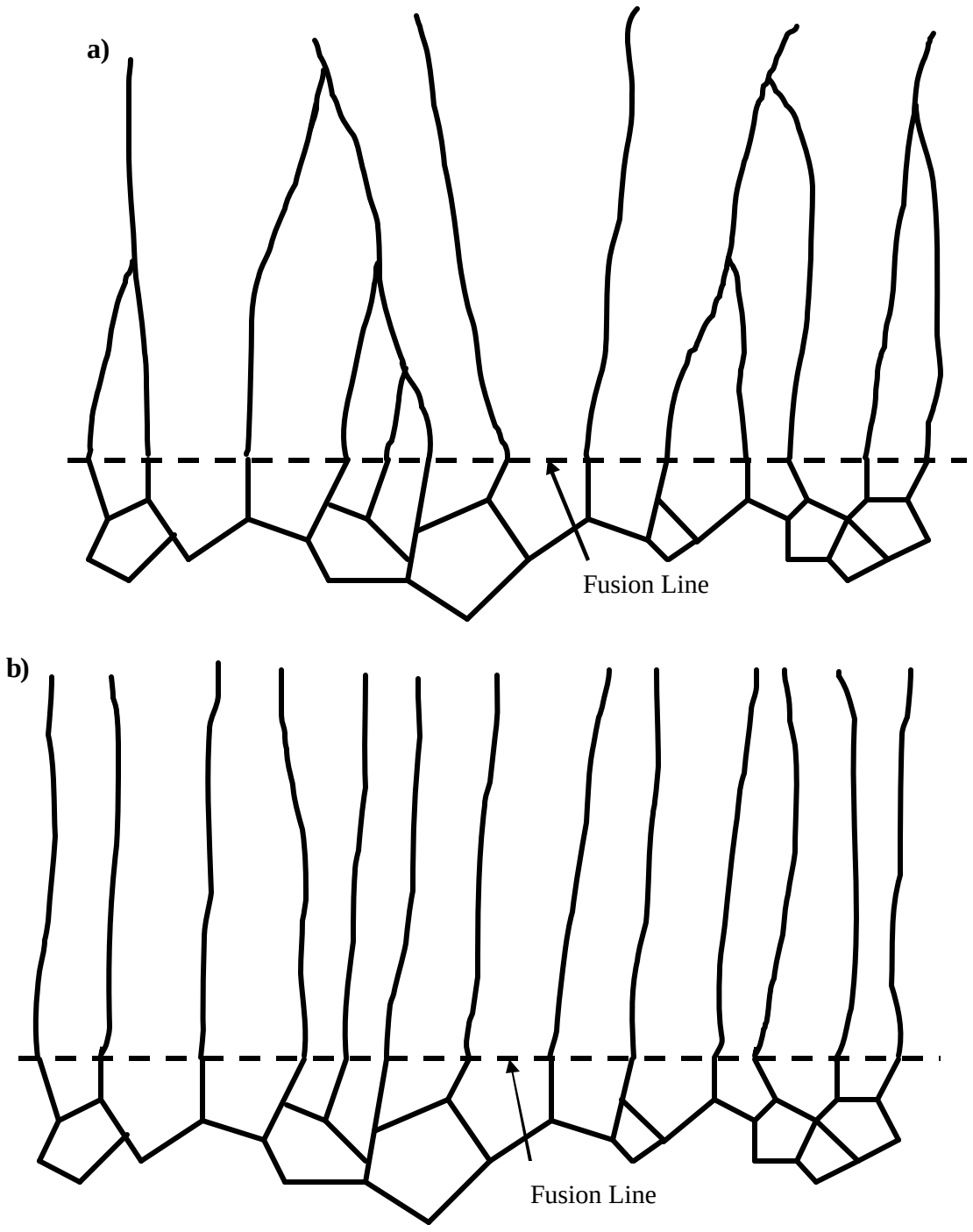

Figure 121: Schematic illustration of possible epitaxial growth processes in the weld FZ. (a) Competitive growth process, no yttrium present. (b) Addition of Y to weld filler metal with resulting formation of yttrium oxysulfide particles in the weld melt which then act to create a drag force on the growth process of the favorably oriented grains, thus allowing for the continued growth of the not-so-favorably oriented grains by "rotation" to a favorable direction. Note how the grain width at the top of the weld decreases, while at the bottom of the weld near the fusion line remains approximately constant.

redistribution via interdiffusion of species across the S/L interface. Examining Equation 43,it can be seen that if the number of particles increases or if the size of the particles increases, thereby increasing the reference area, the drag force on the solidification front will also increase. Similarly, if the velocity of the solidification front increases, the drag force will increase by the square of that.

We may therefore think of the process like this. The easy growth directions of the epitaxial growth grains parallel to the largest temperature gradient are advancing rapidly through the melt. As this interface moves faster as compared to the other directions, it will encounter more yttrium oxysulfide particles than the other advancing fronts. This interface will therefore have a greater drag force exerted on it than the other advancing solidification fronts, thereby causing this solidification front to be slowed down and allowing the other non-preferred growth directions to "rotate" to a preferred growth direction and continue to grow. This eliminates some of the effects of the competitive growth process and results in more grains continuing to grow from pass to pass, which results in an overall reduction in the prior-β grain size in the final solidified weld, again illustrated in Figure 122b.

Another consideration as the number of yttrium particles in the melt increases, involves the degree of undercooling in the melt at the S/L interfaces. The increasing number of particles, as discussed, will slow the advancing solidification front, especially on the sides of the front, as more particles are likely to be encountered in this direction. Since heat is still being removed from the melt at the same rate, the amount of undercooling at the S/L interface will increase. This increase in undercooling will result

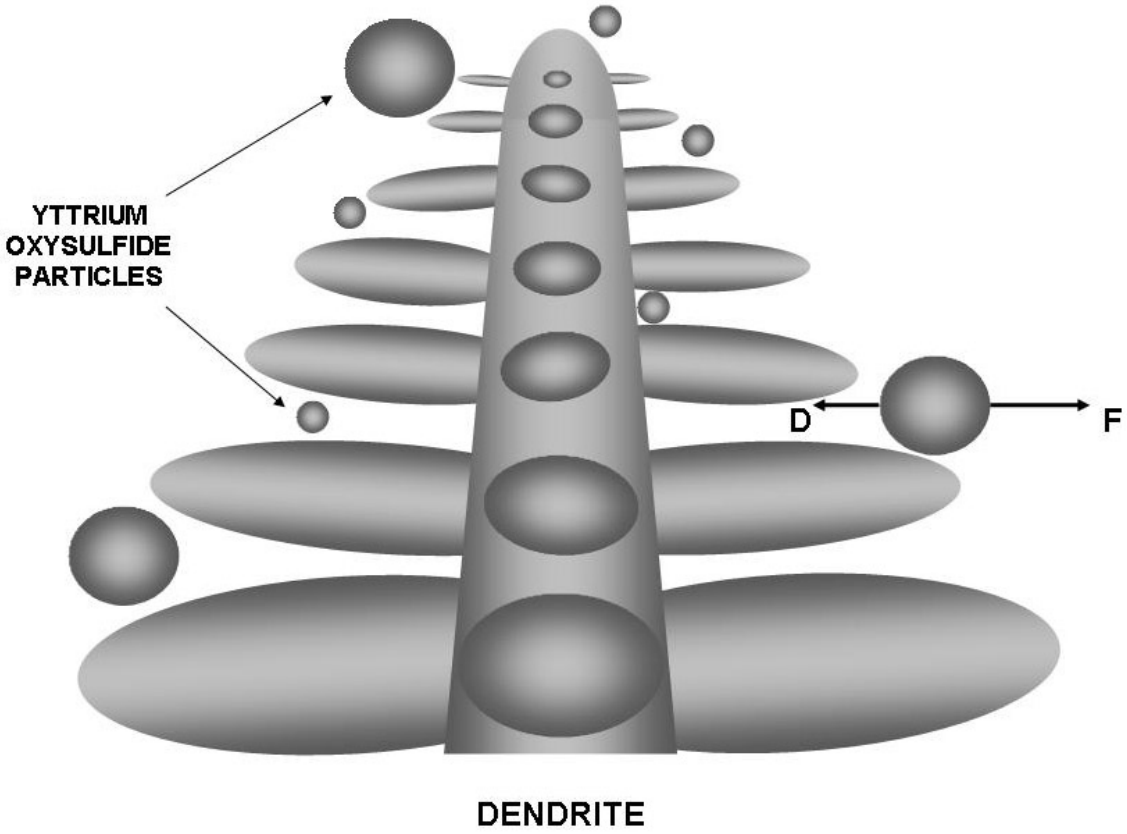

Figure 122: Three dimensional schematic representation of the dendrite growth process in a melt containing yttrium oxysulfide particles. The particles may either be small enough to be engulfed by the advancing dendrite branch solidification, thereby becoming a part of the matrix, or the particles may be large enough such that they are pushed ahead of the advancing solidification front. These larger particles congregate at the grain boundary and serve to create a drag force (D) on the advancing solidification front that pushes these particles ahead (F).

in an increased solidification rate both at the dendrite front and sides. The increased solidification rate at the head of the dendrite leads to a quicker solidification of the melt. The increased solidification rate of the dendrite branches results in an increased velocity of the yttrium oxysulfide particles, which as demonstrated in Equation 43, results in a dramatic increase in the drag force. This again serves to act as a break on the attempted rapid growth of the easy-growth directions. Particles existing at the S/L interface will also tend to disrupt the diffusion of solute/solvent across this interface. This again results in a slowing down of the epitaxial growth rate into the supercooled liquid. As this process continues, the melt becomes supercooled to greater distances, thereby increasing the chance for heterogeneous nucleation to become more dominant in the melt.

XII.7 Weld Zone Oxygen

Another factor affecting the strength and ductility of welded titanium is the addition of oxygen to the weld zone. Titanium is an excellent getter of oxygen, which serves as an α stabilizer, successively filling up various octahedral voids in the titanium hcp lattice with increasing oxygen content up to 33 at. %. Additions of oxygen will cause the weld to become brittle and therefore cause a very low toughness. While GTAW seeks to eliminate oxidation of the titanium in the weld pool by performing the weld under an inert atmosphere, there are almost always some oxygen impurities present in the shield gas and there may be some diffusion of oxygen from the base metal into the weld zone.

Wong et al [70] indicated that ambient oxygen will serve as an external source of oxygen and that base metal oxygen may serve as an internal source of oxygen in the

formation of Ti-O phases across a steep thermal gradient in the vicinity of the HAZ. They detected two TiO phases at the surface of a Ti alloy, TiO_{x1} and TiO_{x2} with x2 > x1, that increased with thickness as position moved towards the centerline. This increasing thickness was indicative of an increase in diffusion of oxygen along the positive temperature gradient in the HAZ towards the liquid weld pool. Another indication of enhanced oxygen diffusion was a much greater increase in Δc of the TiO_x phases than that which would be expected due to the thermal expansion alone, as traveling towards the liquid pool, in the direction of increasing temperature. Given that the c parameter in the TiO_x is known to be strongly dependent upon oxygen content, it is reasonable to attribute this increase in c to both thermal expansion and increased oxygen content due to the diffusion of oxygen along the steep thermal gradient. The higher oxygen containing TiO_{x2} layer was believed to be formed by direct contact with the ambient air after the protective trailing gas passed by. This layer further oxidized to TiO_2 upon cooling.

As seen in studying oxygen concentration in the welds by WDS, oxygen concentration increases across the HAZ towards the FZ. This increase in oxygen concentration was not measured at the surface of the specimen, but well inside, where only internal diffusion of oxygen is to be considered.

An estimation of the three dimensional interstitial oxygen diffusion distance may be estimated by using the formula:

$$x = \sqrt{6Dt} \tag{44}$$

where x is the diffusivity distance, D is the diffusion coefficient, and t is the time for diffusion. The diffusion coefficient is determined by:

$$D = D_o \exp\left(\frac{-Q}{RT}\right) \tag{45}$$

where D_o is the pre-exponential frequency factor, Q is the activation energy, R is the gas constant and T is the temperature. A literature survey conducted by Liu and Welsch [71] was used to determine D_o and Q for diffusivity of oxygen in β-Ti and in α-Ti at temperatures of interest. For β-Ti, D_o was determined to be 4.19×10^{-5} m^2/s and Q was 149 kJ/mol. For α-Ti, D_o was 5.75×10^{-4} m^2/s and Q was 196 kJ/mol. Substituting these values into Equation 45, the diffusion coefficient, D, can be established for the various regions of oxygen diffusion. As an estimate, the diffusion coefficient of oxygen in liquid titanium is 1×10^{-8} m^2/s [72]. If the diffusion is divided into three regions, liquid, beta and alpha, an overall diffusion distance of oxygen can be established that does not account for liquid motion in the melt.

It will be assumed that the maximum temperature the weld FZ achieves is 2273 K (2000°C). Therefore, the liquid titanium region will exist from 2273 K to 1943 K (2000°C to 1670°C) with a diffusion coefficient of 1.0×10^{-8} m^2/s. The β region will exist from 1943 K to 1153 K (1670°C to 880°C) with an average diffusion coefficient of approximately 2.93×10^{-9} m^2/s. From 1153 K to 773 K (880°C to 500°C) (temperature where oxygen diffusion becomes a significant concern), the oxygen will diffuse in the α phase (both in the FZ and HAZ) with a diffusion coefficient of approximately 4.39×10^{-13} m^2/s. Cooling rates of GTAW of titanium are given from 10 K/s to 1000 K/s [9]. Assuming that the weld takes from approximately 5-7 seconds to harden [21], a cooling rate of approximately 55 K/s is obtained. The liquid stage will therefore exist for 6 seconds, the β stage for 14.4 seconds and the α stage for 6.9 seconds. Substituting these values into Equation 44 yields a diffusivity distance of 1107 μm. This means that at each weld pass, oxygen may diffuse over 1 mm into the weld FZ. If the motion of the fluid

flow of the molten pool were to be taken into account, the distance of oxygen travel would be even greater.

Considering now internal oxygen diffusion, if we add up the total time that the weld FZ is above 773 K (500°C), we will obtain a length of time that oxygen diffusion is of concern in the base metal HAZ. This length is 27.3 seconds. Substituting this value into Equation 44 with the appropriate value of D, gives us a total oxygen diffusion distance of approximately 693 μm. Therefore, all oxygen within this 693 μm distance is capable of diffusing into the weld FZ, thereby leading to increased hardness values of the weld zone.

The diffusion of oxygen will be towards the higher temperature weld pool. In Chapter IX we saw that there was clearly a buildup of oxygen inside the base metal HAZ as the FZ is approached. There was also a buildup of oxygen at the far edge of the HAZ near the BM. These different areas with increased oxygen concentrations are likely the result of differences in oxygen diffusion constants between the α and β phases of titanium. Since the oxygen diffuses quicker through the β phase, this will leave a zone of depleted oxygen in the HAZ. This depleted oxygen region may then possess a low hardness (strength) value where premature failure of the weld zone is possible. Clearly this is an important aspect that must eventually be more fully studied.

The formation of yttrium oxysulfide has the benefit of removing oxygen introduced during the welding process from the melt. Oxidation of the yttrium oxysulfide to yttrium oxide sulfate as the temperature of the weld cools removes even more of the available oxygen in the matrix. By removing this oxygen, possible interstitials inside the FZ are removed. At low yttrium concentrations, this results in a weld FZ that is not quite

as strong as the matching filler metal welds, but one that has a significant amount of increased ductility. This increased ductility could be of great advantage to commercial applications. Furthermore, the addition of yttrium and subsequent formation of yttrium oxysulfide, as discussed previously, will increase the amount of supercooling inside the melt. This increase will most likely lead to higher solidification rates due to both increased growth rates of the dendrites into the supercooled liquid and due to increased chances for heterogeneous nucleation sites to grow. This will lead to a decreased amount of time allowed for oxygen diffusion into the melt, where diffusion distances are large.

Another catalyst may be required, along with the yttrium particles, in order to provide heterogeneous nucleation sites at the FZ outer edges that will block the epitaxial growth process while not causing a buildup of particles at the solidification front. Also, while yttrium does indeed appear to be a possibility for heterogeneous nucleation, there may be other possibilities as well. Other REM's that are not very soluble in titanium and will easily form an oxide that will exist at high temperatures include cerium, lanthanum, gadolinium and erbium [73]. To date there has been no known research into the effects of other REM's on titanium weld microstructures.

XIII. SUGGESTIONS FOR FUTURE STUDIES

Possible future studies indicated by questions arising from the results of this work include:

1. Determine exactly why yttrium affects the penetration depth in GTAW of titanium alloys. Does yttrium itself act as a surface active element in the weld pool or does it serve to enhance the effects of sulfur or oxygen in the weld pool? This could be of extreme value in that greater penetration depths lead to reduced costs in processing.
2. Determine what effects a commercial (non-glovebox) GTAW process would have on enhancing heterogeneous nucleation and mechanical properties in the weld. That is, what is the effect of additional amounts of oxygen introduced into the weld melt during the welding process?
3. Determine the effects of yttrium on high temperature creep properties and corrosion characteristics of these welds.
4. Determine definitively what type of yttrium particles are forming in the melt and how they may be changing as the temperature decreases.
5. Investigate means to promote heterogeneous nucleation inside the fusion zone to prevent the internal diffusion of oxygen from the base metal towards the fusion zone and the external diffusion of oxygen from the shield gas/atmosphere to the weld melt/fusion zone. This may involve use of another catalyst along with yttrium in order to promote a greater amount of heterogeneous nucleation at low concentrations of additives or may involve using another inoculant.

XIV. CONCLUSIONS

1. It was observed that the addition of small amounts of yttrium to gas tungsten arc welds of Ti-5111, near-alpha titanium alloy, yields a refined prior-beta grain boundary structure, especially near the centerline of a weld. These additions, however, are unable to prevent epitaxial growth from the outer edges of the fusion zone across the weld pass. While it was initially believed that yttria would form in the weld melt, the reason for the grain refinement is now believed to be due to the formation of yttrium oxysulfide particles in the weld melt. These particles are then believed to create a drag force on the solidification front, thereby slowing down the growth of preferentially oriented grains and allowing other non-favorably oriented grains to "rotate" to a preferred growth direction and continue to grow. This process limits the effects of the competitive growth process of grains typically seen in weld microstructures.
2. The yttrium oxysulfide particles formed in the melt may either be small enough such that they are encased into the matrix or large enough such that they are pushed ahead of the solidification front thereby leading to increased concentrations at the grain boundaries.
3. In order to accomplish heterogeneous nucleation in the weld, a much greater amount of yttrium must be added so that the time required for grains to heterogeneously nucleate is lower than the time required for a grain to epitaxially grow across an entire weld pass. However, it has been seen that additions over 200 ppm Y have an adverse affect on mechanical properties of the weld as compared to 50 ppm Y additions. The reason for this decrease in mechanical properties may be

the result of excessive buildup of particles at the prior-β grain boundaries. Perhaps another catalyst, such as another rare earth element, is required, along with the yttrium particles, in order to provide heterogeneous nucleation sites at the fusion zone outer edges that will block the epitaxial growth process while not causing this buildup of particles at the solidification front.

4. While yttrium does indeed appear to be a possibility for heterogeneous nucleation, there may be other possibilities as well. Other rare earth metals that are not very soluble in titanium and will easily form an oxide that will exist at high temperatures include cerium, lanthanum, gadolinium and erbium. To date there has been no known research into the effects of other rare earth metals on titanium weld microstructures.
5. Adding yttrium to the weld filler metal resulted in a much more turbulent weld with much greater penetrations as compared to the matching filler metal. This result is believed to be due to yttrium either acting as a surface activant itself or serving as an enhancement to the surface active elements sulfur or oxygen.
6. Microhardness testing indicates that the fusion zone in the modified 50 ppm Y filler metal weld is softer than the 200 ppm Y filler metal weld, which is softer than that of the matching filler metal weld. The reason for this is believed to be due to the formation of yttrium oxysulfide particles in the melt and then further oxidation of these particles to yttrium oxide sulfate, thereby scavenging oxygen that would otherwise fill interstitial sites in the weld matrix. The increases value of hardness in the 200 ppm Y filler metal weld as compared to the 50 ppm Y filler metal weld is

likely the result of either platelet refinement, increased platelet randomization or of oxide dispersion strengthening.

7. The tensile ductility in a gas tungsten arc weld has been shown to be dramatically increased with the addition of 50 ppm Y, while addition of 200 ppm Y showed a loss of ductility as compared to the 50 ppm Y, but still above that of the matching filler metal weld. This increase in ductility was believed to be due to the refinement of the prior-β grain boundaries and reduced amount of interstitial oxygen in the weld FZ. The loss of ductility with increasing yttrium concentrations is believed to be due to the increasing concentrations of particles at the weld's prior-beta grain boundaries.
8. Results of wave-length dispersive spectroscopy scans indicate that oxygen is indeed diffusing from the base metal into the weld fusion zone. This diffusion creates a buildup of oxygen in the base metal heat affected zone, and an area of depleted oxygen, which may lead to points where premature failure of the weld may occur.
9. Fracture toughness, as measured by J_{IC}, was shown to drastically decrease in all the welds made as compared to the base metal. Matching filler metal welds and modified Y welds showed values of J_{IC} that were approximately the same. Therefore, the additions of small amounts of yttrium did not have much of an effect on J_{IC} fracture toughness values. As in other metal systems, such as C-Mn steels, it may be necessary to alloy various metals in order to improve weld toughness.
10. The tearing modulus, which is a measure of the ability of a metal to resist crack propagation, in the modified 50 ppm Y filler metal weld was seen to dramatically increase over that of the matching filler metal weld. This increase in the tearing

modulus leads to increased amount of energy required for complete failure of a component. This extra energy requirement for failure may prevent catastrophic failure of a component, thus making identification and repair of a crack easier.

APPENDIX A

INSTRON Operating Procedures

Some important points learned involving use of the INSTRON test equipment that must be remembered for use by future students are listed here:

1. Strain and thus strain rate is based upon the gage length of the strain gage and not the length of the specimen.
2. The maximum number of data points that may be stored per interval run is 5,160.
3. Minimum strain rate allowed is $2x10^{-4}$ %/min.
4. When position is used to end the run, the actual value inputted must be exceeded to stop the run, not a delta reading on the strain gage.
5. When setting a value of displacement that you want the specimen achieve, it must be remembered to convert how much the strain gage must displace to give the total value of displacement required.
6. When using the waveform generator on the control panel, if the red stop button is pushed, the machine will automatically switch to *Position Control*, no matter what you were using for control previously (i.e. Load Control).

The points learned here took much trial and error. It is hoped that these points provide valuable input to the next student.

To conduct a tensile test using the INSTRON 8502 testing machine, the following procedure is employed:

1. Ensure water is supplied to cool hydraulic system.
2. Ensure extensometer connected to channel-1 on tower.
3. Ensure load gage connected on tower.
4. Power on the control tower.
5. Power on the hydraulic system.
6. INSTRON control panel will run a self-diagnostic.
7. Ensure cross-head adjusted to proper height.
    a. If adjustment is necessary, actuator hydraulics should be set to low.
    b. Remove safety restraint.
    c. Adjust cross-head height.
    d. Replace safety restraint.
8. Set actuator hydraulics to high.
9. Remove pin from extensometer.
10. Select set-up under Strain.
    a. Select – Calibrate – Auto – Go
    b. Calibrated light will blink rapidly while calibrating and then remain on steady when done.
11. Select set-up under Load.
    a. Select – Calibrate – Auto – Go
    b. Calibrated light will blink rapidly while calibrating and then remain on steady when done.
12. Screw specimen into one side of the grips.
13. Raise actuator to allow the specimen to be screwed into the other grip.

14. Start Series IX software.
    a. Select Test
    b. Enter operator/specimen name/test method.
    c. Verify cross-sectional area of sample.
15. Press *Remote* on control panel.
16. Test will automatically run.
17. When test finished, select *Load* – Go to target value of 0 to unload.
18. Remove sample from one of the grips.
19. Select *Position* – Immediate
20. Lower actuator to allow specimen removal.
21. Power off equipment when finished.

Procedure to set up INSTRON 8502 for Tensile Test using Series IX Automated Materials Testing Program:

Series IX is activated by typing MT at the C:/MT> prompt when displayed on the computer screen. To change or create a method, go to METHOD and press Enter. Select Create/Modify/whatever you desire to do, and then select TENSILE. This program is under number 03, but you may create your own, if so desired.

MAIN

Method label: Tensile Test – SI Units

Method description: Sample #

Database file: ASCII

Polarity: No

Input unit type: SI

Machine control: Standard

Extensometer: Standard (or Disabled for cross-head actuator control)

133 data collection: Disabled

SPECIMEN

Type: ASTM

Geometry: Area

Cross-sectional area: Enter your specific cross-sectional area for specimen testing

Entry method: Manual

Limit check: No

Extensometer gage length: Enter specific extensometer gage length (12.7250 mm)

Specimen gage length: Enter your specific gage length for specimen testing

Dimension entry: Before data collection

Specimen label: Disabled

TEST

Test direction: Down

Control Channel: Strain (or Actuator for cross-head control)

Control: (strain control – loop shaping parameters in 8502 must be set to match specimen characteristics)

Break detect: Load threshold

Load level: Enter load that will determine break detect

High extension: Enter maximum extension for specimen to achieve

Load cell used: 250 kN

Strain rate: Enter strain rate to be used (0.003 to 0.007 min^{-1} typical through specified yield stress and then increase rate so as to produce failure in approximately one additional minute)

Rate change by: If necessary

Second ramp rate: Enter desired second ramp rate to use if necessary (~0.0025 mm/min)

Action: Stop

Machine stop: disable

DATA

Begin data sampling: Computer

Data compression: Enabled

Sampling rate: 0.5-1 pts/sec

Data rate reduction: Enable (Use reduction factor of 4 after 30 min if a long test)

Axial strain: Channel 1

Transverse strain: Disabled

Switch to extension: 5%

REPORT

Report header: Enter your name and description of sample

Temp: Enter room temperature

Default: 73F

Humidity: No

Default: 50%

Statistical analysis: Enabled

Min & max: No

Mean std deviation: No

Coefficient of variance: No

Reduced report: Disabled

Report output default: File

GRAPHICS

Test screen graphics: Enabled

Plot size: Large screen

Plot # per screen: 10

Show construction lines: Yes

Calculation lines displayed: 8

Auto plot to plotter: Disabled

Automatic scaled axis limits

X-axis type: Displacement

Y-axis type: Load

CALCULATIONS

To screen and printer (max of 7 to screen)

Calc #	Description	Unit
1.2	Max Load	kN
1.4	Max Stress	MPa
1.5	Max Strain	mm/mm
10.4	Yield Stress	MPa
15.4	Break Stress	MPa
15.5	Break Strain	mm/mm
19.3	Young's Modulus	MPa

APPENDIX B

Additional Fractography Images from Tensile Specimens

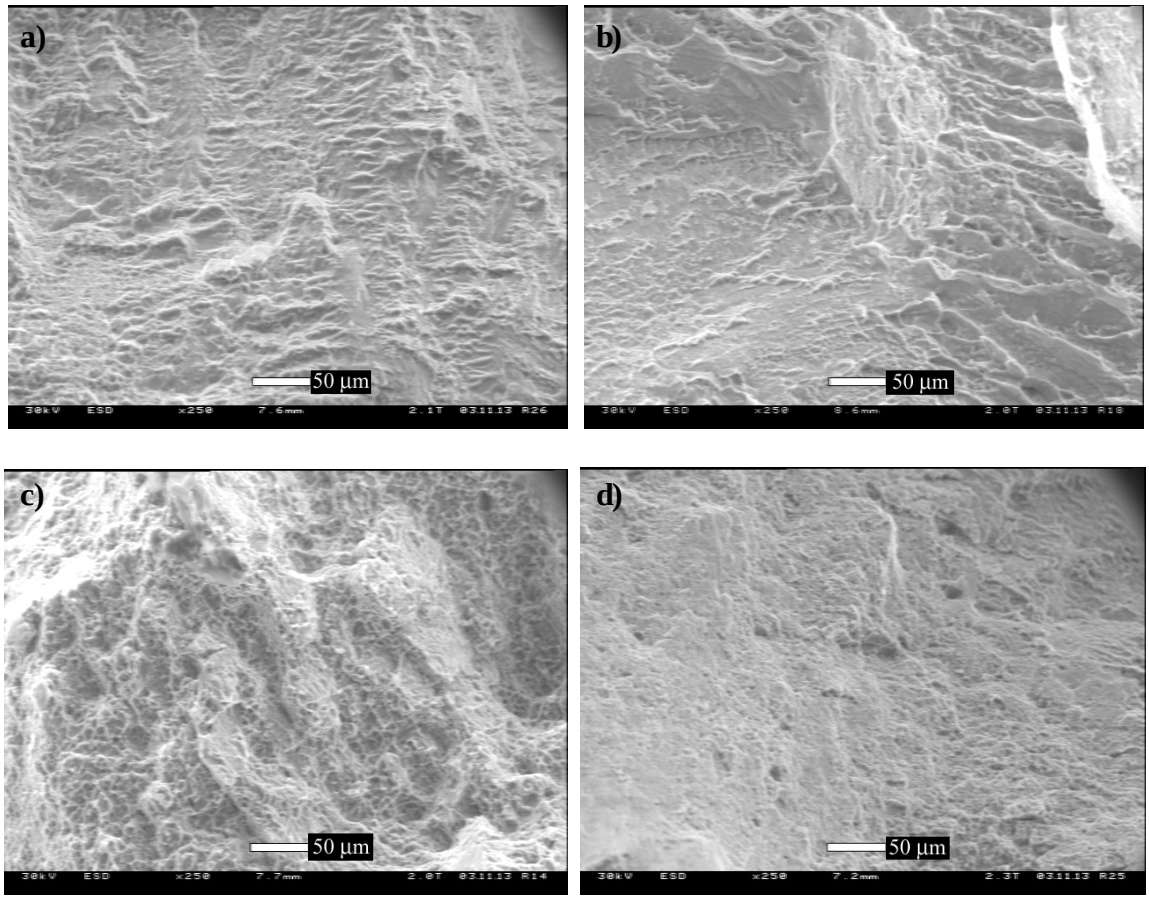

Figure 123: Fracture surfaces of tensile specimens, 250x. (a) Base metal, (b) matching filler metal weld, (c) modified 50 ppm Y filler metal weld, and (d) modified 200 ppm Y metal.

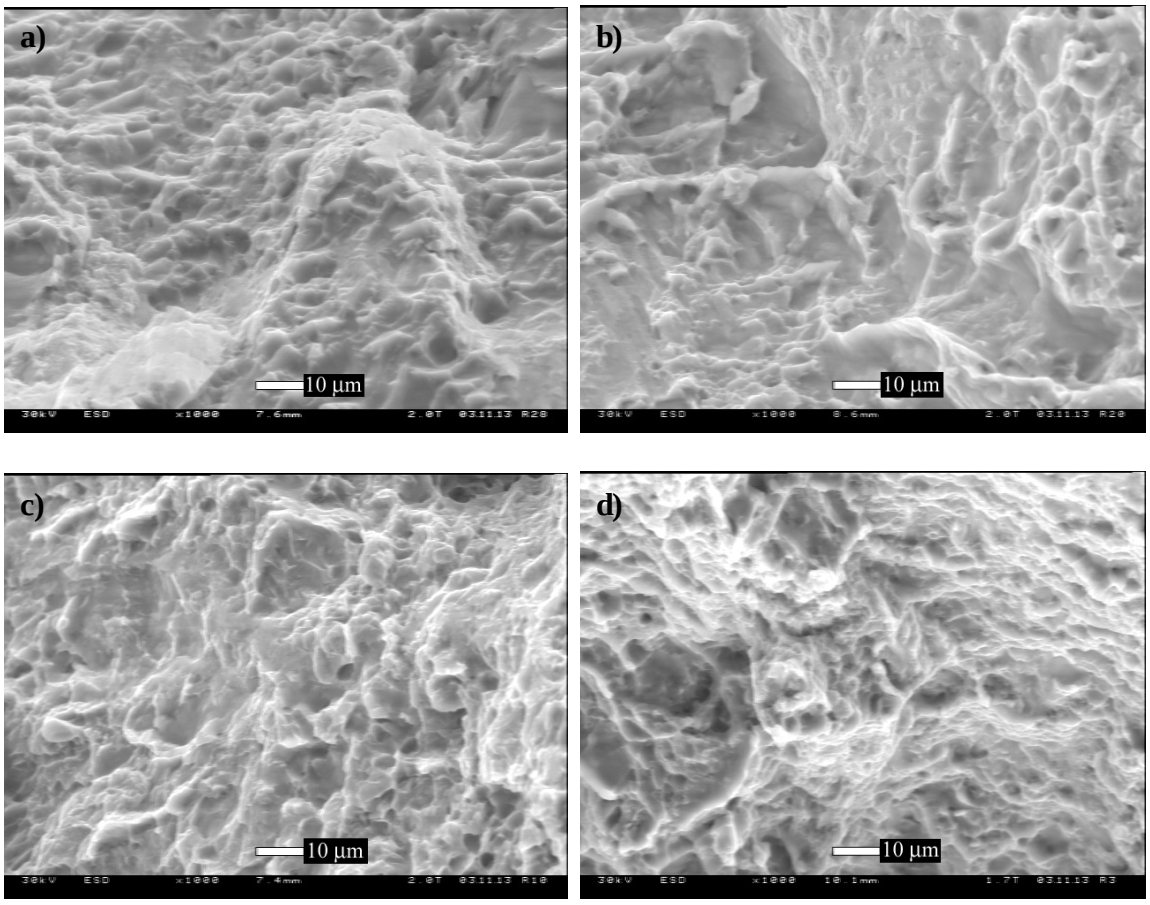

Figure 124: Fracture surfaces of tensile specimens, 1000x. (a) Base metal, (b) matching filler metal weld, (c) modified 50 ppm Y filler metal weld, and (d) modified 200 ppm Y metal.

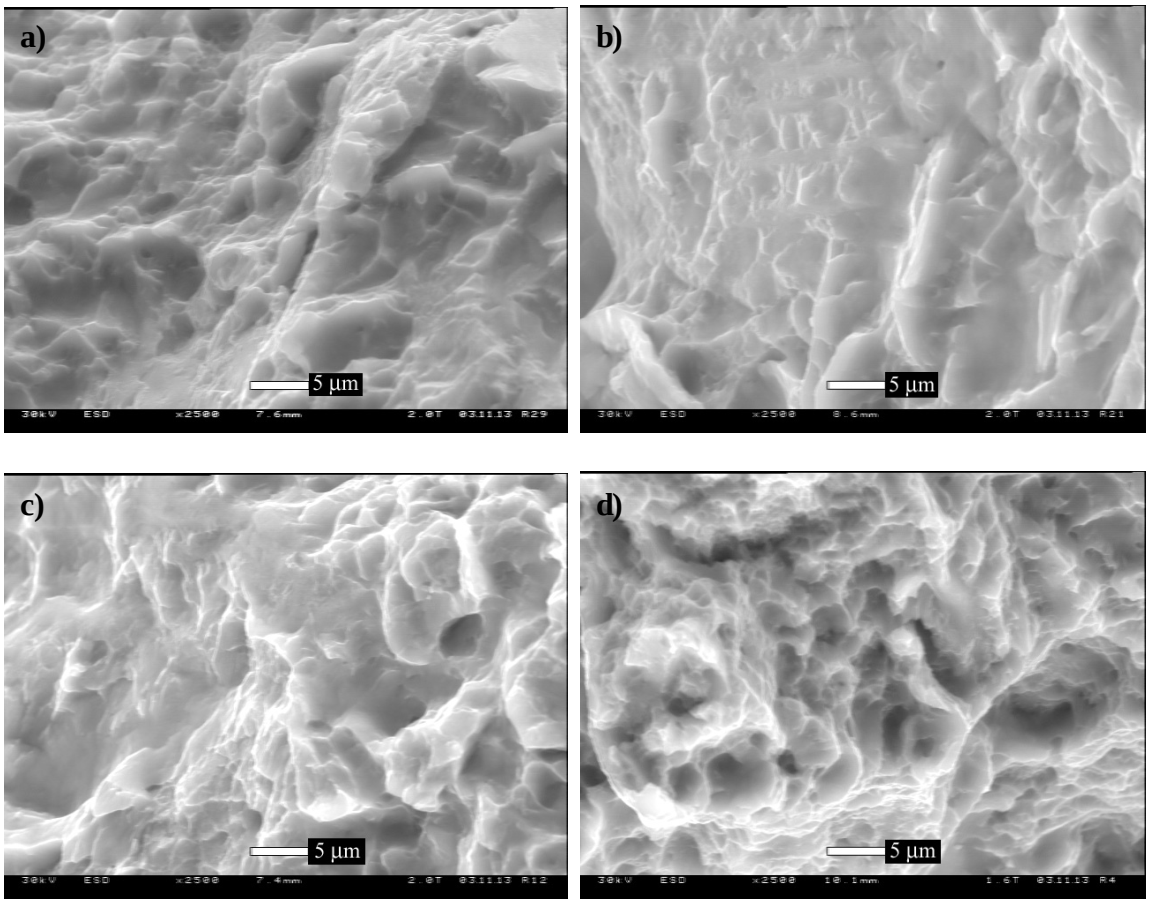

Figure 125: Fracture surfaces of tensile specimens, 2500x. (a) Base metal, (b) matching filler metal weld, (c) modified 50 ppm Y filler metal weld, and (d) modified 200 ppm Y metal.

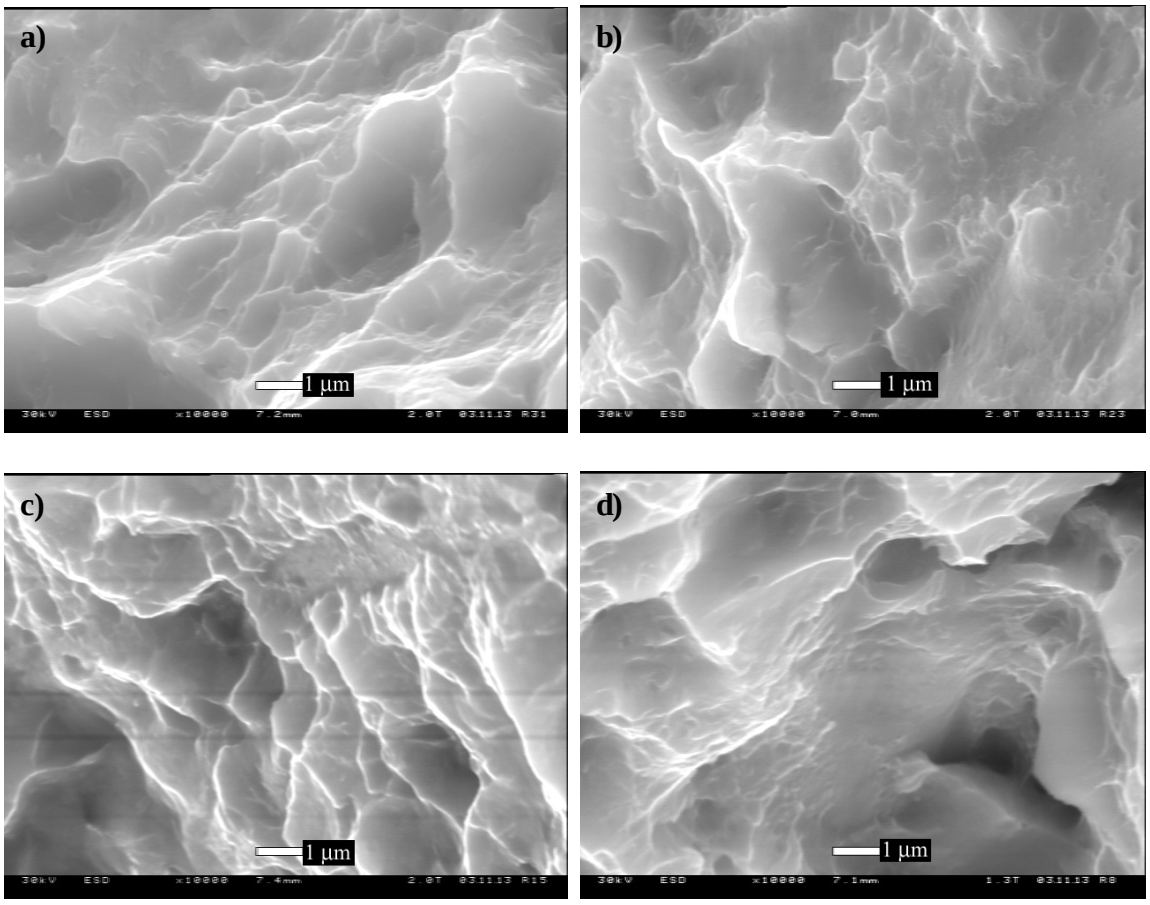

Figure 126: Fracture surfaces of tensile specimens, 10,000x. (a) Base metal, (b) matching filler metal weld, (c) modified 50 ppm Y filler metal weld, and (d) modified 200 ppm Y metal.

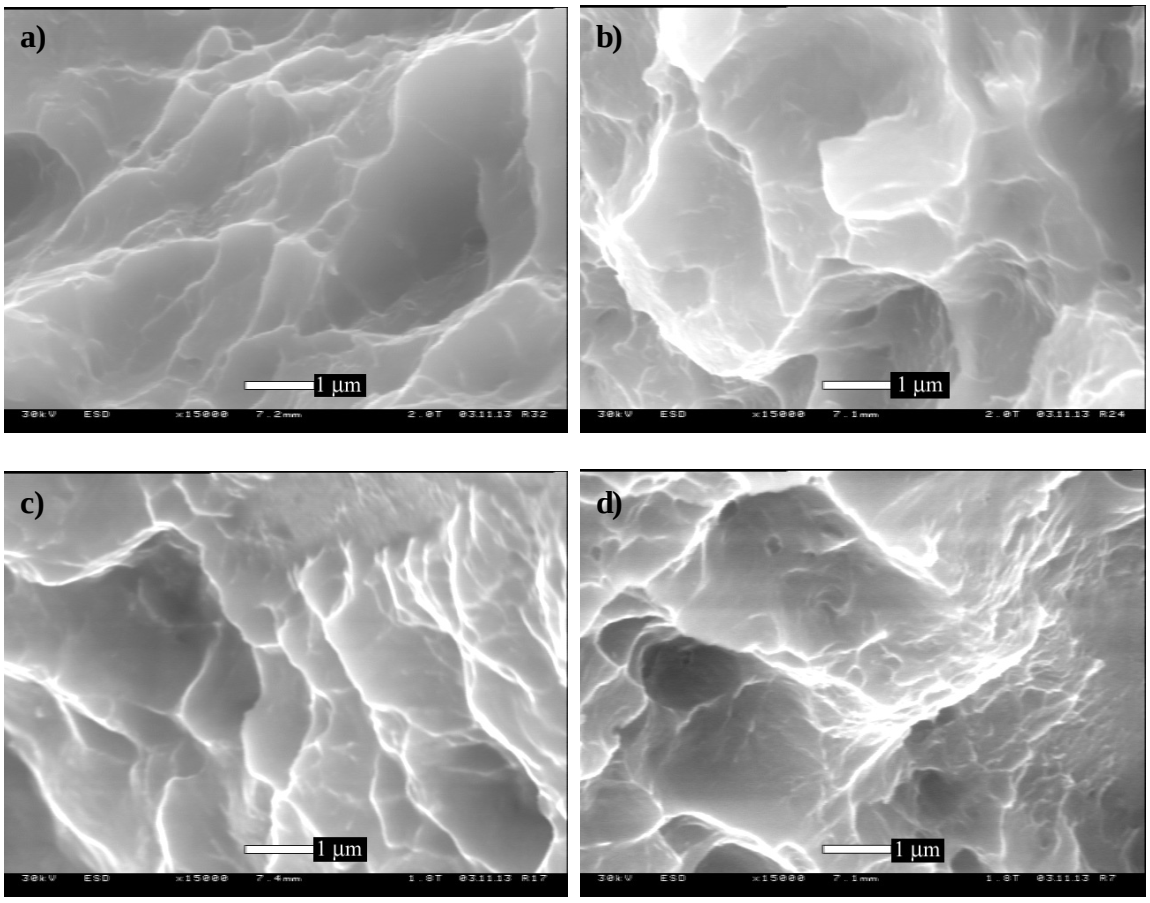

Figure 127: Fracture surfaces of tensile specimens, 15,000x. (a) Base metal, (b) matching filler metal weld, (c) modified 50 ppm Y filler metal weld, and (d) modified 200 ppm Y metal.

APPENDIX C

Additional WDS Scans

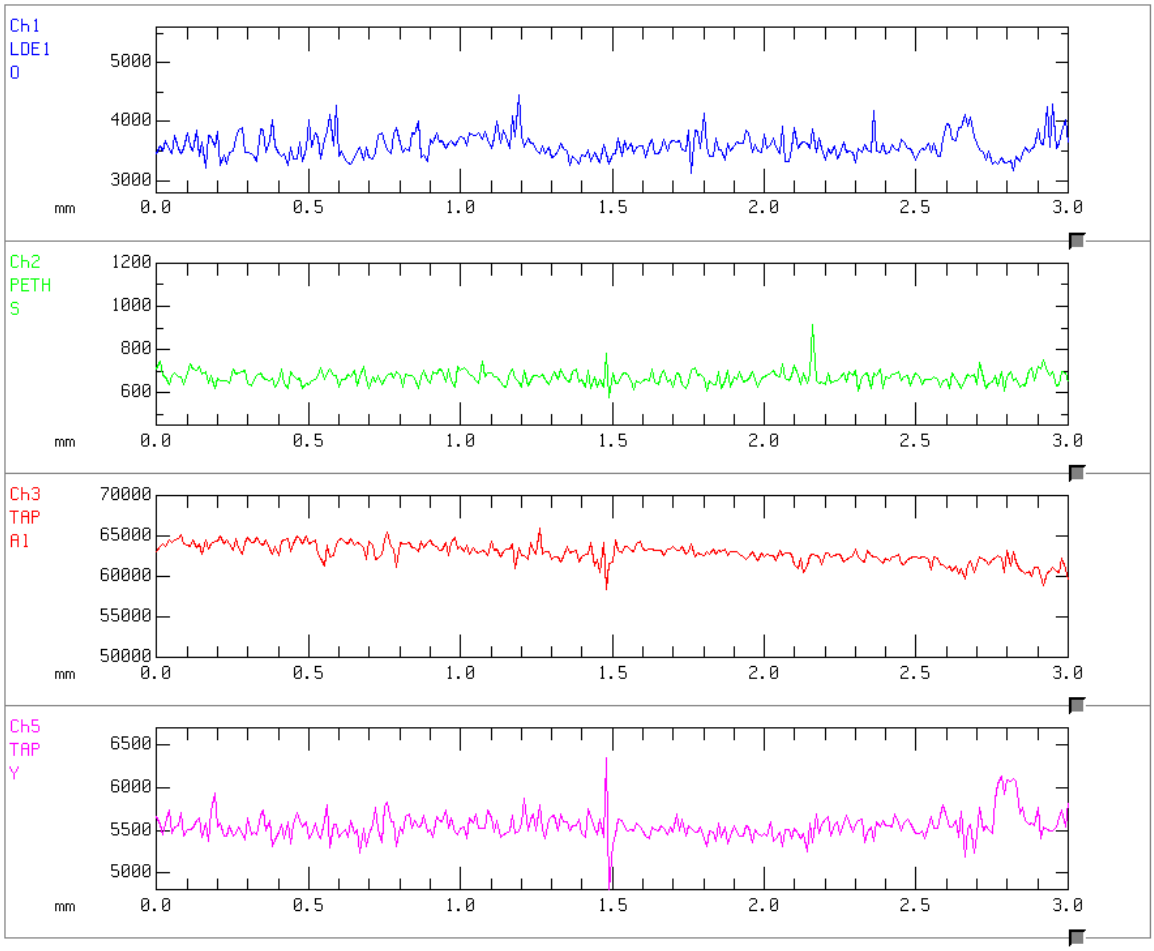

Figure 128: WDS scan of Ti5111 base metal plate 0 to establish background (1000ms dwell time).

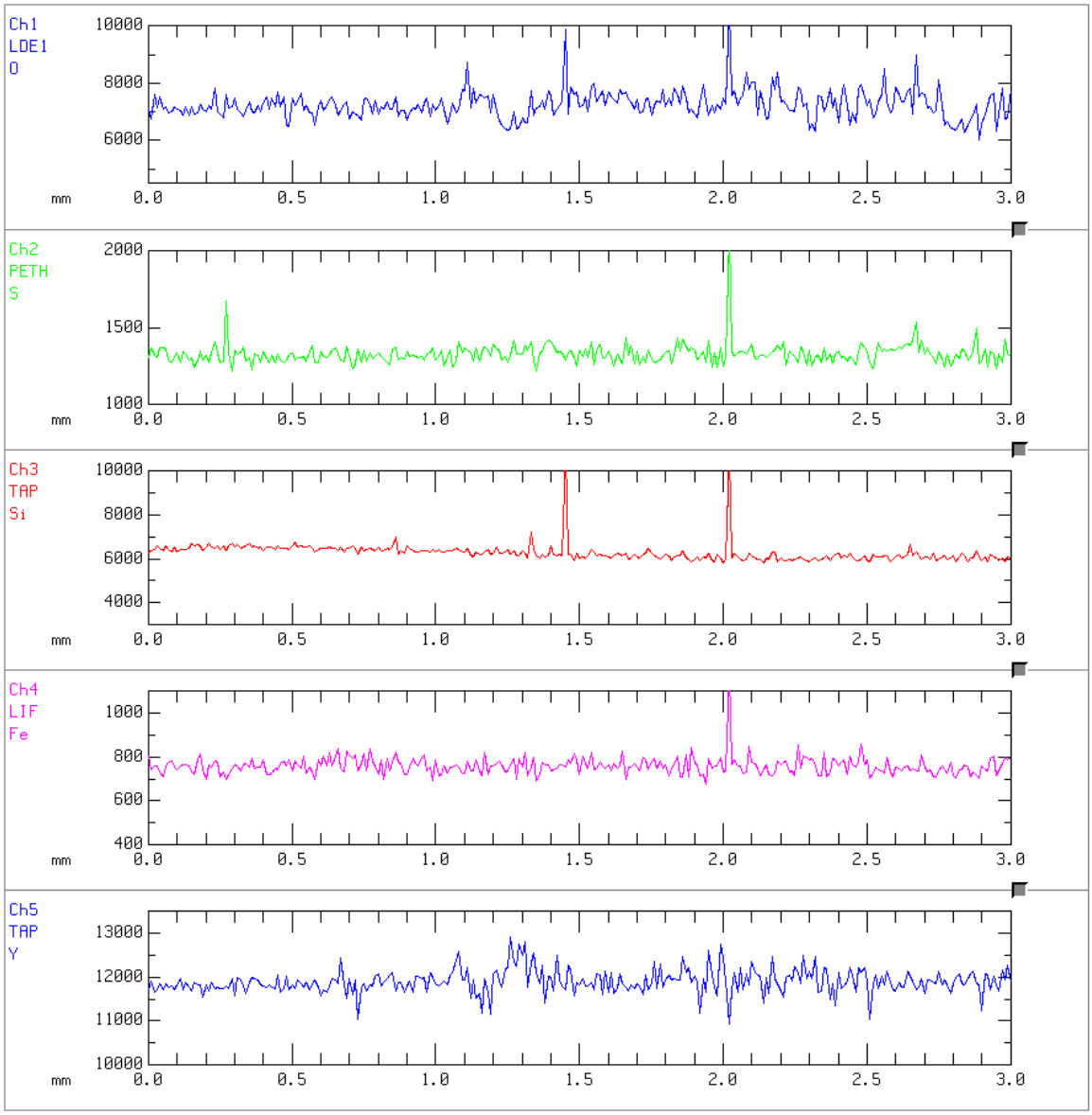

Figure 129: WDS scan of Ti5111 base metal plate 0 to establish background (2000ms dwell time). Elements O, S, Y, Si, Fe.

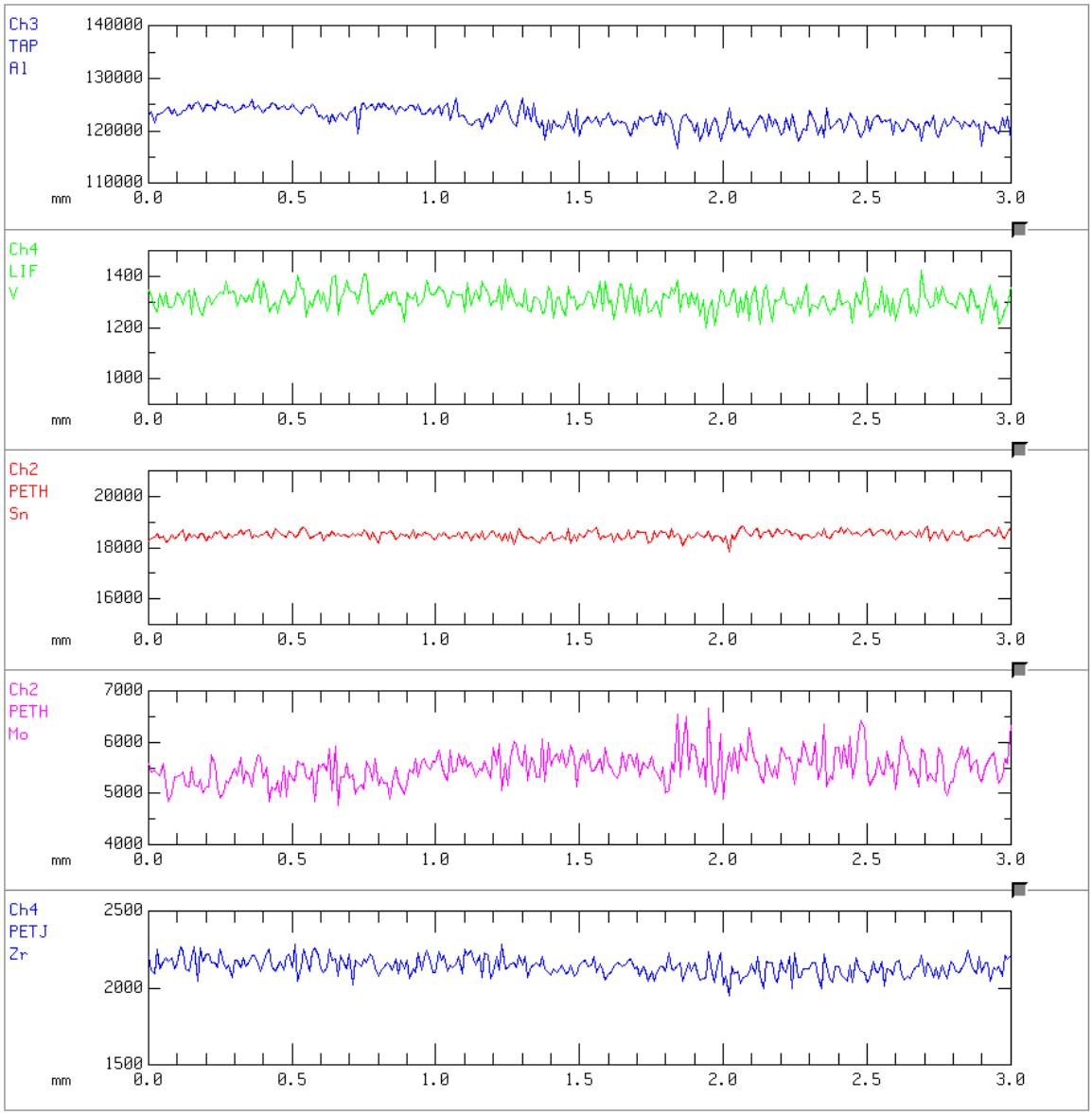

Figure 130: WDS scan of Ti5111 base metal plate 0 to establish background (2000ms dwell time). Elements Al, V, Sn, Mo, Zr.

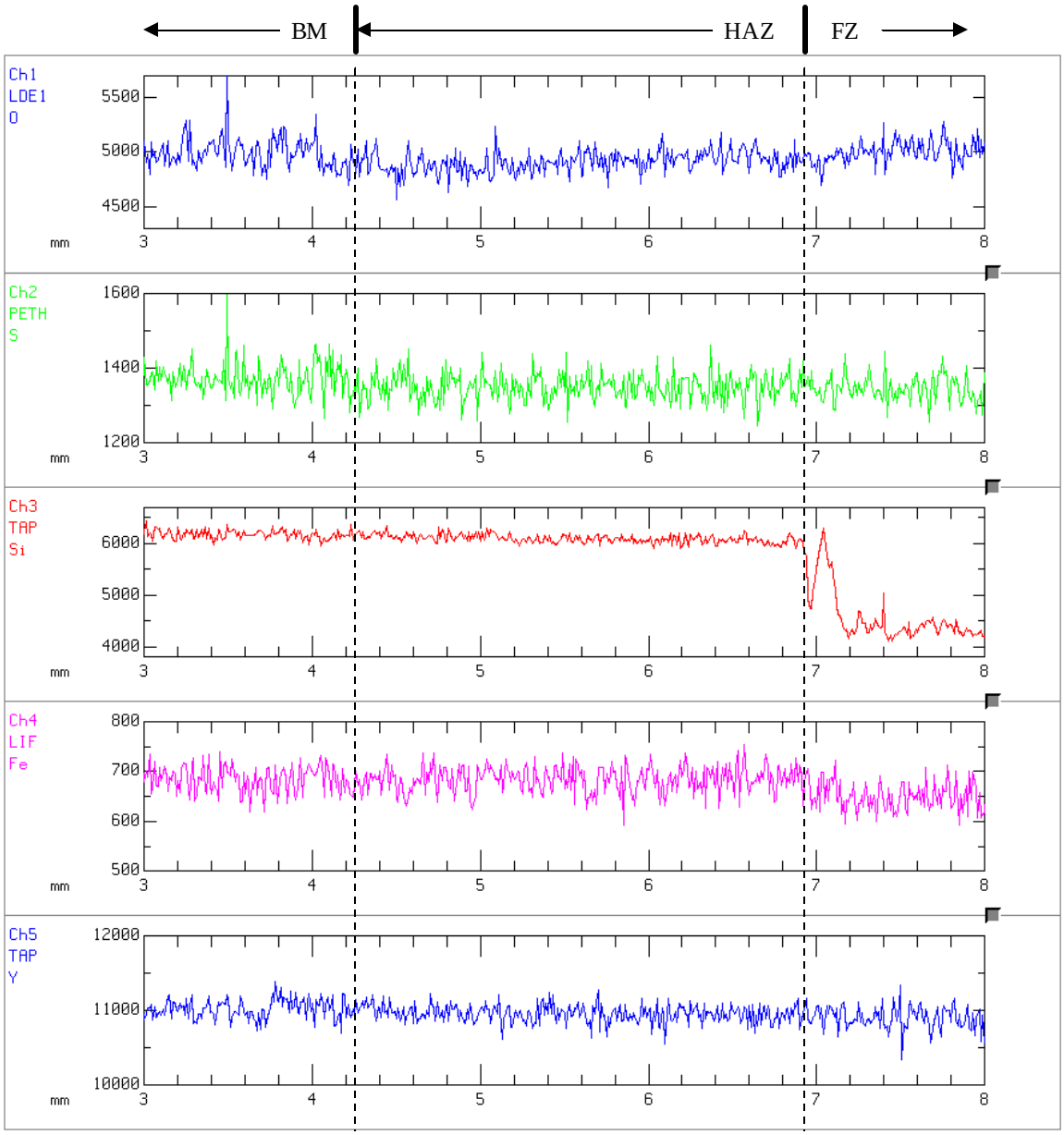

Figure 131: WDS scan of Ti5111 matching filler metal weld showing expanded HAZ area from Figure 50 (2000ms dwell time). Elements O, S, Y, Si, Fe. Observe that the O levels just outside the HAZ in the BM are lower than the average and then increases just inside the HAZ before it falls for the next ~ 1mm and then increases steadily towards the FZ.

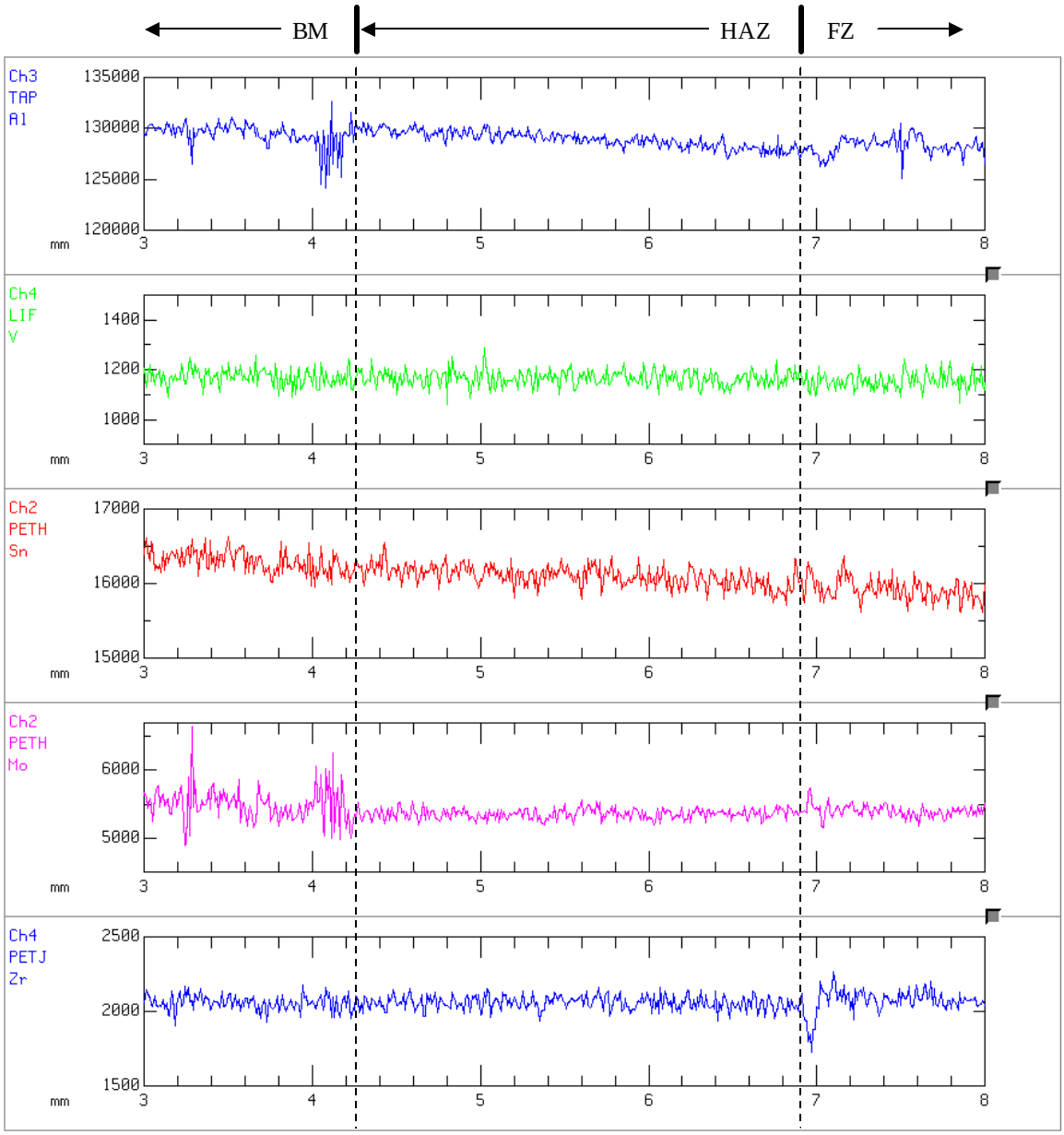

Figure 132: WDS scan of Ti5111 matching filler metal weld showing expanded HAZ area from Figure 51 (2000ms dwell time). Elements Al, V, Sn, Mo, Zr.

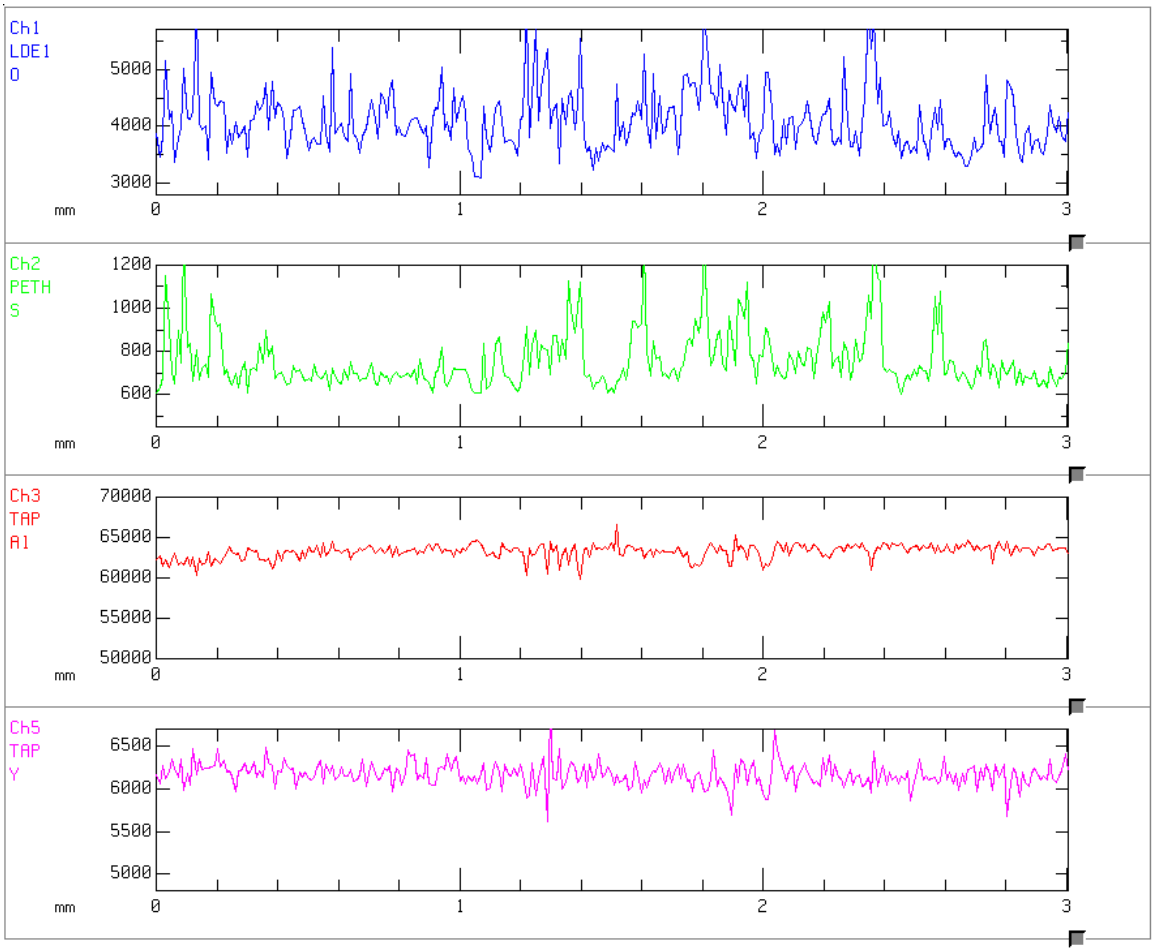

Figure 133: WDS scan of Ti5111 base metal plate 1 to establish background (1000ms dwell time). Elements: O, S, Al, Y.

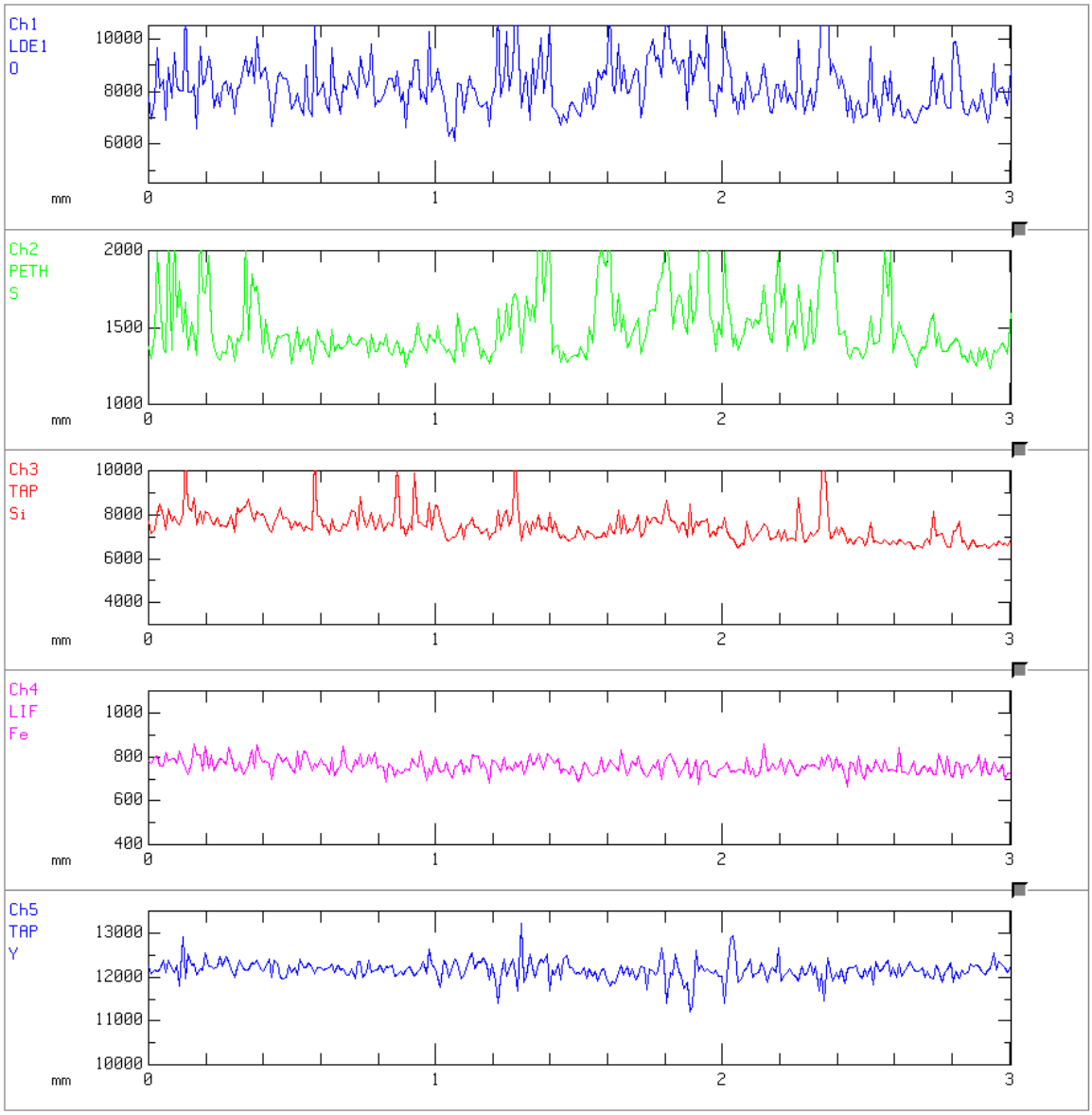

Figure 134: WDS scan of base metal plate 1 to establish background (2000ms dwell time). Elements: O, S, Y, Si, Fe.

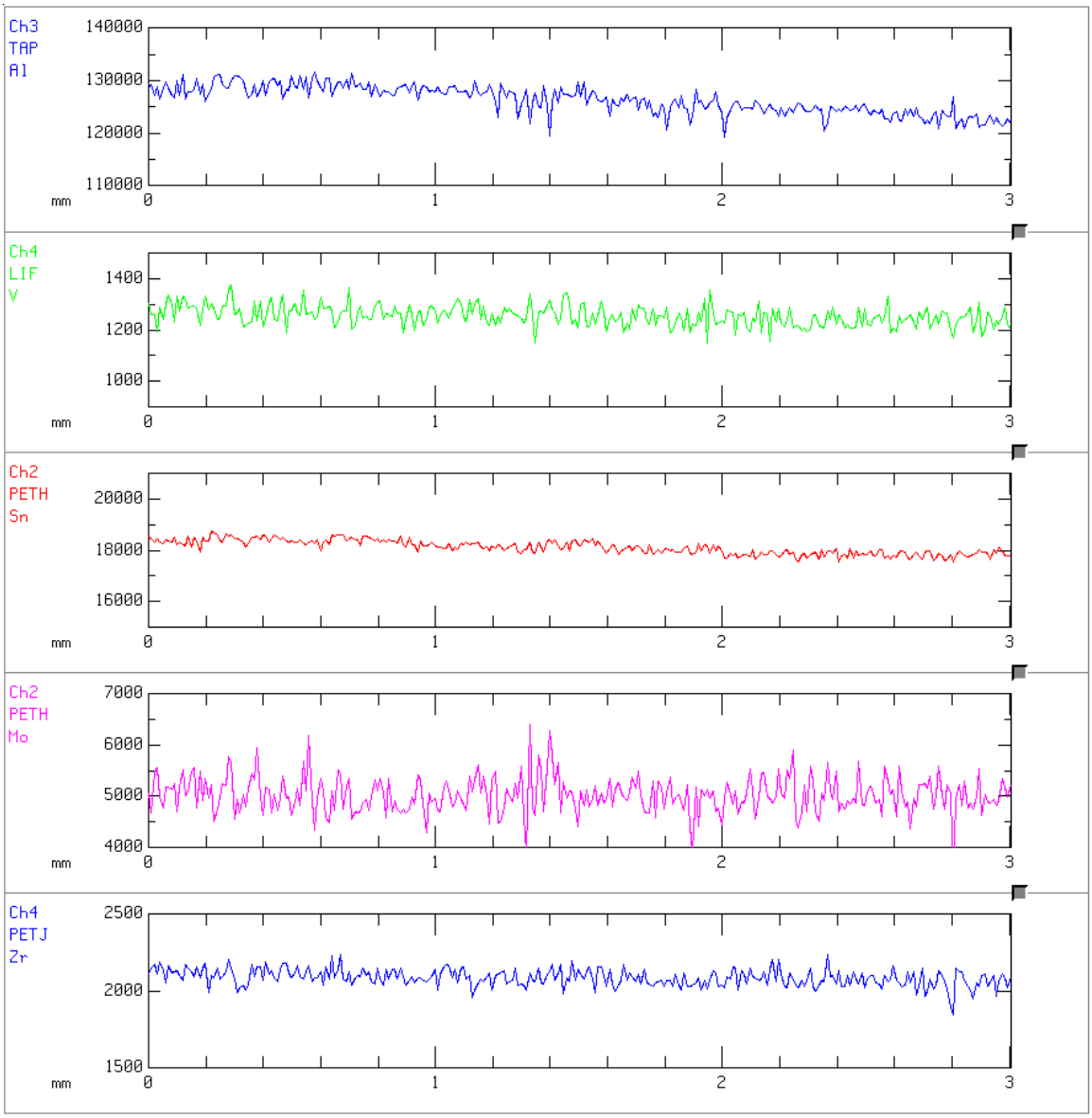

Figure 135: WDS scan of Ti5111 base metal plate 1 to establish background (2000ms dwell time). Elements: Al, V, Sn, Mo, Zr.

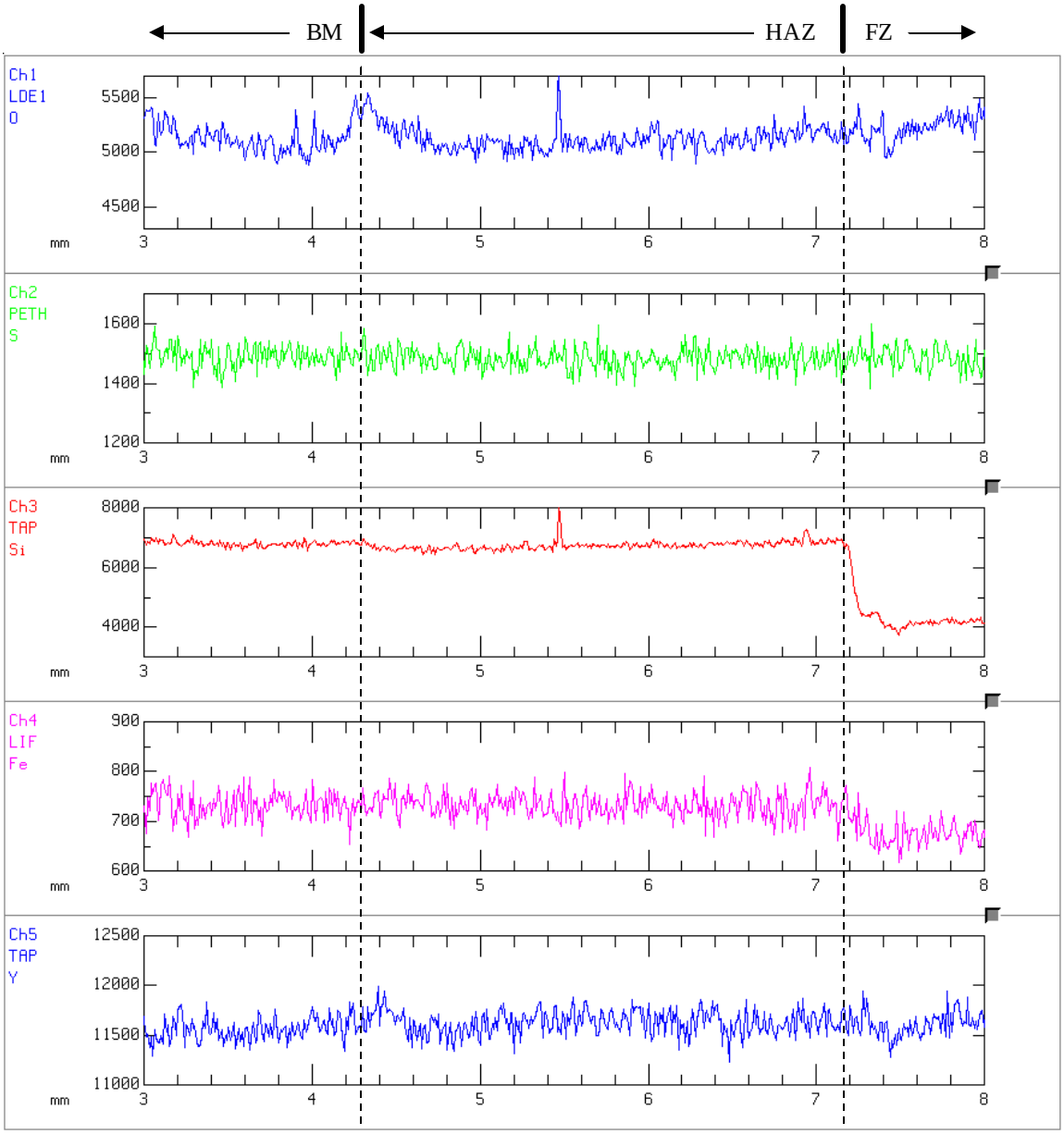

Figure 136: WDS scan of Ti5111 modified 50 ppm Y filler metal weld showing expanded HAZ area from Figure 55 (2000ms dwell time). Elements O, S, Y, Si, Fe. Observe that the O levels from the BM to FZ behave very similarly to those of the matching filler metal.

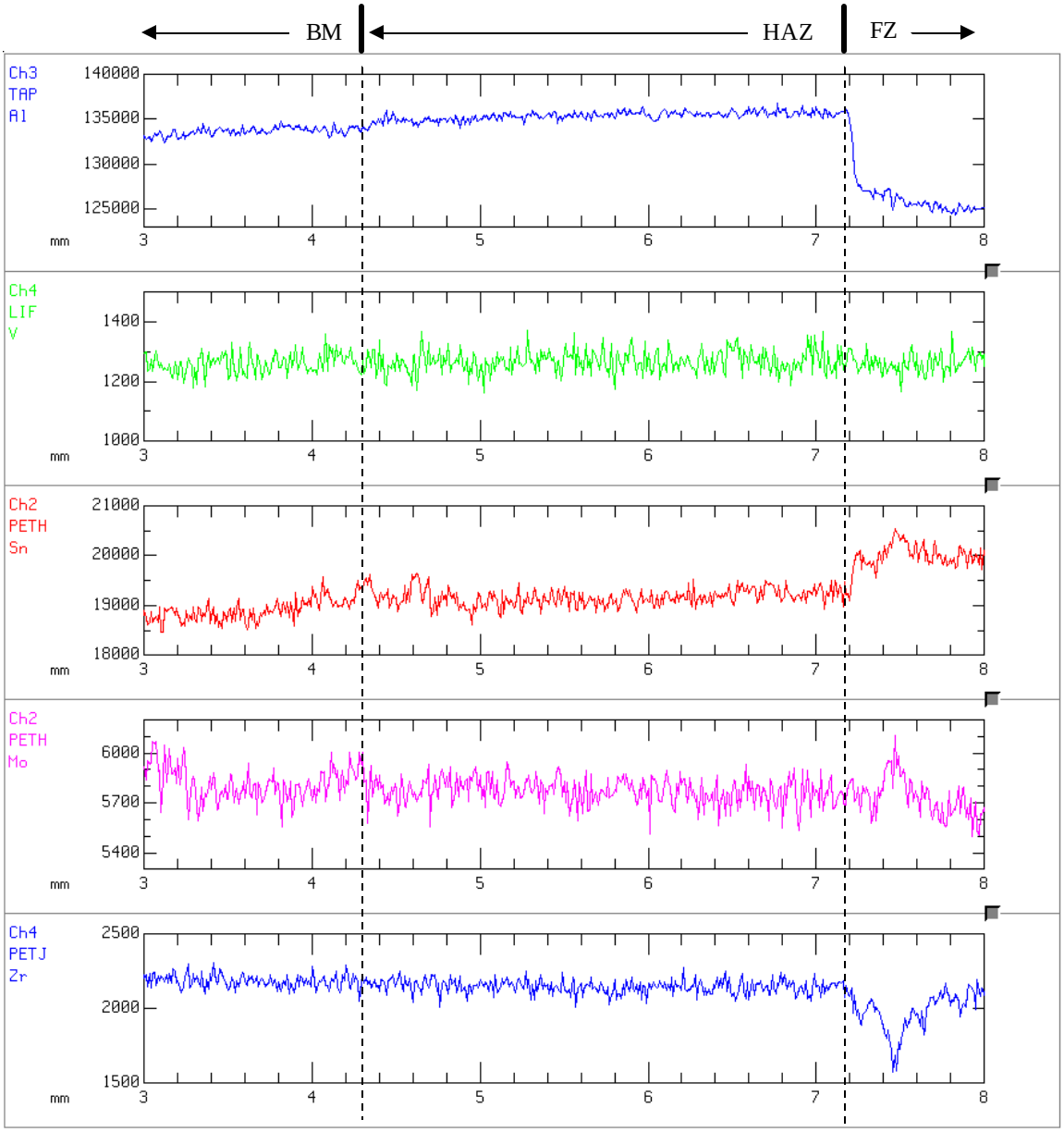

Figure 137: WDS scan of Ti5111 modified 50 ppm Y filler metal weld showing expanded HAZ area from Figure 56 (2000ms dwell time). Elements Al, V, Sn, Mo, Zr. Note valleys of Zr and Al just inside the weld FZ corresponding to peaks of Mo and Sn.

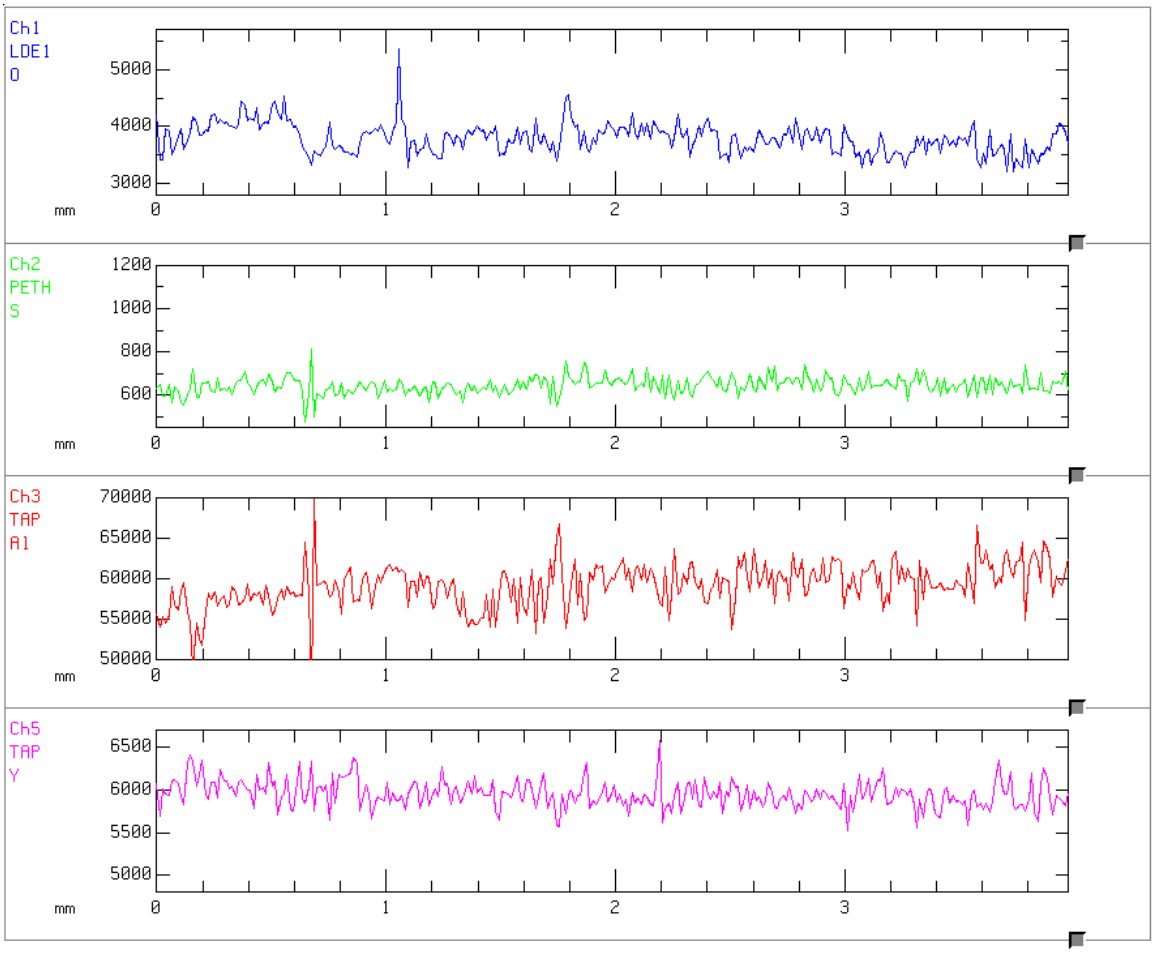

Figure 138: WDS scan of Ti5111 base metal plate 2 to establish background (1000ms dwell time). Elements: O, S, Al, Y.

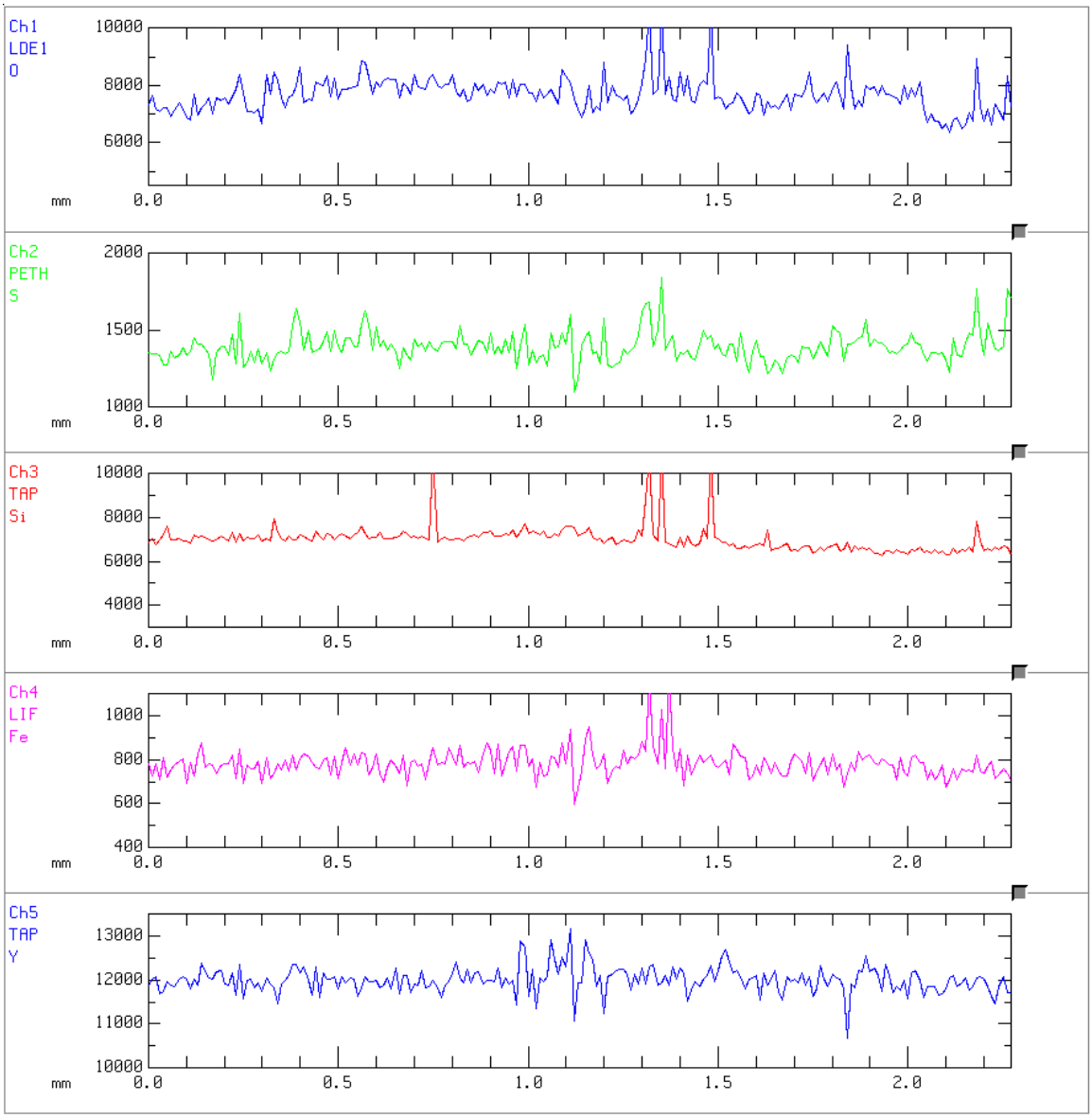

Figure 139: WDS scan of Ti5111 base metal plate 2 to establish background (2000ms dwell time). Elements: O, S, Y, Si, Fe.

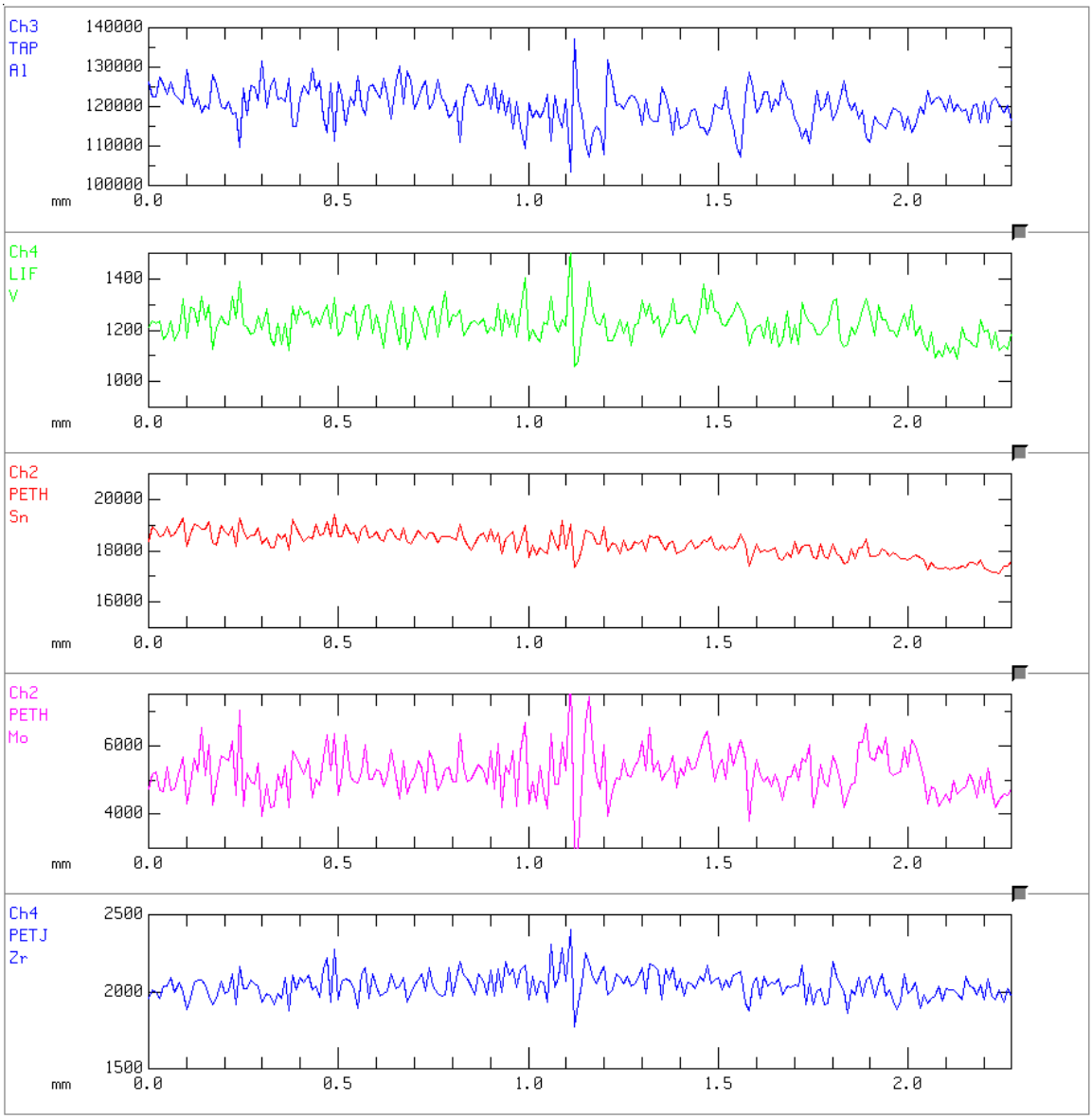

Figure 140: WDS scan of Ti5111 base metal plate 2 to establish background (2000ms dwell time). Elements: Al, V, Sn, Mo, Zr.

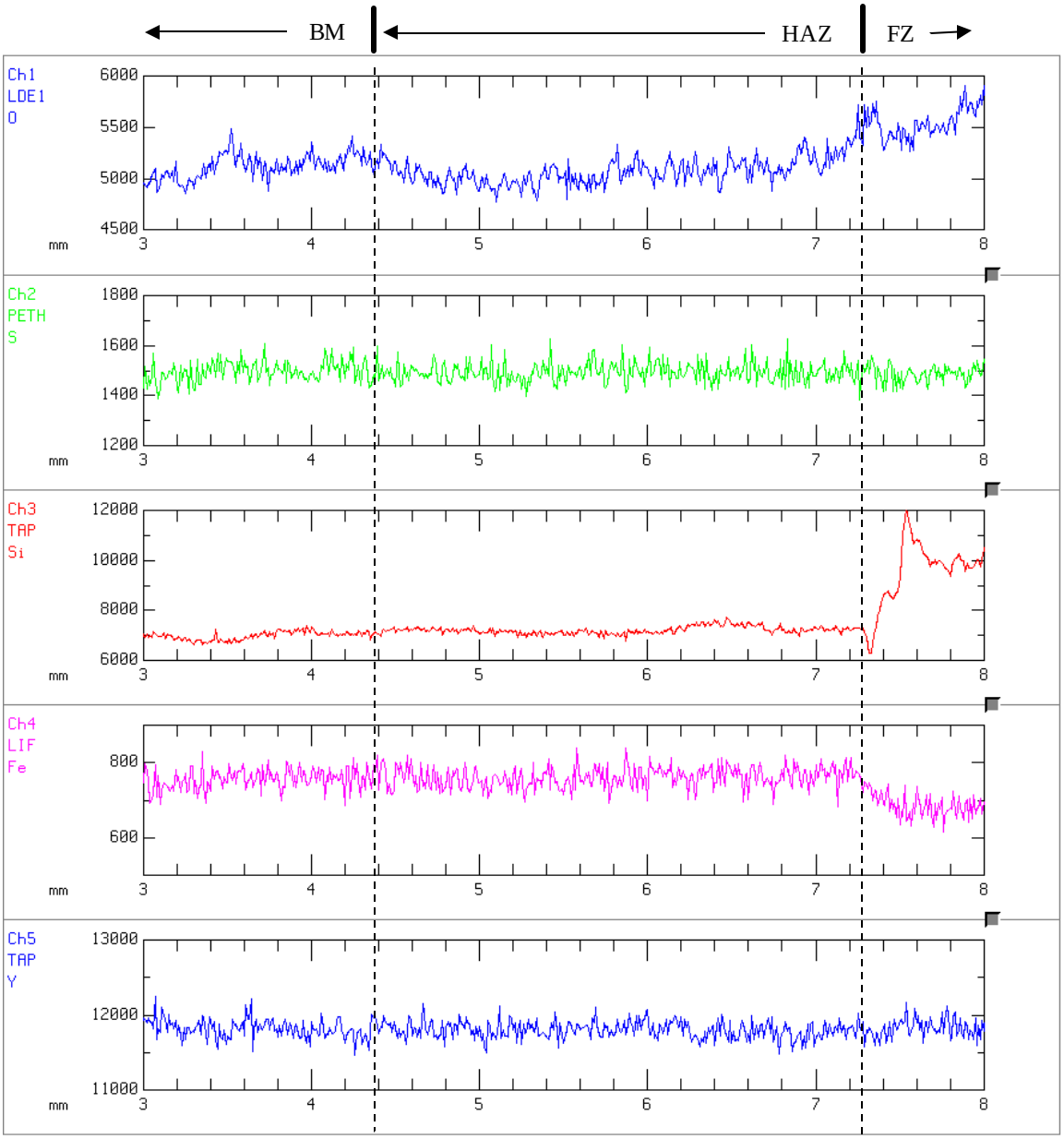

Figure 141: WDS scan of Ti5111 modified 200 ppm Y filler metal weld showing expanded HAZ area from Figure 61 (2000ms dwell time). Elements O, S, Y, Si, Fe. Observe that the O levels from the BM to FZ correspond very similarly to that of the matching and modified 50 ppm Y filler metal with the exception that there is neither a strong valley nor peak in concentration at the BM/HAZ interface.

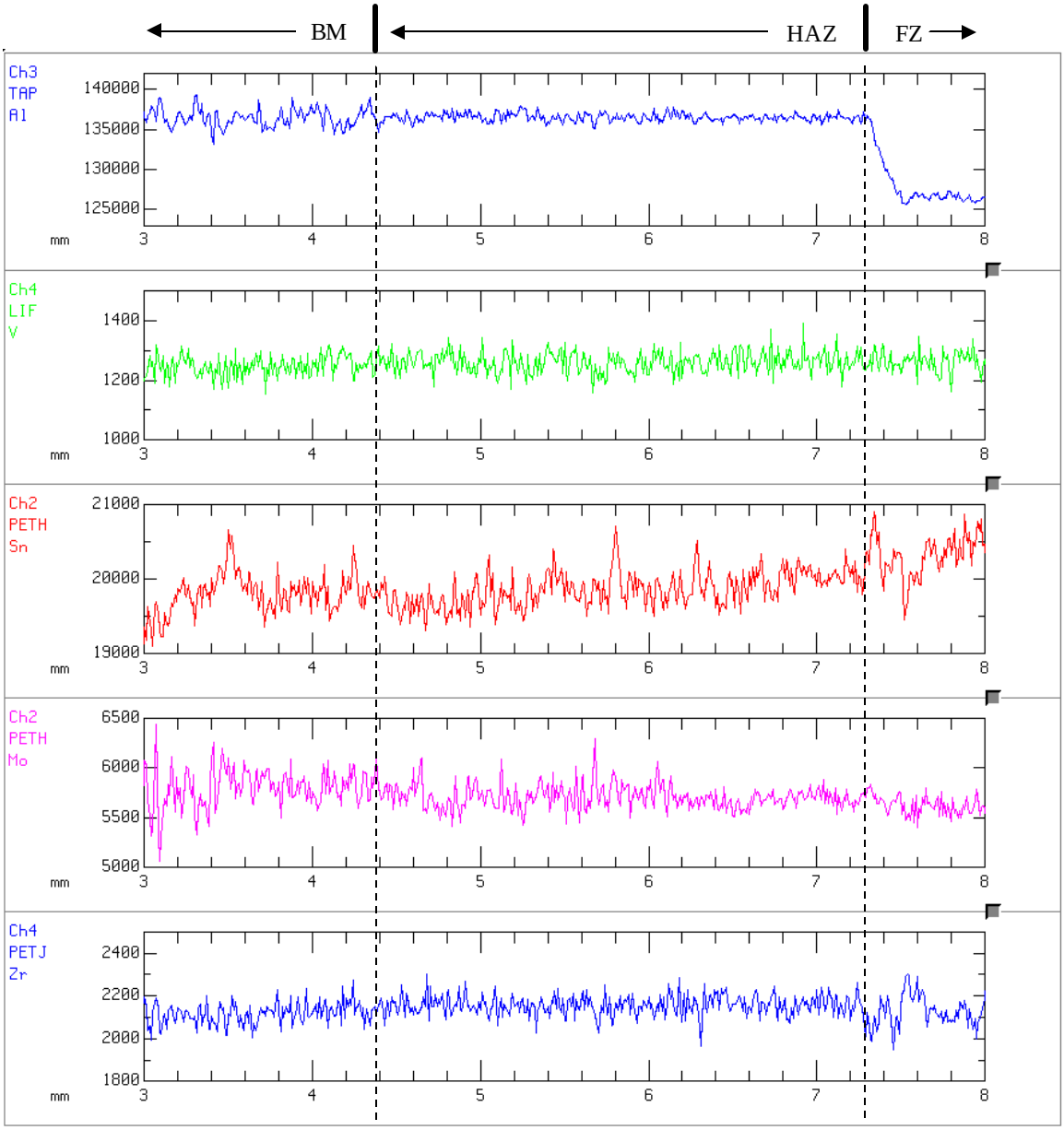

Figure 142: WDS scan of Ti5111 modified 200 ppm Y filler metal weld showing expanded HAZ area from Figure 62 (2000ms dwell time). Elements Al, V, Sn, Mo, Zr.

REFERENCES

1. E.W. Collings, The Physical Metallurgy of Titanium Alloys, ASM International, 1984, p. 1-4, 39-48, 85-91
2. Allegheny Technologies, http://www.alleghenytechnologies.com
3. R.T. Webster, Welding of Titanium Alloys, ASM Handbook, Volume 6, ASM International, 1993, p. 783-786
4. S. Kou, Welding Metallurgy, 2nd Edition, John Wiley & Sons, Inc., 2003
5. T. Mohandas, D. Banerjee, V.V. Kutumba Rao, "Observations on Impact Toughness of Electron Beam Welds of an α+β Titanium Alloy," Materials Science and Engineering A, Vol. 254A, 1998, p.147-154
6. K. Keshava Murthy, S. Sundaresan, "Fatigue Crack Growth Behavior in a Welded α-β Ti-Al-Mn Alloy in Relation to Microstructural Features," Materials Science and Engineering A, Vol. 222A, 1997, p. 201-211
7. G.K Hicken, Gas Tungsten Arc Welding, ASM Handbook, Volume 6, ASM International, 1993, p. 190-195
8. S. Sundaresan, G.D. Janaki Ram, G. Madhusudhan Reddy, "Microstructural Refinement of Weld Fusion Zones in α-β Titanium Alloys Using Pulsed Current Welding," Materials Science and Engineering A, Vol. 262A, 1999, p. 88-100
9. K. Keshava Murthy, S. Sundaresan, "Phase Transformations in a Welded Near-α Titanium Alloy as a Function of Weld Cooling Rate and Post-Weld Heat Treatment Conditions," Journal of Materials Science, Vol. 33, No. 3, 1998, p.817-826

10. K. Keshava Murthy, N.C. Sekhar, S. Sundaresan, "Thermomechanical Processing of Welded α+β Ti-Al-Mn Alloy and its Effect on Microstructure and Mechanical Properties," Materials Science and Technology, Vol. 13, No. 4, 1997, p. 343-348
11. J.W. Elmer, J. Wong, M. Fröba, P.A. Waide, E.M. Larson, "Analysis of Heat-Affected Zone Phase Transformations Using In Situ Spatially Resolved X-Ray Diffraction with Synchotron Radiation," Metallurgical and Materials Transactions A, Vol. 27A, No. 3, 1996, p. 775-783
12. T. Mohandas, D. Banerjee, V.V. Kutumba Rao, "Fusion Zone Microstructure and Porosity in Electron Beam Welds of an α+β Titanium Alloy," Metallurgical and Materials Transactions A, Vol. 30A, No. 3A, 1999, p. 789-798
13. D.J. Abson, R.J. Pargeter, "Factors Influencing As-Deposited Strength, Microstructure, and Toughness of Manual Metal Arc Welds Suitable for C-Mn Steel Fabrications," International Metals Reviews, Vol. 31, No. 4, 1986, p. 141-194
14. A.F. Norman, V. Drazhner, P.B. Prangnell, "Effect of Welding Parameters on the Solidification Microstructure of Autogenous TIG Welds in an Al-Cu-Mg-Mn alloy," Materials Science and Engineering A, Vol. 259, 1999, p. 53-64
15. R.E. Lewis, W.C. Coons, F.A. Crossley, I.L. Caplan, W.E. Lukens, "The Effect of Boron on Weldment Microstructures in the Ti-6Al-2Nb-1Ta-1Mo Alloy," Titanium Science and Technology, Proceedings of the Fifth International Conference on Titanium, 1984, Munich, FRG, September 10-14, 1984, Edited by G. Lütjering, U. Zwicker, W. Bunk, p. 799-805
16. G.R. Seagle, G.S. Hall, H.B. Bomberger, "Effect of Yttrium on the Microstructure of Titanium Alloys," Titanium'80 Science and Technology, Proceedings of the Fourth

International Conference on Titanium, Kyoto, Japan, May 19-22, 1980, Edited by H. Kimura and O. Izumi, p. 2169-2175

17. B.B. Rath, B.A. MacDonald, S.M.L. Sastry, R.J. Lederich, J.E. O'Neal, C.R. Whitsett, "Influence of Erbium and Yttrium Additions on the Microstructure and Mechanical Properties of Titanium Alloys, " Titanium'80 Science and Technology, Proceedings of the Fourth International Conference on Titanium, Kyoto, Japan, May 19-22, 1980, Edited by H. Kimura and O. Izumi, p.1185-1196
18. S. Ankem, G.K. Scarr, J.C. Williams, "The Effect of Yttrium on Hot Workability of Ti-5Al Alloy," Titanium – Science and Technology, Proceedings of the Fifth International Conference on Titanium, Munich, FRG, September 10-14, 1984, Edited by G. Lütjering, U. Zwicker, W. Bunk, p. 531-538
19. R.P. Simpson, "Controlled Weld-Pool Solidification Structure and Resultant Properties with Yttrium Inoculation of Ti-6Al-6V-2Sn Welds," Welding Journal, Vol. 56, No. 3, 1977, p. 67s-77s
20. J.W. Chasteen, M.H. Horowitz, "Some Effects of Yttrium on Ti-5522S Alloy Welds," Welding Journal, Vol. 57, No. 7, 1978, p. 196s-200s
21. M.S. Misra, D.L. Olson, G.R. Edwards, "The Influence of Process Parameters and Specific Additions on Epitaxial Growth in Multiple Pass Ti-6Al-4V Welds," Grain Refinement in Castings and Welds, Proceedings, Symposium, St. Louis, MO, 25-26 Oct. 1982, 1983, p. 259-274
22. M.C. Nordin, G.R. Edwards, D.L. Olson, "The Influence of Yttrium Microadditions on Titanium Weld Cracking Susceptibility and Grain Morphology," Welding Journal Supplement, Vol. 66, No. 11, 1987, p. 342s-352s

23. Ti-Y: J.L. Murray, 1987, p. 2•379, Binary Alloy Phase Diagrams, ASM Handbook, Volume 3: Alloy Phase Diagrams, ASM International, 1992

24. Y-O: O.N. Carlson, 1990, p. 2•326, Binary Alloy Phase Diagrams, ASM Handbook, Volume 3: Alloy Phase Diagrams, ASM International, 1992

25. S. Ankem, S.R. Seagle, G.K. Skarr, J.C. Williams, "Heat Affected Zone Softening in Ti-6211," Presented at 1985 TMS-AIME Annual Meeting

26. Annual Book of ASTM Standards, "Standard Specification for Titanium and Titanium Alloy Strip, Sheet, and Plate," Designation B 265-98, Vol. 02.04, 2003, p. 159-166

27. Annual Book of ASTM Standards, "Standard Test Methods for Tension Testing of Metallic Materials," Designation E 8-00b, Vol. 03.01, 2003, p. 56-76

28. W.F. Hosford, Tensile Testing, Edited by Patricia Han, ASM International, Materials Park, OH, 1992, p. 1-24

29. G.E. Dieter, Mechanical Metallurgy, McGraw-Hill, Inc., New York, NY, 1986, p. 241-272

30. B.V. Whiteson, A. Phillips, V. Kerlins, R.A. Rawe, "Special Fractographic Techniques for Failure Analysis," Electron Fractography, Seventh Annual Mtg ASTM, Boston, MA, 25-30 June 1967, ASTM Special Technical Publication No. 436, ASTM, Philadelphia, PA, 1968, p. 151-178

31. H.L. Ewalds., R.J.H. Wanhill, Fracture Mechanics, Edward Arnold Ltd., Baltimore, MD, 1984

32. R.J. Sanford, Principles of Fracture Mechanics, Pearson Education, Inc., Upper Saddle River, NJ, 2003

33. G.R. Irwin, "Analysis of Stresses and Strains Near the End of a Crack Traversing a Plate," Journal of Applied Mechanics, Vol. 24, 1957, p. 361-364

34. A.A. Griffith, "The Theory of Rupture," First International Congress for Applied Mechanics Proceedings, Edited by: C.B. Bienzo and J.M. Burgers, 1925, p. 55-63

35. M.F. Kanninen, C.H. Popelar, Advanced Fracture Mechanics, Oxford University Press, New York, NY, 1985

36. Annual Book of ASTM Standards, "Standard Test Methods for Measurement of Fracture Toughness," Designation E 1820-99a, Vol. 03.01, 2003, p. 1000-1033

37. H.E. Boyer, Hardness Testing, Material Compiled by ASM Committee on Hardness Testing, ASM International, 1987

38. Annual Book of ASTM Standards, "Standard Test Methods for Microindentation Hardness of Materials," Designation E 384-99, Vol. 03.01, 2003, p. 427-434

39. D.W. Moon, S.G. Lambrakos, R.J. Wong, E.A. Metzbower, "Macrostructure, Hardness, and Temperature in HSLA100 Steel Weld," Science and Technology of Welding and Joining, Vol. 8, No. 2, 2003, p. 95-101

40. G. Spanos, D.W. Moon, R.W. Fonda, E.S.K. Menon, A.G. Fox, "Microstructural, Compositional, and Microhardness Variations Across a Metal Arc Weldment Made with an Ultralow-Carbon Consumable," Metallurgical and Materials Transactions A, Vol. 32A, Dec. 2001, p. 3043-3054

41. H. Li, L. Salamanca-Riba, "The Concept of High Angle Wedge Polishing and Thickness Monitoring in TEM Sample Preparation," Ultramicroscopy, Vol. 88, No. 3, p. 171-178, Aug. 2001

42. T.A. Carlson, Photoelectron and Auger Spectroscopy, Plenum Press, 1975, p. 68-76

43. NIST X-ray Photoelectron Spectroscopy Database, http://srdata.nist.gov/xps/

44. R.P. Vasquez, "XPS Core Level Spectra of Some Y Compounds," Journal of Electron Spectroscopy and Related Phenomena, Vol. 50, 1990, p. 167-170

45. D.D. Wagman, W.H. Evans, V.B. Parker, R.H. Schumm, I. Halow, S.M. Bailey, K.L. Churney, R.L. Nuttall, "The NBS tables of chemical thermodynamic properties, Selected values for inorganic and C_1 and C_2 organic substances in SI units," Journal of Physical and Chemical Reference Data, Vol. 11, Supplement No. 2, 1982, Tables 57 & 61, p. 2-209 & 2-216-217

46. C.B. Alcock, "Gibbs Energy of Formation of Metal Oxides," CRC Handbook of Chemistry and Physics, 75th Edition, Eds: D.R. Lide, H.P.R. Frederikse, CRC Press, 1994-95, p. 5-72 – 5-73

47. F.D. Richardson, J.H.E. Jeffes, Metal-Metal Oxide Equilibria Plot, Journal of the Iron and Steel Institute, Vol. 160, The Metals Society, 1948, p. 263

48. O.F. Devereux, Topics in Metallurgical Thermodynamics, Wiley & Sons, 1983, p. 82-89

49. S. Ankem, G.K. Scarr, I.L. Caplan, J.C. Williams, S.R. Seagle, H.B. Bomberger, "Multiple Regression Analysis of the Effects of Various Alloying Elements on the Properties of Titanium Alloys," Sixth World Conference on Titanium, Proceedings – Part I, France, June 6-9, 1988, Edited by: P. Lacombe, R. Tricot, G. Beranger, p. 265-268

50. C.R. Heiple and J.R. Roper, "Mechanism for Minor Element Effect on GTA Fusion Zone Geometry," Welding Journal, Vol. 61, No. 4, April, 1982, p. 97s-102s

51. K.C. Mills and B.J. Keene, "Factors Affecting Variable Weld Penetration," International Materials Reviews, Vol. 35, No. 4, 1990, p. 185-216

52. A. Matsunawa, S. Yokoya, "Fluid Flow and its Effect on Penetration Shape in Stationary Arc Weld," Recent Trends in Welding Science and Technology, TWR'89, Proceedings of the 2nd International Conference on Trends in Welding Research, Gatlinburg, TN, May 14-18, 1989, Edited by: S.A. David and J.M. Vitek, ASM International, 1990, p. 31-35

53. T. Zacharia, S.A. David, J.M Vitek, H.G. Kraus, "Computational Modeling of Stationary Gas-Tungsten-Arc Weld Pools and Comparison to Stainless Steel 304 Experimental Results," Metallurgical Transactions B, Vol. 22B, No. 2, Apr. 1991, p. 243-257

54. Y. Wang, Q. Shi, H.L. Tsai, "Modeling the Effects of Surface-Active Elements on Flow Patterns and Weld Penetration," Metallurgical and Materials Transactions B, Vol. 32B, February, 2001, p. 145-161

55. R.W. Messler, Jr., Principles of Welding, John Wiley & Sons, Inc., 1999

56. M.W. Nathans, W.W. Wendlandt, "The Thermal Decomposition of the Rare Earth Sulfates," Journal of Inorganic and Nuclear Chemistry, Vol. 24, 1962, p. 869-879

57. R.G. Wells, "Nonmetallic and Intermetallic Phases Containing Rare Earths in Low Alloy Steels Treated with Mischmetal Alloys," The Rare Earths in Modern Science and Technology, Ed by G.J. McCarthy and J.J. Rhyne, Plenum Press, NY, 1979, p.341-346

58. D. Ting, W. Longmei, "Interaction Between Yttrium and Oxygen, Sulfur, Carbon in Liquid Iron," New Frontiers in Rare Earth Science and Applications, Proceedings of

the International Conference on Rare Earth Development and Applications, Beijing, China, September 10-14, 1985, Ed. By S. Guangxian and X. Jimei, Academic Press, 1985, p.1238-1242

59. W. Longmei, D. Ting, "A Study of Some Thermodynamic Properties of Rare Earth Elements in Liquid Nickel and Aluminum," New Frontiers in Rare Earth Science and Applications, Proceedings of the International Conference on Rare Earth Development and Applications, Beijing, China, September 10-14, 1985, Ed. By S. Guangxian and X. Jimei, Academic Press, 1985, p.1165-1169
60. D.A.R. Kay, R.K. Dwivedi, R.V. Kumar, "The High Temperature Thermodynamics of the La-O-S System," ," New Frontiers in Rare Earth Science and Applications, Proceedings of the International Conference on Rare Earth Development and Applications, Beijing, China, September 10-14, 1985, Ed. By S. Guangxian and X. Jimei, Academic Press, 1985, p.1204-1208
61. K.T. Jacob, R. Akila, A.K. Shukla, "Oxygen Potentials for the Oxidation of Rare Earth Oxysulfides to Oxysulfates," Journal of Solid State Chemistry, Vol. 69, 1987, p. 109-115
62. Q. Yang, Y. Zhao, Y. Li, M. Yao, "Thermodynamics of Modifying Effect of Rare Earth Oxide on Inclusions in Hardfacing Metal of Medium-High Carbon Steel," Journal of Rare Earths, Vol. 20, No. 4, 2002, p. 291-294
63. J.J. Moore, Chemical Metallurgy, Butterworth & Co. Ltd, 2nd ed., 1990, p. 127-151
64. G.A. Chadwick, Metallography of Phase Transformations, Crane, Russak & Co. Inc., 1972, p. 58-159

65. G. Thewlis, J.A. Whiteman, D.J. Senogles, “Dynamics of Austenite to Ferrite Phase Transformation in Ferrous Weld Metals,” Materials Science and Technology, Vol. 13, No. 3, 1997, p. 257-274

66. D. Turnbull, "Kinetics of Heterogeneous Nucleation," Journal of Chemical Physics, Vol. 18, 1950, p. 198-203

67. J.W. Rutter, B. Chalmers, “A Prismatic Substructure Formed During Solidification of Metals,” Canadian Journal of Physics, Vol. 31, 1953, p. 15-39

68. W.F. Savage, C.D. Lundin, H. Aronson, “Weld Metal Solidification Mechanics,” Welding Journal, Vol. 44, No. 4, 1965, p. 175s-181s

69. W.F. Savage, A.H. Aronson, “Preferred Orientation in the Weld Fusion Zone,” Welding Journal, Vol. 45, No. 2, 1969, p. 85s-89s

70. J. Wong, M. Fröba, J.W. Elmer, P.A. Waide, “In-Situ Phase Mapping and Transformation Study in Fusion Welds,” Journal of Materials Science, Vol. 32, No. 6, 1997, p. 1493-1500

71. Z. Liu, G. Welsch, “Literature Survey on Diffusivities of Oxygen, Aluminum, and Vanadium in Alpha Titanium, Beta Titanium, and in Rutile,” Metallurgical Transactions A, Vol. 19A, No. 4, 1988, p. 1121-1125

72. R.P. Chhabra, A.K. Roy, “Diffusivity of Oxygen and Nitrogen in Liquid Metals: An Explicit Formation,” Zeitschrift fur Metallkunde, Vol. 79, No. 1, 1988, p. 64-67

73. Phase Diagrams of Binary Titanium Alloys, Ed. By J.L. Murray, ASM International, 1987